THEORETICAL METHODS FOR BLUR-CORRECTION IN ELECTRON AND SOFT X-RAY MICROSCOPY

by

JOANNA KLUKOWSKA

A dissertation submitted to the Graduate Faculty in Computer Science

in partial fulfillment of the requirements for the degree of

Doctor of Philosophy, The City University of New York

2013

This manuscript has been read and accepted for the
Graduate Faculty in Computer Science in satisfaction of the
dissertation requirements for the degree of Doctor of Philosophy.

Dr. Gabor T. Herman

Date — Chair of Examining Committee

Dr. Robert Haralick

Date — Executive Officer

Dr. T. Yung Kong

Dr. Ioannis Stamos

Dr. José-María Carazo

Supervisory Committee

THE CITY UNIVERSITY OF NEW YORK

Abstract

Theoretical Methods for Blur-Correction in Electron
and Soft X-ray Microscopy

by

Joanna Klukowska

Adviser: Dr. Gabor T. Herman

The process of object reconstruction from projections is widely used in many fields. One of the applications is the reconstruction of biological specimens from two-dimensional projections in transmission electron microscopy and transmission x-ray microscopy. Various methods have been developed for correcting the blurring that occurs when the projections are obtained by a real instrument. As the attainable resolution increases, new issues become apparent and need to be taken into account in the imaging model. In this dissertation we concentrate on the point spread function and its impact on the quality and usefulness of the reconstructions from images obtained according to image formation models for the two types of microscopy. Specifically, we consider spatial variance of the point spread function in the direction of the electron or x-ray propagation. The correction methods for this type of blurring in both cases are related, but not identical due to nature of the respective imaging processes. We propose correction methods and demonstrate their efficacy using computer simulations.

To my husband, whose love and support brought me to this point.

Acknowledgments

Writing this dissertation signifies the end of my academic career as a student. It would not have been possible without the encouragement, guidance and support of a great many people and the financial support of several funding agencies.

I would like to thank my adviser, Dr. Gabor T. Herman. His accessibility and responsiveness has always been appreciated! His commitment to guide and mentor was always above my expectations. He made the journey through the research projects fascinating, engaging and challenging. I always admired his knowledge and expertise, and his ability to turn seemingly complicated concept into straight forward ideas accessible to students. I hope I can follow in his footsteps in my own career.

A special thanks goes to the rest of my committee members: Dr. T. Yung Kong, Dr. Ioannis Stamos and Dr. José-María Carazo. I would like to thank them for contributing their time and ideas and making themselves available despite their busy schedules. They have been great teachers and mentors and invaluable research collaborators.

There are many other members of the CUNY community whom I wish to recognize for making the completion of my work possible. I thank Dr. Robert Haralick for numerous discussions about my research projects during my talks in many seminars. I thank Dr. Paul Gottlieb and Dr. Al Katz for discussions on electron tomography that greatly increased my understanding of the field. I thank Dr. Amotz Bar-Noy for guiding me through the first couple of years of graduate school and providing me with an excellent introduction to research. I also thank Dr. Theodore Brown for his support as the Executive Officer of the computer science program and Dr. Virginia Teller for giving me the opportunity to teach at Hunter College.

I am grateful for the interactions I had with the many members and visitors of the Discrete Imaging and Graphics (DIG) Group throughout the years: Younes Benkarroum, Dr. Yair Censor, Dr. Wei Chen, Dr. Ran Davidi, Dr. Edgar Garduño, Dr. Miroslaw Kalinowski, Dr. Ivan Kazantsev, Dr. Hstau Liao, Lucas de Melo Oliveira, Dr. Stuart Rowland, and Dr. Eilat Vardi-Gonen. Their friendship and assistance were invaluable.

I am grateful to our collaborators from the National Center for Biotechnology of Madrid University, specifically to Dr. José-María Carazo, Dr. Joaquín Otón, Dr. Roberto Marabini and Dr. Carlos Oscar Sánchez Sorzano, and to Dr. Joachim Frank from Columbia University. Their contribution to my interdisciplinary research was very important.

I thank Lina Garcia and Joseph Driscoll for their help with all my needs over the years at the Graduate Center and Hunter College.

I would like to acknowledge the financial support I received along the way. I was supported through Dr. Gabor Herman's grants from National Institute of Health (grant number HL070472) and National Science Foundation (grant number DMS-1114901). I was a recipient of the Science Fellowship and several Doctoral Student Research Grants from the Graduate Center of CUNY. Without this support the work on this dissertation would have been much harder.

Finally, I would like to thank my family: my husband Stewart and my daughter Shayna for believing in me, for their support and endless patience. Without them I would not have been able to reach this destination.

Contents

List of Tables

List of Figures

Nomenclature

$\Rightarrow$	operator mapping
$\circ$	Hadamard product (element-wise product) of two matrices of the same size
$\rightarrow$	function mapping
$*$	convolution operator, see Eq. (2.18)
δ	Dirac delta, see Eq. (A.1)
$\mathscr{A}^{3t}$	tomographic attenuation operator, see Eq. (5.4)
$\mathscr{A}^{n}$	attenuation operator, see Eq. (5.1)
$\mathscr{B}^{n}$	backprojection operator, see Eq. (2.28)
$\mathscr{B}^{3t}$	tomographic backprojection operator, see Eq. (2.32)
$\mathscr{B}_{h}^{n}$	distance-dependent backprojection operator, see Eq. (4.7)
$\mathscr{C}^{n}$	compressing operator, see Eq. (2.21)
$\mathscr{C}^{3t}$	tomographic compressing operator, see Eq. (2.24)
$\mathscr{C}_{h}^{n}$	distance-dependent compressing operator, see Eq. (4.1)
$\mathscr{D}^{n}$	deblurring operator, see Eq. (2.29)
D_2	2D rotation matrix, see Eq. (2.1)

$D_3, D_{3,\theta_1}, D_{3,\theta_2}$	3D rotation matrices, see Eqs. (2.2) and (2.3)
$\mathscr{F}$	Fourier transform operator; see Eq. (2.15)
$\mathscr{F}^{-1}$	inverse Fourier transform operator; see Eq. (2.16)
$\lvert J(\boldsymbol{\theta})\rvert$	determinant of the Jacobian matrix, see page 14
$\mathscr{K}$	slicing operator, see Eqs. (2.12) - (2.14)
$\mathscr{N}$	ray transform operator, see Eq. (2.33)
$\mathscr{P}^n$	projection operator, see Eq. (2.22)
$\mathscr{P}^{3t}$	tomographic projection operator, see Eq. (2.25)
$\mathscr{P}_h^n$	distance-dependent projection operator, see Eq. (4.2)
$\mathbb{R}$	the set of all real numbers
$\mathscr{R}^n$	rotation operator, see Eq. (2.20)
$\mathscr{R}^{3t}$	tomographic rotation operator, see Eq. (2.23)
R_{01}^n	n-dimensional column vector with $n-1$ zeros, followed by a one in the last postion
R_{10}^n	n-dimensional column vector with $n-1$ ones, followed by a zero in the last postion
$\mathbb{S}^1$	$[0,2\pi)$ is the set of directions on the unit circle in $\mathbb{R}^2$
$\mathbb{S}^2$	$[0,2\pi)\times[0,\pi)$ is the set of directions on the unit sphere in $\mathbb{R}^3$
$\mathscr{S}^n$	spreading back operator, see Eq. (2.26)
$\mathscr{S}^{3t}$	tomographic spreading back operator, see Eq. (2.30)
$\mathscr{S}_h^n$	distance-dependent spreading back operator, see Eq. (4.6)
$\mathscr{T}^n$	totaling operator, see Eq. (2.27)

$\mathscr{T}^{3t}$	tomographic totaling operator, see Eq. (2.31)
$\mathscr{W}$	backprojection operator for ray transform, see Eq. (2.34)
$\mathscr{X}^{3t}$	tomographic attenuated projection operator, see Eq. (5.5)
$\mathscr{X}^{n}$	attenuated projection operator, see Eq. (5.2)
$\mathscr{X}_h^{3t}$	tomographic distance-dependent attenuated projection operator, see Eq. (5.6)
$\mathscr{X}_h^{n}$	distance-dependent attenuated projection operator, see Eq. (5.3)

Chapter 1

Problem Statement

The process of object reconstruction from projections is widely used in many fields. A projection of an object is an image obtained by a device, for example a microscope. In the ideal case such image is a set of (approximate) line integrals obtained along parallel lines going through the object that are perpendicular to a projection image plane. Unfortunately, due to physical interaction of radiation used for imaging (light, electrons, x-rays) with the sample and the imaging device itself, what is recorded as a projection may not be very much like mathematical line integrals. In this thesis we discuss distance-dependent blurring that is among the many factors that cause the actual images obtained by imaging devices to contain only approximations to the ideal line integrals through the sample. We demonstrate how distance-dependent blurring effects change in the presence of other effects, specifically attenuation that affects imaging techniques using x-rays. The contribution of this thesis is the development of correction techniques that can be used to improve the quality of reconstructions that are computed from projections affected by distance-dependent blurring.

The process of reconstruction uses the projection data to obtain an approximation of the original object. In our work we handle two-dimensional (2D) and three-dimensional (3D) objects. Each projection taken of a 2D object is a one-dimensional (1D) array of numbers. Each projection taken of a 3D object is a 2D array of numbers that is often represented by an image in which grayscale values of pixels are related to the projection values at corresponding sample points. One

of the applications of reconstruction from projections is in three-dimensional microscopy: given 2D images of the specimen obtained using a microscope, the task is to create a 3D model of the specimen. The material presented in this thesis is directly relevant to transmission electron microscopy (TEM) and transmission x-ray microscopy (TXM) of biological specimens.

In the field of image reconstruction from projections, the imaging process is often referred to as a forward problem - it is a mathematical description of the physical process by which the images are created. Understanding of the forward problem is crucial for reconstruction, because the forward problem describes the relationship between the images and the unknown object. Often, useful reconstructions can be produced even without accurate knowledge of the forward problem, but they could be improved (and hence in most cases provide more information) if the reconstruction process took into account a more accurate image formation model. A trivial example of such behavior is an imaging system that records only half of the value that would have been recorded by true line integral computation through the object. If we reconstruct ignoring that fact, the values in the reconstruction will not reflect accurately the values in the original object. But if we know that behavior of the imaging system, the values of projection images can be corrected by simple multiplication by the factor of two, and then correct values will be recovered in the reconstruction.

Transmission electron microscopy is used for imaging thin specimens. The images are formed based on the interaction of the electron wave as it passes through the sample. Electron microscopy allows viewing of much more details than light microscopy due to a smaller wavelength of the electrons as compared to visible light. The limiting factor is electron penetration depth that restricts the thickness of samples that can be used in an electron microscope. For a brief overview of applications of TEM in different areas see Jensen and Briegel [26] and Midgley et al. [38]. General recent reviews of issues related to electron microscopic reconstruction are provided by Reimer and Kohl [43], Midgley et al. [38], Frank [15], Fernandez et al. [14], and Leis et al. [35].

Transmission x-ray microscopy of biological specimens is a relatively new field, see Jacobsen et al. [25] and Kirz et al. [29] for early work on imaging of biological samples using soft x-rays. This imaging technique takes advantage of the so-called water window (x-ray energies between

280 eV and 517 eV, equivalently wavelengths between 2.34 nm and 4.4 nm) in which the contrast between protein and water is very high; see Attwood [1] and Weiss et al. [52]. X-rays at this energy range can penetrate into biological matter up to a depth of 15 μm [34, 39], which is much more than what can be achieved using electrons. This allows for TXM imaging of entire cells intact in their native aqueous environment. The resolution of images and reconstructions obtained using x-rays is higher than using light microscopy since the wavelength of x-rays is smaller than that of light. The microscopes are placed on beam-lines of synchrotrons in order to obtain monochromatic x-rays of appropriate energy. At the time of writing this dissertation, TXM for biological samples is performed using Bessy II in the Helmholtz Zentrum[1] in Berlin, the Advanced Light Source[2] in Berkeley, CA, and the MISTRAL beam-line at ALBA[3] near Barcelona. For recent reviews of use and applications of TXM see, for example, Howells et al. [24], McDermott et al. [37], Leis et al. [34], Falcone et al. [12], and Müller et al. [39]. In addition to microscopes at synchrotrons, more recently, there have been attempts at using laboratory scale transmission soft x-ray microscopes based on laser-plasma sources, see, for example, Hertz et al. [23] and Carlson et al. [3]. In this thesis we only discuss matters related to synchrotron-based TXM.

There are multiple issues affecting both TEM and TXM images. They include extremely low signal-to-noise ratio, missing data for some directions, limited number of projection images, sample degradation during the imaging process, need to estimate from the images some of the parameters of the forward model and need for data alignment before reconstruction. We concentrate only on the issue of the distance-dependent blurring (also known as defocus-gradient effect) that is present in both TEM and TXM. As the electrons or x-rays pass through the object their interaction with each layer of the object changes. Since the objects are transparent to electrons and x-rays, the projection data contains overlaps of all the layers blurred in different ways. The traditional approaches to deblurring assume that each part of the image is blurred in the same way and hence, they cannot handle the data that are affected by distance-dependent blurring. We discuss methods

[1] http://www.helmholtz-berlin.de/
[2] http://www-als.lbl.gov/
[3] https://www.cells.es/Beamlines/XM/

of dealing with such blurring in order to improve the quality of the reconstructions. Some of our results relevant to TEM were published in Klukowska et al. [31] and Kazantsev et al. [28]. The preliminary results relevant to TXM will appear in a book chapter by Klukowska and Herman [30] and further results will be submitted for publication in the near future.

Chapter 2

Background

In this chapter we discuss background information necessary for development of our work. In Section 2.1, we cover some of the mathematical notation used in the rest of this manuscript. In Sections 2.2 and 2.3 we define the mathematical operators that describe the image formation model and its inversion when the projections are in the form of mathematical line integrals. We prove that, in the mathematical limit, these operators can be used to reconstruct the original object exactly. The stationary phase approximation is briefly reviewed in Section 2.4. Finally, we discuss different data collection geometries in Section 2.5.

2.1 Mathematical Notation and Conventions

Let $X_1, \ldots, X_n$ be the coordinate axes of an n-dimensional (nD) Cartesian coordinate system. In our applications $n \in \{2,3\}$. We restate this fact in theorems and definitions for more clarity. It is common in biological reconstruction from projections literature to attach the coordinate system to the object to be reconstructed, i.e., a specimen. The imaging device, i.e., a microscope, is treated as if it were rotating around this object during the imaging process to obtain views from various directions. We follow a different, but equivalent, convention. Our coordinate system is attached to the imaging device. The X_n-axis is always parallel to the imaging direction. Thus it is the object to be reconstructed that is rotated to obtain various projections. This allows for a

simpler mathematical description of distance dependent-blurring than what would be needed using the more common convention.

2.1.1 Spaces of Vectors and Functions

We use several different spaces, $\mathbb{R}$, $\mathbb{R}^2$, $\mathbb{R}^3$, $\mathbb{C}$, $\mathbb{C}^2$, $\mathbb{C}^3$, $\mathbb{S}^1$, $\mathbb{S}^2$, and several spaces that are cross products of these. $\mathbb{R}$ is a set of all real numbers, $\mathbb{R}^2$ and $\mathbb{R}^3$ are short for $\mathbb{R}\times\mathbb{R}$ and $\mathbb{R}\times\mathbb{R}\times\mathbb{R}$, respectively. Similarly, $\mathbb{C}$ is a set of all complex numbers, $\mathbb{C}^2$ and $\mathbb{C}^3$ are short for $\mathbb{C}\times\mathbb{C}$ and $\mathbb{C}\times\mathbb{C}\times\mathbb{C}$, respectively. $\mathbb{S}^1 = [0, 2\pi)$ is the set of directions on the unit circle in $\mathbb{R}^2$, and $\mathbb{S}^2 = [0, 2\pi)\times[0, \pi)$ is the set of directions on the unit sphere in $\mathbb{R}^3$.

Let V_1 and V_2 be any two spaces. We use the term *function* to describe a mapping from V_1 to V_2. This mapping is denoted by a single right arrow, $\rightarrow$. For example, $v : V_1 \rightarrow V_2$ is a function that maps V_1 to V_2.

Functions that map a particular space into another particular space can be grouped into *function spaces*. For example, all functions that map $\mathbb{R}^3$ into $\mathbb{R}$ constitute a function space. Let G_1 and G_2 be any two function spaces. We use the term *operator* to describe a mapping of functions from G_1 to functions from G_2. This mapping is denoted by a double right arrow, $\Rightarrow$. For example, $\mathscr{G} : G_1 \Rightarrow G_2$ is an operator that maps a function $g_1 \in G_1$ to a function $g_2 \in G_2$. We do not define function spaces with complete mathematical rigor; such treatment can be found in Herman and Tuy [22] or in Natterer and Wübbeling [40]. We use spaces of functions that are general enough to include ordinary functions as well as generalized functions, such as the impulse functions defined based on the Dirac delta (see Appendix A for details). We adapted a notation for function spaces that gives an intuitive indication of the space under consideration, without any claim to mathematical rigor; for example, we will use $\left(\mathbb{R}^3 \rightarrow \mathbb{R}\right)$ to denote "the" space of all functions that map $\mathbb{R}^3$ into $\mathbb{R}$, but we leave the determination of exactly what kind of functions are included in the function space to the context in which the notation appears.

When we are imaging nD objects, with $n \in \{2, 3\}$, $\mathbb{R}^n$ is the vector space of the object to be reconstructed. We represent points in $\mathbb{R}^n$ using vectors, an arbitrary point is given by $\boldsymbol{x} =$

$(x_1,\ldots,x_n)^T$. Similarly, we use $\boldsymbol{\xi} = (\xi_1,\ldots,\xi_n)^T$ to represent points in the frequency domain. We denote by $v : \mathbb{R}^n \to \mathbb{R}$ the object being imaged. The value $v(\boldsymbol{x}) = v(x_1,\ldots,x_n)$ of the function v at a point $\boldsymbol{x} = (x_1,\ldots,x_n)^T$ is the value of the object at the appropriate place. $\mathbb{S}^{n-1} \times \mathbb{R}^n$ is the space of rotated objects. A point is specified by $(\boldsymbol{\theta},\boldsymbol{x})^T = (\theta_1,\ldots,\theta_{n-1},x_1,\ldots,x_n)^T$, where $\boldsymbol{\theta} = (\theta_1,\ldots,\theta_{n-1}) \in \mathbb{S}^{n-1}$ is an angle vector, referred to as an angle, that specifies how the object was rotated inside the imaging device and $\boldsymbol{x} = (x_1,\ldots,x_n)^T \in \mathbb{R}^n$ is a position vector that refers to the device's coordinate system. The value of a rotated object at $(\boldsymbol{\theta},\boldsymbol{x})^T$ for a fixed $\boldsymbol{x}$ is different for different values of $\boldsymbol{\theta}$. $\mathbb{R}^{n-1}$ is the space of single projection images. $\mathbb{S}^{n-1} \times \mathbb{R}^{n-1}$ is the space of projection data. An arbitrary point is given by $(\boldsymbol{\theta},x_1,\ldots,x_{n-1})^T$, where $(x_1,\ldots,x_{n-1})^T$ specifies a location in the projection and $\boldsymbol{\theta}$ specifies how the object was rotated before the projection was taken.

2.1.2 Rotation Matrices

We make use of the two and three dimensional rotation matrices. For an angle $\boldsymbol{\theta} = (\theta_1) \in \mathbb{S}^1$, the right-hand rotation matrix in the X_1X_2-plane in 2D is defined by:

$$D_2 = \begin{pmatrix} \cos\theta_1 & -\sin\theta_1 \\ \sin\theta_1 & \cos\theta_1 \end{pmatrix}. \tag{2.1}$$

For an angle $\boldsymbol{\theta} = (\theta_1,\theta_2) \in \mathbb{S}^2$, the rotation matrices in 3D are defined by:

$$D_{3,\theta_1} = \begin{pmatrix} \cos\theta_1 & -\sin\theta_1 & 0 \\ \sin\theta_1 & \cos\theta_1 & 0 \\ 0 & 0 & 1 \end{pmatrix}, D_{3,\theta_2} = \begin{pmatrix} \cos\theta_2 & 0 & \sin\theta_2 \\ 0 & 1 & 0 \\ -\sin\theta_2 & 0 & \cos\theta_2 \end{pmatrix}, \tag{2.2}$$

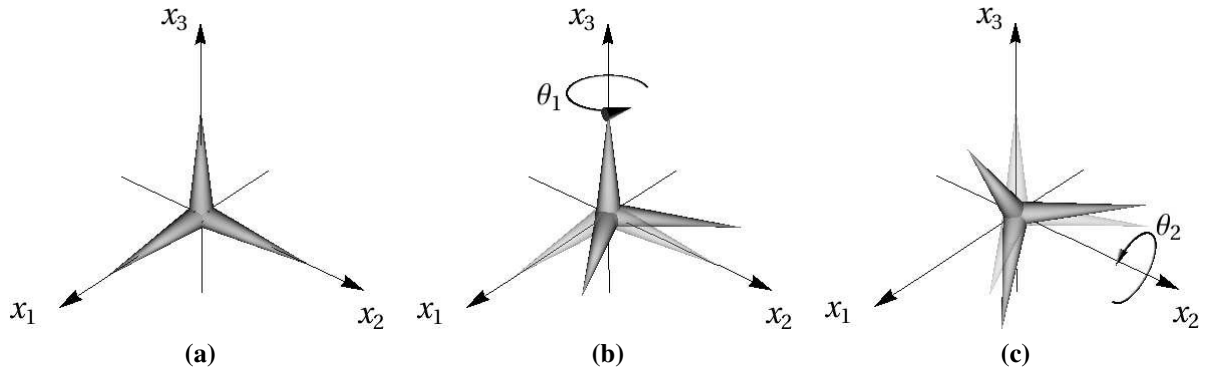

Figure 2.1: Rotations of a 3D object: (a) an object in its original position, (b) first rotation by θ_1 around X_3-axis using matrix D_{3,θ_1}, (c) second rotation by θ_2 around X_2-axis using matrix D_{3,θ_2}.

and

$$D_3 = D_{3,\theta_2} D_{3,\theta_1} = \begin{pmatrix} \cos\theta_1 \cos\theta_2 & -\sin\theta_1 \cos\theta_2 & \sin\theta_2 \\ \sin\theta_1 & \cos\theta_1 & 0 \\ -\cos\theta_1 \sin\theta_2 & \sin\theta_1 \sin\theta_2 & \cos\theta_2 \end{pmatrix}. \tag{2.3}$$

D_{3,θ_1} is a right-hand rotation by θ_1 in the X_1X_2-plane and D_{3,θ_2} is a right-hand rotation by θ_2 in the X_1X_3-plane, D_3 describes a rotation by θ_1 followed by a rotation by θ_2. The rotation of a 3D object is shown in Figure 2.1.

The inverse matrices of D_{3,θ_1}, D_{3,θ_2}

$$D^{-1}_{3,\theta_1} = \begin{pmatrix} \cos\theta_1 & \sin\theta_1 & 0 \\ -\sin\theta_1 & \cos\theta_1 & 0 \\ 0 & 0 & 1 \end{pmatrix}, \; D^{-1}_{3,\theta_2} = \begin{pmatrix} \cos\theta_2 & 0 & -\sin\theta_2 \\ 0 & 1 & 0 \\ \sin\theta_2 & 0 & \cos\theta_2 \end{pmatrix}, \tag{2.4}$$

are the left-hand rotation by θ_1 in the X_1X_2-plane and left-hand rotation by θ_2 in the X_1X_3-plane,

respectively. The inverse matrix of D_3 is

$$D_3^{-1} = D_{3,\theta_1}^{-1} D_{3,\theta_2}^{-1} = \begin{pmatrix} \cos\theta_1 \cos\theta_2 & \sin\theta_1 & -\cos\theta_1 \sin\theta_2 \\ -\sin\theta_1 \cos\theta_2 & \cos\theta_1 & \sin\theta_1 \sin\theta_2 \\ \sin\theta_2 & 0 & \cos\theta_2 \end{pmatrix}. \tag{2.5}$$

We also define the following vectors for shorter and clearer notation. Let $n \in \{2,3\}$, then

$$\boldsymbol{x}^F(\boldsymbol{\theta}) = D_n^{-1}\boldsymbol{x} \tag{2.6}$$

and

$$\boldsymbol{x}^B(\boldsymbol{\theta}) = D_n\boldsymbol{x}. \tag{2.7}$$

Given a point $\boldsymbol{x}$ in a rotated object, $\boldsymbol{x}^F(\boldsymbol{\theta})$ is this point's location before rotation. Similarly, given a point $\boldsymbol{x}$ in an object before rotation, $\boldsymbol{x}^B(\boldsymbol{\theta})$ is this point's location after rotation. F in Eq. (2.6) stands for forward, since it is used in forward model of data collection. B in Eq. (2.7) stands for back, since it is used in the reconstruction.

In the expanded form for $n = 2$ and $n = 3$ the vectors in Eqs. (2.6) and (2.7) are

$$\begin{pmatrix} x_1^F(\theta_1) \\ x_2^F(\theta_1) \end{pmatrix} = D_2^{-1} \begin{pmatrix} x_1 \\ x_2 \end{pmatrix} = \begin{pmatrix} x_1\cos\theta_1 + x_2\sin\theta_1 \\ -x_1\sin\theta_1 + x_2\cos\theta_1 \end{pmatrix}, \tag{2.8}$$

$$\begin{pmatrix} x_1^B(\theta_1) \\ x_2^B(\theta_1) \end{pmatrix} = D_2 \begin{pmatrix} x_1 \\ x_2 \end{pmatrix} = \begin{pmatrix} x_1\cos\theta_1 - x_2\sin\theta_1 \\ x_1\sin\theta_1 + x_2\cos\theta_1 \end{pmatrix}, \tag{2.9}$$

$$\begin{pmatrix} x_1^F(\theta_1,\theta_2) \\ x_2^F(\theta_1,\theta_2) \\ x_3^F(\theta_1,\theta_2) \end{pmatrix} = D_{3,\theta_1}^{-1} D_{3,\theta_2}^{-1} \begin{pmatrix} x_1 \\ x_2 \\ x_3 \end{pmatrix} = \begin{pmatrix} x_1\cos\theta_1\cos\theta_2 + x_2\sin\theta_1 - x_3\cos\theta_1\sin\theta_2 \\ -x_1\sin\theta_1\cos\theta_2 + x_2\cos\theta_1 + x_3\sin\theta_1\sin\theta_2 \\ x_1\sin\theta_2 + x_3\cos\theta_2 \end{pmatrix} \tag{2.10}$$

and

$$\begin{pmatrix} x_1^B(\theta_1,\theta_2) \\ x_2^B(\theta_1,\theta_2) \\ x_3^B(\theta_1,\theta_2) \end{pmatrix} = D_{3,\theta_2} D_{3.\theta_1} \begin{pmatrix} x_1 \\ x_2 \\ x_3 \end{pmatrix} = \begin{pmatrix} x_1\cos\theta_1\cos\theta_2 - x_2\sin\theta_1\cos\theta_2 + x_3\sin\theta_2 \\ x_1\sin\theta_1 + x_2\cos\theta_1 \\ -x_1\cos\theta_1\sin\theta_2 + x_2\sin\theta_1\sin\theta_2 + x_3\cos\theta_2 \end{pmatrix}. \tag{2.11}$$

2.2 Operators

We introduce several operators that are used in the rest of this manuscript.

Slicing Operators

The *slicing operators* are used for defining various Fourier transform and convolution operators. We use them when an operation, for example a Fourier transform, is performed with respect to a subset of variables for a given function. For mapping the functions $v \in \mathbb{R}^n \to \mathbb{R}$, $w \in \mathbb{S}^{n-1} \times \mathbb{R}^n \to \mathbb{R}$ and $g \in \mathbb{S}^{n-1} \times \mathbb{R}^{n-1} \to \mathbb{R}$ into functions of $n-1$ variables $x_1, \ldots, x_{n-1}$, they are defined by

$$\left[\mathscr{K}_{x_n} v\right](x_1,\ldots,x_{n-1}) = v(\boldsymbol{x}), \tag{2.12}$$

$$\left[\mathscr{K}_{\boldsymbol{\theta},x_n} w\right](x_1,\ldots,x_{n-1}) = w(\boldsymbol{\theta},\boldsymbol{x}), \tag{2.13}$$

$$\left[\mathscr{K}_{\boldsymbol{\theta}} g\right](x_1,\ldots,x_{n-1}) = g(\boldsymbol{\theta},x_1,\ldots,x_{n-1}). \tag{2.14}$$

Slicing operators for other function spaces can be defined in a similar way.

Fourier Transform Operators

The general *n-dimensional Fourier transform operator* $\mathscr{F} : (\mathbb{R}^n \to \mathbb{C}) \Rightarrow (\mathbb{R}^n \to \mathbb{C})$ and its inverse $\mathscr{F}^{-1} : (\mathbb{R}^n \to \mathbb{C}) \Rightarrow (\mathbb{R}^n \to \mathbb{C})$ are defined by

$$[\mathscr{F} f](\boldsymbol{\xi}) = (2\pi)^{-n/2} \int_{\mathbb{R}^n} f(\boldsymbol{x}) e^{-i\langle \boldsymbol{x}, \boldsymbol{\xi} \rangle} d\boldsymbol{x}, \tag{2.15}$$

$$\left[\mathscr{F}^{-1} f\right](\boldsymbol{x}) = (2\pi)^{-n/2} \int_{\mathbb{R}^n} f(\boldsymbol{\xi}) e^{i\langle \boldsymbol{x}, \boldsymbol{\xi} \rangle} d\boldsymbol{\xi}, \tag{2.16}$$

where $\boldsymbol{x} = (x_1, \ldots, x_n)^T$, $\boldsymbol{\xi} = (\xi_1, \ldots, \xi_n)^T$, and $\langle \boldsymbol{x}, \boldsymbol{\xi} \rangle = x_1\xi_1 + \ldots + x_n\xi_n$ denotes the inner product of $\boldsymbol{x}$ and $\boldsymbol{\xi}$.

For a function f in the function space that we denote by $(\mathbb{R}^n \to \mathbb{C})$ we have

$$\mathscr{F}^{-1}\mathscr{F} f = f. \tag{2.17}$$

We often apply the Fourier transform and its inverse only with respect to some of the variables involved in the function. Such Fourier transforms can be formally performed by first using one of the slicing operators and then applying the Fourier transform. For example, the 2D Fourier transform operator for a functions $f : \mathbb{S}^2 \times \mathbb{R}^3 \to \mathbb{R}$ that is taken with respect to x_1 and x_2 variables is performed by first applying $\mathscr{K}_{\boldsymbol{\theta}, x_3}$ to f and then taking the Fourier transform of the resulting 2D function: $\left[\mathscr{F}\mathscr{K}_{\boldsymbol{\theta}, x_3} f\right](\xi_1, \xi_2)$. Since the result is really a function of several variables we would need to map it back using $g(\boldsymbol{\theta}, \xi_1, \xi_2, x_3) = \left[\mathscr{F}\mathscr{K}_{\boldsymbol{\theta}, x_3} f\right](\xi_1, \xi_2)$. Instead, in the rest of this document we use a shorthand notation in which we apply the Fourier transform operator directly to such functions, listing in the subscript the variables with respect to which the Fourier transform is taken; i.e., we use $[\mathscr{F}_{x_1, x_2} f](\boldsymbol{\theta}, \xi_1, \xi_2, x_3)$ instead of $\left[\mathscr{F}\mathscr{K}_{\boldsymbol{\theta}, x_3} f\right](\xi_1, \xi_2)$ followed by remapping to function of five variables. The number of terms in the subscript indicates the dimensionality of the Fourier transform. The inverse Fourier transform applied with respect to only a subset of variables of a function is handled in the same fashion.

Convolution Operators

The *n-dimensional convolution operator* $*:\Big((\mathbb{R}^n\to\mathbb{R})\times(\mathbb{R}^n\to\mathbb{R})\Big)\Rightarrow(\mathbb{R}^n\to\mathbb{R})$ is defined by

$$[f_1 * f_2](\boldsymbol{x}) = \int_{\mathbb{R}^n} f_1(\boldsymbol{x}')\, f_2(\boldsymbol{x}-\boldsymbol{x}')\, d\boldsymbol{x}', \tag{2.18}$$

where $\boldsymbol{x} = (x_1,\ldots,x_n)^T$.

As with Fourier transforms, sometimes we need to apply a convolution with respect to only some of the variables of two functions. This can be formally performed by first using one of the slicing operators and then applying convolution to the resulting functions. For example, to perform 2D convolution with respect to x_1 and x_2 for two functions $f_1:\mathbb{S}^2\times\mathbb{R}^3\to\mathbb{R}$ and $f_2:\mathbb{R}^3\to\mathbb{R}$, we first apply slicing operators $\mathscr{K}_{\theta_1,\theta_2,x_3}$ to f_1 and $\mathscr{K}_{x_3}$ to f_2 and then convolve the two: $\left[\left[\mathscr{K}_{\theta_1,\theta_2,x_3}f_1\right]*\left[\mathscr{K}_{x_3}f_2\right]\right](x_1,x_3)$. The result needs to be mapped back to a function of five variables. Again, we use a shorthand notation instead. We apply the convolution operator directly to the two functions, listing in the subscript the variables with respect to which convolution is performed; i.e., we use $\left[f_1 \underset{x_1,x_2}{*} f_2\right](\theta_1,\theta_2,x_1,x_2,x_3)$ instead of $\left[\left[\mathscr{K}_{\theta_1,\theta_2,x_3}f_1\right]*\left[\mathscr{K}_{x_3}f_2\right]\right](x_1,x_3)$ followed by mapping to a function of five variables.

The *convolution theorem* provides a well-known relationship between the convolution operator in the spatial domain and multiplication in the frequency domain. For all $f_1:\mathbb{R}^n\to\mathbb{R}$, $f_2:\mathbb{R}^n\to\mathbb{R}$, and $\boldsymbol{\xi}=(\xi_1,\ldots,\xi_n)^T\in\mathbb{R}^n$, we have (see, for example, Natterer and Wübbeling [40], Eq. (1.7))

$$[\mathscr{F}[f_1 * f_2]](\boldsymbol{\xi}) = (2\pi)^{n/2}[\mathscr{F}f_1](\boldsymbol{\xi})\,[\mathscr{F}f_2](\boldsymbol{\xi}). \tag{2.19}$$

Projection Operators

A rotation of the function $v:\mathbb{R}^n\to\mathbb{R}$, $n\in\{2,3\}$, can be represented by a multiplication by a matrix D_n of Eqs. (2.1) and (2.3). The *rotation operator* $\mathscr{R}^n:(\mathbb{R}^n\to\mathbb{R})\Rightarrow\left(\mathbb{S}^{n-1}\times\mathbb{R}^n\to\mathbb{R}\right)$ models the rotation of a function v by an angle $\boldsymbol{\theta}\in\mathbb{S}^{n-1}$. $[\mathscr{R}^n v](\boldsymbol{\theta},\boldsymbol{x})$ is the value of a function v at a point $\boldsymbol{x}$

after it is rotated according to $\boldsymbol{\theta}$. The rotation operator is defined by

$$[\mathscr{R}^n v](\boldsymbol{\theta}, \boldsymbol{x}) = v\left(\boldsymbol{x}^F(\boldsymbol{\theta})\right). \tag{2.20}$$

The *compressing operator* $\mathscr{C}^n : \left(\mathbb{S}^{n-1} \times \mathbb{R}^n \to \mathbb{R}\right) \Rightarrow \left(\mathbb{S}^{n-1} \times \mathbb{R}^{n-1} \to \mathbb{R}\right)$ performs integration along the X_n-axis. The compressing operator $\mathscr{C}^n$ is defined by

$$[\mathscr{C}^n w](\boldsymbol{\theta}, x_1, \ldots, x_{n-1}) = \int_{\mathbb{R}} w(\boldsymbol{\theta}, x_1, \ldots, x_n)\, \mathrm{d}x_n. \tag{2.21}$$

The first variable is included to denote the angle by which the object was rotated before the compression, and the other variables indicate the location of a point.

The composition $\mathscr{C}^n\mathscr{R}^n$ of these two operators defines the *projection operator* $\mathscr{P}^n : (\mathbb{R}^n \to \mathbb{R}) \Rightarrow \left(\mathbb{S}^{n-1} \times \mathbb{R}^{n-1} \to \mathbb{R}\right)$, such that, for all $v : \mathbb{R}^n \to \mathbb{R}$,

$$\mathscr{P}^n v = \mathscr{C}^n \mathscr{R}^n v. \tag{2.22}$$

We refer to data that are collected according to the projection operator, $\mathscr{P}^n v$, as the ideal data.

Tomographic Projection Operators

In tomography of 3D objects, the rotation is performed only around a single axis passing through the object. Using our notation, this can be achieved by allowing one angle to range over the entire interval $[0, 2\pi]$ and fixing the second angle at $\pi/2$. We define a set of operators that model tomographic data collection of a 3D object.

A rotation of the function $v : \mathbb{R}^3 \to \mathbb{R}$ can be represented by a multiplication by a matrix D_3 of Eq. (2.3) with angle θ_2 set to $\pi/2$. The *rotation operator* $\mathscr{R}^{3t} : \left(\mathbb{R}^3 \to \mathbb{R}\right) \Rightarrow \left(\mathbb{S}^1 \times \mathbb{R}^3 \to \mathbb{R}\right)$ is defined by

$$\left[\mathscr{R}^{3t} v\right](\theta_1, \boldsymbol{x}) = \left[\mathscr{R}^3 v\right]\left(\theta_1, \frac{\pi}{2}, \boldsymbol{x}\right). \tag{2.23}$$

The *tomographic compressing operator* $\mathscr{C}^{3t} : \left(\mathbb{S}^1 \times \mathbb{R}^n \to \mathbb{R}\right) \Rightarrow \left(\mathbb{S}^1 \times \mathbb{R}^2 \to \mathbb{R}\right)$ performs the integration along the X_3-axis. The compressing operator $\mathscr{C}^{3t}$ is defined by

$$\left[\mathscr{C}^{3t} w\right](\theta_1, x_1, x_2) = \int_{\mathbb{R}} w(\theta_1, x_1, x_2, x_3)\, \mathrm{d}x_3. \tag{2.24}$$

The composition $\mathscr{C}^{3t}\mathscr{R}^{3t}$ of these two operators defines the *tomographic projection operator* $\mathscr{P}^{3t} : \left(\mathbb{R}^3 \to \mathbb{R}\right) \Rightarrow \left(\mathbb{S}^1 \times \mathbb{R}^3 \to \mathbb{R}\right)$, such that, for all $v : \mathbb{R}^3 \to \mathbb{R}$

$$\left[\mathscr{P}^{3t} v\right](\theta_1, x_1, x_2) = \left[\mathscr{C}^{3t}\mathscr{R}^{3t} v\right](\theta_1, x_1, x_2). \tag{2.25}$$

Reconstruction Operators

During the reconstruction process we make use of operators that, so to speak, undo the actions of the operators described above (we show later in this chapter that these operators provide, in fact, mathematical inversions for the operators used to describe projections). For $n \in \{2,3\}$, $\mathscr{S}^n : \left(\mathbb{S}^{n-1} \times \mathbb{R}^{n-1} \to \mathbb{R}\right) \Rightarrow \left(\mathbb{S}^{n-1} \times \mathbb{R}^n \to \mathbb{R}\right)$ is the *spreading back operator*. If $g \in \left(\mathbb{S}^{n-1} \times \mathbb{R}^{n-1} \to \mathbb{R}\right)$, then $\mathscr{S}^n g$ is commonly referred to as a *ridge function* resulting from spreading back g (ridge functions are functions whose values do not change in one direction, in this case it is the direction of the X_n-axis). The value of $\mathscr{S}^n g$ at the point $(\boldsymbol{\theta}, \boldsymbol{x})$ is

$$\left[\mathscr{S}^n g\right](\boldsymbol{\theta}, \boldsymbol{x}) = g(\boldsymbol{\theta}, x_1, \ldots, x_{n-1}). \tag{2.26}$$

$\mathscr{T}^n : \left(\mathbb{S}^{n-1} \times \mathbb{R}^n \to \mathbb{R}\right) \Rightarrow \left(\mathbb{R}^n \to \mathbb{R}\right)$ is the *totaling operator* that performs integration of functions in $\left(\mathbb{S}^{n-1} \times \mathbb{R}^n \to \mathbb{R}\right)$ over the unit sphere $\mathbb{S}^{n-1}$. The value of $\mathscr{T}^n w$, which is sometimes referred to as an *integral image*, at the point $\boldsymbol{x}$ is

$$\left[\mathscr{T}^n w\right](\boldsymbol{x}) = \int_{\mathbb{S}^{n-1}} w\left(\boldsymbol{\theta}, \boldsymbol{x}^B(\boldsymbol{\theta})\right) \left|J(\boldsymbol{\theta})\right| \mathrm{d}\boldsymbol{\theta}, \tag{2.27}$$

where the term $|J(\boldsymbol{\theta})|$ is the determinant of the Jacobian to assure uniform integration over all directions when spherical coordinates are used; (note that for us, the radius of the sphere of integration is always equal to one); $|J(\boldsymbol{\theta})| = 1$ for $\boldsymbol{\theta} \in \mathbb{S}^1$ and $|J(\boldsymbol{\theta})| = \sin\theta_2$ for $\boldsymbol{\theta} \in \mathbb{S}^2$. $\mathscr{T}^n$ unrotates the ridge functions $w(\boldsymbol{\theta}, \boldsymbol{x})$ by the angle $\boldsymbol{\theta}$ (the same angle by which the object was rotated before the projection was obtained), and then the unrotated ridge functions for all $\boldsymbol{\theta}$ are added (totaled) together.

The composition $\mathscr{T}^n\mathscr{S}^n$ defines the *backprojection operator* $\mathscr{B}^n : \left(\mathbb{S}^{n-1} \times \mathbb{R}^{n-1} \to \mathbb{R}\right) \Rightarrow (\mathbb{R}^n \to \mathbb{R})$, such that, for all $g \in \left(\mathbb{S}^{n-1} \times \mathbb{R}^{n-1} \to \mathbb{R}\right)$

$$[\mathscr{B}^n g](\boldsymbol{x}) = [\mathscr{T}^n \mathscr{S}^n g](\boldsymbol{x}). \tag{2.28}$$

Using the inverse Fourier transform, Eq. (2.16), and convolution, Eq. (2.18), operators, we define the *deblurring operator* $\mathscr{D}^n : (\mathbb{R}^n \to \mathbb{R}) \Rightarrow (\mathbb{R}^n \to \mathbb{R})$ as follows. Let $\hat{r} \in (\mathbb{R}^n \to \mathbb{R})$ be the function defined by $\hat{r}(\boldsymbol{\xi}) = |\boldsymbol{\xi}|$. Then, for any $v \in (\mathbb{R}^n \to \mathbb{R})$,

$$\mathscr{D}^n v = \left((2\pi)^{n/2+1} \left|\mathbb{S}^{n-1}\right|\right)^{-1} \left[\mathscr{F}^{-1}_{\boldsymbol{\xi}} \hat{r}\right] \underset{\boldsymbol{x}}{*} v, \tag{2.29}$$

where $\left|\mathbb{S}^{n-1}\right|$ is the surface area of a unit sphere in $\mathbb{R}^n$. For $n \in \{2,3\}$ we have $\left|\mathbb{S}^1\right| = 2\pi$ and $\left|\mathbb{S}^2\right| = 4\pi$.

Tomographic Reconstruction Operators

We also define tomographic reconstruction operators that, so to speak, undo the actions of the tomographic projection operators. They are defined for reconstruction of 3D objects in a similar fashion to general reconstruction operators, but deal only with rotation around a single axis. $\mathscr{S}^{3t} : \left(\mathbb{S}^1 \times \mathbb{R}^2 \to \mathbb{R}\right) \Rightarrow \left(\mathbb{S}^1 \times \mathbb{R}^3 \to \mathbb{R}\right)$ is the *tomographic spreading back operator*. It is defined by

$$\left[\mathscr{S}^{3t} g\right](\boldsymbol{\theta}, \boldsymbol{x}) = g(\boldsymbol{\theta}, x_1, \ldots, x_{n-1}). \tag{2.30}$$

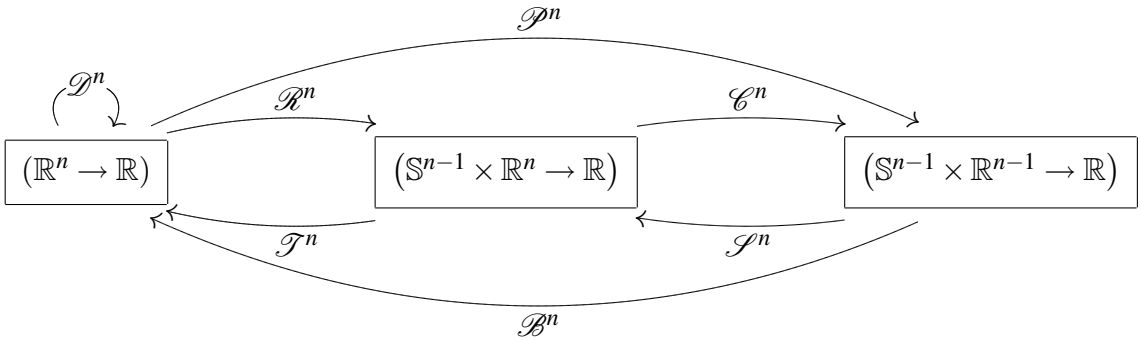

(a) Operators for $n \in \{2,3\}$.

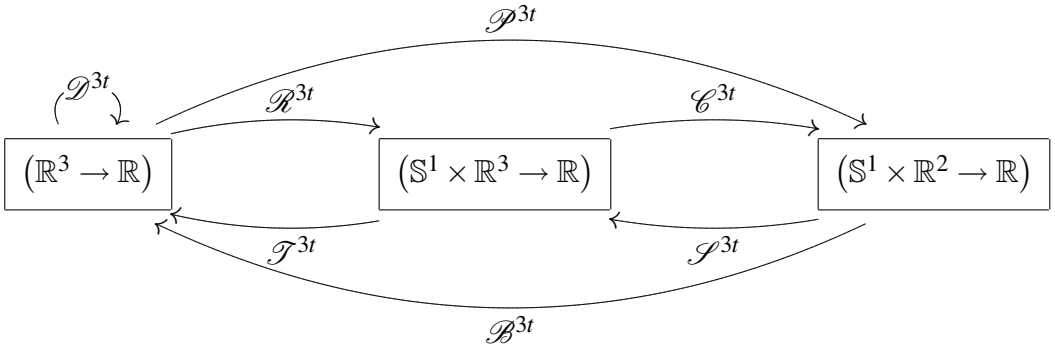

(b) Tomographic operators.

Figure 2.2: Operators and the spaces of functions on which they act.

$\mathscr{T}^{3t} : (\mathbb{S}^1 \times \mathbb{R}^3 \to \mathbb{R}) \Rightarrow (\mathbb{R}^3 \to \mathbb{R})$ is the *tomographic totaling operator* defined by

$$\left[\mathscr{T}^{3t} w\right](\boldsymbol{x}) = \int_{\mathbb{S}^1} w\left(\boldsymbol{\theta}, \boldsymbol{x}^B(\boldsymbol{\theta})\right) |J(\boldsymbol{\theta})| \, \mathrm{d}\boldsymbol{\theta}. \tag{2.31}$$

The composition of $\mathscr{T}^{3t}$ and $\mathscr{S}^{3t}$ operators defines the *tomographic backprojection operator* $\mathscr{B}^{3t} : (\mathbb{S}^1 \times \mathbb{R}^2 \to \mathbb{R}) \Rightarrow (\mathbb{R}^3 \to \mathbb{R})$, such that, for all $g \in (\mathbb{S}^1 \times \mathbb{R}^2 \to \mathbb{R})$

$$\left[\mathscr{B}^{3t} g\right](\boldsymbol{x}) = \left[\mathscr{T}^{3t} \mathscr{S}^{3t} g\right](\boldsymbol{x}). \tag{2.32}$$

The operators and spaces of functions on which they act are summarized in Figure 2.2.

2.3 Inversion of the Projection Operator

The data collected according to our projection operator $\mathscr{P}^n$ of Eq. (2.22) is the mathematical idealization of data collection in 3D TEM and 3D TXM (no noise, no blurring, no attenuation, and data from all projection directions available). A well-known significant fact is that a function $v : \mathbb{R}^n \to \mathbb{R}$, $n \in \{2,3\}$ can be recovered from $\mathscr{P}^n v$ by application of backprojection, modeled by our backprojection operator $\mathscr{B}^n$ of Eq. (2.28), followed by deblurring, modeled by our deblurring operator $\mathscr{D}^n$ of Eq. (2.29). We now prove that our operators, described in the previous subsection, perform this inversion. The proof for the case of $n = 3$ was included in our publication Kazantsev et al. [28]; in this section we provide the proof for $n \in \{2,3\}$.

Theorem 2.1. *For any function $v : \mathbb{R}^n \to \mathbb{R}$, $n \in \{2,3\}$, $\mathscr{D}^n \mathscr{B}^n \mathscr{P}^n v = v$.*

The proof of this theorem appeals to known results presented in the book by Natterer and Wübbeling [40]. Essentially, all we need to do is to establish the relationship between our notation and that used in [40]. Before we proceed with the proof, we describe the operators used by Natterer and Wübbeling [40] for ease of references.

Let $S^{n-1} = \left\{ \boldsymbol{\beta} = (\beta_1, \ldots, \beta_D)^T \,|\, |\boldsymbol{\beta}| = 1 \right\}$ (the unit sphere in $\mathbb{R}^n$). S^{n-1} is the same physical unit sphere in $\mathbb{R}^n$ as previously defined $\mathbb{S}^{n-1}$. The difference is that $\mathbb{S}^{n-1}$ uses polar/spherical coordinates (an angle vector and a radius equal to 1) to describe a point, whereas S^{n-1} uses rectangular coordinates to describe a point. For $\boldsymbol{\beta} \in S^{n-1}$, let $\boldsymbol{\beta}^\perp = \{\mathbf{x} \in \mathbb{R}^n |\ \langle \mathbf{x}, \boldsymbol{\beta} \rangle = 0\}$, where $\langle \mathbf{x}, \boldsymbol{\beta} \rangle = \sum_{k=1}^n x_k \beta_k$, for $\mathbf{x} = (x_1, \ldots, x_n)^T$ and $\boldsymbol{\beta} = (\beta_1, \ldots, \beta_n)^T$ ($\boldsymbol{\beta}^\perp$ is the plane through the origin perpendicular to $\boldsymbol{\beta}$). Let $\mathbb{L} = \left\{ (\boldsymbol{\beta}, \mathbf{x}) | \boldsymbol{\beta} \in S^{n-1}, \mathbf{x} \in \beta^\perp \right\}$ (the set of all lines in $\mathbb{R}^n$).

The *ray transform operator* $\mathscr{N} : (\mathbb{R}^n \to \mathbb{R}) \Rightarrow (\mathbb{L} \to \mathbb{R})$ is defined by Natterer and Wübbeling [40], Eq. (2.28) by

$$[\mathscr{N} v](\boldsymbol{\beta}, \mathbf{x}) = \int_{\mathbb{R}} v(\mathbf{x} + t\boldsymbol{\beta})\, dt, \tag{2.33}$$

for all $\boldsymbol{\beta} \in S^{n-1}$ and $\mathbf{x} \in \boldsymbol{\beta}^\perp$.

The *backprojection operator for the ray transform* $\mathscr{W} : (\mathbb{L} \to \mathbb{R}) \Rightarrow (\mathbb{R}^n \to \mathbb{R})$ is defined by Natterer and Wübbeling [40], Eq. (2.31) by

$$[\mathscr{W}\ell](\mathbf{x}) = \int_{S^{n-1}} \ell(\boldsymbol{\beta}, \mathbf{x} - \langle \mathbf{x}, \boldsymbol{\beta} \rangle \boldsymbol{\beta}) \, d\boldsymbol{\beta}, \tag{2.34}$$

for $\mathbf{x} \in \mathbb{R}^n$.

Theorem 2.14 of [40] (with $\alpha = 1$) together with Eqs. (1.15) and (1.7) of [40] state that for all $v : \mathbb{R}^n \to \mathbb{R}$,

$$v = \left((2\pi)^{n/2+1} \left| \mathbb{S}^{n-1} \right| \right)^{-1} \left[\mathscr{F}_{\boldsymbol{\xi}}^{-1} \hat{r} \right] \underset{\boldsymbol{x}}{*} \mathscr{W} \mathscr{N} v, \tag{2.35}$$

where, as for Eq. (2.29), $\hat{r} \in (\mathbb{R}^n \to \mathbb{R})$ is defined by $\hat{r}(\boldsymbol{\xi}) = |\boldsymbol{\xi}|$.

Proof of Theorem 2.1. The theorem is proved by demonstrating the equivalence of the operators $\mathscr{P}^n$ and $\mathscr{N}$, and $\mathscr{B}^n$ and $\mathscr{W}$. The validity of our theorem then follows from Eq. (2.35) that demonstrates that the operator $\mathscr{W}$ followed by some deblurring steps provides inversion for the operator $\mathscr{N}$.

We first show that the operators $\mathscr{P}^n$ and $\mathscr{N}$ are in some sense the same. When computing $\mathscr{N} v$ of Eq. (2.33) the integral through the object is taken along the line determined by a direction $\boldsymbol{\beta} \in S^2$ and a point $\mathbf{y} \in \beta^{\perp}$; the line consists of the points in the set $\{\mathbf{y} + t\boldsymbol{\beta} : t \in \mathbb{R}\}$. When computing $\mathscr{P}^n v$ of Eq. (2.22) the object has been rotated according to the angle $\boldsymbol{\theta}$ and the integral is always taken along a line parallel to the X_n-axis. The two lines are really the same line through the object provided that $\boldsymbol{\beta}$ and $\mathbf{y}$ are appropriately defined in terms of $\boldsymbol{\theta}$ and $\boldsymbol{x}$.

Let $v : \mathbb{R}^n \to \mathbb{R}$, $\boldsymbol{\theta} \in \mathbb{S}^{n-1}$, and $\boldsymbol{x} \in \mathbb{R}^n$. Let R_{01}^n be an n-dimensional column vector with $n-1$ zeros, followed by a 1 in the last position. Let R_{10}^n be an n-dimensional column vector with $n-1$ ones, followed by a zero in the last position. Choose

$$\boldsymbol{\beta} = D_n^{-1} R_{01}^n \tag{2.36}$$

and

$$\mathbf{y} = D_n^{-1}\left(R_{10}^n \circ \boldsymbol{x}\right), \tag{2.37}$$

where $\circ$ denotes the Hadamard product (element-wise product) of two matrices of the same size. For this choice of $\boldsymbol{\beta}$ and $\boldsymbol{y}$, we show that $[\mathscr{P}^n v](\boldsymbol{\theta}, x_1, \ldots, x_{n-1}) = [\mathscr{N} v](\boldsymbol{\beta}, \boldsymbol{y})$.

First, observe that

$$\begin{aligned}
\boldsymbol{y} + x_n\boldsymbol{\beta} &= D_n^{-1}\left(R_{10}^n \circ \boldsymbol{x}\right) + x_n D_n^{-1} R_{01}^n \\
&= D_n^{-1}\left(R_{10}^n \circ \boldsymbol{x} + x_n R_{01}^n\right) = D_n^{-1}\boldsymbol{x} \\
&= \boldsymbol{x}^F(\boldsymbol{\theta}).
\end{aligned} \tag{2.38}$$

Using the above we show that the integral expression for $\mathscr{N} v$ of Eq. (2.33) is the same as the one for $\mathscr{P}^n v$ of Eq. (2.22) by first renaming the dummy variable t as x_n, then using the definitions of $\boldsymbol{\beta}$ and $\boldsymbol{y}$, and Eq. (2.38), and finally applying the operators $\mathscr{R}^n$, $\mathscr{C}^n$ and $\mathscr{P}^n$ of Eqs (2.20), (2.24) and (2.22), respectively, as follows

$$\begin{aligned}
[\mathscr{N} v](\boldsymbol{\beta}, \boldsymbol{y}) &= \int_{\mathbb{R}} v(\boldsymbol{y} + t\boldsymbol{\beta})\,\mathrm{d}t \\
&= \int_{\mathbb{R}} v\left(\boldsymbol{x}^F(\boldsymbol{\theta})\right)\mathrm{d}x_n \\
&= [\mathscr{P}^n v](\boldsymbol{\theta}, x_1, \ldots, x_{n-1}).
\end{aligned} \tag{2.39}$$

We now proceed to show that, for all $v : \mathbb{R}^n \to \mathbb{R}$ and $\mathbf{x} \in \mathbb{R}^n$,

$$[\mathscr{B}^n \mathscr{P}^n v](\mathbf{x}) = [\mathscr{W} \mathscr{N} v](\mathbf{x}). \tag{2.40}$$

Using the definitions of the operators $\mathscr{B}^n$, $\mathscr{T}^n$ and $\mathscr{S}^n$ we can rewrite the left-hand side of

Eq. (2.40) as

$$[\mathscr{B}^n \mathscr{P}^n v](\mathbf{x}) = \int_{\mathbb{S}^{n-1}} [\mathscr{P}^n v]\left(\boldsymbol{\theta}, x_1^B(\boldsymbol{\theta}), \ldots, x_{n-1}^B(\boldsymbol{\theta})\right) |J(\boldsymbol{\theta})| \, \mathrm{d}\boldsymbol{\theta}. \tag{2.41}$$

By Eq. (2.39) we know that $[\mathscr{P}^n v]\left(\boldsymbol{\theta}, x_1^B(\boldsymbol{\theta}), \ldots, x_{n-1}^B(\boldsymbol{\theta})\right) = [\mathscr{N} v][\boldsymbol{\beta}, \boldsymbol{z}]$, when $\boldsymbol{\beta} = D_n^{-1} R_{01}^n$ and $\boldsymbol{z} = D_n^{-1}\left(R_{10}^n \circ \boldsymbol{x}^B(\boldsymbol{\theta})\right)$ (according to Eqs. (2.36) and (2.37)). It is also the case that $\boldsymbol{z} = \boldsymbol{x} - \langle \boldsymbol{x}, \boldsymbol{\beta} \rangle \boldsymbol{\beta}$. (The derivation of this fact requires only elementary trigonometric operations, but it needs to be performed separately for $n = 2$ and $n = 3$. It is provided in Appendix B.) Using a change of coordinates for the integration from polar for $n = 2$ or spherical for $n = 3$ ($r = 1, \boldsymbol{\theta} \in \mathbb{S}^{n-1}$) to rectangular coordinates ($\boldsymbol{\beta} \in S^{n-1}$) and the definition of the operator $\mathscr{W}$, we obtain

$$\begin{aligned}
[\mathscr{B}^n \mathscr{P}^n v](\mathbf{x}) &= \int_{\mathbb{S}^{n-1}} [\mathscr{P}^n v]\left(\boldsymbol{\theta}, x_1^B(\boldsymbol{\theta}), \ldots, x_{n-1}^B(\boldsymbol{\theta})\right) |J(\boldsymbol{\theta})| \, \mathrm{d}\boldsymbol{\theta} \\
&= \int_{S^{n-1}} [\mathscr{N} v](\boldsymbol{\beta}, \boldsymbol{x} - \langle \boldsymbol{x}, \boldsymbol{\beta} \rangle \boldsymbol{\beta}) \, \mathrm{d}\boldsymbol{\beta} \\
&= [\mathscr{W} \mathscr{N} v](\mathbf{x}).
\end{aligned} \tag{2.42}$$

To complete the proof of Theorem 2.1, observe that by the definition of the operator $\mathscr{D}^n$ of Eq. (2.29), Eq. (2.35) is equivalent to $v = \mathscr{D}^n \mathscr{W} \mathscr{N} v$. Since we just demonstrated in Eq. (2.42) that $\mathscr{B}^n \mathscr{P}^n v = \mathscr{W} \mathscr{N} v$, it follows that $v = \mathscr{D}^n \mathscr{B}^n \mathscr{P}^n v$. □

2.4 Stationary Phase Approximation

The method of stationary phase, see, for example, Guillemin and Sternberg [18], Chapter 1, is used for evaluating highly oscillatory integrals of the form

$$I(\xi) = \int_{c_1}^{c_2} G(\sigma) e^{i\xi F(\sigma)} d\sigma. \tag{2.43}$$

If G is a smooth function, F is twice differentiable, and all critical points of F (i.e., points at which the first derivative F' is zero-valued) are non-degenerate (i.e., the second derivative F'' is not zero-valued), then as $\xi \to \infty$

$$I(\xi) = \sum_{s \in S} e^{i\xi F(s)} G(s) \sqrt{\frac{2}{\xi \left| F''(s) \right|}} e^{i\frac{\pi}{4} sgn(F''(s))} + O\left(\xi^{-1/2}\right), \tag{2.44}$$

where S is the set of critical points of F and $sgn(a)$ denotes the sign of the argument a. This result implies that $I(\xi)$ can be well approximated by the sum on the right hand side, as long as ξ is sufficiently large. However, it has been shown in many practical applications Defrise [6], Defrise et al. [7], Dubowy and Herman [8], Varslot et al. [49], Xia et al. [54] that the sum approximates the original integral very well even for small values of ξ.

We consider the following a reasonable working tool based on the method of stationary phase. If two integrals of the kind shown in Eq. (2.43) differ only in G (they use the same ξ and F) and the values of G at the critical points of F are approximately the same, then the values of the integrals are also approximately the same.

2.5 Data Collection Geometries

Physical devices, such as microscopes, use specific data collection geometries. For the purpose of development of data correction methods and reconstruction methods, one often works with simplified or similar data collection geometries. We define all our operators and theorems to be able to handle three different data collection geometries: 1) arbitrary angle rotation of 2D objects, 2) arbitrary angle rotation of 3D objects, and 3) single axis rotation of 3D objects. We discuss details of each of these schemes indicating which of them are device specific and which are used only for simulation and development.

2.5.1 Single Axis Rotation Geometry

In single axis rotation mode of data collection, the object is rotated around a single axis and the images are taken in each position. The axis of rotation for a 3D object can be chosen arbitrarily from the plane perpendicular to the X_3 axis, but has to remain the same throughout imaging. We achieve such rotation by fixing θ_2 at $\pi/2$ and allowing θ_1 range over the whole of $[0, 2\pi)$, i.e., for single axis rotation we use the angles $\left\{ \boldsymbol{\theta} = (\theta_1, \theta_2)^T \in \mathbb{S}^2 \mid \theta_2 = \pi/2 \right\}$.

With this mode of data collection the 3D object can be subdivided into 2D slices (in the mathematical limit, the thickness of such slices is infinitesimal). If the data for each slice are recorded independently from all the other slices, then the reconstruction of the 3D object can be reduced to reconstruction of all its 2D slices. This is the basis of computed tomography in which the data are collected according to the model described by the $\mathscr{P}^{3t}$ operator of Eq. (2.25).

The single axis rotation mode of data collection for 3D objects is used in electron microscopy and in soft x-ray microscopy.

In the actual devices it is sometimes impossible to collect data from the entire range of angles that is desirable. The reasons for this are the embedding of samples in a layer of ice and the use of tilt stages for imaging. At high tilt angles the thickness of ice becomes too large to provide useful images. When tilt stages are used in TEM and TXM, the data from a range of angles can not be obtained. This is commonly referred to as a missing wedge in the data and results in additional artifacts in the reconstruction. In this dissertation, we do not handle the case of missing wedge.

In TXM imaging, there is an alternative method of collecting data using single axis rotation. Glass capillaries are used to hold the sample in aqueous solution which is rapidly frozen for imaging, see, e.g., Le Gros et al. [33]. This allows for data collection without a missing wedge. The possible sources of problems using this mode of data collection are the need for accounting for possibly variable thickness of the glass capillary and stability of the capillary during rotation.

2.5.2 Arbitrary Rotation Geometry

The arbitrary rotation geometry mode of data collection is applicable to both 2D and 3D objects. For 2D objects, the data are collected for the angles ranging over the entire $\mathbb{S}^1$, and for 3D objects, the data are collected for the angles ranging over the entire $\mathbb{S}^2$.

The arbitrary rotation mode of data collection is used in electron microscopy in, so called, single particle imaging. The assumption is made that there exist a large number of identical 3D samples. Instead of rotating a single sample to collect data, the entire collection of identical samples is frozen in random orientation and imaged all at once. Since samples may have preferential orientation this may lead to ranges of angles that are over-represented and others that are missing.

Chapter 3

Distance-Dependent Blurring

A microscope, as any other imaging device, cannot record a perfect image. The response of an imaging device to a single point in space is not a single point in the image, but a function called the *point spread function* (PSF) of the device. An ideal PSF allows for recording of mathematical points as points in an image. The only PSF that does that is the n-dimensional Dirac delta function (see Appendix A). In actual devices, the closer the PSF is to the Dirac delta function, the better the image. The less the PSF is like a mathematical delta function, the more blurred the image appears. The PSF is said to be space invariant if it does not depend on the location of the point in space. When it is space invariant the entire image is blurred uniformly by a single function. For most imaging devices, it is unlikely that the PSF is truly space invariant, but often the change in the function is so small (especially compared to other possible sources of errors) that it can be assumed to be space invariant.

The mathematical specification of blurring in transmission electron microscopy (TEM) and in transmission x-ray microscopy (TXM) is dependent on the parameter called defocus, which in turn depends on the distance from the zero-defocus plane (in which defocus is zero). The defocus gradient describes how fast the blurring changes in the imaging direction. Large changes in blurring result in projection images to which different parts of the specimen contribute in very different ways. The attenuation effects are due to x-ray attenuation as it passes through matter; they

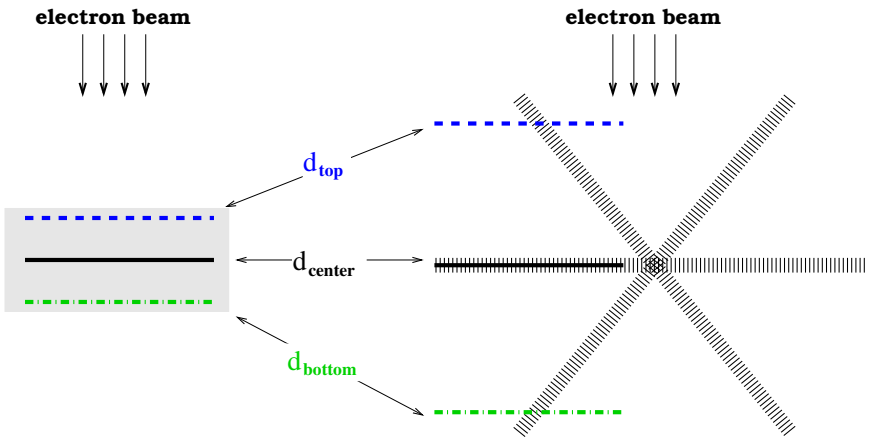

Figure 3.1: During imaging different parts of the specimen are located at different defocus values.

affect all images obtained using x-rays. If the defocus-gradient is very small within the specimen, then the assumption that the blurring is uniform everywhere in the 2D or 3D space can be made without causing a significant loss of resolution in the reconstructions. When specimens are placed on the imaging stage that is tilted around an axis perpendicular to the imaging direction, which is one of the modes of data collection in TEM), then the stage may be moving through layers with varying blurring functions. Figure 3.1 schematically illustrates simulations in which, for a large specimen (left side) or when an imaging stage is used (right side), the layers d_{top}, d_{center} and d_{bottom} are far apart and therefore are blurred in different ways.

In image processing, the Fourier transform of the PSF is called the *optical transfer function* (OTF); see, for example, Rosenfeld and Kak [44]. In electron microscopy, though, the term *contrast transfer function* (CTF) is used to describe the effects of the microscope on image formation. The CTF encapsulates many effects, description of which is beyond the scope of this work; for details see, for example, Frank [15], Reimer and Kohl [43]. For the purpose of this work, we think of the CTF as the Fourier transform of the PSF of the electron microscope. In x-ray microscopy, the blurring is usually described by the PSF. It incorporates the effects of a complex system of focusing and condenser zone planes.

Distance-dependent blurring is present in other imaging modalities. For example, it is a well known problem in single photon emission computed tomography (SPECT). The frequency distance

relation method of correcting for the distance-dependent blurring was, in fact, first discussed in the context of SPECT reconstructions; see Lewitt et al. [36], Xia et al. [54]. One of our approaches of correcting for distance-dependent blurring is based on that work.

In the rest of this chapter we discuss the PSFs and CTFs of electron and x-ray microscopes.

3.1 Blurring in Transmission Electron Microscopy

The contrast transfer function (CTF) in transmission electron microscopy affects various frequencies by modulating their magnitudes and by changing the sign of their amplitudes. As long as the CTF affects each layer of an object in the same way, it does not cause a significant problem in reconstruction, since the blurring and integration commute and one can deblur the projections and then reconstruct. In electron microscopy, the CTF (and therefore the PSF) is translation invariant within any plane perpendicular to the direction of the electron beam, but changes from one such plane to the next. This is due to the dependence of the CTF on defocus, which is different from one layer to the next.

Our mathematical definition of the CTF is a standard one; specifically, we base it on formulas that appeared in Frank [15], (Chapter 3, Eqs 2.4, 2.5, 2.13-2.15, 2.17). In our definition we assume that there is no astigmatism.

The CTF for a transmission electron microscope, $H : \mathbb{R}^n \to \mathbb{C}$, $n \in \{2,3\}$ is defined as

$$H(\xi_1,\ldots,\xi_{n-1},x_n) = H_{CTF}\left(\sqrt{\xi_1^2+\ldots+\xi_{n-1}^2},x_n\right) E_{spat}\left(\sqrt{\xi_1^2+\ldots+\xi_{n-1}^2},x_n\right) E_{temp}\left(\sqrt{\xi_1^2+\ldots+\xi_{n-1}^2}\right), \tag{3.1}$$

where

$$H_{CTF}(\xi,x_n) = (1-a)\sin(D(\xi,x_n)) - a\cos(D(\xi,x_n)), \tag{3.2}$$

$$D(\xi,x_n) = 2\pi\lambda\xi^2\left(-\Delta f(x_n)/2 + \lambda^2\xi^2 C_s/4\right), \tag{3.3}$$

$$E_{spat}(\xi, x_n) = \exp\left(-\pi^2 q_0^2 \left(C_s \lambda^3 \xi^3 - \Delta f(x_n)\lambda\xi\right)^2\right), \tag{3.4}$$

$$E_{temp}(\xi) = \exp\left(-\left(\frac{1}{2}\pi F_s \lambda \xi^2\right)^2\right), \tag{3.5}$$

and the parameters involved are:

$\xi \equiv \sqrt{\xi_1^2 + \ldots + \xi_{n-1}^2}$ is a spatial frequency,

a is a fraction of the amplitude contrast, $0 \leq a \leq 1$,

λ is the electron wavelength,

C_s is the lens spherical aberration coefficient,

$\Delta f(x_n)$ is the defocus that depends on location along the X_n-axis,

q_0 is a quantity of dimension 1/length specifying the size of the source as it appears in the back focal plane,

F_s is the lens focal spread coefficient.

The PSF, $h : \mathbb{R}^n \to \mathbb{R}$, $n \in \{2,3\}$ is defined by the inverse Fourier transform of the CTF

$$h(x_1, \ldots, x_n) = \left[\mathscr{F}^{-1}_{\xi_1,\ldots,\xi_{n-1}} H\right](x_1, \ldots, x_n). \tag{3.6}$$

We illustrate the shape of the PSF and CTF functions for specific values of their parameters, namely, the fraction of the amplitude contrast $a = 0.3$, the electron wavelength $\lambda = 0.033487$ Å, the lens spherical aberration coefficient $C_s = 28{,}000{,}000$ Å, the size of the source as it appears in the back focal plane $q_0 = 0.00746558$ Å^{-1}, and the lens focal spread coefficient $F_s = 141.35$ Å. We use signed distance to the zero-defocus plane as the defocus function Δf; changing the form of Δf results in different CTFs even if all the other parameters are fixed.

In 2D the PSF for a fixed x_2 is a one-dimensional function. Plots of such function for three selected values of the defocus $\Delta f(x_2) = -1$, $\Delta f(x_2) = 0$, and $\Delta f(x_2) = 1$ are shown in Figure 3.2a.

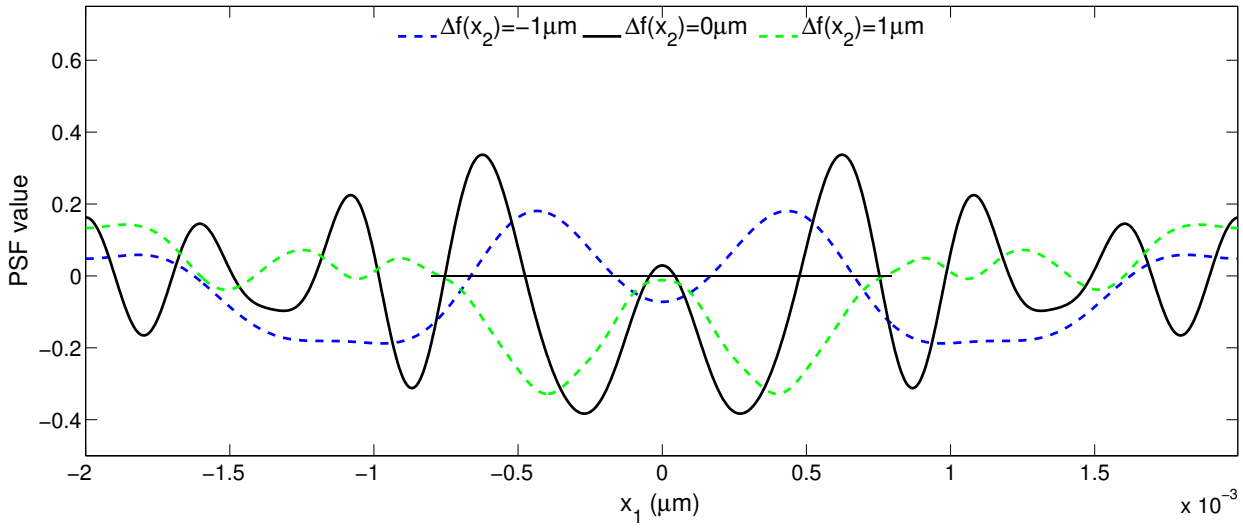

(a)

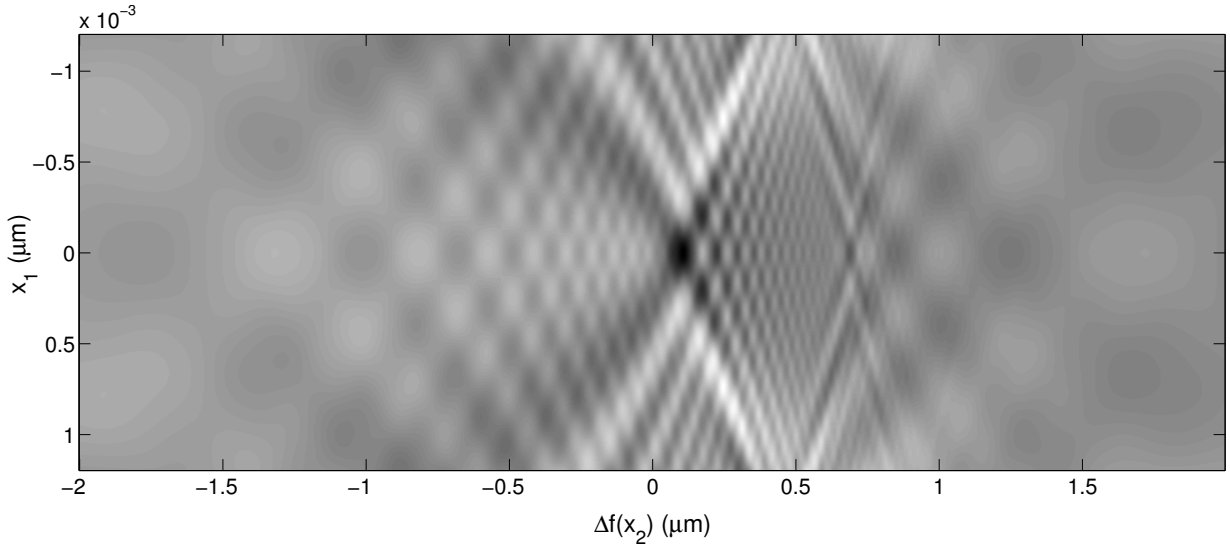

(b)

Figure 3.2: PSF of a transmission electron microscope: **(a)** plots for selected values of the defocus $\Delta f(x_2) = -1$, $\Delta f(x_2) = 0$, and $\Delta f(x_2) = 1$; **(b)** 2D representation of the function for $\Delta f(x_2)_2 \in (-2\mu\text{m}, 2\mu\text{m})$, each column of pixels in the image corresponds to a single plot like the ones shown in (a).

In 3D the PSF for a fixed x_3 is a circularly symmetric two-dimensional function, and plots shown in Figure 3.2a are the profile curves of such planes for corresponding values of defocus. For that reason we only show plots of 2D PSF's. Figure 3.2b illustrates a 2D PSF for defocus values of $\Delta f(x_2) = -2\mu\text{m}$ up to $\Delta f(x_2) = 2\mu\text{m}$. Each column of pixels corresponds to a particular

defocus value $\Delta f(x_2)$. The grayscale values in the image represent values of the function with black corresponding to the most negative and white to the most positive value.

As with the PSF, the plot of a function obtained by fixing the value of x_2 in a 2D CTF is identical to the plot of the profile curve of the circularly symmetric function obtained by fixing the value of x_3 in a 3D CFT. The plots for several different defocus values $\Delta f(x_2)$ are shown in Figures 3.3a and 3.4, and the 2D visualization of the CTF for a range of values of the defocus values of $\Delta f(x_2) = -2\,\mu$m up to $\Delta f(x_2) = 2\,\mu$m is shown in Figure 3.3b.

The change in the blurring function within any fixed thickness of the specimen depends on where the sample is placed along the electron beam. Consider the schematic picture in Figure 3.1. The reason for change in defocus can be two-fold, either due to the specimen thickness (left-hand side of Figure 3.1) or due to the tilt of the stage during acquisition of multiple images (right-hand side of Figure 3.1). We look at three different distances along the imaging direction, i.e., along the x_2 direction: 1) $x_2 = \mathrm{d}_{\mathrm{top}}$ is the first value of x_2 in the specimen where the electrons enter the specimen during the imaging; 2) $x_2 = \mathrm{d}_{\mathrm{center}}$ is the value of x_2 corresponding roughly to the central layer of the specimen; and 3) $x_2 = \mathrm{d}_{\mathrm{bottom}}$ is the last value of x_2 in the specimen where the electrons leave the specimen. The graphs in Figure 3.4 show profile plots of the CTF for three values of $\mathrm{d}_{\mathrm{center}}$ and two values of $\mathrm{d}_{\mathrm{bottom}} - \mathrm{d}_{\mathrm{top}}$. The shape of the CTF changes much more slowly away from the zero-defocus plane (for example, for $\Delta f(\mathrm{d}_{\mathrm{center}}) = -1.00\,\mu$m or $\Delta f(\mathrm{d}_{\mathrm{center}}) = 1.00\,\mu$m, see Figure 3.4a,b,e,f) than around the zero-defocus plane (where $\Delta f(\mathrm{d}_{\mathrm{center}}) = 0.00\,\mu$m, see Figures 3.4c,d). On the other hand, to correct for blurring one typically uses a division by the CTF value. The reliability of such a procedure on measured (and, hence, noisy) data increases with the absolute value of the CTF. Hence, in order to be able to correct reliably for blurring, a CTF that has greater absolute values at low frequencies is preferable. Based on this, we see that the graphs in Figure 3.4 illustrate the principle that placing a particle so that the defocus at its center is positive (e.g., $1.00\,\mu$m) is preferable to placing it so that the defocus at its center is zero or negative. If we further assume that the specimen is thin (e.g., the difference between $\Delta f(\mathrm{d}_{\mathrm{bottom}})$ and $\Delta f(\mathrm{d}_{\mathrm{top}})$ is $0.1\,\mu$m), then the variation in the shape of the CTF profile curves corresponding to $\mathrm{d}_{\mathrm{top}}$, $\mathrm{d}_{\mathrm{center}}$ and

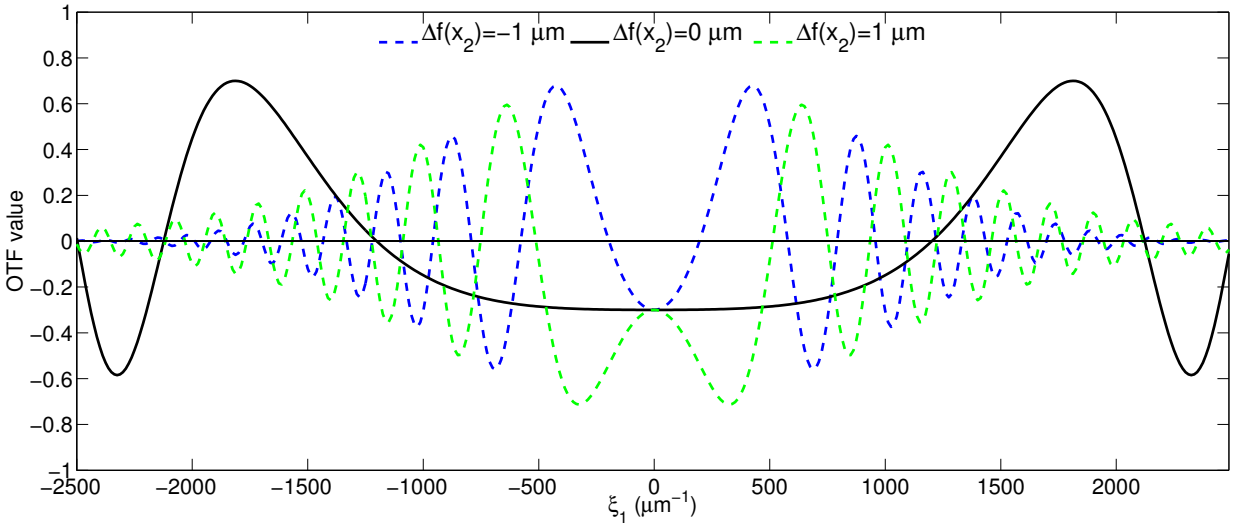

(a)

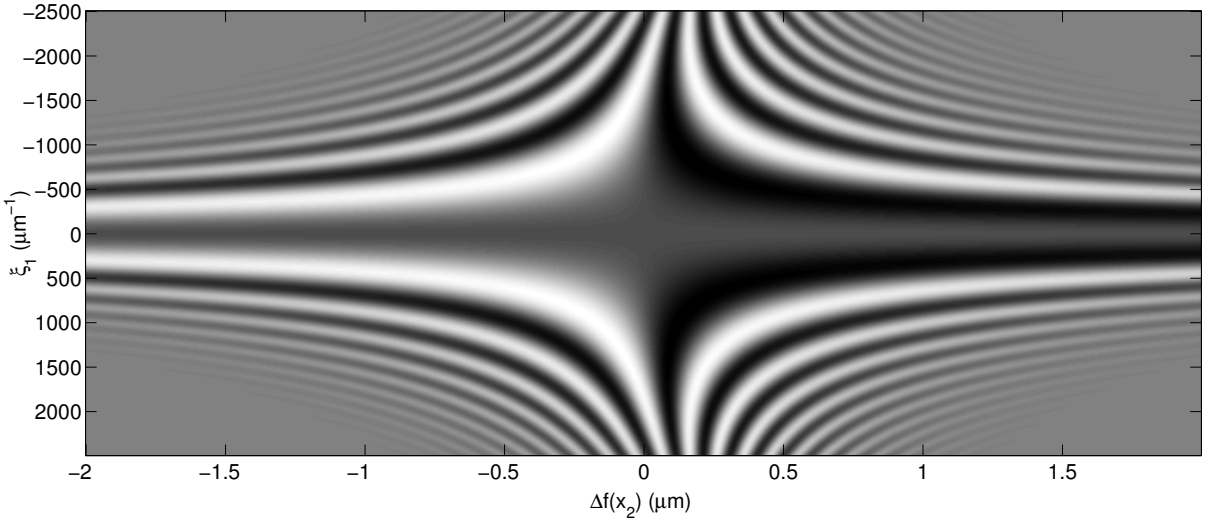

(b)

Figure 3.3: CTF of a transmission electron microscope: **(a)** plots for selected values of the defocus $\Delta f(x_2) = -1$, $\Delta f(x_2) = 0$, and $\Delta f(x_2) = 1$; **(b)** 2D representation of the function for $\Delta f(x_2)_2 \in (-2\mu\text{m}, 2\mu\text{m})$, each column of pixels in the image corresponds to a single plot like the ones shown in (a).

d_{bottom} is hardly visible (see Figure 3.4e) and consequently the CTF can be assumed to be space invariant. However, such an assumption is no longer justified if the difference between $\Delta f(d_{bottom})$ and $\Delta f(d_{top})$ is $1\,\mu$m even if $\Delta f(d_{center}) = 1.00\,\mu$m (see Figure 3.4f) and this indicates that, in order to achieve accuracy, we should use a reconstruction method that takes into consideration the variation in blurring due to the defocus gradient.

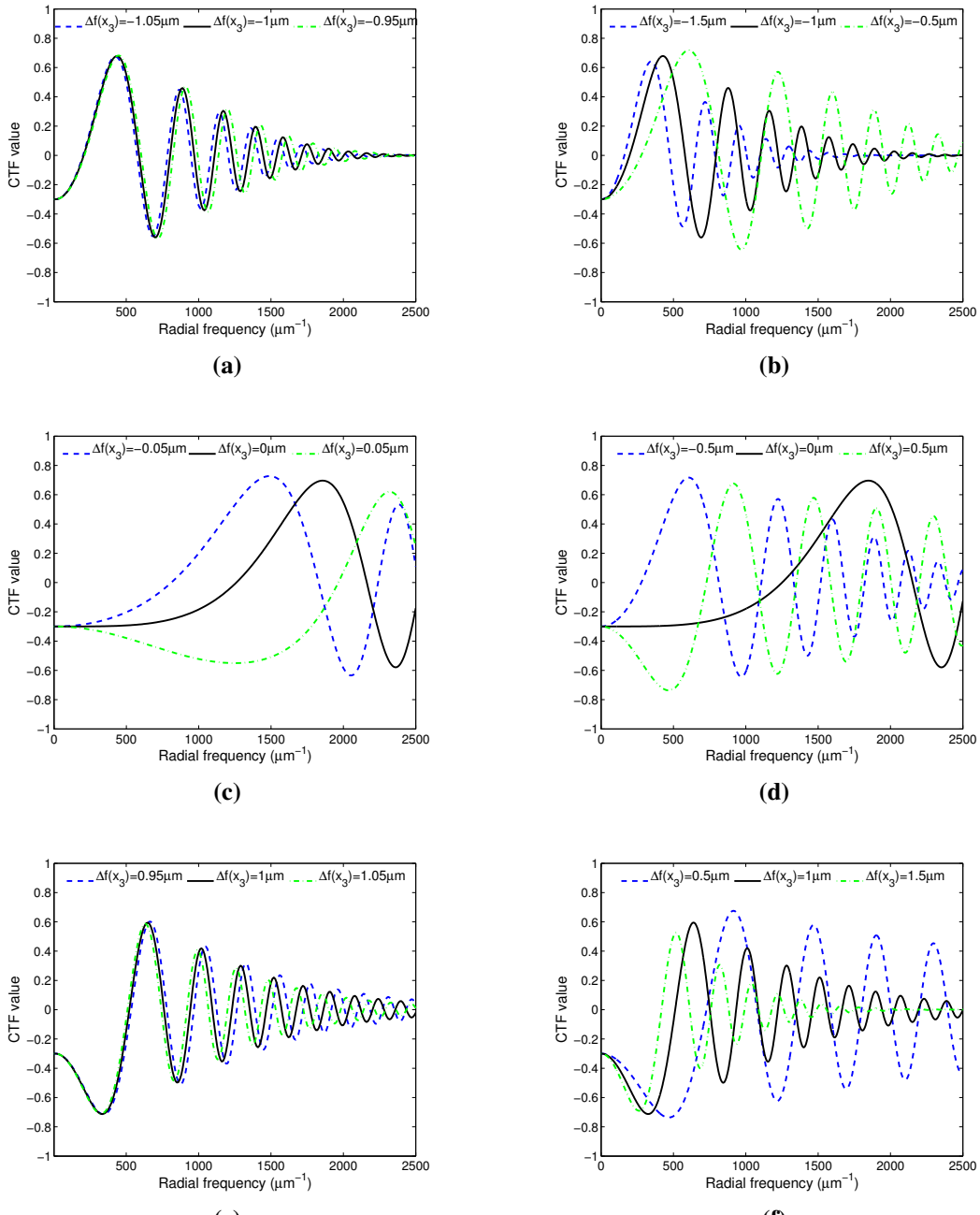

Figure 3.4: Profile curves of the CTF for different defocus values $\Delta f\,(x_2)$:
(a) $\Delta f\left(\mathrm{d_{top}}\right) = -1.05\,\mu\mathrm{m}$, $\Delta f\left(\mathrm{d_{center}}\right) = -1.00\,\mu\mathrm{m}$, $\Delta f\left(\mathrm{d_{bottom}}\right) = -0.95\,\mu\mathrm{m}$, **(b)** $\Delta f\left(\mathrm{d_{top}}\right) = -1.50\,\mu\mathrm{m}$, $\Delta f\left(\mathrm{d_{center}}\right) = -1.00\,\mu\mathrm{m}$, $\Delta f\left(\mathrm{d_{bottom}}\right) = -0.50\,\mu\mathrm{m}$, **(c)** $\Delta f\left(\mathrm{d_{top}}\right) = -0.05\,\mu\mathrm{m}$, $\Delta f\left(\mathrm{d_{center}}\right) = 0.00\,\mu\mathrm{m}$, $\Delta f\left(\mathrm{d_{bottom}}\right) = 0.05\,\mu\mathrm{m}$, **(d)** $\Delta f\left(\mathrm{d_{top}}\right) = -0.50\,\mu\mathrm{m}$, $\Delta f\left(\mathrm{d_{center}}\right) = 0.00\,\mu\mathrm{m}$, $\Delta f\left(\mathrm{d_{bottom}}\right) = 0.50\,\mu\mathrm{m}$. **(e)** $\Delta f\left(\mathrm{d_{top}}\right) = 0.95\,\mu\mathrm{m}$, $\Delta f\left(\mathrm{d_{center}}\right) = 1.00\,\mu\mathrm{m}$, $\Delta f\left(\mathrm{d_{bottom}}\right) = 1.05\,\mu\mathrm{m}$, **(f)** $\Delta f\left(\mathrm{d_{top}}\right) = 0.50\,\mu\mathrm{m}$, $\Delta f\left(\mathrm{d_{center}}\right) = 1.00\,\mu\mathrm{m}$, $\Delta f\left(\mathrm{d_{bottom}}\right) = 1.50\,\mu\mathrm{m}$,

3.2 Blurring in Transmission X-ray Microscopy

The blurring in transmission x-ray microscopy also depends on defocus, but the shape of the function is different from that in electron microscopy. The blurring function in TXM is related to the PSF of the focusing and condenser zone planes. It was shown in Oton et al. [41] and references therein that the PSF can be well approximated by the PSF of a so-called ideal lens. We use that approximation here. The mathematical formula that we use for the PSF is based on Oton et al. [41], Goodman [17] and our discussions with Dr. Oton and Dr. Carazo.

We define the PSF of the transmission soft x-ray microscope in terms of two other function, $T : \mathbb{R}^{n-1} \to \mathbb{R}$ and $P : \mathbb{R}^n \to \mathbb{C}$ for $n \in \{2,3\}$

$$T(\xi_1,\ldots,\xi_{n-1}) = \begin{cases} 1, & \lambda x^f M \sqrt{\xi_1^2+\ldots+\xi_{n-1}^2} \le R \\ 0, & \text{otherwise} \end{cases} \tag{3.7}$$

and

$$P(\xi_1,\ldots,\xi_{n-1},x_n) = \exp\left(\mathrm{i}\pi\lambda\left(x^f M\right)^2\left(\frac{1}{x_n}-\frac{1}{x^f}\right)\left(\xi_1^2+\ldots+\xi_{n-1}^2\right)\right), \tag{3.8}$$

where

λ is the wavelength of x-rays used;

M is the magnification factor;

x^f is the location of the zero-defocus plane along X_n-axis; it is calculated based on the zone plate parameters and λ as $x^f = 4(1+1/M)N_z\rho^2/\lambda$, where N_z is the number of zones and ρ is the diameter of the outermost zone;

R is a parameter of the zone plate computed as $R = 2N_z\rho$, where N_z and ρ are as above.

Then the PSF of a transmission x-ray microscope is

$$h(\boldsymbol{x}) = \left(\left[\mathscr{F}^{-1}_{\xi_1,\ldots,\xi_{n-1}} \left(T\left(\xi_1,\ldots,\xi_{n-1}\right) P\left(\xi_1,\ldots,\xi_{n-1},x_n\right)\right)\right](\boldsymbol{x}) \right)^2 \tag{3.9}$$

The optical transfer function (OTF) of a transmission x-ray microscope is defined as the Fourier transform of the above PSF

$$H = \mathscr{F}_{x_1,\ldots,x_{n-1}} h. \tag{3.10}$$

For any fixed value of x_n both the PSF and OTF are symmetric with respect to the origin. This allows us to show only plots of 2D PSF and OTF (they are identical to cross sections of the corresponding plots in 3D). The function is also symmetric with respect to the x^f line in 2D or plane in 3D.

We illustrate the shape of the PSF and OTF functions for selected values of parameters: $\lambda = 2.43 \times 10^{-9}$m, $M = 2304$, $\rho = 40 \times 10^{-9}$m, $N_z = 560$. The same values of parameters are used in all simulations in Chapter 5. The PSF is illustrated in Figure 3.5. We plot the shape of the function for several values of $\left|x_2 - x^f\right|$ in Figure 3.5a. When x_2 is close to x^f the function has high peak and goes down to near zero values very quickly. As we move further away from the zero-defocus plane at x^f the a high peak at the center decreases and the range of coefficients for which the function has non-negligible values increases. Figure 3.5b illustrates a 2D PSF for values of $\left(x_2 - x^f\right) \in (-5\,\mu\text{m}, 5\,\mu\text{m})$. Each column of pixels corresponds to a particular value of $\left(x_2 - x^f\right)$. The grayscale values in the image represent values of the function with black corresponding to the most negative and white to the most positive value. The limited depth of focus can be clearly seen in that figure.

The OTF plots for several different values of $\left|x_2 - x^f\right|$ are illustrated in Figure 3.6a and the 2D image representation of the OTF is shown in Figure 3.6b. The high frequencies are completely removed by this function and, hence, cannot be recovered by any data correction or reconstruction method. Some of the low frequencies are inverted for parts of the sample that are located further

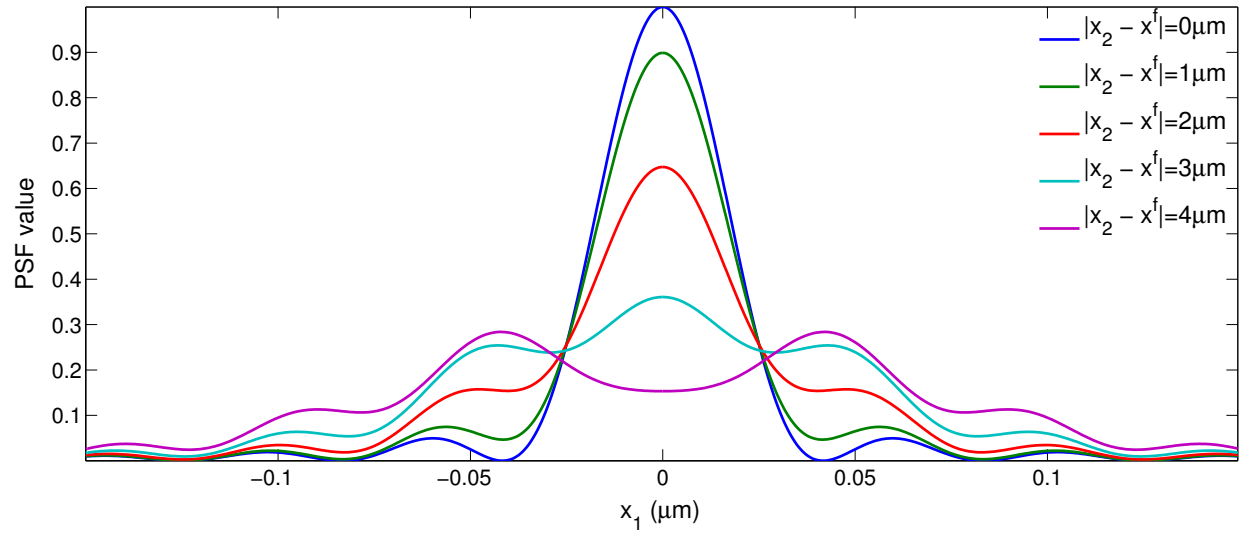

(a)

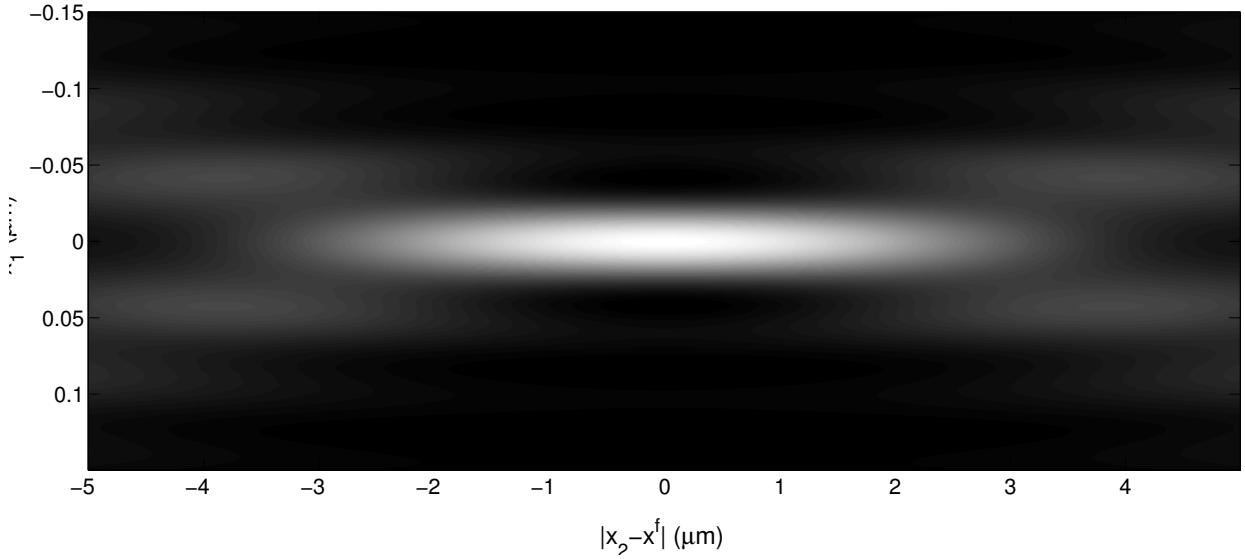

(b)

Figure 3.5: PSF of a transmission x-ray microscope: **(a)** plots for selected values of the distance from the zero-defocus plane $\left|x_2 - x^f\right| = 0\,\mu$m, $\left|x_2 - x^f\right| = 1\,\mu$m, $\left|x_2 - x^f\right| = 2\,\mu$m, $\left|x_2 - x^f\right| = 3\,\mu$m, and $\left|x_2 - x^f\right| = 4\,\mu$m ; **(b)** 2D representation of the function for $\left(x_2 - x^f\right) \in (-5\,\mu\text{m}, 5\,\mu\text{m})$, each column of pixels in the image corresponds to a single plot like the ones shown in (a).

away from the zero-defocus plane, and those should be corrected appropriately when reconstructing from TXM data.

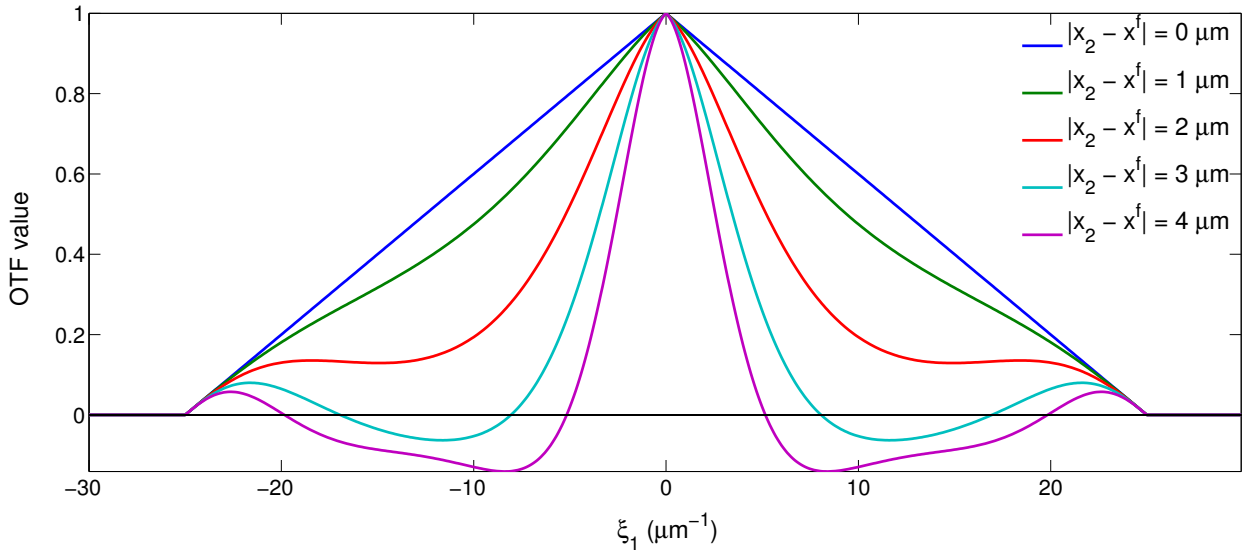

(a) Plots

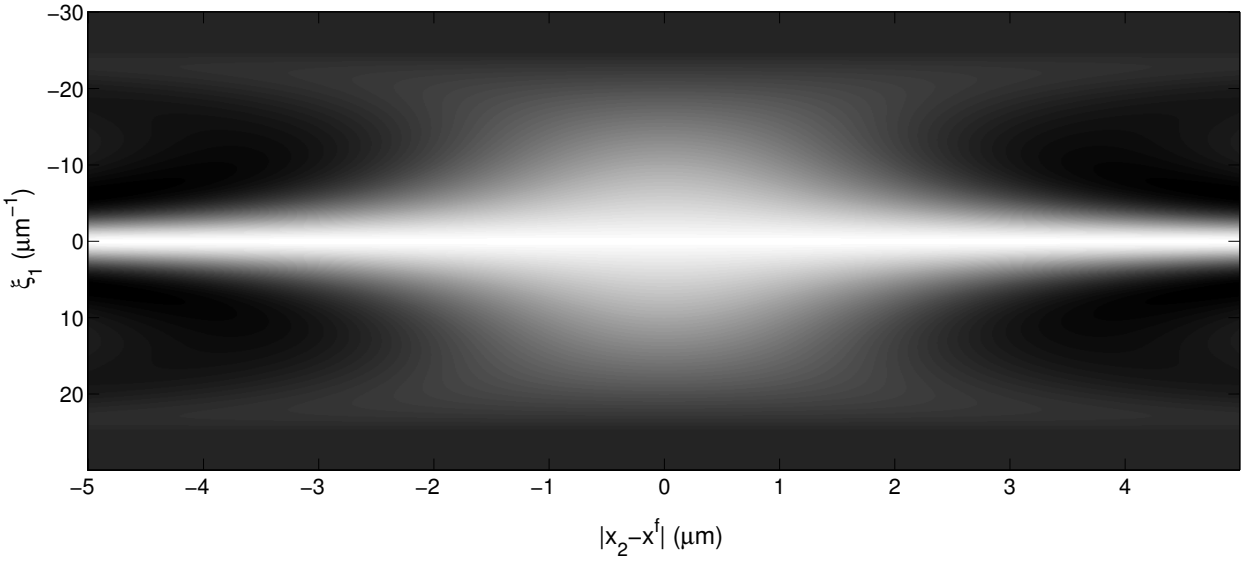

(b) Plots

Figure 3.6: OTF of a transmission x-ray microscope: **(a)** plots for selected values of the distance from the zero-defocus plane $|x_2 - x^f| = 0\,\mu$m, $|x_2 - x^f| = 1\,\mu$m, $|x_2 - x^f| = 2\,\mu$m, $|x_2 - x^f| = 3\,\mu$m, and $|x_2 - x^f| = 4\,\mu$m; **(b)** 2D representation of the function for $(x_2 - x^f) \in (-5\,\mu\text{m}, 5\,\mu\text{m})$, each column of pixels in the image corresponds to a single plot like the ones shown in (a).

Chapter 4

Correction of Blurring in Transmission Electron Microscopy

Transmission electron microscopy produces images of thin biological samples that can be used to produce high resolution 3D reconstructions. The majority of the reconstruction methods assume a space-invariant PSF and yet obtain satisfactory results. It is not clear that in the current state of art of the electron microscopy technology there is much advantage in using distance-dependent blurring correction. The reasons for this are two-fold. First, the thickness of the specimen that can be imaged using single particle electron microscopy (i.e., arbitrary rotation geometry) is limited by the electron penetration depth. For the reasons discussed in Section 3.1, the imaging in TEM is always done by placing the specimen away from the zero-defocus plane and at that point within the thickness of the specimen the change in PSF is negligible. Second, the resolution of the reconstructions is limited by factors other than the blurring and the slight improvement that might be achieved by distance-dependent blurring correction does not provide any benefit to the resolution of the final reconstruction.

The benefit of distance-dependent correction was shown in the case of electron tomography, i.e., when the data are collected using single axis rotation. The need to address the distance-dependence in that case was first realized in the field of electron tomography in the pioneering work

of Henderson and Unwin [20] on the structure of purple membrane, and the issue was handled by dividing the tilt image into strips parallel to the tilt axis that can be considered as blurred by a fixed PSF function. Theoretically, within each of the strips the PSF is still varying, but if the strips are narrow enough it can be considered space-invariant. Each such strip can be corrected with appropriate values of the deblurring function and then reconstruction can be performed. Similar approaches were taken later by Winkler and Taylor [53] and Fernandez et al. [13], and used by Eibauer et al. [10]. Recently, a different approach to correction for distance-dependent blurring was proposed by Voortman et al. [50] and [51]. They perform the reconstruction with correction in Fourier space taking advantage of specific properties of the electron microscope PSF.

In this chapter we concentrate on distance-dependent correction for transmission electron microscopy of single particles, although these techniques can be applied to electron tomography as well. Even though these developments may not produce immediate benefit by improving resolution of the current reconstructions, they provide the basis for further development in the future and in other imaging fields that are affected by distance-dependent blurring. If other resolution limiting factors are significantly reduced, see for example discussion on possibilities of attaining atomic resolution by Zhang and Zhou [55], or the imaging is performed with the specimen at a defocus for which the defocus gradient is much greater, then the correction techniques developed here may result in higher resolution reconstructions than would have been the case without such corrections. Other imaging techniques, among them soft x-ray microscopy discussed in the next chapter, suffer from distance-dependent blurring as well. The correction methods discussed in this chapter may provide a good starting point for corrections of images obtained by other devices.

Some of the results discussed in this chapter were published in Klukowska et al. [31] and Kazantsev et al. [28].

4.1 Image Formation Model

We define all the operators in this chapter to be appropriate for 2D and 3D objects. In practical TEM imaging the objects are 3D, but a lot of theoretical development can be performed in 2D and it is much easier to demonstrate certain results for 2D images in the printed figures.

Image formation by an electron microscope includes a blurring, which is different in each layer (plane perpendicular to the electron beam) of the specimen during the projection generation. A projection data set that consists of all distorted projections (micrographs) is defined as a compression of the rotated version of the object $\mathscr{R}^n v : \mathbb{S}^{n-1} \times \mathbb{R}^n \to \mathbb{R}$, $n \in \{2,3\}$, after it has been convolved with a point spread function $h \in \mathbb{R}^n \to \mathbb{R}$. Mathematically, the *distance-dependent compressing operator* $\mathscr{C}_h^n : \left(\mathbb{S}^{n-1} \times \mathbb{R}^n \to \mathbb{R}\right) \Rightarrow \left(\mathbb{S}^{n-1} \times \mathbb{R}^{n-1} \to \mathbb{R}\right)$ is defined by

$$\mathscr{C}_h^n w = \mathscr{C}^n \left[w \underset{x_1,\ldots,x_{n-1}}{*} h \right], \tag{4.1}$$

where $w : \mathbb{S}^{n-1} \times \mathbb{R}^n \to \mathbb{R}$. In practice we only apply this operator to functions w that result from rotation of a specimen in a microscope, i.e., functions of the form $\mathscr{R}^n v$. The *distance-dependent projection operator* $\mathscr{P}_h^n : (\mathbb{R}^n \to \mathbb{R}) \Rightarrow \left(\mathbb{S}^{n-1} \times \mathbb{R}^{n-1} \to \mathbb{R}\right)$ is defined by

$$\mathscr{P}_h^n = \mathscr{C}_h^n \mathscr{R}^n. \tag{4.2}$$

Observe that for the choice of blurring function $h(x_1,\ldots,x_{n-1},x_n) = \iota(x_1,\ldots,x_{n-1})$, where ι is $(n-1)$-dimensional Dirac delta function as defined in Eq. (A.3), we have $\mathscr{C}_\iota = \mathscr{C}$ and $\mathscr{P}_\iota = \mathscr{P}$.

Lemma 4.1. *The Fourier transform of the distance-dependent projection data satisfies the formula*

$$\begin{aligned}
&\left[\mathscr{F}_{x_1,\ldots,x_{n-1}} \mathscr{P}_h^n v\right](\boldsymbol{\theta}, \xi_1, \ldots, \xi_{n-1}) \\
&\quad = (2\pi)^{(n-1)/2} \int_{\mathbb{R}} \left[\mathscr{F}_{x_1,\ldots,x_{n-1}} \mathscr{R}^n v\right](\boldsymbol{\theta}, \xi_1, \ldots, \xi_{n-1}, x_n) H(\xi_1, \ldots, \xi_{n-1}, x_n) dx_n,
\end{aligned} \tag{4.3}$$

where

$$H = \mathscr{F}_{x_1,\ldots,x_{n-1}} h. \tag{4.4}$$

Proof. This is proved by applying the previously defined operators and cited theorems. We start by expanding the left hand side using the definitions of the distance-dependent projection operators, $\mathscr{P}_h^n$ of Eq. (4.2), $\mathscr{C}_h^n$ of Eq. (4.1) and $\mathscr{C}^n$ of Eq. (2.21), then use the linearity of the Fourier transform operator to move it inside the integral, apply the convolution theorem stated in Eq. (2.19), and finally perform the substitution according to definition of H of Eq. (4.4):

$$\begin{aligned}
&\left[\mathscr{F}_{x_1,\ldots,x_{n-1}} \mathscr{P}_h^n v\right](\boldsymbol{\theta}, \xi_1, \ldots, \xi_{n-1}) \\
&\quad = \mathscr{F}_{x_1,\ldots,x_{n-1}} \left(\int_{\mathbb{R}} \left[\mathscr{R}^n v\right](\boldsymbol{\theta}, \boldsymbol{x}) \underset{x_1,\ldots,x_{n-1}}{*} h(\boldsymbol{x}) \, \mathrm{d}x_n \right) \\
&\quad = (2\pi)^{(n-1)/2} \int_{\mathbb{R}} \left[\mathscr{F}_{x_1,\ldots,x_{n-1}} \mathscr{R}^n v\right](\boldsymbol{\theta}, \xi_1, \ldots, \xi_{n-1}, x_n) \left[\mathscr{F}_{x_1,\ldots,x_{n-1}} h\right](\xi_1, \ldots, \xi_{n-1}, x_n) \, \mathrm{d}x_n \\
&\quad = (2\pi)^{(n-1)/2} \int_{\mathbb{R}} \left[\mathscr{F}_{x_1,\ldots,x_{n-1}} \mathscr{R}^n v\right](\boldsymbol{\theta}, \xi_1, \ldots, \xi_{n-1}, x_n) H(\xi_1, \ldots, \xi_{n-1}, x_n) \, \mathrm{d}x_n
\end{aligned} \tag{4.5}$$

□

Lemma 4.1 indicates an efficient layer-by-layer method of calculating $\mathscr{P}_h^n v$.

4.2 Defocus-Gradient Corrected Backprojection

The *defocus-gradient corrected back-projection* (DGCBP) is a reconstruction method that incorporates correction for a distance dependent PSF.

Jensen and Kornberg [27] suggested a modification to the backprojection algorithm that is frequently used in reconstruction from electron micrographs, see Radermacher [42]. The projection data are collected from arbitrary angles. The essence of this method is to perform correction of projection images for PSF appropriate to different layers of the particle in each backprojection step.

This guarantees that each layer of the reconstructed volume is corrected for the PSF appropriate for its distance from the electron source - hence we can consider this part of a reconstruction to be a valid signal. Each layer of the reconstructed volume contains also data that came from other layers and that contributes to noise in a reconstructed volume. The step by step description of this method is provided in Algorithm 4.1 and the schematic illustration in Figure 4.1.

This method assumes that superposition of corrected data and miscorrected data enhances the appropriately corrected signal while suppressing the noise from miscorrected layers. As the number of layers increases, the reconstruction should be more accurate. In Kazantsev et al. [28], we provided mathematical analysis of DGCBP algorithm as the number of layers goes to infinity and proved that it provides the approximate inverse for the distance dependent projection operator $\mathscr{P}_h^n$ of Eq. (4.2) for the case of $n = 3$. This proof, generalized to the case of $n \in \{2,3\}$, is discussed in the next section.

4.3 Inversion of the Distance-Dependent Projection Operator

We define operators that are generalizations of the spreading back operator of Eq. (2.26) and of the backprojection operator of Eq. (2.28). The *distance-dependent spreading back operator* $\mathscr{S}_h^n : \left(\mathbb{S}^{n-1} \times \mathbb{R}^{n-1} \to \mathbb{R}\right) \Rightarrow \left(\mathbb{S}^{n-1} \times \mathbb{R}^n \to \mathbb{R}\right)$ is defined by

$$\left[\mathscr{S}_h^n g\right](\boldsymbol{\theta}, \boldsymbol{x}) = \left(\frac{1}{2\pi}\right)^{(n-1)/2} \left[\mathscr{F}^{-1}_{\xi_1,\ldots,\xi_{n-1}} \frac{\left[\mathscr{F}_{x_1,\ldots,x_{n-1}} g\right](\boldsymbol{\theta}, \xi_1, \ldots, \xi_{n-1})}{\left[\mathscr{F}_{x_1,\ldots,x_{n-1}} h\right](\xi_1, \ldots, \xi_{n-1}, x_n)}\right](\boldsymbol{\theta}, \boldsymbol{x}). \tag{4.6}$$

This is a generalization of the spreading back operator because $\mathscr{S}_h^n = \mathscr{S}^n$ when h is equal to the $(n-1)$-dimensional Dirac delta function.

The *distance-dependent backprojection operator* $\mathscr{B}_h^n : \left(\mathbb{S}^{n-1} \times \mathbb{R}^{n-1} \to \mathbb{R}\right) \Rightarrow \left(\mathbb{R}^n \to \mathbb{R}\right)$ is defined by

$$\mathscr{B}_h^n = \mathscr{T}^n \mathscr{S}_h^n. \tag{4.7}$$

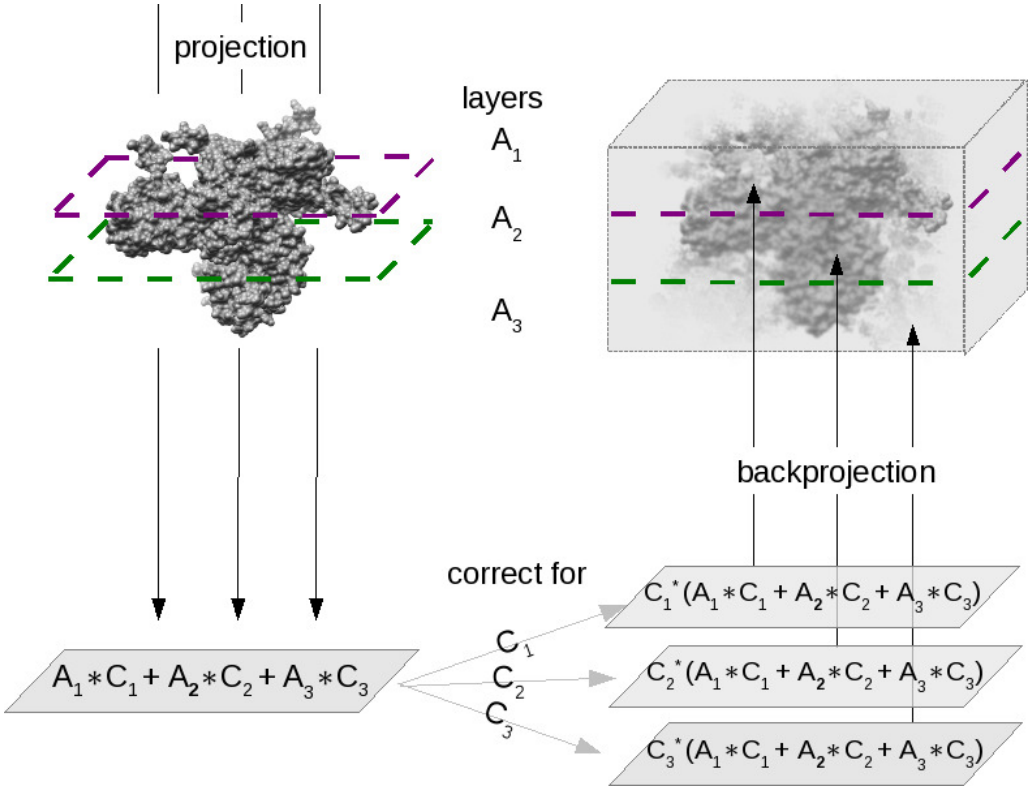

Figure 4.1: Schematic explanation of the DGCBP algorithm. A particle is divided into hypothetical layers A_1, A_2, A_3 with the assumption that within each layer the CTF can be considered to be constant. The values of the CTF in layers A_1, A_2, A_3 are C_1, C_2, C_3, respectively. During the correction process, each projection is replicated several times (three in this example) and each copy is corrected for the CTF corresponding to one of the layers of the particle. Then layers of a back-projection body are filled with data from the appropriately corrected copy of the projection. (Our figure is based on Figure 2 in Jensen and Kornberg [27].)

Algorithm 4.1 DGCBP (with example referring to Figure 4.1)

1: **for** all projection directions **do**
2: divide the object into hypothetical layers (three layers A_1, A_2 and A_3 are shown) and determine the CTF appropriate for each layer (CTFs C_1, C_2 and C_3 are shown)
3: obtain a micrograph (it will have data corrupted by different CTFs for different layers)
4: make as many copies of the micrograph as there are layers (3 in the example)
5: correct each copy of the micrograph by a different CTF
6: backproject data filling each voxel in the back-projected body with data from appropriately corrected micrograph
7: **end for**

This is a generalization of the backprojection operator because $\mathscr{B}_h^n = \mathscr{B}^n$ when h is equal to the $(n-1)$-dimensional Dirac delta function.

Theorem 4.2. *For functions $v : \mathbb{R}^n \to \mathbb{R}$ and $h : \mathbb{R}^n \to \mathbb{R}$, $n \in \{2,3\}$, and the distance-dependent operators $\mathscr{P}_h^n$ and $\mathscr{B}_h^n$ defined in Eqs. 4.2 and 4.7,*

$$\mathscr{B}^n \mathscr{P}^n v \approx \mathscr{B}_h^n \mathscr{P}_h^n v, \tag{4.8}$$

where $\approx$ stands for approximately equal.

Corollary 4.3. *A function $v : \mathbb{R}^n \to \mathbb{R}$, $n \in \{2,3\}$ can be reconstructed from its distance-dependently blurred projection data, $\mathscr{P}_h^n v$ by applying to it first the distance-dependent back-projection operator $\mathscr{B}_h^n$ and then the deblurring operator $\mathscr{D}^n$:*

$$\mathscr{D}^n \mathscr{B}_h^n \mathscr{P}_h^n v \approx v. \tag{4.9}$$

Proof. The validity of this corollary follows immediately from Theorem 4.2 (which we prove below) and Theorem 2.1. □

4.3.1 Proof of Theorem 4.2

By the linearity of the operators, Theorem 4.2 for an arbitrary $v : \mathbb{R}^n \to \mathbb{R}$, $n \in \{2,3\}$ follows from the special case when v is the impulse function centered at an arbitrary point $\widehat{\boldsymbol{x}} \in \mathbb{R}^n$. We use κ, defined by

$$\kappa(\boldsymbol{x}) = \delta(\widehat{x}_1 - x_1) \ldots \delta(\widehat{x}_n - x_n), \tag{4.10}$$

to denote such impulse function. Several properties of κ that we use later are stated in Appendix A. One of these properties is an alternate expression for the rotation of κ

$$[\mathscr{R}^n \kappa](\boldsymbol{\theta}, \boldsymbol{x}) = \delta\left(\widehat{x}_1^{\mathcal{B}}(\boldsymbol{\theta}) - x_1\right) \ldots \delta\left(\widehat{x}_n^{\mathcal{B}}(\boldsymbol{\theta}) - x_n\right). \tag{4.11}$$

Appendix A.2 shows the equivalence of this expression to $\mathscr{R}^n\kappa$ that would have been obtained by application of $\mathscr{R}^n$ operator of Eq. (2.20). The reason for use of this alternate expression becomes apparent in the rest of the proof.

The proof follows in three steps. In Step 1 (starting on page 43) we derive the integral expression for $\mathscr{B}_h^n\mathscr{P}_h^n\kappa$. In Step 2 (starting on page 44) we derive the integral expression for $\mathscr{B}^n\mathscr{P}^n\kappa$. In Step 3 starting on (page 45) we show that the two expressions are approximately equal. The last step is the longest and the most involved. We consider separately the expressions for $n=2$ (starting on page 46) and for $n=3$ (starting on page 48).

***Step 1*:** Derive integral expression for $\mathscr{B}_h^n\mathscr{P}_h^n\kappa$.

First observe that the Fourier transform with respect to $x_1,\ldots,x_{n-1}$ of $[\mathscr{R}^n\kappa](\boldsymbol{\theta},\boldsymbol{x})$ is obtained by using the shifting property of the Fourier transform of the impulse function (see Eqs. (A.1) and (A.12)):

$$\begin{aligned}
&\left[\mathscr{F}_{x_1,\ldots,x_{n-1}}\mathscr{R}^n\kappa\right](\boldsymbol{\theta},\xi_1,\ldots,\xi_{n-1},x_n) = \\
&\quad = \left(\frac{1}{2\pi}\right)^{(n-1)/2}\delta\left(\widehat{x}_n^{\mathcal{B}}(\boldsymbol{\theta})-x_n\right)\mathrm{e}^{-\mathrm{i}\left(\widehat{x}_1^{\mathcal{B}}(\boldsymbol{\theta})\xi_1+\ldots+\widehat{x}_{n-1}^{\mathcal{B}}(\boldsymbol{\theta})\xi_{n-1}\right)}.
\end{aligned} \tag{4.12}$$

Using Lemma 4.1 and the equation on the line above, we derive the expression for the Fourier transform of the projection data of κ

$$\begin{aligned}
&\left[\mathscr{F}_{x_1,\ldots,x_{n-1}}\mathscr{P}_h^n\kappa\right](\boldsymbol{\theta},\xi_1,\ldots,\xi_{n-1}) = \\
&\quad = (2\pi)^{(n-1)/2}\int_{\mathbb{R}}\left[\mathscr{F}_{x_1,\ldots,x_{n-1}}\mathscr{R}^n\kappa\right](\boldsymbol{\theta},\xi_1,\ldots,\xi_{n-1},x_n)\,H(\xi_1,\ldots,\xi_{n-1},x_n)\,\mathrm{d}x_n \\
&\quad = \int_{\mathbb{R}}\delta\left(\widehat{x}_n^{\mathcal{B}}(\boldsymbol{\theta})-x_n\right)\mathrm{e}^{-\mathrm{i}\left(\widehat{x}_1^{\mathcal{B}}(\boldsymbol{\theta})\xi_1+\ldots+\widehat{x}_{n-1}^{\mathcal{B}}(\boldsymbol{\theta})\xi_{n-1}\right)}H(\xi_1,\ldots,\xi_{n-1},x_n)\,\mathrm{d}x_n \\
&\quad = H\left(\xi_1,\ldots,\xi_{n-1},\widehat{x}_n^{\mathcal{B}}(\boldsymbol{\theta})\right)\mathrm{e}^{-\mathrm{i}\left(\widehat{x}_1^{\mathcal{B}}(\boldsymbol{\theta})\xi_1+\ldots+\widehat{x}_{n-1}^{\mathcal{B}}(\boldsymbol{\theta})\xi_{n-1}\right)}.
\end{aligned} \tag{4.13}$$

Next, we compute the integral expression for $\mathscr{B}_h^n\mathscr{P}_h^n\kappa$. To do so we need to first compute $\mathscr{S}_h^n\mathscr{P}_h^n\kappa$ by using the definition of $\mathscr{S}_h^n$ operator, the expression for $\mathscr{F}_{x_1,\ldots,x_{n-1}}\mathscr{P}_h^n$ from Eq. (4.13) and the

definition of the inverse Fourier transform operator:

$$
\begin{aligned}
&\left[\mathscr{S}_h^n \mathscr{P}_h^n \kappa\right](\boldsymbol{\theta}, \boldsymbol{x}) = \\
&\quad = \left(\frac{1}{2\pi}\right)^{(n-1)/2} \left[\mathscr{F}^{-1}_{\xi_1,\ldots,\xi_{n-1}} \frac{\left[\mathscr{F}_{x_1,\ldots,x_{n-1}} \mathscr{P}_h^n \kappa\right](\boldsymbol{\theta}, \xi_1, \ldots, \xi_{n-1})}{H(\xi_1, \ldots, \xi_{n-1}, x_n)}\right](\boldsymbol{\theta}, \boldsymbol{x}) \\
&\quad = \left(\frac{1}{2\pi}\right)^{(n-1)/2} \left[\mathscr{F}^{-1}_{\xi_1,\ldots,\xi_{n-1}} \frac{H\left(\xi_1, \ldots, \xi_{n-1}, \widehat{x}_n^B(\boldsymbol{\theta})\right) \mathrm{e}^{-\mathrm{i}\left(\widehat{x}_1^B(\boldsymbol{\theta})\xi_1 + \ldots + \widehat{x}_{n-1}^B(\boldsymbol{\theta})\xi_{n-1}\right)}}{H(\xi_1, \ldots, \xi_{n-1}, x_n)}\right](\boldsymbol{\theta}, \boldsymbol{x}) \\
&\quad = \left(\frac{1}{2\pi}\right)^{n-1} \int\limits_{\mathbb{R}^{n-1}} \frac{H\left(\xi_1, \ldots, \xi_{n-1}, \widehat{x}_n^B(\boldsymbol{\theta})\right) \mathrm{e}^{-\mathrm{i}\left(\widehat{x}_1^B(\boldsymbol{\theta})\xi_1 + \ldots + \widehat{x}_{n-1}^B(\boldsymbol{\theta})\xi_{n-1}\right)}}{H(\xi_1, \ldots, \xi_{n-1}, x_n)} \qquad (4.14) \\
&\qquad\qquad \mathrm{e}^{i(x_1\xi_1 + \ldots + x_{n-1}\xi_{n-1})} \mathrm{d}\xi_1 \ldots \mathrm{d}\xi_{n-1}
\end{aligned}
$$

By the definition of the distance-dependent backprojection operator $\mathscr{B}_h^n$ of Eq. (4.7), we obtain $\mathscr{B}_h^n \mathscr{P}_h^n \kappa$ by applying the $\mathscr{T}^n$ operator to the expression of Eq. (4.14) obtained above:

$$
\begin{aligned}
&\left[\mathscr{B}_h^n \mathscr{P}_h^n \kappa\right](\boldsymbol{x}) = \left[\mathscr{T}^n \mathscr{S}_h^n \mathscr{P}_h^n \kappa\right](\boldsymbol{x}) = \\
&\quad = \left(\frac{1}{2\pi}\right)^{n-1} \int\limits_{\mathbb{S}^{n-1}} \int\limits_{\mathbb{R}^{n-1}} \frac{H\left(\xi_1, \ldots, \xi_{n-1}, \widehat{x}_n^B(\boldsymbol{\theta})\right) \mathrm{e}^{-\mathrm{i}\left(\widehat{x}_1^B(\boldsymbol{\theta})\xi_1 + \ldots + \widehat{x}_{n-1}^B(\boldsymbol{\theta})\xi_{n-1}\right)}}{H(\xi_1, \ldots, \xi_{n-1}, x_n^B(\boldsymbol{\theta}))} \\
&\qquad\qquad \mathrm{e}^{i\left(x_1^B(\boldsymbol{\theta})\xi_1 + \ldots + x_{n-1}^B(\boldsymbol{\theta})\xi_{n-1}\right)} \left|J(\boldsymbol{\theta})\right| \mathrm{d}\xi_1 \ldots \mathrm{d}\xi_{n-1} \mathrm{d}\boldsymbol{\theta} \\
&\quad = \left(\frac{1}{2\pi}\right)^{n-1} \int\limits_{\mathbb{R}^{n-1}} \int\limits_{\mathbb{S}^{n-1}} \frac{H\left(\xi_1, \ldots, \xi_{n-1}, \widehat{x}_n^B(\boldsymbol{\theta})\right)}{H(\xi_1, \ldots, \xi_{n-1}, x_n^B(\boldsymbol{\theta}))} \mathrm{e}^{-\mathrm{i}\left(\widehat{x}_1^B(\boldsymbol{\theta}) - x_1^B(\boldsymbol{\theta})\right)\xi_1} \qquad (4.15) \\
&\qquad\qquad \ldots \mathrm{e}^{-\mathrm{i}\left(\widehat{x}_{n-1}^B(\boldsymbol{\theta}) - x_{n-1}^B(\boldsymbol{\theta})\right)\xi_{n-1}} \left|J(\boldsymbol{\theta})\right| \mathrm{d}\boldsymbol{\theta} \mathrm{d}\xi_1 \ldots \mathrm{d}\xi_{n-1}
\end{aligned}
$$

***Step* 2:** Derive integral expression for $\mathscr{B}^n \mathscr{P}^n \kappa$.

For the purpose of comparison of the integral expression for $\mathscr{B}^n \mathscr{P}^n \kappa$ with the integral expression for $\mathscr{B}_h^n \mathscr{P}_h^n \kappa$ that we derived in step 1, we write

$$
\mathscr{B}^n \mathscr{P}^n \kappa = \mathscr{T}^n S^n \mathscr{F}^{-1}_{x_1,\ldots,x_{n-1}} \mathscr{F}_{x_1,\ldots,x_{n-1}} \mathscr{P}^n \kappa \qquad (4.16)
$$

which follows from the definition of the operator $\mathscr{B}^n$ of Eq. (2.28) and invertability of the Fourier

transform stated in Eq. (2.17). Using the definitions of operators $\mathscr{P}^n$, $\mathscr{C}^n$, $\mathscr{R}^n$ and Eq. (4.12) we compute first $\mathscr{F}_{x_1,\ldots,x_{n-1}}\mathscr{P}^n\boldsymbol{\kappa}$ to be

$$\begin{aligned}
&\left[\mathscr{F}_{x_1,\ldots,x_{n-1}}\mathscr{P}^n\boldsymbol{\kappa}\right](\boldsymbol{\theta},\xi_1,\ldots,\xi_{n-1}) \\
&\quad=\left[\mathscr{F}_{x_1,\ldots,x_{n-1}}\mathscr{C}^n\mathscr{R}^n\boldsymbol{\kappa}\right](\boldsymbol{\theta},\xi_1,\ldots,\xi_{n-1}) \\
&\quad=\left[\mathscr{C}^n\mathscr{F}_{x_1,\ldots,x_{n-1}}\mathscr{R}^n\boldsymbol{\kappa}\right](\boldsymbol{\theta},\xi_1,\ldots,\xi_{n-1}) \\
&\quad=\left(\frac{1}{2\pi}\right)^{(n-1)/2}\int\limits_{\mathbb{R}}\delta\left(\hat{x}_n^B(\boldsymbol{\theta})-x_n\right)\mathrm{e}^{-\mathrm{i}\left(\hat{x}_1^B(\boldsymbol{\theta})\xi_1+\ldots+\hat{x}_{n-1}^B(\boldsymbol{\theta})\xi_{n-1}\right)}\mathrm{d}x_n \\
&\quad=\left(\frac{1}{2\pi}\right)^{(n-1)/2}\mathrm{e}^{-\mathrm{i}\left(\hat{x}_1^B(\boldsymbol{\theta})\xi_1+\ldots+\hat{x}_{n-1}^B(\boldsymbol{\theta})\xi_{n-1}\right)},
\end{aligned}\tag{4.17}$$

and then apply the inverse Fourier transform and the $\mathscr{S}^n$ operator

$$\begin{aligned}
&\left[\mathscr{S}^n\mathscr{F}^{-1}_{x_1,\ldots,x_{n-1}}\mathscr{F}_{x_1,\ldots,x_{n-1}}\mathscr{P}^n\boldsymbol{\kappa}\right](\boldsymbol{\theta},x_1,\ldots,x_n)= \\
&\quad=\left(\frac{1}{2\pi}\right)^{(n-1)/2}\int\limits_{\mathbb{R}^{n-1}}\left[\mathscr{F}_{x_1,\ldots,x_{n-1}}\mathscr{P}^n\boldsymbol{\kappa}\right](\boldsymbol{\theta},\xi_1,\ldots,\xi_{n-1})\,\mathrm{e}^{\mathrm{i}(x_1\xi_1,\ldots,x_{n-1}\xi_{n-1})}\mathrm{d}\xi_1\ldots\mathrm{d}\xi_{n-1} \\
&\quad=\left(\frac{1}{2\pi}\right)^{n-1}\int\limits_{\mathbb{R}^{n-1}}\mathrm{e}^{-\mathrm{i}\left(\hat{x}_1^B(\boldsymbol{\theta})\xi_1+\ldots+\hat{x}_{n-1}^B(\boldsymbol{\theta})\xi_{n-1}\right)}\mathrm{e}^{\mathrm{i}(x_1\xi_1,\ldots,x_{n-1}\xi_{n-1})}\mathrm{d}\xi_1\ldots\mathrm{d}\xi_{n-1} \\
&\quad=\left(\frac{1}{2\pi}\right)^{n-1}\int\limits_{\mathbb{R}^{n-1}}\mathrm{e}^{-\mathrm{i}\left(\hat{x}_1^B(\boldsymbol{\theta})-x_1\right)\xi_1}\ldots\mathrm{e}^{-\mathrm{i}\left(\hat{x}_{n-1}^B(\boldsymbol{\theta})-x_{n-1}\right)\xi_{n-1}}\mathrm{d}\xi_1\ldots\mathrm{d}\xi_{n-1}.
\end{aligned}\tag{4.18}$$

Finally, we use the computation above to derive the integral expression for $\mathscr{B}^n\mathscr{P}^n\boldsymbol{\kappa}$ as follows,

$$\begin{aligned}
\mathscr{B}^n\mathscr{P}^n\boldsymbol{\kappa}(\boldsymbol{x})&=\mathscr{T}^n\mathscr{S}^n\mathscr{F}^{-1}_{x_1,\ldots,x_{n-1}}\mathscr{F}_{x_1,\ldots,x_{n-1}}\mathscr{P}^n\boldsymbol{\kappa}(\boldsymbol{x}) \\
&=\left(\frac{1}{2\pi}\right)^{n-1}\int\limits_{\mathbb{R}^{n-1}}\int\limits_{\mathbb{S}^{n-1}}\mathrm{e}^{-\mathrm{i}\left(\hat{x}_1^B(\boldsymbol{\theta})-x_1^B(\boldsymbol{\theta})\right)\xi_1}\ldots\mathrm{e}^{-\mathrm{i}\left(\hat{x}_{n-1}^B(\boldsymbol{\theta})-x_{n-1}^B(\boldsymbol{\theta})\right)\xi_{n-1}}\left|J(\boldsymbol{\theta})\right|\mathrm{d}\boldsymbol{\theta}\mathrm{d}\xi_1\ldots\mathrm{d}\xi_{n-1}.
\end{aligned}\tag{4.19}$$

***Step 3*:** Show the equivalence between $\mathscr{B}_h^n\mathscr{P}_h^n\boldsymbol{\kappa}$ and $\mathscr{B}^n\mathscr{P}^n\boldsymbol{\kappa}$ using stationary phase approximation of Eq. (2.44). This step is handled separately for $n=2$ and $n=3$. The derivations are related, but they are easier to follow when treated individually.

***Step 3a*:** $n = 2$

When $n = 2$, the angle vector $\boldsymbol{\theta}$ is a one element vector, in what follows we use θ_1 instead of (θ_1) notation. The Eqs. (4.15) and (4.19) can be rewritten as follows

$$\left[\mathscr{B}_h^2 \mathscr{P}_h^2 \kappa\right](\boldsymbol{x}) = \left(\frac{1}{2\pi}\right) \int_{\mathbb{R}^1} \int_{\mathbb{S}^1} \frac{H\left(\xi_1, \widehat{x}_2^B(\theta_1)\right)}{H\left(\xi_1, x_2^B(\theta_1)\right)} \mathrm{e}^{-\mathrm{i}\left(\widehat{x}_1^B(\boldsymbol{\theta}) - x_1^B(\boldsymbol{\theta})\right)\xi_1} \mathrm{d}\theta_1 \mathrm{d}\xi_1. \tag{4.20}$$

$$\left[\mathscr{B}^2 \mathscr{P}^2 \kappa\right](\boldsymbol{x}) = \left(\frac{1}{2\pi}\right) \int_{\mathbb{R}^1} \int_{\mathbb{S}^1} \mathrm{e}^{\mathrm{i}\left(x_1^B(\theta_1) - \widehat{x}_1^B(\theta_1)\right)\xi_1} \mathrm{d}\theta_1 \mathrm{d}\xi_1. \tag{4.21}$$

We analyze this expression considering different cases of the relationship between $\widehat{\boldsymbol{x}}$ and $\boldsymbol{x}$:

Case 1. Consider first the special case when $(x_1, x_2)^T = (\widehat{x}_1, \widehat{x}_2)^T$. In this case it follows trivially from Eq. (2.9) that $\widehat{x}_2^B(\theta_1) = x_2^B(\theta_1)$, for all $\boldsymbol{\theta} = (\theta_1) \in \mathbb{S}^1$, and so the value of the fraction inside the integral in Eq. (4.20) is always 1, independently of the choice of h. This means that $\left[\mathscr{B}_h^2 \mathscr{P}_h^2 \kappa\right](\widehat{x}_1, \widehat{x}_2) = \left[\mathscr{B}^2 \mathscr{P}^2 \kappa\right](\widehat{x}_1, \widehat{x}_2)$ and Theorem 4.2 is satisfied exactly at this point.

Case 2. Either $x_1 \neq \widehat{x}_1$, or $x_2 \neq \widehat{x}_2$, or both. In this case we make use of the stationary phase approximation discussed in Subsection 2.4. We concentrate on the integral over $\mathbb{S}^1$ and take ξ_1, x_1 and x_2 as fixed. We define

$$I = \int_{\mathbb{S}^1} G^{\xi_1, x_1, x_2}(\theta_1) \mathrm{e}^{-\mathrm{i}\xi_1 F^{x_1, x_2}(\theta_1)} \mathrm{d}\theta_1, \tag{4.22}$$

where

$$G^{\xi_1, x_1, x_2}(\theta_1) = \frac{H\left(\xi_1, \widehat{x}_2^B(\theta_1)\right)}{H\left(\xi_1, x_2^B(\theta_1)\right)} \tag{4.23}$$

and

$$\begin{aligned} F^{x_1, x_2}(\theta_1) &= \widehat{x}_1^B(\theta_1) - x_1^B(\theta_1) \\ &= \widehat{x}_1 \cos\theta_1 - \widehat{x}_2 \sin\theta_1 - x_1 \cos\theta_1 + x_2 \sin\theta_1 \end{aligned}$$

$$= (\widehat{x}_1 - x_1)\cos\theta_1 - (\widehat{x}_2 - x_2)\sin\theta_1. \tag{4.24}$$

According to the stationary phase approximation, the integral I receives non-negligible contributions only from values of θ_1 that are non-degenerate critical points of $F^{x_1,x_2}(\theta_1)$. We next evaluate these critical points. The first derivative of F^{x_1,x_2} is

$$\begin{aligned}\frac{\mathrm{d}F^{x_1,x_2}}{\mathrm{d}\theta_1}(\theta_1) &= -(\widehat{x}_1 - x_1)\sin\theta_1 - (\widehat{x}_2 - x_2)\cos\theta_1 \\ &= x_2^B(\theta_1) - \widehat{x}_2^B(\theta_1).\end{aligned} \tag{4.25}$$

There are exactly two critical points $\theta_1^* \in [0, 2\pi)$ of this function. We show that they are non-degenerate by contradiction. The second derivative of F^{x_1,x_2} is

$$\frac{\mathrm{d}^2F^{x_1,x_2}}{\mathrm{d}\theta_1^2}(\theta_1) = -(\widehat{x}_1 - x_1)\cos\theta_1 + (\widehat{x}_2 - x_2)\sin\theta_1. \tag{4.26}$$

Assume that at least one of the stationary points θ_1^* is degenerate; then $\dfrac{\mathrm{d}^2F^{x_1,x_2}}{\mathrm{d}\theta_1^2}(\theta_1^*) = 0$. Combining this equation with $\dfrac{\mathrm{d}F^{x_1,x_2}}{\mathrm{d}\theta_1}(\theta_1^*) = 0$ (which follows from the fact that θ_1^* is a critical point of F^{x_1,x_2}) we get the following system of equations

$$\begin{cases} -(\widehat{x}_1 - x_1)\cos\theta_1^* + (\widehat{x}_2 - x_2)\sin\theta_1^* &= 0, \\ -(\widehat{x}_1 - x_1)\sin\theta_1^* - (\widehat{x}_2 - x_2)\cos\theta_1^* &= 0. \end{cases} \tag{4.27}$$

Multiplying the first equation by $\cos\theta_1^*$, the second by $\sin\theta_1^*$ and adding the two equations we get $\widehat{x}_1 - x_1 = 0$, which contradicts the assumption of this case. Similarly, multiplying the first equation by $\sin\theta_1^*$, the second equation by $\cos\theta_1^*$ and subtracting the second equation from the first, we get $\widehat{x}_2 - x_2 = 0$, which also contradicts the assumption of this case. This confirms that the two stationary points of F^{x_1,x_2} are non-degenerate.

Finally, observe that at the stationary points $x_2^B(\theta_1^*) = \widehat{x}_2^B(\theta_1^*)$ (see Eq. (4.25)) and hence

$G^{\xi_1,x_1,x_2}(\theta_1^*) = 1$, independently of the choice of h. For values of θ_1 other than θ_1^* the contributions to the integral are negligible. This means that $\left[\mathscr{B}_h^2 \mathscr{P}_h^2 \kappa\right](x_1,x_2) \approx \left[\mathscr{B}^2 \mathscr{P}^2 \kappa\right](x_1,x_2)$ and Theorem 4.2 is satisfied.

***Step 3b*:** $n = 3$

Eqs. (4.15) and (4.19) can be rewritten using the fact that $n = 3$ as follows

$$\left[\mathscr{B}_h^3 \mathscr{P}_h^3 \kappa\right](\boldsymbol{x}) = \left(\frac{1}{2\pi}\right)^2 \int_{\mathbb{R}^2} \int_{\mathbb{S}^2} \frac{H\left(\xi_1,\xi_2,\widehat{x}_3^B(\boldsymbol{\theta})\right)}{H\left(\xi_1,\xi_2,x_3^B(\boldsymbol{\theta})\right)} \mathrm{e}^{-\mathrm{i}\left(\widehat{x}_1^B(\boldsymbol{\theta})-x_1^B(\boldsymbol{\theta})\right)\xi_1} \mathrm{e}^{-\mathrm{i}\left(\widehat{x}_2^B(\boldsymbol{\theta})-x_2^B(\boldsymbol{\theta})\right)\xi_2} \sin(\theta_2)\,\mathrm{d}\theta_1\mathrm{d}\theta_2\mathrm{d}\xi_1\mathrm{d}\xi_2. \tag{4.28}$$

$$\begin{aligned}\mathscr{B}^3 \mathscr{P}^3 \kappa(\boldsymbol{x}) &= \\ &= \left(\frac{1}{2\pi}\right)^2 \int_{\mathbb{R}^{n-1}} \int_{\mathbb{S}^{n-1}} \mathrm{e}^{-\mathrm{i}\left(\widehat{x}_1^B(\boldsymbol{\theta})-x_1^B(\boldsymbol{\theta})\right)\xi_1} \mathrm{e}^{-\mathrm{i}\left(\widehat{x}_2^B(\boldsymbol{\theta})-x_2^B(\boldsymbol{\theta})\right)\xi_2} \sin(\theta_2)\,\mathrm{d}\theta_1\mathrm{d}\theta_2\mathrm{d}\xi_1\mathrm{d}\xi_2.\end{aligned} \tag{4.29}$$

To work with the outermost two integrals in Eq. (4.28), we rewrite $\mathscr{B}_h^3 \mathscr{P}_h^3 \kappa$ further by introducing two functions

$$\Psi_1(\theta_1,\theta_2) = x_1^B(\theta_1,\theta_2) - \widehat{x}_1^B(\theta_1,\theta_2), \tag{4.30}$$

$$\Psi_2(\theta_1) = x_2^B(\theta_1,0) - \widehat{x}_2^B(\theta_1,0). \tag{4.31}$$

In the definition of Ψ_2, we set arbitrarily $\theta_2 = 0$ in x_2^B and $\widehat{x}_2^B$ because, by Eq. (2.11), they do not depend on θ_2. With these definitions Eq. (4.28) becomes

$$\left[\mathscr{B}_h^3 \mathscr{P}_h^3 \kappa\right](\boldsymbol{x}) = \frac{1}{2\pi} \int_{\mathbb{R}^2} \int_{\mathbb{S}^2} \frac{H\left(\xi_1,\xi_2,\widehat{x}_3^B(\boldsymbol{\theta})\right)}{H\left(\xi_1,\xi_2,x_3^B(\boldsymbol{\theta})\right)} \mathrm{e}^{-\mathrm{i}\Psi_1(\theta_1,\theta_2)\xi_1} \mathrm{e}^{-\mathrm{i}\Psi_2(\theta_1)\xi_1} \sin(\theta_2)\,\mathrm{d}\theta_1\mathrm{d}\theta_2\mathrm{d}\xi_1\mathrm{d}\xi_2 \tag{4.32}$$

We analyze this expression considering different cases of the relationship between $\widehat{\boldsymbol{x}}$ and $\boldsymbol{x}$:

Case 1. Consider first the special case when $(x_1,x_2,x_3)^T = (\widehat{x}_1,\widehat{x}_2,\widehat{x}_3)^T$. In this case it follows trivially from Eq. (2.11) that $\widehat{x}_3^B(\theta_1,\theta_2) = x_3^B(\theta_1,\theta_2)$, for all $\boldsymbol{\theta} = (\theta_1,\theta_2) \in \mathbb{S}^2$, and so the value of the fraction inside the integral in Eq. (4.32) is always 1, independently of the choice of h. This means that $\left[\mathscr{B}_h^3\mathscr{P}_h^3\kappa\right](\widehat{x}_1,\widehat{x}_2,\widehat{x}_3) = \left[\mathscr{B}^3\mathscr{P}^3\kappa\right](\widehat{x}_1,\widehat{x}_2,\widehat{x}_3)$ and Theorem 4.2 is satisfied exactly at this point.

In the other two cases we make use of the stationary phase approximation discussed in Subsection 2.4. We concentrate on the integral over $\mathbb{S}^2$ in Eq. (4.32)

$$\int\limits_{\mathbb{S}^2} \frac{H\left(\xi_1,\xi_2,\widehat{x}_3^B(\theta_1,\theta_2)\right)}{H\left(\xi_1,\xi_2,x_3^B(\theta_1,\theta_2)\right)} \mathrm{e}^{-\mathrm{i}\Psi_1(\theta_1,\theta_2)\xi_1} \mathrm{e}^{-\mathrm{i}\Psi_2(\theta_1)\xi_1} \sin(\theta_2)\,\mathrm{d}\theta_1\mathrm{d}\theta_2. \tag{4.33}$$

For a fixed ξ_1, ξ_2, x_1, x_2, x_3 and θ_1, we define

$$I_1^{\xi_1,\xi_2,x_1,x_2,x_3\theta_1} = \int\limits_0^{\pi} G_1^{\theta_1}(\theta_2)\, e^{i\xi_1 F_1^{\theta_1}(\theta_2)} d\theta_2, \tag{4.34}$$

where

$$G_1^{\xi_1,\xi_2,x_1,x_2,x_3\theta_1}(\theta_2) = \frac{H\left(\xi_1,\xi_2,\widehat{x}_3^B(\theta_1,\theta_2)\right)}{H\left(\xi_1,\xi_2,x_3^B(\theta_1,\theta_2)\right)} \sin\theta_2, \tag{4.35}$$

$$F_1^{x_1,x_2,x_3,\theta_1}(\theta_2) = -\Psi_1(\theta_1,\theta_2), \tag{4.36}$$

and for a fixed ξ_1, ξ_2, x_1, x_2, and x_3, we define

$$I_2^{\xi_1,\xi_2,x_1,x_2,x_3} = \int\limits_0^{2\pi} G_2(\theta_1)\, e^{i\xi_2 F_2(\theta_1)} d\theta_1, \tag{4.37}$$

where

$$G_2^{\xi_1,\xi_2,x_1,x_2,x_3}(\theta_1) = I_1^{\xi_1,\xi_2,x_1,x_2,x_3\theta_1}, \tag{4.38}$$

$$F_2^{x_1,x_2,x_3}(\theta_1) = -\Psi_2(\theta_1). \tag{4.39}$$

The iterated integral of Eq. (4.33) can be written, using these functions, as $I_2^{\xi_1,\xi_2,x_1,x_2,x_3}$. What we are going to show is that $I_2^{\xi_1,\xi_2,x_1,x_2,x_3}$ is (essentially) independent of the blurring function h.

According to the stationary phase approximation, the integral $I_2^{\xi_1,\xi_2,x_1,x_2,x_3}$ receives non-negligible contributions only from values of θ_1 that are non-degenerate critical points of $F_2^{x_1,x_2,x_3}(\theta_1)$. The first derivative of $F_2^{x_1,x_2,x_3}$ is

$$\frac{\mathrm{d}F_2^{x_1,x_2,x_3}}{\mathrm{d}\theta_1}(\theta_1) = (\widehat{x}_1 - x_1)\cos\theta_1 - (\widehat{x}_2 - x_2)\sin\theta_1, \tag{4.40}$$

so any critical point $\theta_1^*$of $F_2^{x_1,x_2,x_3}(\theta_1)$ satisfies

$$(\widehat{x}_1 - x_1)\cos\theta_1^* - (\widehat{x}_2 - x_2)\sin\theta_1^* = 0. \tag{4.41}$$

According to the stationary phase approximation, for any value of $\theta_1 \in [0, 2\pi)$, the integral $I_1^{\xi_1,\xi_2,x_1,x_2,x_3,\theta_1}$ receives non-negligible contributions only from values of θ_2 that are non-degenerate critical points of $F_1^{x_1,x_2,x_3,\theta_1}(\theta_2)$. The first derivative of $F_1^{x_1,x_2,x_3,\theta_1}$ is

$$\begin{aligned}\frac{\mathrm{d}F_1^{x_1,x_2,x_3,\theta_1}}{\mathrm{d}\theta_2}(\theta_2) &= -(\widehat{x}_1 - x_1)\cos\theta_1\sin\theta_2 + (\widehat{x}_2 - x_2)\sin\theta_1\sin\theta_2 + (\widehat{x}_3 - x_3)\cos\theta_2 \\ &= \widehat{x}_3^B(\theta_1,\theta_2) - x_3^B(\theta_1,\theta_2),\end{aligned} \tag{4.42}$$

so any critical point $\theta_2^*$of $F_1^{x_1,x_2,x_3,\theta_1}(\theta_2)$ satisfies

$$\widehat{x}_3^B(\theta_1,\theta_2^*) - x_3^B(\theta_1,\theta_2^*) = 0. \tag{4.43}$$

We consider two more cases (in addition to the one discussed before):

Case 2. $x_1 = \widehat{x}_1$, $x_2 = \widehat{x}_2$ and $x_3 \neq \widehat{x}_3$.

In this case it follows from the first derivative of $F_1^{x_1,x_2,x_3,\theta_1}$ in Eq. (4.42) that the only critical point in the range of $[0,\pi)$ is $\theta_2^* = \pi/2$. Furthermore, this critical point is non-degenerate, since the second derivative of $F_1^{x_1,x_2,x_3,\theta_1}$ at $\theta_2^* = \pi/2$ is $(x_3 - \widehat{x}_3)\sin\pi/2 \neq 0$. This implies that at the only non-degenerate stationary point, $\widehat{x}_3^B(\theta_1,\theta_2) = x_3^B(\theta_1,\theta_2)$ and $G_1^{\xi_1,\xi_2,x_1,x_2,x_3\theta_1}(\theta_2^*) = 1$ for all $\theta_1 \in [0,2\pi)$, independently of the choice of h. For values of θ_2 other than θ_2^* the contributions to the integrals $I_1^{\xi_1,\xi_2,x_1,x_2,x_3\theta_1}$ and $I_2^{\xi_1,\xi_2,x_1,x_2,x_3}$ are negligible. This means that $\left[\mathscr{B}_h^3\mathscr{P}_h^3\kappa\right](x_1,x_2,x_3) \approx \left[\mathscr{B}^3\mathscr{P}^3\kappa\right](x_1,x_2,x_3)$ and Theorem 4.2 is satisfied.

Case 3. Either $x_1 \neq \widehat{x}_1$, or $x_2 \neq \widehat{x}_2$, or both.

There are exactly two critical points $\theta_1^* \in [0,2\pi)$ of $F_2^{x_1,x_2,x_3}(\theta_1)$. They both satisfy Eq. (4.41). We show that they are both non-degenerate by demonstrating that the alternative leads to a contradiction. The second derivative of $F_2^{x_1,x_2,x_3}$ is

$$\frac{\mathrm{d}^2F_2^{x_1,x_2,x_3}}{\mathrm{d}\theta_1^2}(\theta_1) = -(\widehat{x}_1 - x_1)\sin\theta_1 - (\widehat{x}_2 - x_2)\cos\theta_1. \tag{4.44}$$

Assume that at least one of the stationary points θ_1^* is degenerate; then $\dfrac{\mathrm{d}^2F_2^{x_1,x_2,x_3}}{\mathrm{d}\theta_1^2}(\theta_1^*) = 0$, and we get the following system of equations

$$\begin{cases} (\widehat{x}_1 - x_1)\cos\theta_1^* - (\widehat{x}_2 - x_2)\sin\theta_1^* & = 0, \\ -(\widehat{x}_1 - x_1)\sin\theta_1^* - (\widehat{x}_2 - x_2)\cos\theta_1^* & = 0. \end{cases} \tag{4.45}$$

Multiplying the first equation by $\cos\theta_1^*$, the second by $-\sin\theta_1^*$ and adding the two equations we get $\widehat{x}_1 - x_1 = 0$, which contradicts the assumption of this case. Similarly, multiplying the first equation by $\sin\theta_1^*$, the second equation by $\cos\theta_1^*$ and adding then together we get $\widehat{x}_2 - x_2 = 0$, which also contradicts the assumption of this case. This confirms that the two stationary points of $F_2^{x_1,x_2,x_3}$ are non-degenerate.

It follows from Eqs. (4.42) and (4.40) that if θ_1^* is a critical point of $F_2^{x_1,x_2,x_3}$, then θ_2^* is a critical point of $F_1^{x_1,x_2,x_3,\theta_1}$ if, and only if,

$$(\widehat{x}_3 - x_3)\cos\theta_2^* = 0. \tag{4.46}$$

Subcase 3a. $x_3 = \widehat{x}_3$.

In this subcase, $(\widehat{x}_3 - x_3)\cos\theta_2$ is equal to zero for all $\theta_2 \in [0,\pi)$. This fact combined with the condition for stationary points of $F_2^{x_1,x_2,x_3}$: $(\widehat{x}_1 - x_1)\cos\theta_1^* - (\widehat{x}_2 - x_2)\sin\theta_1^* = 0$ implies that $\widehat{x}_3^B(\theta_1^*,\theta_2) = x_3^B(\theta_1^*,\theta_2)$, and hence, $G_1^{\xi_1,\xi_2,x_1,x_2,x_3\theta_1}(\theta_2) = 1$ when $\theta_1 = \theta_1^*$ and for all $\theta_2 \in [0,\pi)$, independently of the choice of h. For values of θ_1 other than θ_1^* the contributions to the integrals $I_1^{\xi_1,\xi_2,x_1,x_2,x_3\theta_1}$ and $I_2^{\xi_1,\xi_2,x_1,x_2,x_3}$ are negligible. This means that $\left[\mathscr{B}_h^3\mathscr{P}_h^3\kappa\right](x_1,x_2,x_3) \approx \left[\mathscr{B}^3\mathscr{P}^3\kappa\right](x_1,x_2,x_3)$ and Theorem 4.2 is satisfied.

Subcase 3b. $x_3 \neq \widehat{x}_3$.

In this subcase the only critical point of $F_1^{x_1,x_2,x_3,\theta_1}$ is $\theta_2^* = \pi/2$. Furthermore, this critical point is non-degenerate, since the second derivative of $F_1^{x_1,x_2,x_3,\theta_1}$ for $\theta_1 = \theta_1^*$ evaluated at $\theta_2^* = \pi/2$, $(x_3 - \widehat{x}_3)\sin\frac{\pi}{2} \neq 0$, is non-zero. Combining the conditions for stationary points of $F_2^{x_1,x_2,x_3}$ and stationary points of $F_1^{x_1,x_2,x_3,\theta_1}$ we get that $(\widehat{x}_1 - x_1)\cos\theta_1^* - (\widehat{x}_2 - x_2)\sin\theta_1^* = 0$ and $\theta_2^* = \pi/2$, which leads to $\widehat{x}_3^B(\theta_1^*,\theta_2^*) = x_3^B(\theta_1^*,\theta_2^*)$. This implies that $G_1^{\xi_1,\xi_2,x_1,x_2,x_3\theta_1}(\theta_2^*) = 1$ for all $\theta_1 = \theta_1^*$, independently of the choice of h. For values of θ_2 other than θ_2^* and values of θ_1 other than θ_1^* the contributions to the integrals $I_1^{\xi_1,\xi_2,x_1,x_2,x_3\theta_1}$ and $I_2^{\xi_1,\xi_2,x_1,x_2,x_3}$ are negligible. This means that $\left[\mathscr{B}_h^3\mathscr{P}_h^3\kappa\right](x_1,x_2,x_3) \approx \left[\mathscr{B}^3\mathscr{P}^3\kappa\right](x_1,x_2,x_3)$ and Theorem 4.2 is satisfied.

This gives us our main mathematical result regarding DGCBP: When projections from all the directions on the unit disk in 2D or sphere in 3D are available and no noise is present during the projection generation process, $\mathscr{B}_h^n\mathscr{P}_h^n v$ is approximately equal to $\mathscr{B}^n\mathscr{P}^n v$. The meaning of this is that the integral image produced by the defocus-gradient corrected backprojection method that uses distance-dependently blurred projection data of an object is approximately the same as the integral image produced by a standard backprojection that uses true mathematical projection

data of the same object. This gives a mathematical verification to the method of correction for distance-dependent blurring proposed by Jensen and Kornberg [27].

4.3.2 Numerical Examples

For our experiments we selected the following parameters for the forward model of TEM (see Section 4.1): $a = 0$, $\lambda = 0.033487$ Å, $C_s = 22,000,000$ Å, $\Delta f \in [1000, 3000]$ (in Å), $q_0 = 0.00746558$ Å^{-1}, $F_s = 141.35$ Å.

We computed the distance-dependently blurred projection data $\mathscr{P}_h^3 v(\theta_1, \theta_2, x_1, x_2)$ of mathematically defined phantoms, for randomly-selected directions $\boldsymbol{\theta} = (\theta_1, \theta_2)$ and 128×128 values of (x_1, x_2) in each direction.

From these values we reconstructed the phantoms by numerically approximating $\mathscr{D}^3 \mathscr{B}_h^3 \mathscr{P}_h^3 v$ at $128 \times 128 \times 128$ values of (x_1, x_2, x_3). We see from Eqs. (4.7) and (4.6) that this involves a division. To avoid dividing by zero, we used a Tikhonov filter approximation

$$\frac{\left[\mathscr{F}_{x_1,\ldots,x_{n-1}} g\right](\boldsymbol{\theta}, \xi_1, \ldots, \xi_{n-1})}{\left[\mathscr{F}_{x_1,\ldots,x_{n-1}} h\right](\xi_1, \ldots, \xi_{n-1}, x_n)} \approx \frac{\left[\mathscr{F}_{x_1,\ldots,x_{n-1}} g\right](\boldsymbol{\theta}, \xi_1, \ldots, \xi_{n-1}) \left[\mathscr{F}_{x_1,\ldots,x_{n-1}} h\right](\xi_1, \ldots, \xi_{n-1}, x_n)}{\left(\left[\mathscr{F}_{x_1,\ldots,x_{n-1}} h\right](\xi_1, \ldots, \xi_{n-1}, x_n)\right)^2 + \alpha\left(\xi_1^2 + \ldots + \xi_{n-1}^2\right)}, \tag{4.47}$$

with $\alpha = 0.01$ Å^2; see [11].

Our implementation was done in MATLAB and follows the mathematical developments presented in this chapter. We made repeated use of rotation routines (using cubic interpolation) and fast Fourier transform and its inverse provided by the MATLAB package.

4.3.2.1 Phantom #1

We first report on an experiment in which the phantom consists of seven identical spheres (Figure 4.2) with centers located in a horizontal plane. We chose this phantom to illustrate the effects of distance-dependent blurring in the projection data. A 128×128 digital approximation of the

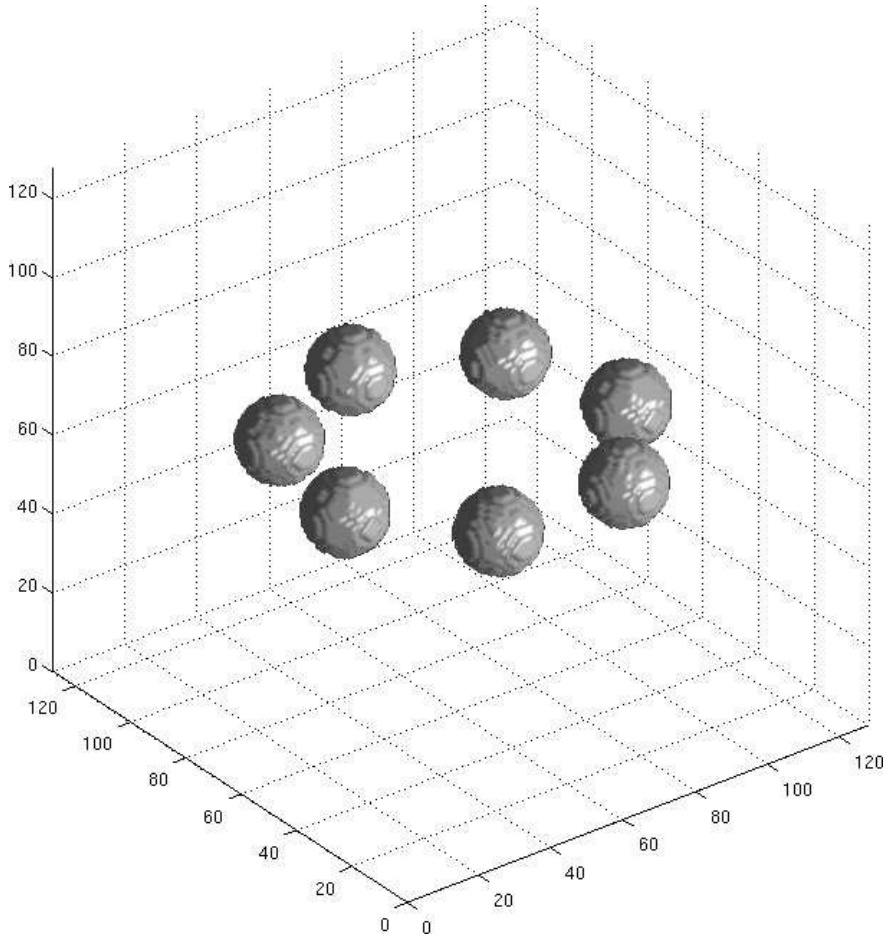

Figure 4.2: Numerical test phantom.

central slice of the phantom and its 3D plot can be compared with matching images of the DGCBP reconstruction in Figure 4.3.

A single tilted view (from one of the 5,000 generated directions) was chosen to illustrate the projection $\mathscr{P}^3 v$, Figure 4.4a and the distance-dependently blurred projection $\mathscr{P}_h^3 v$, Figure 4.4b. The variation in distortion (for example, for the spheres marked as A and B in Figure 4.4b caused by change in defocus is clearly seen. Profiles of the upper half of column number 59 and bottom half of column 53, as indicated in Figure 4.4a, are shown in Figure 4.4c and 4.4d.

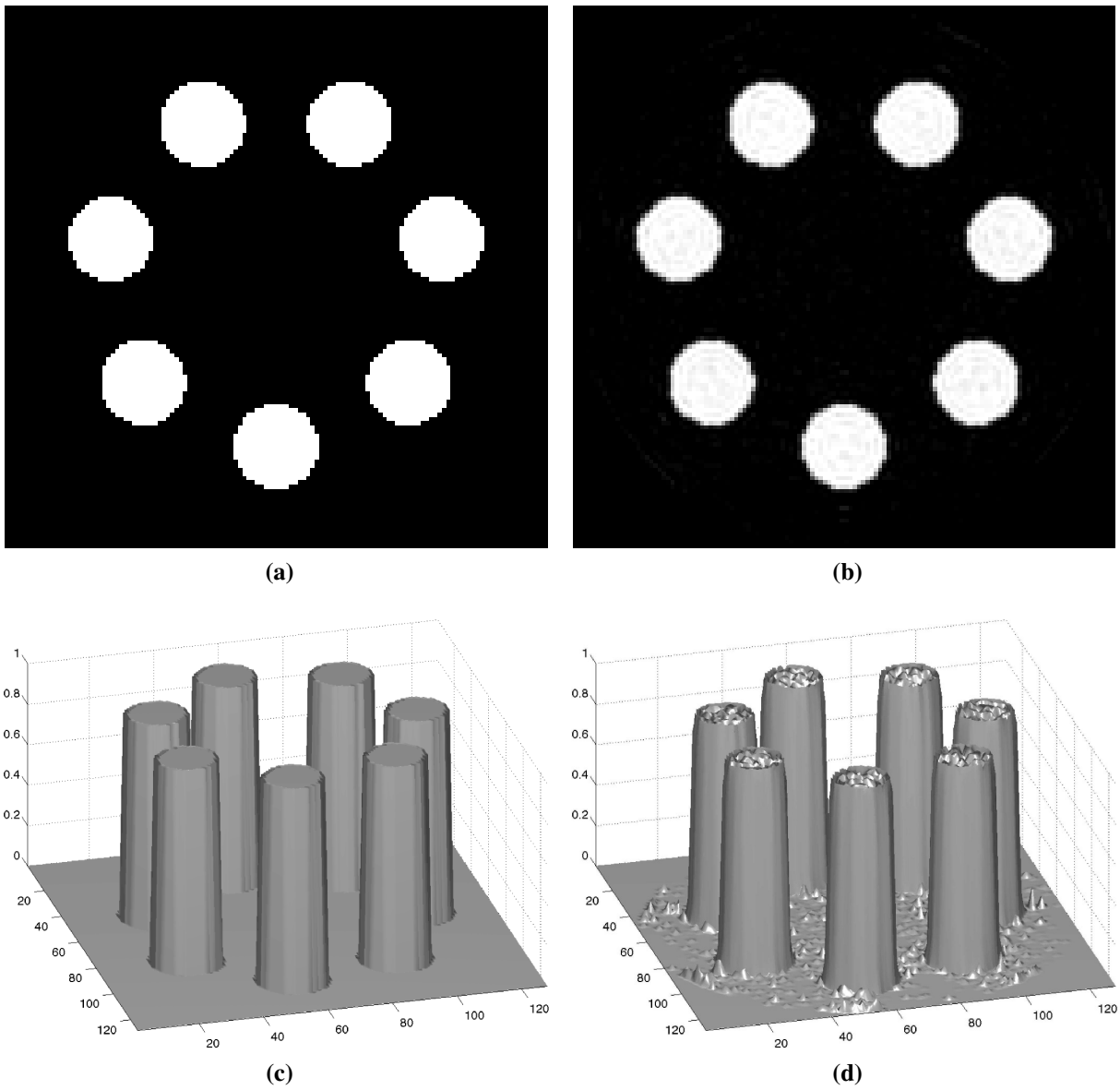

Figure 4.3: (a) Image of a section of the phantom in Figure 4.2. (b) Image of matching section of the DGCBP reconstruction from 5,000 distance-dependently blurred micrographs. (c) MATLAB 3D plot of (a). (d) MATLAB 3D plot of (b).

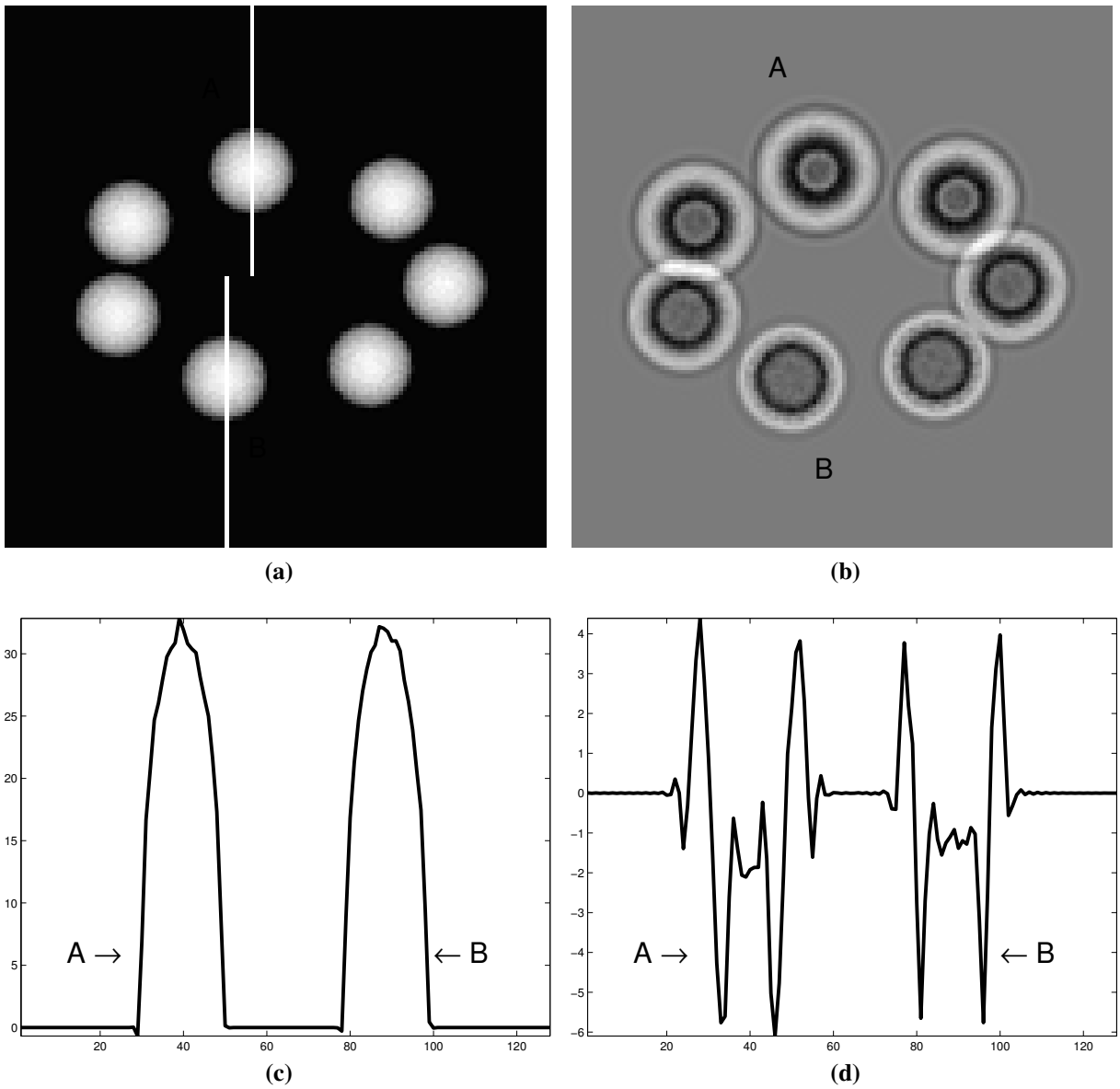

Figure 4.4: (a) Image of a single unblurred projection of the phantom shown in Figure 4.2; white lines indicate the pixels for which profiles are plotted. (b) Image of the matching distance-dependently blurred micrograph of the phantom. (c) Profiles for lines in (a). (d) Matching profiles in (b).

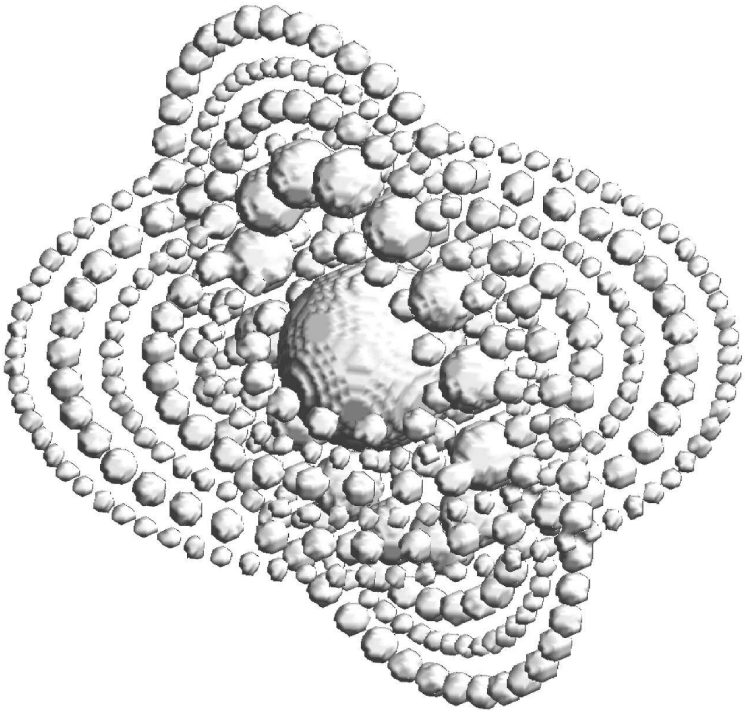

Figure 4.5: Numerical test phantom composed of concentric rings of spheres of various sizes, digitized into a $128 \times 128 \times 128$ voxel array.

4.3.2.2 Phantom #2

We used a more complex phantom, shown in Figure 4.5, to demonstrate the difference between reconstructions that take the distance-dependence of the PSF into account and those that ignore the distance-dependence of the PSF and assume a constant defocus appropriate only for the center layer of the phantom, which in our case is 2000 Å. We ran several simulations with this phantom with varying amounts of noise in the data to examine the sensitivity of our DGCBP-like correction. In the rest of this section we refer to a reconstruction that takes distance-dependence into account as *a DD backprojection* and to a reconstruction that corrects for the PSF corresponding to the center layer of the phantom as a *CL backprojection*.

Figure 4.6 demonstrates cross sections through the phantom, column (a), corresponding cross sections through the DD backprojection, column (b), cross sections through the CL backprojection, column (c), and the reconstruction that does not correct for the PSF at all, column (d). The projection data used for these reconstruction consisted of 5000 projection images that were affected only

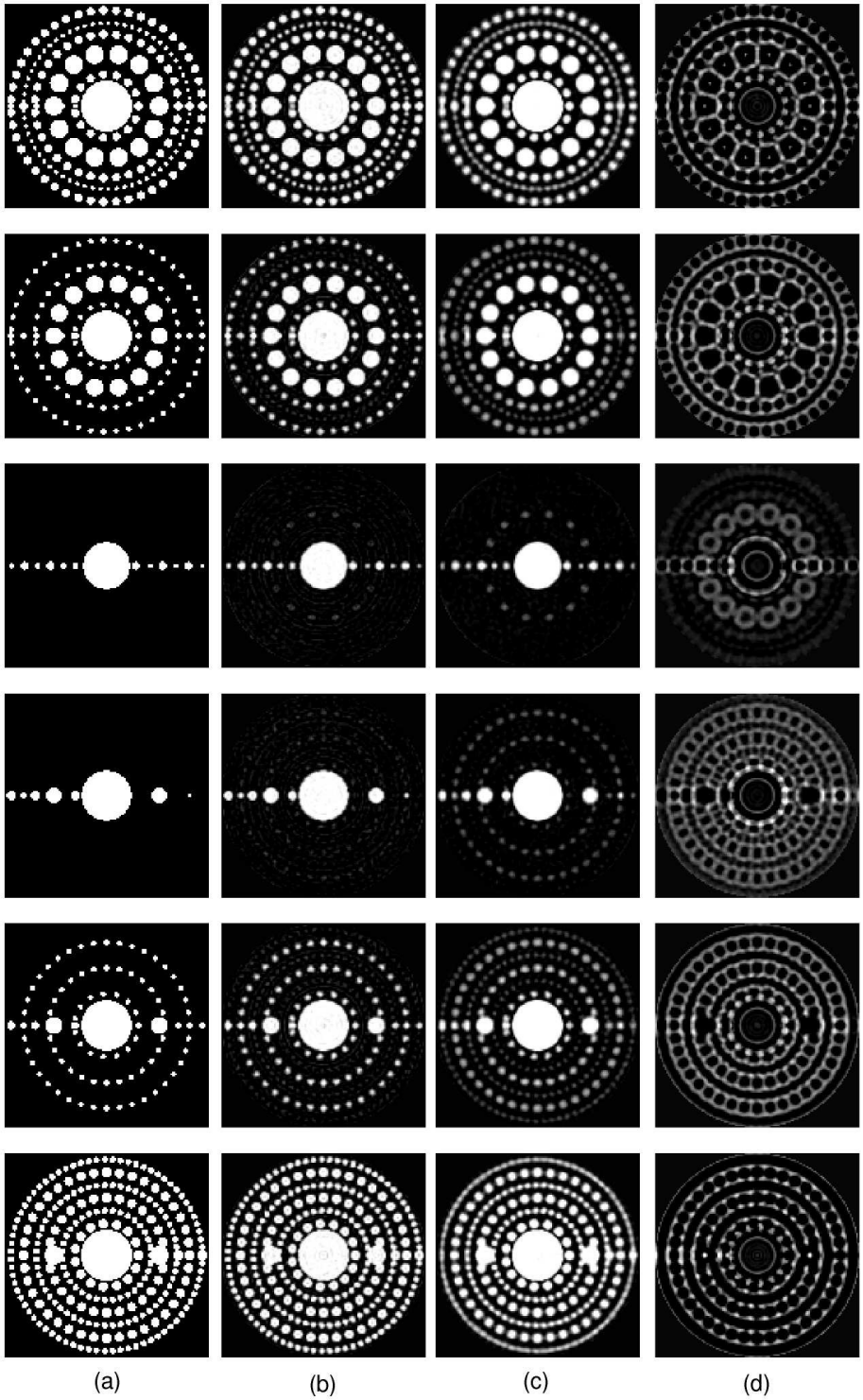

Figure 4.6: Cross sections of a phantom (a) and of three reconstructions from projection data that were calculated with distance-dependent blurring: with correction for the distance-dependent contrast transfer function (b), with correction appropriate for the central layer of the specimen (c) and with no correction for the contrast transfer function (d).

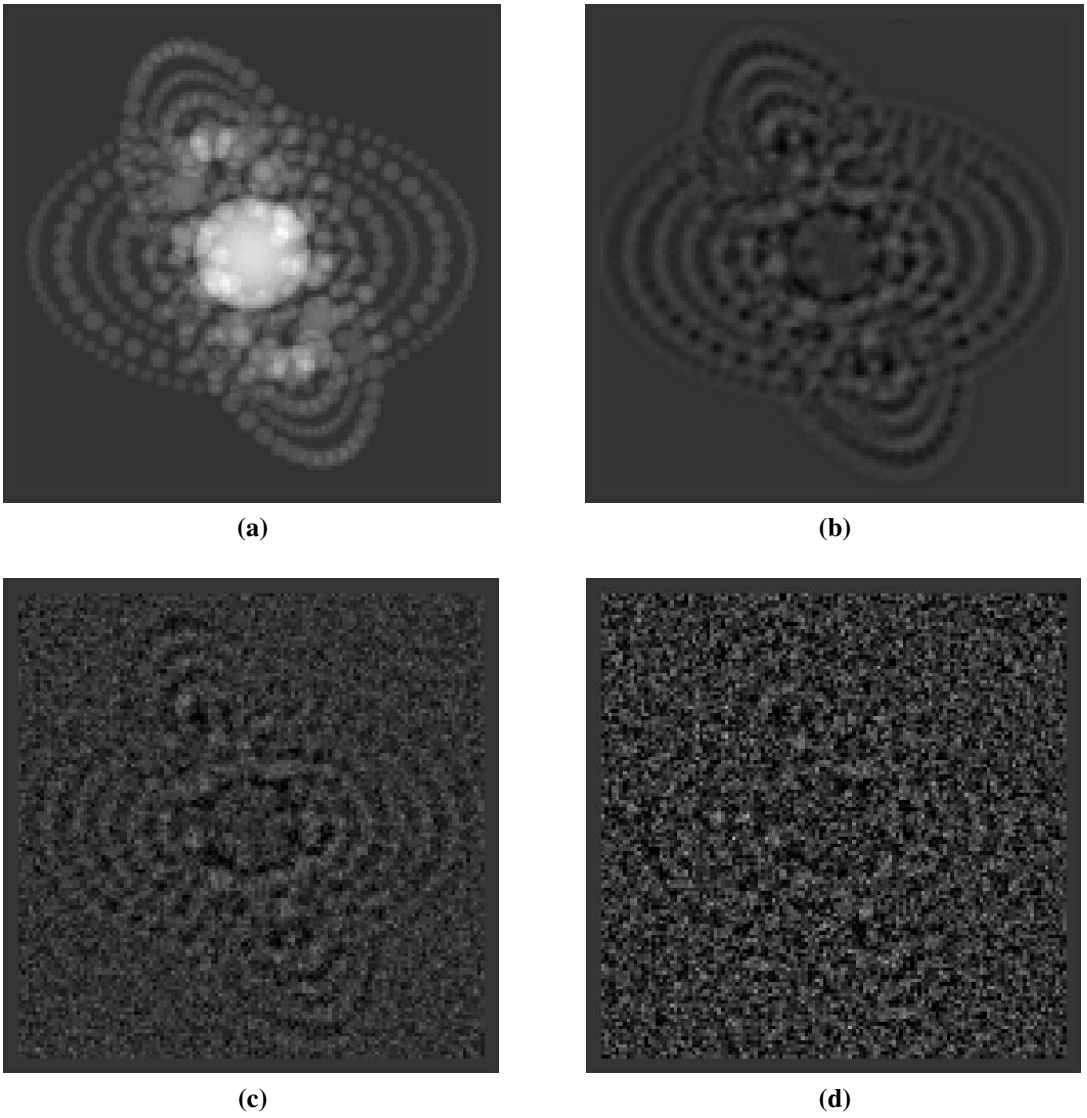

Figure 4.7: A single projection of the phantom in Figure 4.5: (a) ideal projection with no CTF blurring, (b) distance-dependently blurred projection, (c) distance-dependently blurred projection with added noise using $\sigma_1 = 0.3052$ and $\sigma_2 = 2.99$, (d) distance-dependently blurred projection with added noise using $\sigma_1 = 0.6103$ and $\sigma_2 = 6$.

by the distance-dependent PSF blurring with no noise added to the distance-dependently blurred projections. In the CL backprojection the smallest spheres are blurred to the point that they do not appear to be separate from each other and there is also more cross-slice blurring than in the DD backprojection.

Next we modified our experiment by introducing different types of noise. We simulated structural noise, shot noise and digitization noise based on the guidance provided in Baxter et al. [2]. We

needed to modify the model of noise suggested there in order to incorporate distance-dependent blurring into the structural noise. The structural noise originates from ice and often carbon film surrounding the molecule during imaging. As such it is different for each molecule and is subject to distance-dependent blurring. As a rough simulation of this phenomenon, prior to the distance-dependent projection taking we added to each voxel value in the rotated molecule a random sample from a zero-mean Gaussian distribution with standard deviation σ_1. This was done independently for each projection direction. This noise is convolved during the projection taking with the point spread function resulting in correlated noise in the projection images. Then, we simulated the shot noise and the digitization noise by adding, this time to each of the pixel values in the projection images, a random sample from a zero-mean Gaussian distribution with standard deviation σ_2. This was also done independently for each projection direction. Sample projection images for different values of σ_1 and σ_2 are compared to the ideal and noiseless projections in Figure 4.7. We used the projection data sets obtained in this manner to reconstruct using DD backprojection and CL back-projection. The results for different values of σ_1 and σ_2 are shown in Figure 4.8. The second and third columns are cross-sections of reconstructions from 5,000 projections with noise described by $\sigma_1 = 0.3052$ and $\sigma_2 = 2.99$. This value of σ_1 results in equal values of standard deviation of signal and noise after projections are taken. The value of σ_2 brings down the signal to noise ratio to $1/2$. The fourth and fifth columns are cross sections of reconstructions from 10,000 projections with noise described by $\sigma_1 = 0.6103$ and $\sigma_2 = 6.0$ (which results in signal to noise ratio of $1/4$). The surface rendering of reconstructions obtained using the second set of standard deviation values are also shown in Figure 4.9. Because surface rendering is done for a particular voxel threshold value, a lot of information is lost in such representations. For the rest of the simulations we only show cross-section images.

The parameters of the CTF, and therefore of the PSF, need to be estimated from the projection images before reconstructions can be performed. To evaluate how DD backprojection is affected by incorrectly determined CTF parameters, we simulated projections in which the defocus parameters were not the same as the ones used in reconstruction. In all our experiments the defocus varies

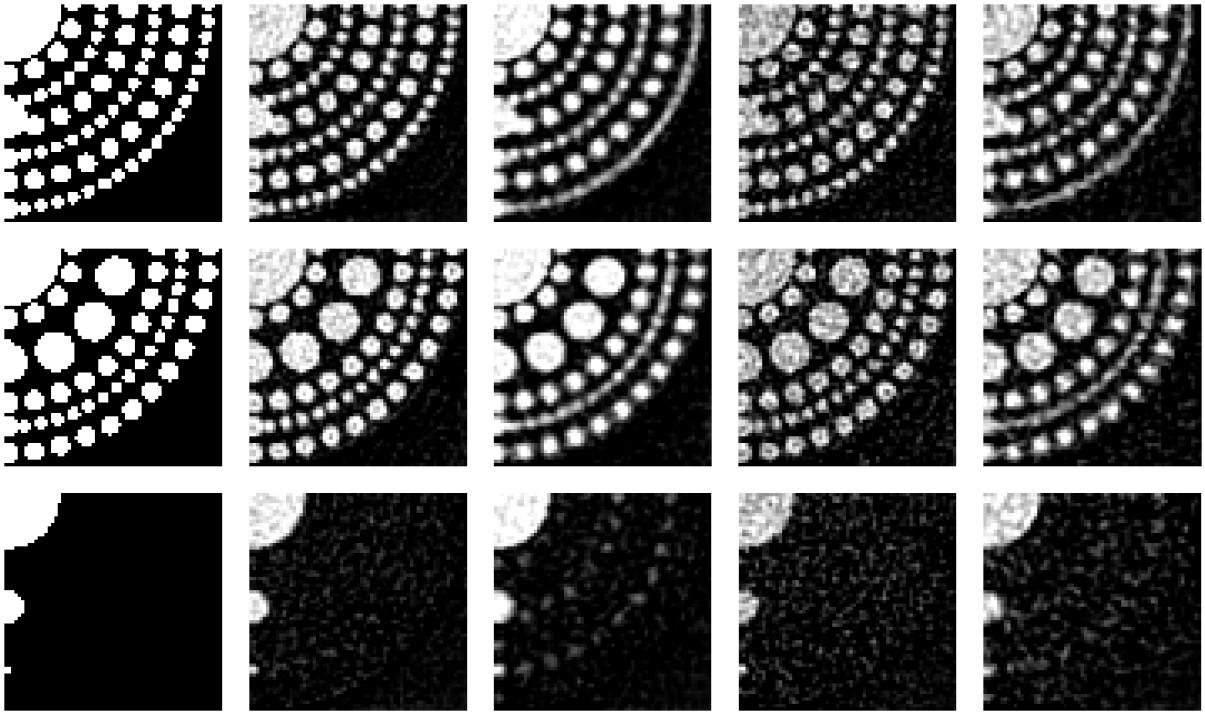

Figure 4.8: Three different cross-sections of the phantom (first column), of the reconstructions from noisy projection data generated using $\sigma_1 = 0.3052$ and $\sigma_2 = 2.99$ obtained by DD backprojection (second column) and by CL backprojection (third column) and of the reconstructions from noisy projection data generated using $\sigma_1 = 0.6103$ and $\sigma_2 = 6$ obtained by DD backprojection (fourth column) and by CL backprojection (fifth column).

from 1000 Å to 3000 Å according to the function $\Delta f\,(x_3) = m(x_3 - 1/2) + b$, where $m = 2000/n$, $b = 1000$, and $n = 128$ is the number of discrete layers into which the molecule is subdivided. (Here x_3 is the layer index that goes from 1 to 128.) For each projection direction, we introduced a random variation to the distance-dependent CTF, by using a defocus function in which we added to m a sample from a zero-mean Gaussian distribution with standard deviation σ_3 and added to b a sample from a zero-mean Gaussian distribution with standard deviation σ_4. The reconstructions were performed by correcting for the CTF with the unperturbed values of m and b. We demonstrate the results for two different values of σ_3 and σ_4. The cross-sections of reconstructions are shown in Figure 4.10. The DD backprojection results are again less blurred than the reconstructions obtained using CL backprojection on the same projection data.

In TEM the direction of each projection has to be estimated before the reconstruction can be

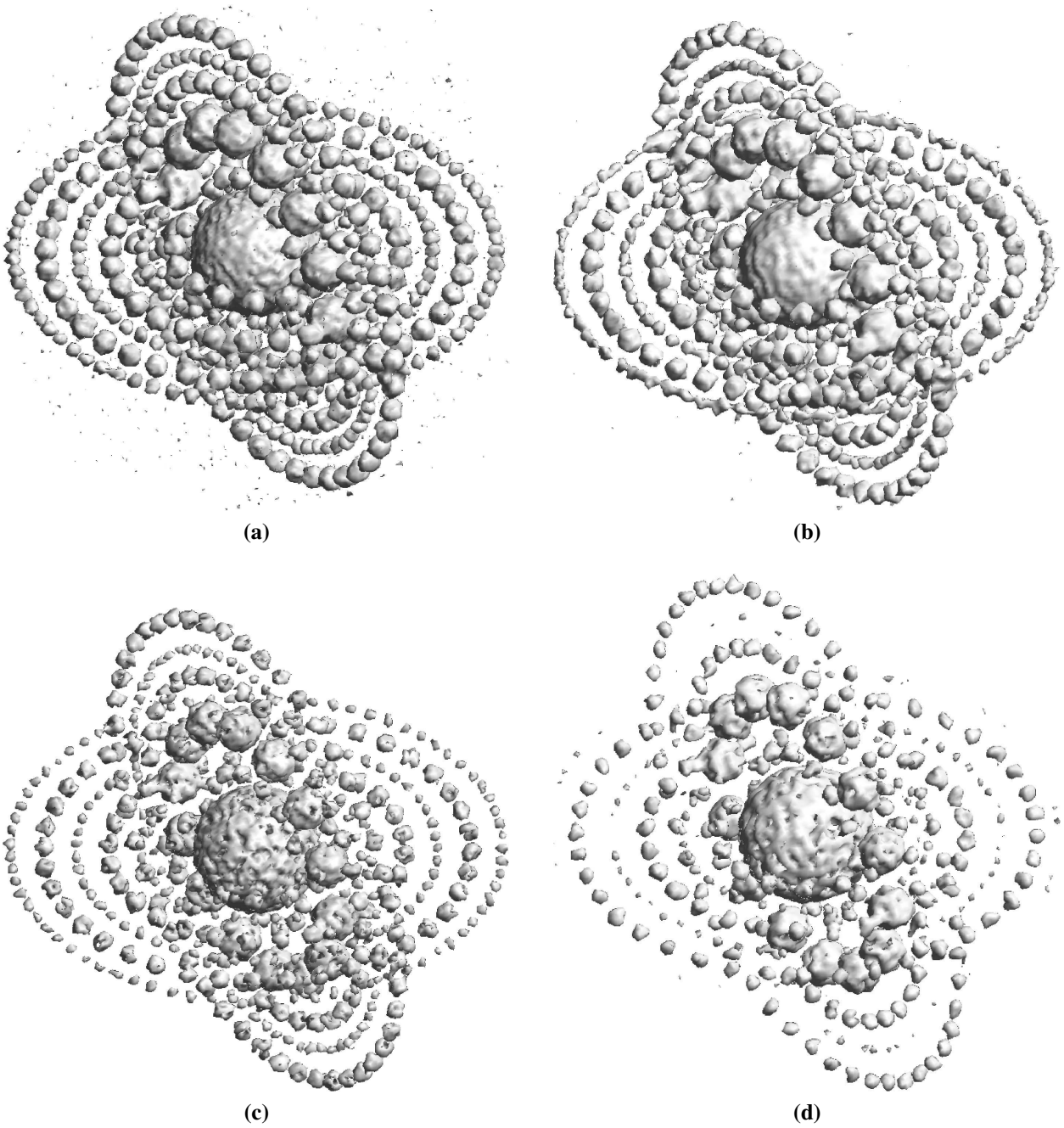

Figure 4.9: Surface renderings of two reconstructions from the noisy projection data generated using $\sigma_1 = 0.6103$ and $\sigma_2 = 6$. (a) and (b) are rendered for voxel values thresholded at 0.5; (c) and (d) are rendered for voxel value thresholded at 0.9. (a) and (c) were obtained using DD backprojection; (b) and (d) were obtained using CL backprojection.

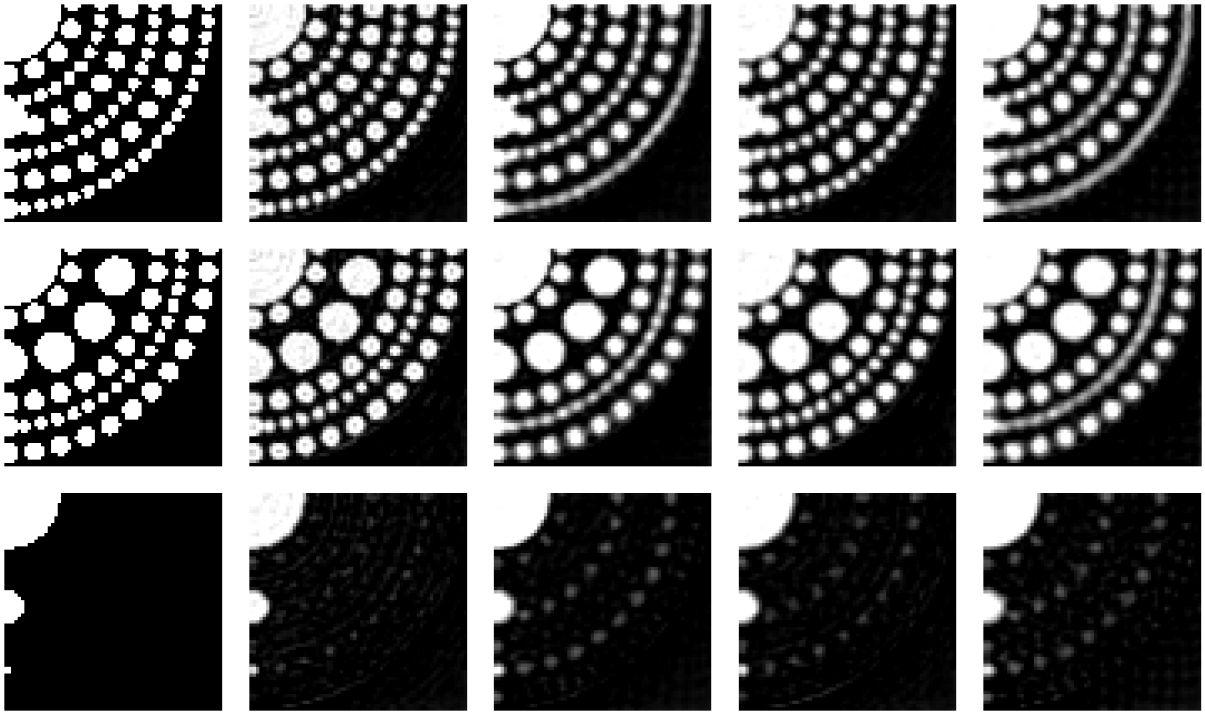

Figure 4.10: Three different cross-sections of the phantom (first column), of the reconstructions from projection data with incorrectly determined defocus parameters using $\sigma_3 = 1$ and $\sigma_4 = 50$ obtained by DD backprojection (second column) and by CL backprojection (third column) and of the reconstructions from projection data with incorrectly determined defocus parameters using $\sigma_3 = 5$ and $\sigma_4 = 100$ obtained by DD backprojection (fourth column) and by CL backprojection (fifth column).

performed. We repeated our experiment, introducing, independently for each projection, a small difference between the direction from which the particular projection was actually obtained and the direction that was used during the reconstruction. The difference was introduced by adding to θ_1 and θ_2 used in the projection simulation two different samples from a zero-mean Gaussian distribution with standard deviation σ_5 and using the modified angles in the reconstruction. The resulting cross sections for two different values of σ_5 are shown in Figure 4.11. For $\sigma_5 = 1$ the DD backprojection is once again less blurred than the CL backprojection from the same data. When we increased σ_5 to 3, both reconstructions are blurred and even the larger spheres become indistinguishable. For comparison we also show a reconstruction obtained from projection data unaffected by the PSF, just by the incorrectly determined projection angles.

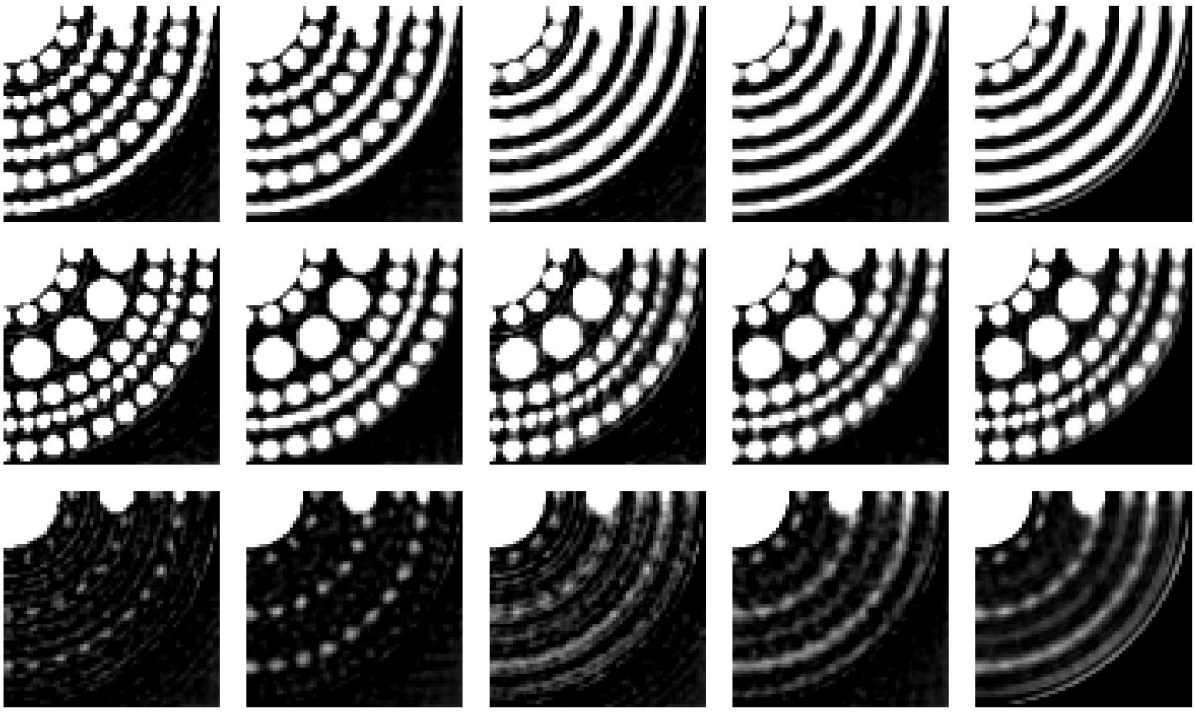

Figure 4.11: Three different cross-sections of the reconstructions from projection data with incorrectly estimated projection angles using $\sigma_5 = 1$ obtained by DD backprojection (first column) and by CL backprojection (second column) and of the reconstructions from projection data with incorrectly estimated projection angles using $\sigma_5 = 3$ obtained by DD backprojection (third column), by CL backprojection (fourth column) and by backprojection from the data unaffected by a CTF (fifth column).

4.4 Frequency Distance Relation

Another approach to deal with distance-dependent blurring effects is to correct the data and then use any of the reconstruction algorithms available for data collected according to $\mathscr{P}^n$ or $\mathscr{P}^{3t}$. The *frequency-distance relation* (FDR) based method performs this task.

An algorithm based on the frequency distance relation was introduced to 3D TEM by Dubowy and Herman [8] based on a method of Xia et al. [54] for solving a related problem in single photon emission computed tomography (SPECT). Such methods, based on a stationary phase approximation (see Section 2.4), provide a frequency distance relation for the inverse filter in the case of reconstructions of 2D objects from distance dependently blurred 1D projections; see Edholm and Lindholm [9] and Xia et al. [54]. Dubowy and Herman [8] adapted this approach to 2D projections of 3D objects obtained from single axis rotation. This approach corrects data collected by an im-

Algorithm 4.2 FDR: Frequency-distance relation based method for correction of distance-dependently blurred data.

1: Compute $\mathscr{F}_{\boldsymbol{\theta},x_1,x_2}\mathscr{P}_h^3 v$ by computing the Fourier transform of the distance dependently blurred data $\mathscr{P}_h^3 v$.
2: Recover an estimate of $\mathscr{F}_{\boldsymbol{\theta},x_1,x_2}\mathscr{P}^3 v$ by computing

$$\frac{\left[\mathscr{F}_{\boldsymbol{\theta},x_1,x_2}\mathscr{P}_h^3 v\right](\boldsymbol{\Theta},\xi_1,\xi_2)}{(2\pi)\left[\mathscr{F}_{x_1,x_2}h\right](\xi_1,\xi_2,-\Theta_2/\xi_1)}$$

3: Compute an estimate of $\mathscr{P}^3 v$ by taking the inverse Fourier transform of the estimate obtained in the previous step.
4: Compute an estimate of the original imaged object using any reconstruction algorithm.

perfect device, modeled by $\mathscr{P}_h^{3t}$, and approximates ideal projections, modeled by $\mathscr{P}^{3t}$, that would be obtained by a blur-free device. The corrected data can be used by any reconstruction algorithm.

We were able to further develop this methodology to make it appropriate for data collected using arbitrary angle rotation geometry, modeled by $\mathscr{P}_h^3$. The results discussed in this section were published in Klukowska et al. [31]. Algorithm 4.2 is based on the mathematical proof that follows in the rest of this section. It provides steps necessary to calculate the ideal projection data, $\mathscr{P}^3$, from the distance-dependently blurred projection data $\mathscr{P}_h^3$ and knowledge of the blurring function h and its Fourier transform. This correction method does not depend on the form of the blurring function.

4.4.1 Frequency Distance Relation

In this subsection we provide the proof of the theorem that establishes the relationship between the distance-dependently blurred projection data and the ideal projection data.

Theorem 4.4. *Given the distance-dependently blurred projection data $\mathscr{P}_h^3 v$ of a function $v:\mathbb{R}^3\rightarrow\mathbb{R}$, and the blurring function $h:\mathbb{R}^3\rightarrow\mathbb{R}$, there exists the following relationship between $\mathscr{P}^3 v$ and $\mathscr{P}_h^3 v$ in frequency space*

$$\left[\mathscr{F}_{\boldsymbol{\theta},x_1,x_2}\mathscr{P}_h^3 v\right](\boldsymbol{\Theta},\xi_1,\xi_2)=(2\pi)\left[\mathscr{F}_{\boldsymbol{\theta},x_1,x_2}\mathscr{P}^3 v\right](\boldsymbol{\Theta},\xi_1,\xi_2)\left[\mathscr{F}_{x_1,x_2}h\right](\xi_1,\xi_2,-\Theta_2/\xi_1)\,. \tag{4.48}$$

Proof of Theorem 4.4. The proof uses the linearity of the forward model which allows us to show its correctness for the impulse signal κ of Eq. (A.4), which we repeat below for ease of reference

$$\kappa(\boldsymbol{x}) = \delta(\widehat{x}_1 - x_1)\dots\delta(\widehat{x}_n - x_n), \tag{4.49}$$

and the alternate expression for the rotation of κ derived in Appendix A.2, i.e.,

$$\left[\mathscr{R}^n\kappa\right](\boldsymbol{\theta},\boldsymbol{x}) = \delta\left(\widehat{x}_1^{\mathcal{B}}(\boldsymbol{\theta}) - x_1\right)\dots\delta\left(\widehat{x}_n^{\mathcal{B}}(\boldsymbol{\theta}) - x_n\right). \tag{4.50}$$

We also make use of the stationary phase approximation discussed in Section 2.4.

The proof demonstrates that based on frequencies of the data one can determine the blurring function appropriate for the correction of those frequencies. We show that in the Fourier space, under the assumptions of the stationary phase approximation, the blurring can be factored out of the distance-dependently blurred projection data. We start by deriving the integral expressions for the four-dimensional Fourier transforms, with respect to θ_1, θ_2, x_1 and x_2, of the projection data of κ and of the distance-dependently blurred projection data of κ.

Observe that by the linearity of the Fourier transform, $\mathscr{F}_{\boldsymbol{\theta},x_1,x_2} = \mathscr{F}_{\boldsymbol{\theta}}\mathscr{F}_{x_1,x_2}$. Using this fact, the definitions of the Fourier transform operator $\mathscr{F}$ of Eq. (2.15) of the projection operator $\mathscr{P}$ of Eq. (2.22) and the expression for $\mathscr{F}_{x_1,x_2}\mathscr{R}^3 v$ based on Eq. (A.12) we first compute the integral expression for $\mathscr{F}_{\boldsymbol{\theta},x_1,x_2}\mathscr{P}^3\kappa$:

$$\begin{aligned}
&\left[\mathscr{F}_{\boldsymbol{\theta},x_1,x_2}\mathscr{P}^3\kappa\right](\boldsymbol{\Theta},\xi_1,\xi_2) = \\
&\quad= \left[\mathscr{F}_{\boldsymbol{\theta}}\mathscr{F}_{x_1,x_2}\mathscr{P}^3\kappa\right](\boldsymbol{\Theta},\xi_1,\xi_2) \\
&\quad= \left[\mathscr{F}_{\boldsymbol{\theta}}\left(\int_{\mathbb{R}}\left[\mathscr{F}_{x_1,x_2}\mathscr{R}^3\kappa\right](\boldsymbol{\theta},\xi_1,\xi_2,x_3)\,\mathrm{d}x_3\right)\right](\boldsymbol{\Theta}) \\
&\quad= \left[\mathscr{F}_{\boldsymbol{\theta}}\left(\left(\frac{1}{2\pi}\right)\int_{\mathbb{R}}\delta\left(\widehat{x}_3^{\mathcal{B}}(\boldsymbol{\theta}) - x_3\right)\mathrm{e}^{-\mathrm{i}\left(\widehat{x}_1^{\mathcal{B}}(\boldsymbol{\theta})\xi_1 + \widehat{x}_2^{\mathcal{B}}(\boldsymbol{\theta})\xi_2\right)}\mathrm{d}x_3\right)\right](\boldsymbol{\Theta}) \\
&\quad= \left[\mathscr{F}_{\boldsymbol{\theta}}\left(\left(\frac{1}{2\pi}\right)\mathrm{e}^{-\mathrm{i}\left(\widehat{x}_1^{\mathcal{B}}(\boldsymbol{\theta})\xi_1 + \widehat{x}_2^{\mathcal{B}}(\boldsymbol{\theta})\xi_2\right)}\right)\right](\boldsymbol{\Theta})
\end{aligned}$$

$$= \left(\frac{1}{2\pi}\right)^2 \int\limits_{\mathbb{S}^2} \mathrm{e}^{-\mathrm{i}\left(\widehat{x}_1^{\mathcal{B}}(\boldsymbol{\theta})\xi_1 + \widehat{x}_2^{\mathcal{B}}(\boldsymbol{\theta})\xi_2\right)} \mathrm{e}^{-\mathrm{i}(\theta_1\Theta_1 + \theta_2\Theta_2)} \mathrm{d}\theta_1 \mathrm{d}\theta_2. \tag{4.51}$$

Similarly we derive the integral expression for $\mathscr{F}_{\boldsymbol{\theta},x_1,x_2}\mathscr{P}_h^3\kappa$. Using the definitions of the Fourier transform operator $\mathscr{F}$ of Eq. (2.15), the distance-dependent projection operator $\mathscr{P}_h$ of Eq. (4.2), Lemma 4.1 and the expression for $\mathscr{F}_{x_1,x_2}\mathscr{R}^3 v$ based on Eq. (A.11) we have

$$\begin{aligned}
&\left[\mathscr{F}_{\boldsymbol{\theta},x_1,x_2}\mathscr{P}_h^3\kappa\right](\boldsymbol{\Theta},\xi_1,\xi_2) = \\
&\quad = \left[\mathscr{F}_{\boldsymbol{\theta}}\mathscr{F}_{x_1,x_2}\mathscr{P}_h^3\kappa\right](\boldsymbol{\Theta},\xi_1,\xi_2) \\
&\quad = \left[\mathscr{F}_{\boldsymbol{\theta}}\left((2\pi)\int\limits_{\mathbb{R}}\left[\mathscr{F}_{x_1,x_2}\mathscr{R}^3\kappa\right](\boldsymbol{\theta},\xi_1,\xi_2,x_3)\,H(\xi_1,\xi_2,x_3)\,\mathrm{d}x_3\right)\right](\boldsymbol{\Theta}) \\
&\quad = \left[\mathscr{F}_{\boldsymbol{\theta}}\left(\int\limits_{\mathbb{R}}\delta\left(\widehat{x}_3^{\mathcal{B}}(\boldsymbol{\theta})-x_3\right)\mathrm{e}^{-\mathrm{i}\left(\widehat{x}_1^{\mathcal{B}}(\boldsymbol{\theta})\xi_1+\widehat{x}_2^{\mathcal{B}}(\boldsymbol{\theta})\xi_2\right)}H(\xi_1,\xi_2,x_3)\,\mathrm{d}x_3\right)\right](\boldsymbol{\Theta}).
\end{aligned} \tag{4.52}$$

Applying the Fourier transform with respect to $\boldsymbol{\theta}$ and then integrating with respect to x_3, and rearranging the terms we get the integral expression for the four-dimensional Fourier transform of the distance-dependently blurred projection data of κ,

$$\begin{aligned}
&\left[\mathscr{F}_{\boldsymbol{\theta},x_1,x_2}\mathscr{P}_h^3\kappa\right](\boldsymbol{\Theta},\xi_1,\xi_2) = \\
&\quad = \left(\frac{1}{2\pi}\right)\int\limits_{\mathbb{S}^{n-1}}\int\limits_{\mathbb{R}}\delta\left(\widehat{x}_3^{\mathcal{B}}(\boldsymbol{\theta})-x_3\right)\mathrm{e}^{-\mathrm{i}\left(\widehat{x}_1^{\mathcal{B}}(\boldsymbol{\theta})\xi_1+\widehat{x}_2^{\mathcal{B}}(\boldsymbol{\theta})\xi_2\right)}H(\xi_1,\xi_2,x_3)\,\mathrm{e}^{-\mathrm{i}(\theta_1\Theta_1+\theta_2\Theta_2)}\mathrm{d}x_3\mathrm{d}\theta_1\mathrm{d}\theta_2 \\
&\quad = \left(\frac{1}{2\pi}\right)\int\limits_{\mathbb{S}^{n-1}}H\left(\xi_1,\xi_2,\widehat{x}_3^{\mathcal{B}}(\boldsymbol{\theta})\right)\mathrm{e}^{-\mathrm{i}\left(\widehat{x}_1^{\mathcal{B}}(\boldsymbol{\theta})\xi_1+\widehat{x}_2^{\mathcal{B}}(\boldsymbol{\theta})\xi_2\right)}\mathrm{e}^{-\mathrm{i}(\theta_1\Theta_1+\theta_2\Theta_2)}\mathrm{d}\theta_1\mathrm{d}\theta_2.
\end{aligned} \tag{4.53}$$

Observe that $\widehat{x}_2^{\mathcal{B}}(\boldsymbol{\theta})$ does not depend on θ_2. Using this fact, we can rewrite the last integral as follows

$$\begin{aligned}
&\left[\mathscr{F}_{\boldsymbol{\theta},x_1,x_2}\mathscr{P}_h^3\kappa\right](\boldsymbol{\Theta},\xi_1,\xi_2) = \\
&\quad = \left(\frac{1}{2\pi}\right)\int_0^{2\pi}\int_0^{\pi}H\left(\xi_1,\xi_2,\widehat{x}_3^{\mathcal{B}}(\boldsymbol{\theta})\right)\mathrm{e}^{-\mathrm{i}\left(\widehat{x}_1^{\mathcal{B}}(\boldsymbol{\theta})\xi_1+\theta_2\Theta_2\right)}\mathrm{d}\theta_2\mathrm{e}^{-\mathrm{i}\left(\widehat{x}_2^{\mathcal{B}}(\boldsymbol{\theta})\xi_2+\theta_1\Theta_1\right)}\mathrm{d}\theta_1.
\end{aligned} \tag{4.54}$$

We now show that under the assumptions of the stationary phase approximation the function H in the last integral is in fact independent of the integration variables θ_1 and θ_2. We concentrate on the innermost integral with respect for θ_2 and take θ_1, ξ_1, and ξ_2 as fixed. We define

$$I = \int_0^\pi G^{\xi_1,\xi_2,\theta_1}(\theta_2)\, \mathrm{e}^{-\mathrm{i}\xi_1 F^{\xi_1,\theta_1}(\theta_2)} \mathrm{d}\theta_2 \tag{4.55}$$

where

$$G^{\xi_1,\xi_2,\theta_1}(\theta_2) = H\left(\xi_1, \xi_2, \widehat{x}_3^{\mathcal{B}}(\boldsymbol{\theta})\right) \tag{4.56}$$

and

$$\begin{aligned} F^{\xi_1,\theta_1}(\theta_2) &= \widehat{x}_1^{\mathcal{B}}(\boldsymbol{\theta})\,\xi_1 + \theta_2 \frac{\Theta_2}{\xi_1} \\ &= \widehat{x}_1 \cos\theta_1 \cos\theta_2 - \widehat{x}_2 \sin\theta_1 \cos\theta_2 + \widehat{x}_3 \sin\theta_2 + \theta_2 \frac{\Theta_2}{\xi_1}. \end{aligned} \tag{4.57}$$

According to the stationary phase approximation, the integral I receives non-negligible contributions only from values of θ_1 that are non-degenerate critical points of F^{ξ_1,θ_1}. The first derivative of F^{ξ_1,θ_1} is

$$\begin{aligned} \frac{\mathrm{d}F^{\xi_1,\theta_1}}{\mathrm{d}\theta_2}(\theta_2) &= -\widehat{x}_1 \cos\theta_1 \sin\theta_2 + \widehat{x}_2 \sin\theta_1 \sin\theta_2 + \widehat{x}_3 \cos\theta_2 + \frac{\Theta_2}{\xi_1} \\ &= \widehat{x}_3^{\mathcal{B}}(\boldsymbol{\theta}) + \frac{\Theta_2}{\xi_1}. \end{aligned} \tag{4.58}$$

This shows that for any stationary point of $F^{\xi_1,\theta_1}(\theta_2)$ we have $\widehat{x}_3^{\mathcal{B}}(\boldsymbol{\theta}) = -\Theta_2/\xi_1$. In other words, if $S_{\theta_1,\theta_2,\xi_1}$ is the (easily shown to be finite) set of stationary points of $F^{\xi_1,\theta_1}(\theta_2)$, then

$$S_{\theta_1,\theta_2,\xi_1} = \left\{ \tilde{\theta}_2 \,|\, \widehat{x}_3^{\mathcal{B}}(\boldsymbol{\theta}) = -\frac{\Theta_2}{\xi_1} \right\}. \tag{4.59}$$

The stationary phase approximation is valid only if the stationary points are non-degenerate. The

second derivative of F^{ξ_1,θ_1} is

$$\begin{aligned}\frac{\mathrm{d}^2 F^{\xi_1,\theta_1}}{\mathrm{d}\theta_2^2}(\theta_2) &= -\widehat{x_1}\cos\theta_1\cos\theta_2 + \widehat{x_2}\sin\theta_1\cos\theta_2 - \widehat{x_3}\sin\theta_2 \\ &= \widehat{x}_1^{\mathcal{B}}(\boldsymbol{\theta}). \end{aligned} \tag{4.60}$$

The stationary points $\tilde{\theta}_2 \in S_{\theta_1,\theta_2,\xi_1}$ are non-degenerate provided that $\widehat{x}_1^{\mathcal{B}}\left(\theta_1,\tilde{\theta}_2\right) \neq 0$. This is true except for the finite set of values of θ_1, which does not affect the value of the outer integral in Eq. .(4.54).

The important result of the stationary phase approximation is that all stationary points satisfy the same equation $\widehat{x}_3^{\mathcal{B}}(\boldsymbol{\theta}) = -\Theta_2/\xi_1$, and therefore at the stationary points, $H\left(\xi_1,\xi_2,\widehat{x}_3^{\mathcal{B}}(\boldsymbol{\theta})\right) = H(\xi_1,\xi_2,)$. Given that and the integral expression for $\mathscr{F}_{\boldsymbol{\theta},x_1,x_2}\mathscr{P}_h^3\kappa$ of Eq. (4.51) we can rewrite the Eq. (4.54) as

$$\begin{aligned}&\left[\mathscr{F}_{\boldsymbol{\theta},x_1,x_2}\mathscr{P}_h^3\kappa\right](\boldsymbol{\Theta},\xi_1,\xi_2) = \\ &\quad= \left(\frac{1}{2\pi}\right) H\left(\xi_1,\xi_2,-\frac{\Theta_2}{\xi_1}\right) \int_{\mathbb{S}^2} \mathrm{e}^{-\mathrm{i}\left(\widehat{x}_1^{\mathcal{B}}(\boldsymbol{\theta})\xi_1+\theta_2\Theta_2\right)} \mathrm{e}^{-\mathrm{i}\left(\widehat{x}_2^{\mathcal{B}}(\boldsymbol{\theta})\xi_2+\theta_1\Theta_1\right)} \mathrm{d}\theta_1\mathrm{d}\theta_2 \\ &\quad= (2\pi) H\left(\xi_1,\xi_2,-\frac{\Theta_2}{\xi_1}\right) \left[\mathscr{F}_{\boldsymbol{\theta},x_1,x_2}\mathscr{P}^3\kappa\right](\boldsymbol{\Theta},\xi_1,\xi_2). \end{aligned} \tag{4.61}$$

This concludes the proof of Theorem 4.4. □

4.4.2 Correction of the Projection Data

Theorem 4.4 suggests a correction method for the Fourier coefficients of the distant-dependently blurred projection data in order to estimate the true projection data.

Corollary 4.5. *Given the distance-dependently blurred projection data $\mathscr{P}_h^3 v$ of a function $v : \mathbb{R}^3 \to \mathbb{R}$, and the blurring function $h : \mathbb{R}^3 \to \mathbb{R}$, then the ideal projection data $\mathscr{P}^3 v$ can be approximated*

by

$$\mathscr{P}^3 v \approx \mathscr{F}^{-1}_{\boldsymbol{\Theta},\xi_1,\xi_2} \left(\frac{\left[\mathscr{F}_{\boldsymbol{\theta},x_1,x_2} \mathscr{P}^3_h v\right](\boldsymbol{\Theta},\xi_1,\xi_2)}{(2\pi)\left[\mathscr{F}_{x_1,x_2} h\right](\xi_1,\xi_2,-\Theta_2/\xi_1)} \right). \tag{4.62}$$

Proof. The proof follows immediately from Theorem 4.4. □

During this correction, depending on the specific form of the blurring function h, regularization is required to avoid division by zero and by very small values which may lead to amplification of noise present in the data.

The advantage of correction in this fashion over incorporating the correction into the reconstruction method is that any of the large collection of reconstruction algorithms can be used.

4.4.3 Numerical Examples

We tested the correction method proposed in the previous section on a simple phantom composed of seven spheres digitized on a $128 \times 128 \times 128$ cubic voxel array. We computed the distance-dependently blurred projection data of that phantom for 1600 directions using the blurring function appropriate for electron microscopy, see Eq. (3.1). The set of micrographs was corrected according to Corollary 4.5. The results are presented in Figure 4.12. Some blurring is still present in the corrected projections; this is due to having only a finite number of projection directions, the discrete Fourier transform implementation and numerical difficulties resulting from regularization at places where the $\mathscr{F}_{x_1,x_2} h$ is near zero.

The reconstruction obtained from the projections corrected by our method is illustrated in Figure 4.13.

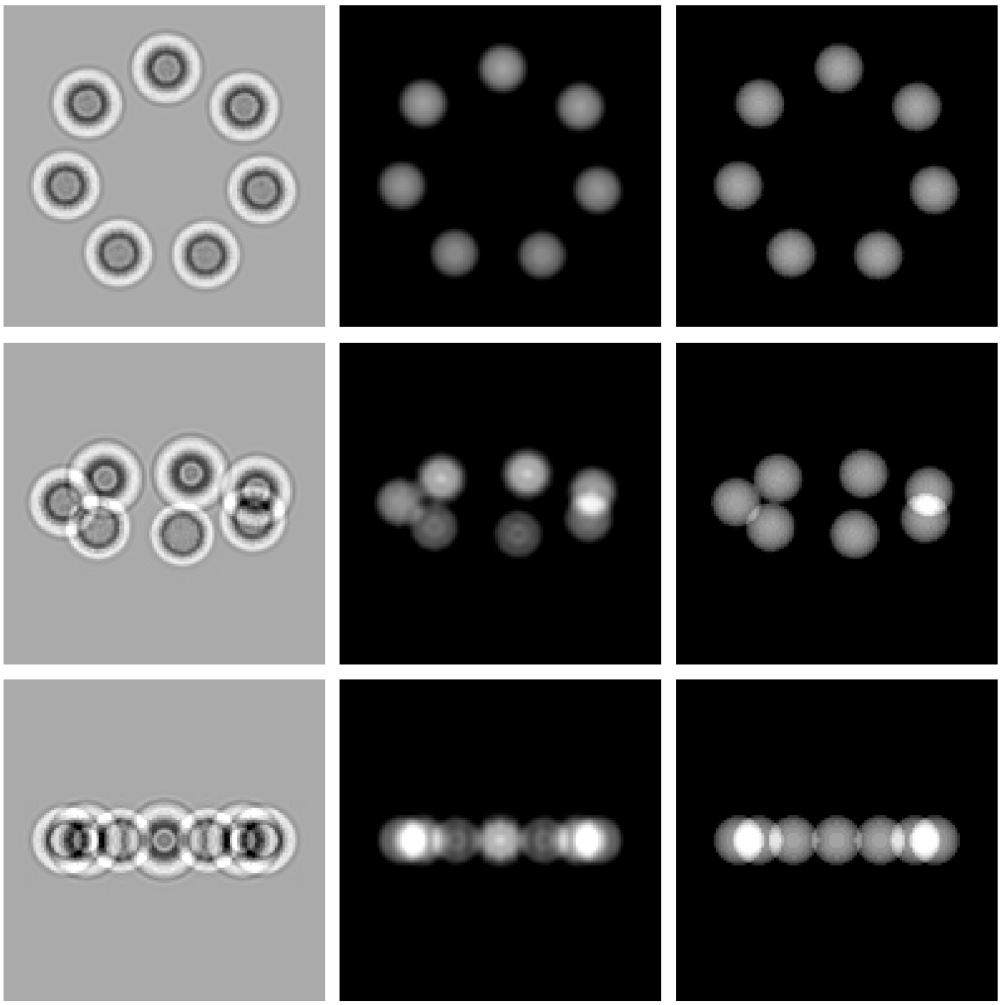

Figure 4.12: Comparison of the distance-dependently blurred projections (first column) with the corrected projections (second column) and the ideal projections obtained with no blurring (third column) for three projection directions.

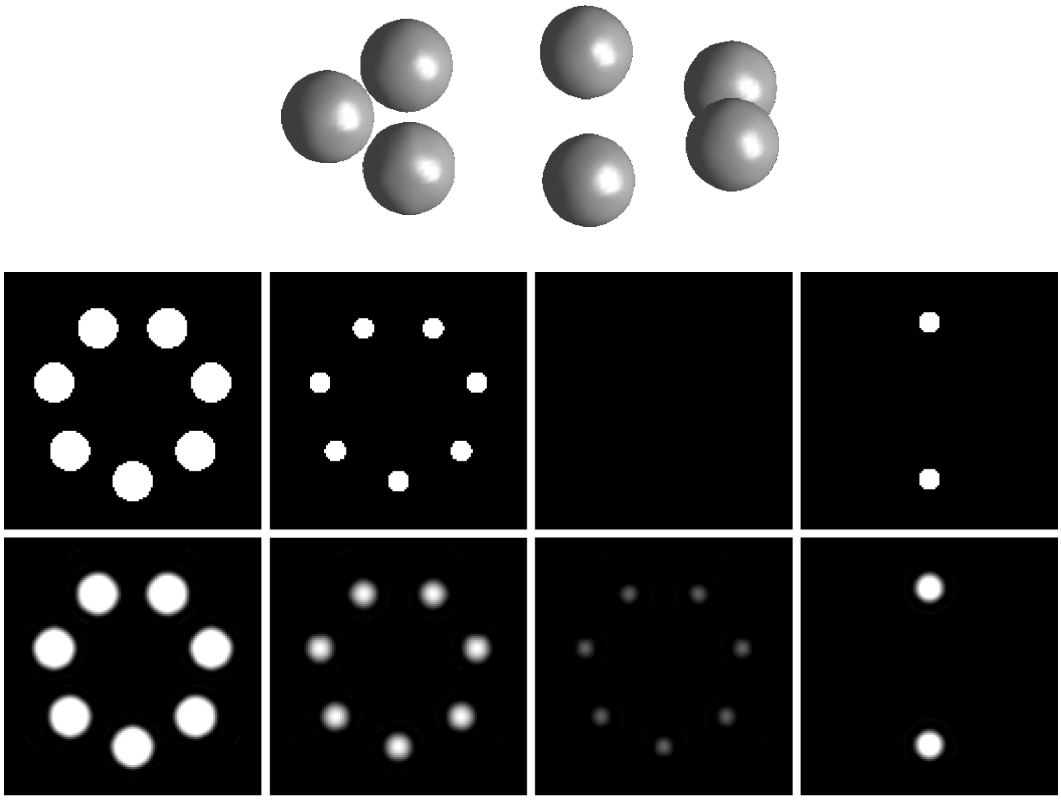

Figure 4.13: Reconstruction from 1600 projections. Top: 3D rendering for voxel values thresholded at 0.5. Bottom: corresponding cross sections through the phantom (top row) and reconstruction (bottom row).

Chapter 5

Correction of Blurring in Transmission X-ray Microscopy

Transmission x-ray microscopy (TXM) produces images of much larger samples than those that can be obtained by transmission electron microscopy (TEM) because the penetration depth of x-rays is much greater than that of electrons, see, for example, Leis et al. [34]. These images are also used to produce high resolution 3D reconstructions. Similarly to image formation model of TEM, the image formation model of TXM includes the distance-dependent blurring, but it also includes the attenuation effects due to the use of x-rays for the imaging. Our simulations, discussed in this chapter, demonstrate that the combination of the two effects results in changes to the projection data that cannot be easily corrected for unless the proper image formation model is taken into account during the reconstruction process. The image formation model for TXM has been published only very recently, see Oton et al. [41]. We use that model in our work.

It is standard current practice to report on reconstructions from soft x-ray microscopy data that were produced without taking into account an image formation model that handles the simultaneous presence of attenuation and distance-dependent blurring. Such an approach can produce biologically useful information (see, for example, McDermott et al. [37], Schneider et al. [46], Hanssen et al. [19], Chichón et al. [5]), but incorporation of an accurate image formation model

into the reconstruction procedure would most definitely result in higher resolution reconstructions and, hence, more accurate biological information from the same type of data. This chapter provides analysis of the distance-dependent blurring on projection data in presence of attenuation and describes techniques that incorporate a complete image formation model into the reconstruction.

5.1 Image Formation Model

We first describe the image formation model for both, arbitrary rotation and single axis rotation geometries. In practice, the single axis rotation is used in currently used microscopes. We also consider a related model in which blurring can be ignored, and show that in this case the inversion of the forward problem exists, and, in fact, is related to the inversion of the projection operator.

5.1.1 Arbitrary Rotation Geometry

The attenuation of x-rays passing through the imaged object is modeled by the *attenuation operator* $\mathscr{A}^n : \left(\mathbb{S}^{n-1} \times \mathbb{R}^n \to \mathbb{R}\right) \Rightarrow \left(\mathbb{S}^{n-1} \times \mathbb{R}^n \to \mathbb{R}\right)$, $n \in \{2,3\}$. The attenuation of the x-rays depends on two separate factors. First is the strength of the x-ray beam itself, which is a function specific to the imaging device settings and we assume that it is the same irrespective of the angle of rotation of the specimen. We use a function $p : \mathbb{R}^{n-1} \to \mathbb{R}$ to model this. $p(x_1,\ldots,x_{n-1})$ is known in advance and can be obtained by calibration measurements on the imaging device. The second factor contributing to the attenuation is the nature of the specimen itself. X-rays interact with matter according to linear attenuation coefficients that vary depending on the chemical composition of the matter. The attenuation operator $\mathscr{A}^n$ models both of these factors. It is defined by

$$\left[\mathscr{A}^n w\right](\boldsymbol{\theta},\boldsymbol{x}) = p(x_1,\ldots,x_{n-1})\, w(\boldsymbol{\theta},x_1,\ldots,x_n) \exp\left(-\int_{-\infty}^{x_n} w(\boldsymbol{\theta},x_1,\ldots,x_{n-1},t)\,\mathrm{d}t\right). \quad (5.1)$$

Using the attenuation operator and the operators defined in previous chapters we define two different projection models. The first one describes the image formation model in which the object

is rotated, attenuated and compressed. The *attenuated projection operator* $\mathscr{X}^n : (\mathbb{R}^n \to \mathbb{R}) \Rightarrow \left(\mathbb{S}^{n-1} \times \mathbb{R}^{n-1} \to \mathbb{R}\right)$, $n \in \{2,3\}$ is defined by

$$\mathscr{X}^n = \mathscr{C}^n \mathscr{A}^n \mathscr{R}^n. \tag{5.2}$$

The second one describes the image formation model with attenuation and blurring effects occurring together, i.e., the object is rotated, attenuated, convolved with a point spread function $h \in \mathbb{R}^n \to \mathbb{R}$, and then compressed. The *distance-dependent attenuated projection operator* $\mathscr{X}_h^n : (\mathbb{R}^n \to \mathbb{R}) \Rightarrow \left(\mathbb{S}^{n-1} \times \mathbb{R}^{n-1} \to \mathbb{R}\right)$, $n \in \{2,3\}$ is defined by

$$\mathscr{X}_h^n = \mathscr{C}_h^n \mathscr{A}^n \mathscr{R}^n. \tag{5.3}$$

5.1.2 Single Axis Rotation Geometry

In currently used microscopes the data are collected following the single axis rotation geometry, with or without the missing wedge, depending on the microscope setup. We define tomographic operators that correspond to the ones defined in the previous section.

The *tomographic attenuation operator* $\mathscr{A}^{3t} : \left(\mathbb{S}^1 \times \mathbb{R}^3 \to \mathbb{R}\right) \Rightarrow \left(\mathbb{S}^1 \times \mathbb{R}^3 \to \mathbb{R}\right)$ is defined by

$$\left[\mathscr{A}^{3t} w\right](\boldsymbol{\theta}, \boldsymbol{x}) = p(x_1, x_2)\, w(\boldsymbol{\theta}, x_1, x_2, x_3) \exp\left(- \int_{-\infty}^{x_3} w(\boldsymbol{\theta}, x_1, x_2, t)\, \mathrm{d}t \right). \tag{5.4}$$

The *tomographic attenuated projection operator* $\mathscr{X}^{3t} : \left(\mathbb{R}^3 \to \mathbb{R}\right) \Rightarrow \left(\mathbb{S}^1 \times \mathbb{R}^2 \to \mathbb{R}\right)$ is defined by

$$\mathscr{X}^{3t} = \mathscr{C}^{3t} \mathscr{A}^{3t} \mathscr{R}^{3t} \tag{5.5}$$

and the *tomographic distance-dependent attenuated projection operator* $\mathscr{X}_h^{3t} : \left(\mathbb{R}^3 \to \mathbb{R}\right) \Rightarrow \left(\mathbb{S}^1 \times \mathbb{R}^2 \to \mathbb{R}\right)$ is defined by

$$\mathscr{X}_h^{3t} = \mathscr{C}_h^{3t} \mathscr{A}^{3t} \mathscr{R}^{3t}. \tag{5.6}$$

Oton et. al, [41], Notation	Our Notation $\boldsymbol{x} \in \mathbb{R}^3$, $\boldsymbol{\theta} \in \mathbb{S}^1$	Physical Interpretation
z_B		location of the plane perpendicular to the imaging direction that is located right before the specimen
z_A		location of the plane perpendicular to the imaging direction that is located right after the specimen
$h(x,y,D(z,z_i))$	$h(\boldsymbol{x})$	point spread function of the imaging device
$\mu(x,y,z)$	$\left[\mathscr{R}^{3t}v\right](\boldsymbol{\theta},\boldsymbol{x})$	function representing linear attenuation coefficients of the specimen
$I_g^{z_i}(x,y,z_B)$	$p(x_1,x_2)$	x-ray beam intensity as it appears in plane $x_3 = z_B$ before passing through the lens (no specimen is present); assumed to be the same for all angles $\boldsymbol{\theta}$
$I^{z_i}(x,y,z_B)$	$p(x_1,x_2) \underset{x_1,x_2}{*} h(x_1,x_2,z_B)$	x-ray intensity measured in the focal plane (after the lens) when no specimen is present (this is the intensity at plane $x_3 = z_B$ after convolution with the PSF of the lens)
$I^{z_i}(x,y,z_A)$	$p(x_1,x_2) \underset{x_1,x_2}{*} h(x_1,x_2,z_B)$ $-\mathscr{X}_h^{3t}(\boldsymbol{\theta},x_1,x_2)$	intensity measured by the detector with the specimen present

Table 5.1: Correspondence between functions, variables and constants between Oton et al. [41] soft x-ray microscopy image formation model and our operator $\mathscr{X}_h^{3t}$ defined in Eq. (5.6).

5.1.3 Correspondence to Oton et. al, 2012 Model

Image formation for cellular x-ray microscopy in the case of incoherent x-rays has been recently described in [41]. Their image formation model uses single axis rotation geometry and describes a single projection for a fixed angle, rather than the set of all projections. The model is described

by Eq. (12) in Oton et al. [41], which we reproduce here for ease of reference:

$$I^{z_i}(x,y,z_A) = I^{z_i}(x,y,z_B) - \int_{z_B}^{z_A} \left(I_g^{z_i}(x,y,z_B)\,\mu(x,y,z) \exp\left(-\int_{z_B}^{z} \mu(x,y,\xi)\mathrm{d}\xi \right) \right) \underset{x,y}{*} h(x,y,D(z,z_i))\,\mathrm{d}z, \tag{5.7}$$

in which the functions, variables and constants have the physical interpretation as described in Table 5.1. The sample represented by our function v has finite support, so we extend the limits of integration to plus/minus infinity. Using these assumptions and Table 5.1 we can rewrite Eq. (5.7) in our notation as

$$\left[\mathscr{X}_h^{3t} v\right](\boldsymbol{\theta}, x_1, x_2) = \\ = \int_{\mathbb{R}} \left(p(x_1,x_2) \left[\mathscr{R}^{3t} v\right](\boldsymbol{\theta},\boldsymbol{x}) \exp\left(-\int_{-\infty}^{x_3} \left[\mathscr{R} v\right](\boldsymbol{\theta}, x_1, x_2, t)\,\mathrm{d}t \right) \right) \underset{x_1,x_2}{*} h(\boldsymbol{x})\,\mathrm{d}x_3, \tag{5.8}$$

which is the integral expression for the operator $\mathscr{X}_h^{3t}$ as defined in Eq. (5.6). Notice that $\mathscr{X}_h^{3t} v$ does not represent the data collected by the detector of the imaging device. Instead, it can be computed based on the collected data, calibration measurements and the knowledge of the blurring function.

5.2 Attenuation Effects

The correction for blurring in transmission x-ray microscopy data needs to take into account the interaction of blurring and attenuation in the image formation model. In this section we discuss the attenuation effect alone to demonstrate its influence on data. We show that for the model of data collection described by $\mathscr{X}^n$ and $\mathscr{X}^{3t}$, the inversion exists and is related to the inversion of projection operators $\mathscr{P}^n$ and $\mathscr{P}^{3t}$ of Eq. (2.22) and (2.25). This inversion method can be used when blurring is negligible during the imaging process, i.e., when the specimen is small.

We use a 2D phantom shown in Figure 5.1 to illustrate the effects of attenuation on projection data. The size of the phantom is $1.004\,\mu\mathrm{m} \times 10.004\,\mu\mathrm{m}$. It is digitized in a 251×2501 array

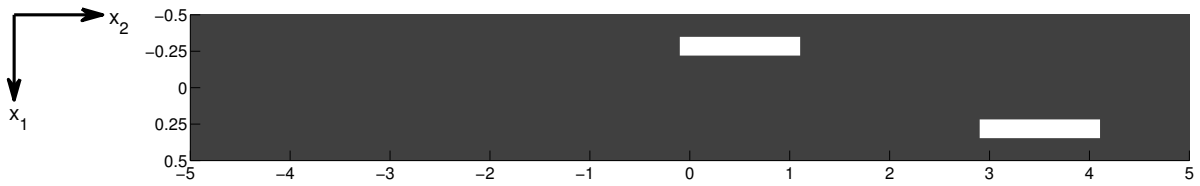

Figure 5.1: A simple phantom for illustration of the source of the replication artifact. Size: $1.004\,\mu\text{m} \times 10.004\,\mu\text{m}$, digitization: 251×2501, linear attenuation coefficients: $0.15\,\mu\text{m}^{-1}$ for the background, $0.6\,\mu\text{m}^{-1}$ for the small bright rectangles.

of pixels with a pixel size of $0.004 \times 0.004\,\mu m$. The two small rectangles are both $0.124\,\mu\text{m}$ in direction perpendicular to the optical axis, and $1.2\,\mu\text{m}$ in the direction of the optical axis. The linear attenuation coefficient of the background is $0.15\,\mu\text{m}^{-1}$ and of the linear coefficient of the two small rectangles is $0.6\,\mu\text{m}^{-1}$.

The attenuated projection, $\mathscr{X}^2 v$, for a single angle $\boldsymbol{\theta}$ is shown in Figure 5.1 in green. The values in that projection are significantly lower than the values in the unattenuated projection, $\mathscr{P}^2 v$, for the same angle $\boldsymbol{\theta}$. The attenuation is related to the linear attenuation coefficients associated with the matter through which the x-rays pass and to the size of the imaged object. If reconstruction is performed without correcting for attenuation, all features can be recovered, but with incorrect linear attenuation coefficient values and with significantly lower contrast than the original object.

The correction for attenuation can be performed using the following theorem.

Theorem 5.1. *For any function $v : \mathbb{R}^n \to \mathbb{R}$, $n \in \{2,3\}$, given the data collected according to the attenuation operator $\mathscr{X}^n v$, the ideal projection data $\mathscr{P}^n v$ can be computed by*

$$[\mathscr{P}^n v](\boldsymbol{\theta}, x_1, \ldots, x_{n-1}) = -\ln\left(1 - \frac{[\mathscr{X}^n v](\boldsymbol{\theta}, x_1, \ldots, x_{n-1})}{p(x_1, \ldots, x_{n-1})}\right). \tag{5.9}$$

Proof. The proof of this theorem requires only elementary calculus, specifically, the Fundamental Theorem of Calculus (if $g(x) = \int_a^x f(t)\,\mathrm{d}t$, then $\mathrm{dg}/\mathrm{dx}(x) = f(x)$). We first write $\mathscr{X}^n v$ in its integral form using the definitions of $\mathscr{X}^n$, $\mathscr{C}^n$, $\mathscr{A}^n$ and $\mathscr{R}^n$ operators of Eqs. (5.2), (2.21), (5.1) and (2.20)

$$[\mathscr{X}^n v](\boldsymbol{\theta}, x_1, \ldots, x_{n-1}) = \tag{5.10}$$

$$= p\left(x_1,\ldots,x_{n-1}\right) \int\limits_{\mathbb{R}} \left[\mathscr{R}^n v\right]\left(x_1,\ldots,x_n\right) \exp\left(- \int\limits_{-\infty}^{x_n} \left[\mathscr{R}^n v\right]\left(x_1,\ldots,x_{n-1},t\right) \mathrm{d}t \right) \mathrm{d}x_n. \tag{5.11}$$

Observe that for a function $f\left(x_1,\ldots,x_n\right) = \exp\left(-\int_{-\infty}^{x_n} \left[\mathscr{R}^n v\right]\left(x_1,\ldots,x_{n-1},t\right) \mathrm{d}t\right)$, its first derivative is equal to the negative of the expression inside the outermost integral in Eq. (5.10). Using this fact, applying the Fundamental Theorem of Calculus, and using the definition of the $\mathscr{P}^n$ operator of Eq. (2.22) we arrive at

$$\begin{aligned}
\left[\mathscr{X}^n v\right]\left(\boldsymbol{\theta}, x_1,\ldots,x_{n-1}\right) &= p\left(x_1,\ldots,x_{n-1}\right) \int\limits_{\mathbb{R}} -\frac{\mathrm{d}}{\mathrm{d}x_3} \exp\left(- \int\limits_{-\infty}^{x_n} \left[\mathscr{R}^n v\right]\left(x_1,\ldots,x_{n-1},t\right) \mathrm{d}t \right) \mathrm{d}x_n \\
&= p\left(x_1,\ldots,x_{n-1}\right) \left(1 - \exp\left(- \int\limits_{\mathbb{R}} \left[\mathscr{R}^n v\right]\left(x_1,\ldots,x_n\right) \mathrm{d}x_n \right) \right) \\
&= p\left(x_1,\ldots,x_{n-1}\right) \left(1 - \exp\left(-\left[\mathscr{P}^n v\right]\left(\boldsymbol{\theta}, x_1,\ldots,x_{n-1}\right)\right)\right).
\end{aligned} \tag{5.12}$$

Finally, rearranging terms and taking the natural logarithm of both sides, we obtain

$$\left[\mathscr{P}^n v\right]\left(\boldsymbol{\theta}, x_1,\ldots,x_{n-1}\right) = -\ln\left(1 - \frac{\left[\mathscr{X}^n v\right]\left(\boldsymbol{\theta}, x_1,\ldots,x_{n-1}\right)}{p\left(x_1,\ldots,x_{n-1}\right)}\right). \tag{5.13}$$

□

Theorem 5.1 provides the correction for attenuated data. In the presence of noise and other effects, this correction has to be performed with care to avoid taking logarithms of negative values. The data corrected using Theorem 5.1 are shown in Figure 5.2 in green dashed line. It overlaps with the ideal projection $\mathscr{P}^2 v$.

The correction of data collected using single axis rotation is performed in exactly same way. For completeness, we state it as a theorem.

Theorem 5.2. *For any function $v : \mathbb{R}^3 \to \mathbb{R}$, given the data collected according to the tomographic*

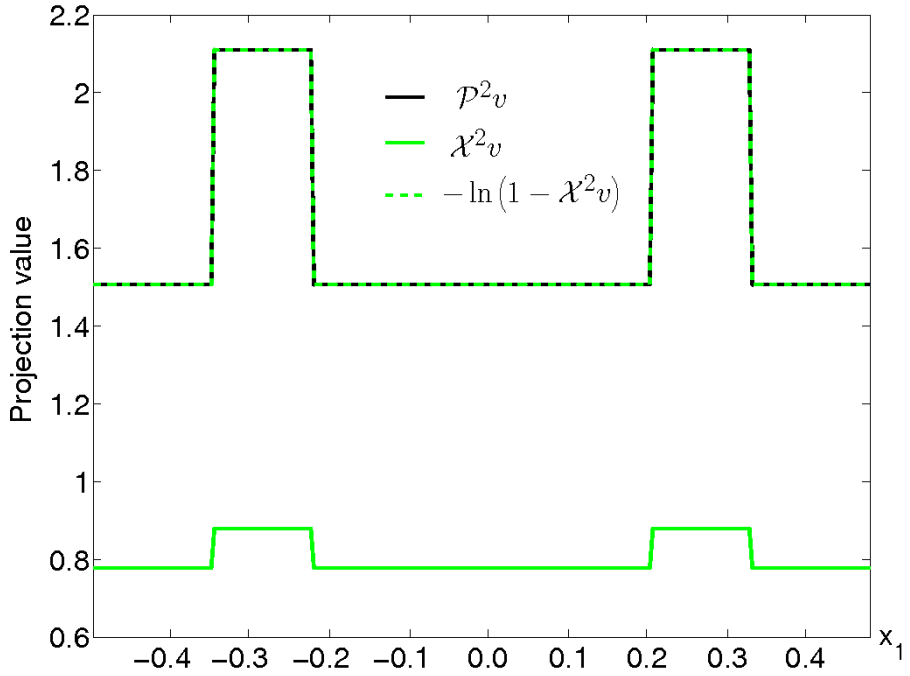

Figure 5.2: Projections of the phantom in Figure 5.1 (for a single angle $\boldsymbol{\theta}$): ideal projection $\mathscr{P}^2 v$ (black solid line), attenuated projection $\mathscr{X}^2 v$ (green solid line), attenuated projection corrected using Theorem 5.1 $-\ln\left(1-\mathscr{X}^2 v\right)$ (green dashed line).

attenuation operator $\mathscr{X}^{3t} v$, the ideal projection data $\mathscr{P}^{3t} v$ can be computed as

$$\left[\mathscr{P}^{3t} v\right](\boldsymbol{\theta}, x_1, x_2) = -\ln\left(1 - \frac{\left[\mathscr{X}^{3t} v\right](\boldsymbol{\theta}, x_1, x_2)}{p(x_1, x_2)}\right). \tag{5.14}$$

Proof. The proof of this theorem is exactly the same of the proof of Theorem 5.1. □

5.3 Blurring and Attenuation Effects Together

In the soft x-ray microscopy image formation model, both attenuation and distance-dependent blurring are present. The result are data that contain various artifacts that are not reflections of the object being imaged, but rather a consequence of non-linear combination of attenuation and blurring effects. The artifact that is most pronounced is replication of features that are away from

the zero-defocus plane. We refer to it as replication artifact. This replication proved to be impossible to correct for using correction methods that work with either attenuation or blurring alone. For an example of this see Figures 5.15, 5.17, on pages 102 and 104, which show reconstructions that correct for attenuation and blurring respectively. The disks further away from the center of the image appear as if they were duplicated. The particular danger of this issue is in the experimental work when the imaged object is unknown and such reconstructions may lead to false conclusions about the structure of the specimen. In the rest of this section we provide analysis of the source of this replication.

We used the phantom from Figure 5.1 to analyze the source of the replication. The center of the phantom was placed at the zero-defocus. We computed two projections of this phantom: the first for $\theta_1 = 0$ and the second for $\theta_1 = \pi$. It is a well known (and easily proved) fact that projections of a 2D object taken π radians apart are equivalent in the sense that $\mathscr{P}^2 v(\theta_1, x_1) = \mathscr{P}^2 v(\theta_1 + \pi, -x_1)$; see, for example, Eq. (6.5) of Herman [21]. This, together with the statements that follow, is illustrated in Figure 5.3. For distance-dependently blurred projections, it is not true in general that $\mathscr{P}_h^2 v(\theta_1, x_1) = \mathscr{P}_h^2 v(\theta_1 + \pi, -x_1)$, but one can easily prove it to be the case if the blurring function h has the property that, for all x_1, $h(x_1, x_2) = h(x_1, -x_2)$. This happens to be the case for the TXM blurring function that we have been using, see Section 3.2. That $\mathscr{X}^2 v(\theta_1, x_1) = \mathscr{X}^2 v(\theta_1 + \pi, -x_1)$ follows trivially from the corresponding result for $\mathscr{P}^2$ and Theorem 5.1. However, the situation changes essentially when both attenuation and blurring are present: for the example illustrated in Figure 5.3, $\mathscr{X}_h^2 v(\theta_1, x_1) \neq \mathscr{X}_h^2 v(\theta_1 + \pi, -x_1)$. The projection in Figure 5.3b of the small rectangle that is located further away from the zero-defocus plane appears as if there were multiple features in the phantom, not one. We refer to this as replication artifact. In the next section we show its effects on the reconstructions.

To determine the source of this phenomenon, we looked at the intermediate steps of the projection generation in our simulations. The implementation of the image formation model $\mathscr{X}_h^2$ of Eq. (5.3) can be subdivided into computation of smaller steps for various values along the imaging

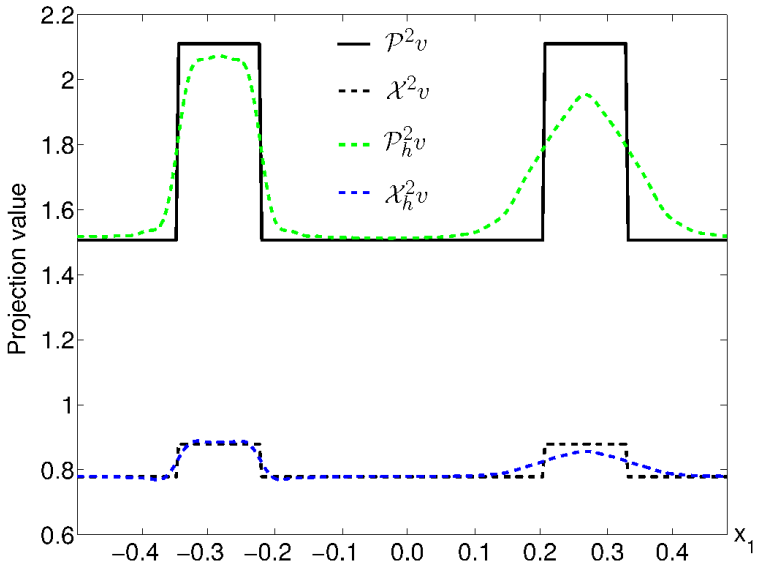

(a)

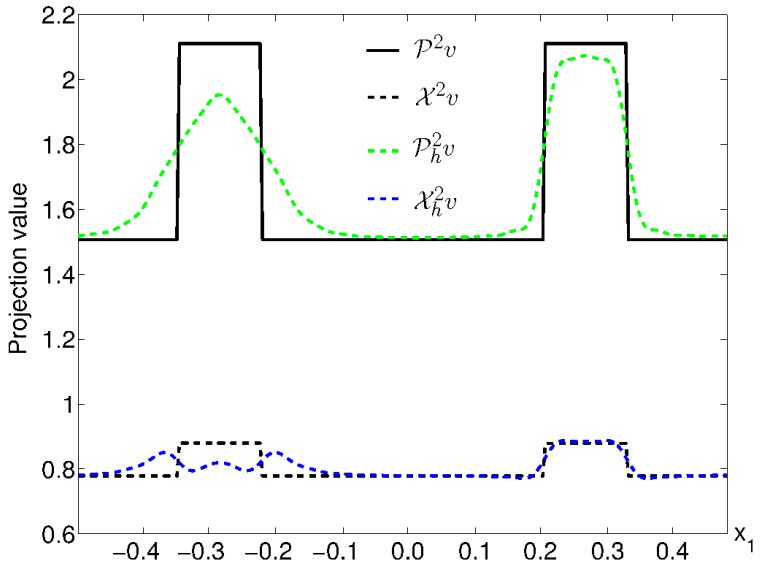

(b)

Figure 5.3: Various types of projections of the phantom in Figure 5.1 from two different directions **(a)** $\theta_1 = 0$ and **(b)** $\theta_1 = \pi$. The types of projections are: ideal microscope projections (no attenuation or blurring) $\left[\mathscr{P}^2 v\right](0, x_1) = \left[\mathscr{P}^2 v\right](\pi, -x_1)$ (solid black); blurred X-ray microscopy projections (no attenuation) $\left[\mathscr{P}_h^2 v\right](0, x_1) = \left[\mathscr{P}_h^2 v\right](\pi, -x_1)$ (dashed green); attenuated X-ray microscopy projections (no blurring) $\left[\mathscr{X}^2 v\right](0, x_1) = \left[\mathscr{X}^2 v\right](\pi, -x_1)$ (dashed black); X-ray microscopy projections $\left[\mathscr{X}_h^2 v\right](0, x_1) \neq \left[\mathscr{X}_h^2 v\right](\pi, -x_1)$ (dashed blue).

direction. For each angle we computed

$$\exp\left(-\int_{-\infty}^{x_2} v_\theta(x_1,t)\,\mathrm{d}t\right), \tag{5.15}$$

$$[\mathscr{R}v](\boldsymbol{\theta},x_1,x_2)\exp\left(-\int_{-\infty}^{x_2}[\mathscr{R}v](\boldsymbol{\theta},x_1,t)\,\mathrm{d}t\right), \tag{5.16}$$

$$\left([\mathscr{R}v](\boldsymbol{\theta},x_1,x_2)\exp\left(-\int_{-\infty}^{x_2}[\mathscr{R}v](\boldsymbol{\theta},x_1,t)\,\mathrm{d}t\right)\right)\underset{x_1}{*}h(x_1,x_2), \tag{5.17}$$

for eleven distinct values of x_2 (the actual implementation of this simulation sampled the phantom in the X_2 direction at every $0.004\,\mu$m, we display plots for a much smaller set of x_2 values). For each of these values we also computed the accumulated projection up to x_2. The graphs associated with these steps for $\theta_1 = 0$ and $\theta_1 = \pi$ (along with the blurring function h appropriate for the particular value of x_2) are shown in Figures 5.4 and 5.5, respectively. The exponential term of Eq. (5.15) and its product with $\mathscr{R}v$ in Eq. (5.16), whose graphs for different values of x_2 are shown in the first and second columns in both figures, are influenced by all the values that come before the specific x_2 - this is how the attenuation of x-rays passing through matter is modeled. X-rays passing through the small rectangles with higher linear attenuation coefficients than the background of the phantom result in the values in the graphs remaining lower thereafter. The contributions of the two small rectangles to each layer corresponding to x_2 are different in the two directions (see the graphs in the first and second columns of Figure 5.4 as compared to the graphs for corresponding values of x_2 in Figure 5.5). When the image formation model includes blurring, each layer of the attenuated specimen is convolved with a blurring function. The PSF in transmission x-ray microscopy is different for different layers in the direction of imaging, x_2 in our example. Once the attenuated layers of the specimen (pictured in second column of Figures 5.4 and 5.5) are convolved with a blurring function (pictured in the third column of Figures 5.4 and 5.5), the resulting values (pictured in the fourth column of Figures 5.4 and 5.5) no longer add up to the same projection values for the two directions (see the last graphs in the last rows of Figures 5.4 and 5.5).

The observed replications in the projection taken from the $\theta_1 = \pi$ direction is due to how the

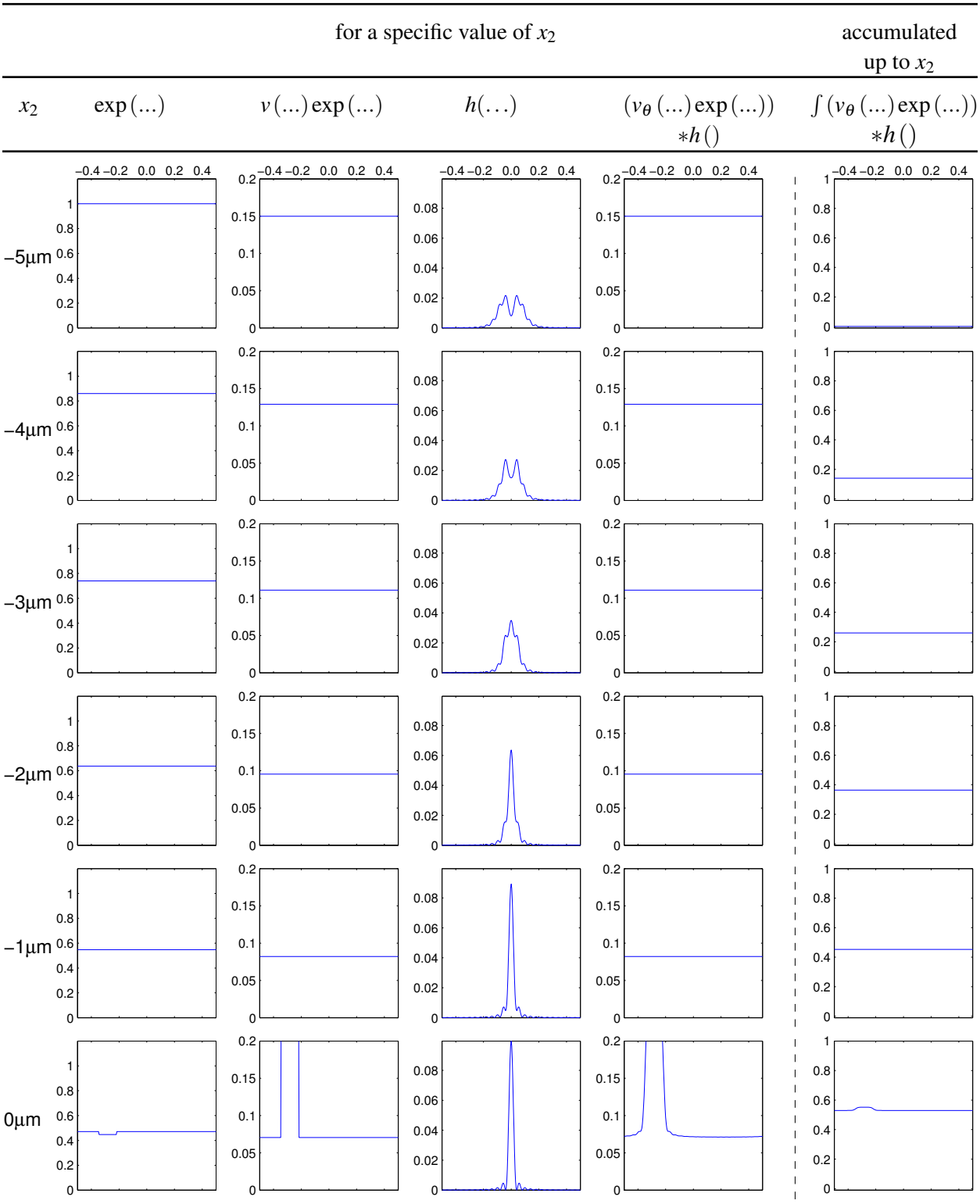

Figure 5.4: Continued on the next page

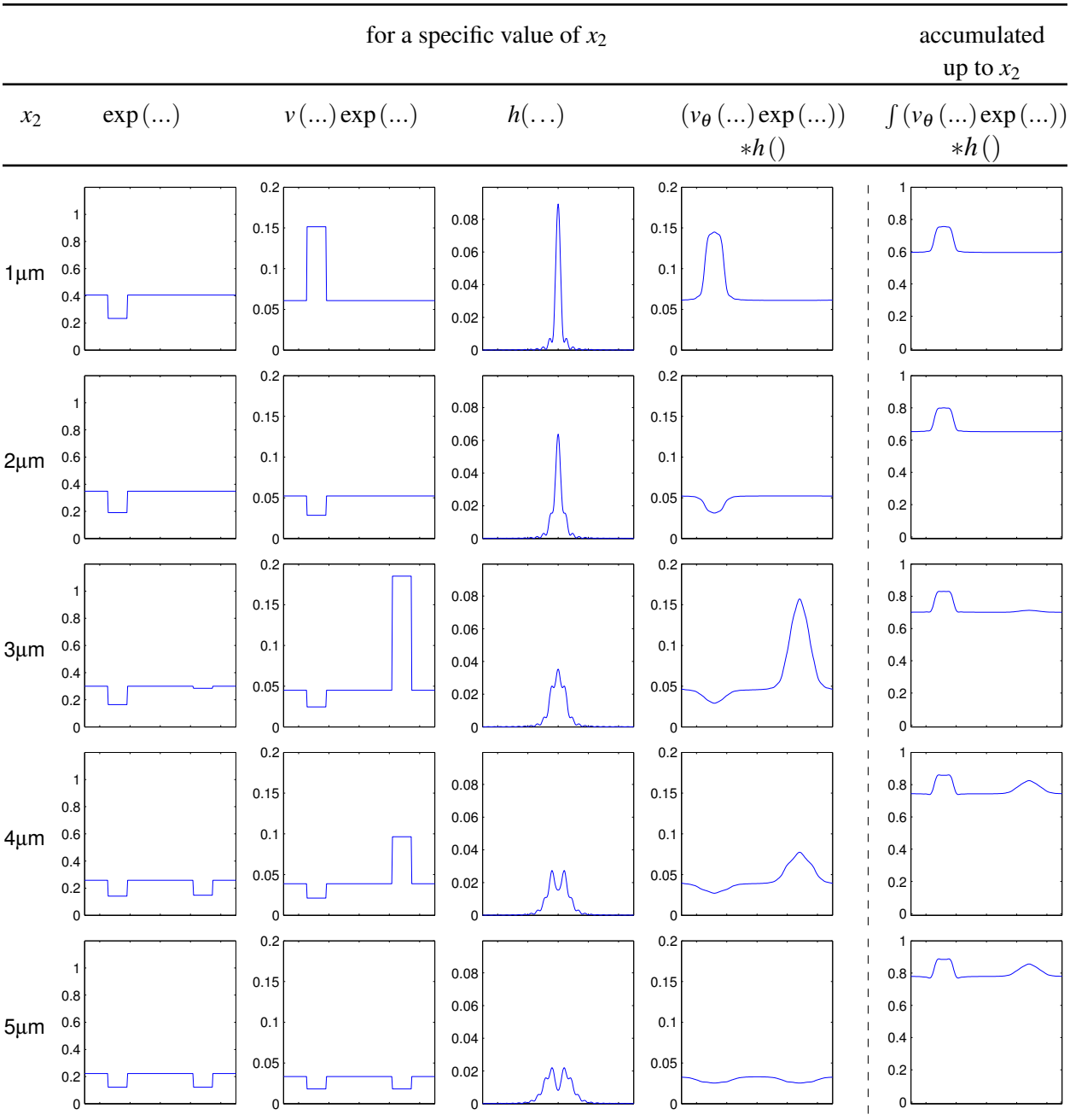

Figure 5.4: Intermediate steps of the projection calculation for the phantom in Figure 5.1 for angle $\theta = 0$. See text for discussion.

layers add together during the projection generation. The second row of Figure 5.5 shows graphs for the first of our selected x_2 values that intersect the small rectangle located further away from the zero-defocus plane. For layers corresponding to $x_2 = -4\,\mu$m and $x_2 = -3\,\mu$m (and all other not shown values of x_2 that cross the small rectangle), the contributions to the projections are positive

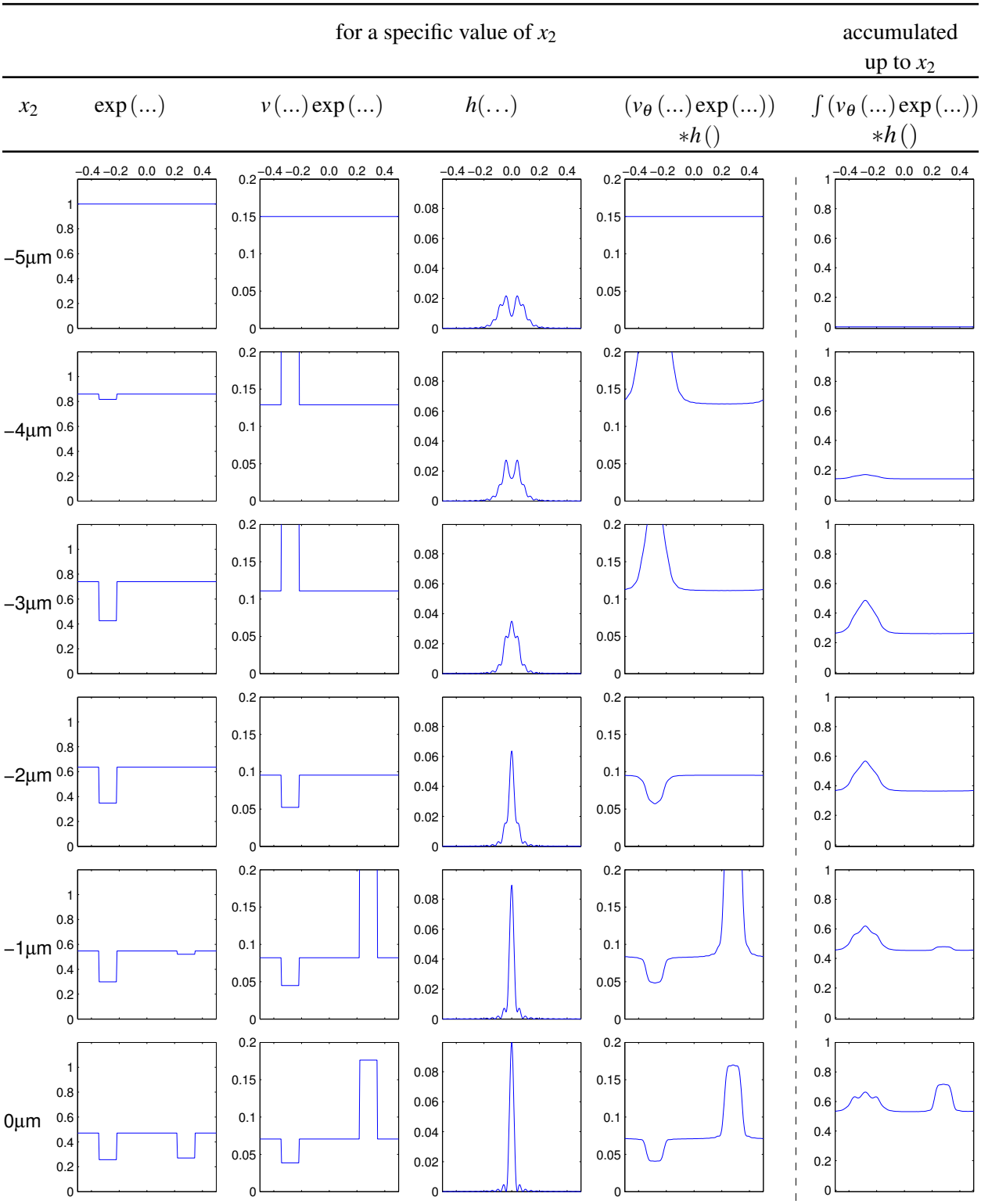

Figure 5.5: Continued on the next page.

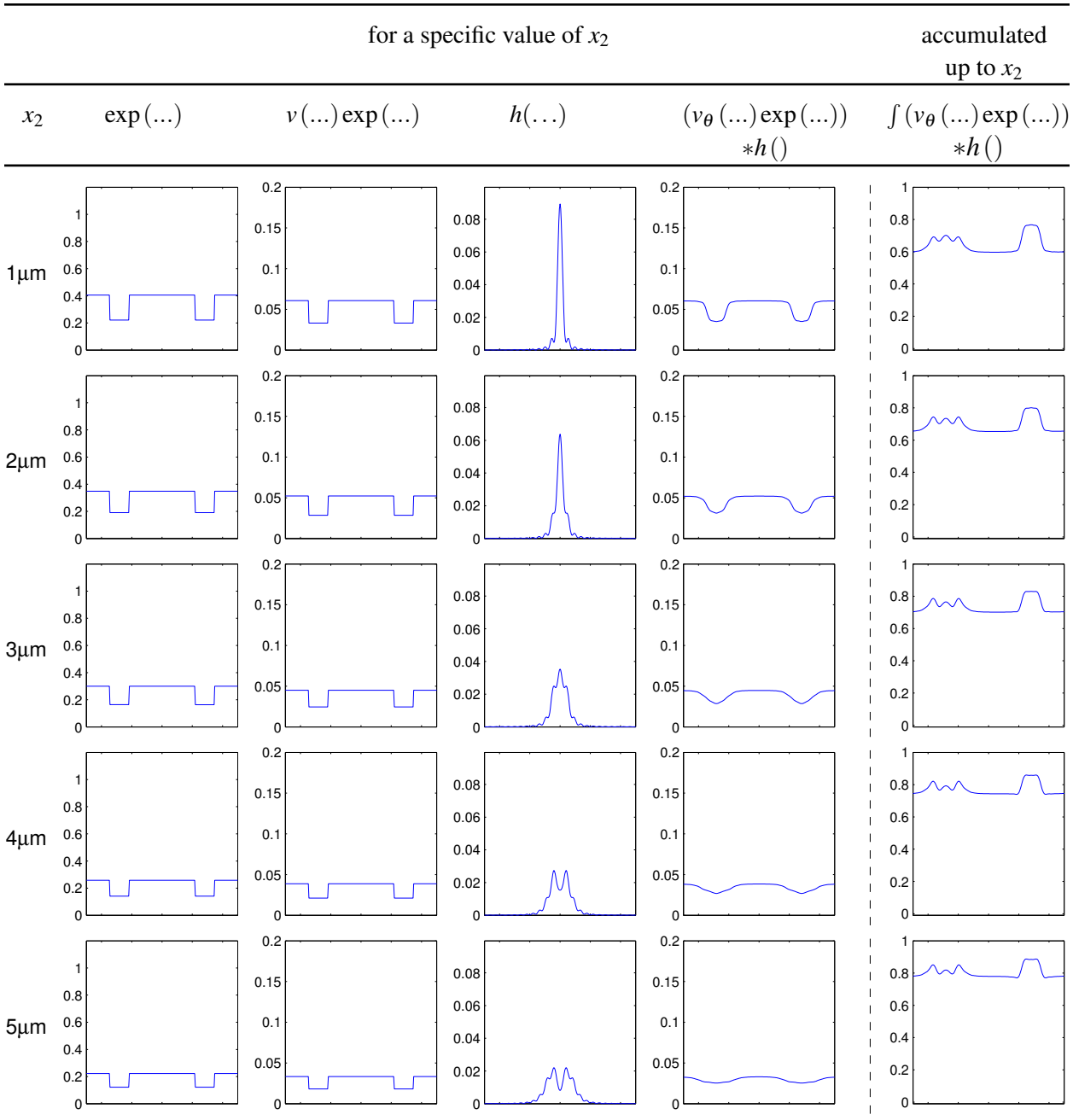

Figure 5.5: Intermediate steps of the projection calculation for the phantom in Figure 5.1 for angle $\theta = \pi$. See text for discussion.

(as evident by high peaks in the graphs for $x_2 = -4\,\mu$m and $x_2 = -3\,\mu$m in the fourth column). The small rectangle attenuates x-rays much more than the background around it. When we look at the contributions of layers for values of x_2 after the small rectangle, the contributions from those x-rays that passed through the small rectangle are lower than the ones that only passed through the

background. Due to the blurring function, the lowest values end up near the centers of the resulting valleys in the graphs. Also the width of the negative valley for an x_2 whose absolute value is not larger than $2\,\mu$m is considerably less than the width of the positive peak for a value of x_2 between $-4\,\mu$m and $-3\,\mu$m. Even though the depths of the valleys for the x_2 after the small rectangle are smaller than the heights of the peaks before it, the valleys occur all through the remaining values of x_2. The combined effect of these narrow valleys is that they erode the central part of the single high peak present in the accumulated projection in the third graph in the last column of Figure 5.5. This results in the appearance of multiple peaks in the last graph in the last column.

The magnitude of this effect depends on the size of the linear attenuation coefficients of the structures through which an x-ray passes: the larger the attenuation, the more pronounced is the artifact. It also depends on the distance of the structure from the zero-defocus plane: the further away from the zero-defocus plane the structure is located, the greater is the artifact.

5.4 Correction Approaches for Small and Large Specimen

There is currently no mathematical inversion method for the forward problem associated with image formation in soft x-ray microscopy which is modeled by our operators $\mathscr{X}_h^{3t}$ and $\mathscr{X}_h^n$ with $n \in \{2,3\}$. The major difficulty comes from non-linearity of the forward model in combination of attenuation and blurring effects. Inversion methods exist for the forward problems that involve only attenuation, as modeled by $\mathscr{X}^{3t}$ and $\mathscr{X}^n$ with $n \in \{2,3\}$, or only blurring, as modeled by $\mathscr{P}_h^{3t}$ and $\mathscr{P}_h^n$ with $n \in \{2,3\}$. In this section, we demonstrate how these inversion methods for related problems can be used to improve the quality of the reconstructions obtained from soft x-ray microscopy data.

5.4.1 Attenuation Correction

The attenuation of x-rays results in decreased contrast of features in the projection data both in data generated using attenuated projection operators ($\mathscr{X}^{3t}$ and $\mathscr{X}^n$) and distance-dependent attenuated

projection operators ($\mathscr{X}_h^{3t}$ and $\mathscr{X}_h^{n}$) (see Figure 5.2) and this reduction in contrast carries over to the reconstructions. The correction methods of Theorems 5.1 and 5.2 restore the contrast between features in projection data obtained according to the models $\mathscr{X}^{3t}$ and $\mathscr{X}^{n}$ and produce data corresponding to ideal projections that could have been obtained using projection operators ($\mathscr{P}^{3t}$ and $\mathscr{P}^{n}$). In soft x-ray microscopy data, the attenuation effects are combined with blurring effects so the above theorems no longer apply, but applying the correction improves the contrast in the data even though the ideal projections cannot be obtained due to the blurring effects.

Figure 5.6 demonstrates the attenuation correction results when applied to the attenuated and blurred x-ray microscopy projections of the phantom in Figure 5.1. As in Figure 5.3 we show data for two projections obtained π radians apart along the long side of the phantom. The attenuated and blurred projections are displayed using solid light blue. The data that are obtained by applying the attenuation correction are shown using dashed light blue. For comparison, we also included the ideal projections (no attenuation and no blurring) using solid black. If the attenuation and blurring were both linear processes, the correction for attenuation should result in data that are identical to blurred projections. Unfortunately this is not the case. Applying attenuation correction restores the contrast and the resulting data are close to the blurred projections for features close to the zero-defocus plane, but it does not provide correction for the replication artifact discussed in the previous section.

The attenuation correction provides improvement in the data and therefore in the reconstructions and may be sufficient for obtaining useful results for small samples (see Figure 5.10 on page 97), but it does not provide any correction for blurring and is, therefore, not sufficient for large samples; see Figure 5.15 on page 102.

5.4.2 Blurring Correction

Another approach to improving the quality of the reconstructions obtained from soft x-ray microscopy data is to correct for blurring, ignoring the attenuation effects. The defocus-gradient corrected backprojection method discussed in Sections 4.2-4.3, can be used to reconstruct ob-

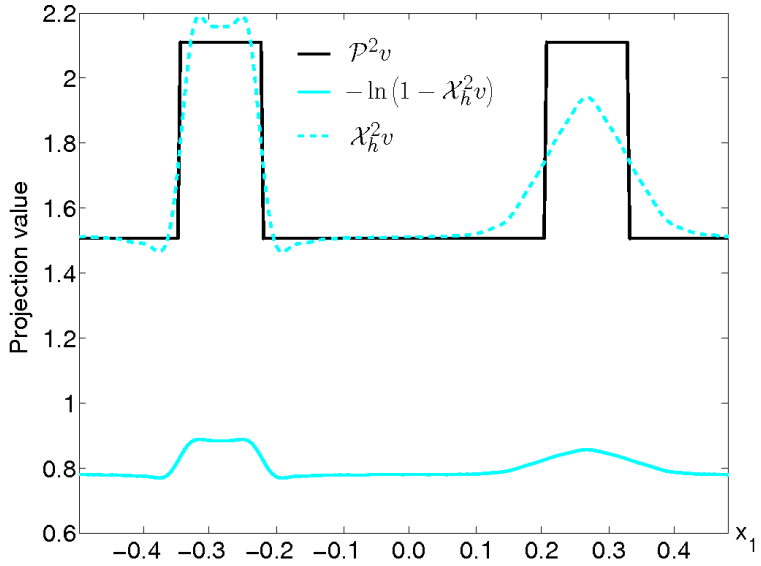

(a)

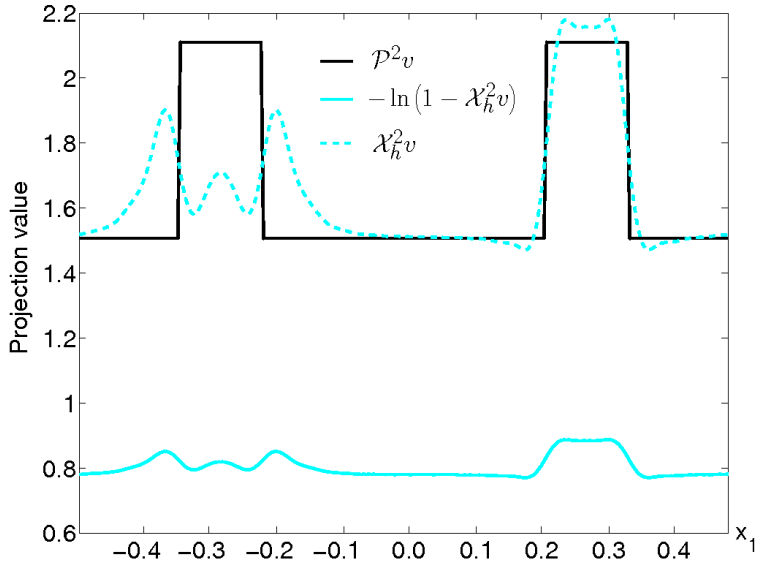

(b)

Figure 5.6: Effects of applying attenuation correction to attenuated and blurred projection data of the phantom in Figure 5.1 for two projection angles: (a) $\theta_1 = 0$ and (b) $\theta_1 = \pi$. The three different plots are: the ideal microscope projections (no attenuation and no blurring) $\left[\mathscr{P}^2 v\right](0, x_1) = \left[\mathscr{P}^2 v\right](\pi, -x_1)$ (solid black); X-ray microscopy projections $\left[\mathscr{X}_h^2 v\right](0, x_1) \neq \left[\mathscr{X}_h^2 v\right](\pi, -x_1)$ (solid light blue); projections obtained by attenuation correction of $\mathscr{X}_h^2 v$ (dashed light blue).

jects from data obtained according to distance-dependent attenuated projection operators ($\mathscr{X}_h^{3t}$ and $\mathscr{X}_h^n$). The reconstructions provide improvement in terms of blurring, but show reduced contrast of features due to uncorrected attenuation effects. If the recovery of the linear attenuation coefficients of the original object is not a primary concern, using this type of correction may produce useful reconstructions; see Figure 5.11 on page 98. This approach does not provide acceptable reconstructions for large samples, because the combined effects of attenuation and blurring cannot be handled by blurring correction alone; see Figure 5.17 on page 104. Due to the fact that this correction is incorporated into the reconstruction method, we cannot show its results for individual projections.

5.4.3 Attenuation and Blurring Correction

The correction for attenuation followed by correction for blurring is a natural extension of the approaches described in the previous two subsections. The attenuation correction is applied to the data in the way described in Section 5.2 and Subsection 5.4.1. The data corrected for attenuation are then used in the defocus-gradient corrected backprojection reconstruction method that corrects for blurring. This reconstruction ignores the fact that the imaging model in TXM is not linear. As a consequence, the reconstructions are not as one would have desired and, especially for large specimens, contain unacceptable artifacts; see Figures 5.12 and 5.18 on pages 98 and 105, respectively.

5.4.4 Iterative Data Refinement

Iterative data refinement (IDR) [4] is a methodology that has been found efficacious for a variety of applications in which reconstruction from projections is performed. IDR assumes that the measuring device (the soft X-ray microscope in our case) provides data that only approximate the data we would have liked to measure (the ideal data). The discrepancy between the actual data (under our assumptions, affected by attenuation and by a distance-dependent PSF) and data that are idealized can be estimated from the actual data and the knowledge of the measuring process,

Algorithm 5.1 IDR - generic

Given:

$\mathscr{P}_{ideal}$ - operator that models idealized measurement, what we would like to measure (no noise, or no attenuation, or no blurring);

$\mathscr{B}_{ideal}$ - operator that provides a known inversion method for ;

$\mathscr{P}_{device}$ - operator that models actual measured data that follow known image formation model, but for which inversion method is not known.

v - a function to be reconstructed;

μ - relaxation parameter

Iterative process:

p^0 = anything, usually based on $\mathscr{P}_{device}v$

$p^{k+1} = \mu\mathscr{P}_{device}v + (\mathscr{P}_{ideal} - \mu\mathscr{P}_{device})\mathscr{B}_{ideal}p^k$

leading to a better approximation to the ideal data. This new approximation can then be used to estimate the new discrepancy, and the process can be repeated. Our knowledge of the measurement process is insufficient to obtain the ideal data exactly, but the original discrepancy is significantly reduced by just a few of such iterative steps. The well-established IDR methodology guarantees convergence under certain conditions, but even when not all of those conditions are satisfied, the iterations are known to improve the experimentally obtained data. An outline of a typical IDR scheme is provided as Algorithm 5.1.

Sorzano et al. [47] proposed an algorithm of this kind that, given a set of PSF corrupted projections, iterates over data and refines them in each step with the ultimate goal of reaching a projection data set that would be collected by an ideal device. Their method was developed for transmission electron microscopy with the assumption of a space-invariant PSF. This process approximates ideal projections that are free of PSF blurring, which then can be used in any reconstruction procedure.

For TXM we do not know of any attempts to use IDR methods. The results of applying the IDR approach to TXM data are shown in Figures 5.19 and 5.20 on pages 106 and 107, respectively.

5.4.5 Numerical Examples

We now present two numerical examples that illustrate the results of the correction and reconstruction approaches outlined in this section. The two examples differ in the size of the phantom that

we use. They demonstrate that, as the size of the specimen increases, it becomes more important to use correction and reconstruction methods that take the image formation into account.

Throughout this subsection we display grayscale images in one of two different ways. In the phantom the values of pixels represent the linear attenuation coefficients: the smallest one is 0.0 and the larges is 0.4. These pixel values are mapped to grayscale values in two different ways. In *full grayscale display* the lowest value, 0.0, is mapped to black and the highest value, 0.4, is mapped to white, and the values between 0.0 and 0.4 are linearly distributed in shades of gray between black and white. In the *narrow grayscale display* the pixels whose values are less than or equal to 0.15 are mapped to black and the pixels whose values are greater than or equal to 0.25 are mapped to back, and the pixels with values in between 0.15 and 0.25 are mapped to shades of gray linearly distributed between black and white. We use the same display windows for reconstructions computed in various ways. The narrow display is centered around the value of the background of our phantoms and provides a more detailed view of how well the boundaries and separations of small features are recovered.

The implementations of data collection and reconstruction were done in C/C++ and used some of the capabilities of user-defined algorithms in the snark09 package (Klukowska et al. [32]). In the data collection simulations and during some of the reconstructions, we used interpolation methods for the rotation of 2D images that were proposed by Thévenaz et al. [48]. We used the implementation provided by them on their website, with the option of B-splines of third degree as interpolators. We also made use of the fast Fourier transform (and inverse) implementations provided by the FFTW package; see Frigo and Johnson [16].

5.4.5.1 Small Phantom

We use two different 2D phantoms. The first one (see Figure 5.7) measures $5.51\,\mu\text{m} \times 5.51\,\mu\text{m}$. It is digitized in a 551×551 array. The pixel size is $0.01\,\mu\text{m} \times 0.01\,\mu\text{m}$. This phantom is used to demonstrate what happens when reconstructing a relatively small (from the point of view of soft x-ray microscopy imaging) specimen placed with its center at the zero-defocus plane. It is composed

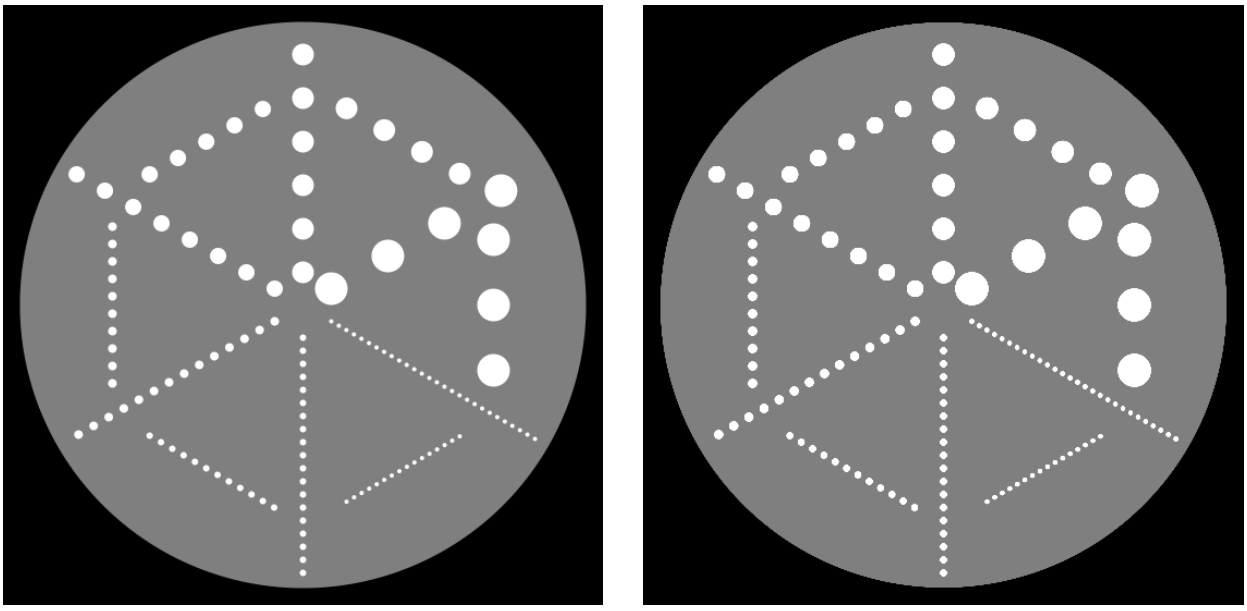

(a) **(b)**

Figure 5.7: A small phantom for illustration of the quality of the reconstructions from soft x-ray microscopy data of small specimen: **(a)** full grayscale display, **(b)** narrow grayscale display. Size: $5.51\,\mu\text{m} \times 5.51\,\mu\text{m}$, digitization: 551×551 array, linear attenuation coefficients $0.2\,\mu\text{m}^{-1}$ for the large disk and $0.4\,\mu\text{m}^{-1}$ for the small disks.

of a large disk which serves as a background with a linear attenuation coefficient of $0.2\,\mu\text{m}^{-1}$, and of sequences of much smaller disks of different sizes. The linear attenuation coefficient of the small disks is $0.4\,\mu\text{m}^{-1}$. Their sizes are, from largest to smallest, $0.3\,\mu$m, $0.2\,\mu$m, $0.15\,\mu$m, $0.08\,\mu$m, $0.06\,\mu$m, and $0.04\,\mu$m. Figure 5.7a shows the phantom in the full display of grayscale values and Figure 5.7b shows the same phantom in the narrow display of grayscale values. In the case of the phantom, those two images are practically identical. The differences will become visible when we present the reconstructions.

Data Collection We simulated data collection using the image formation model described by the operators $\mathscr{P}^2$ and $\mathscr{X}_h^2$. We use the $\mathscr{P}^2 v$ data as a reference point as to how good a reconstruction can be obtained from the data uncorrupted by blurring or attenuation that are used in a rho-filtered layergram algorithm. The blurring function used in computation of the attenuated distance-dependently blurred projections was the same as the one we discussed in Section 3.2. In

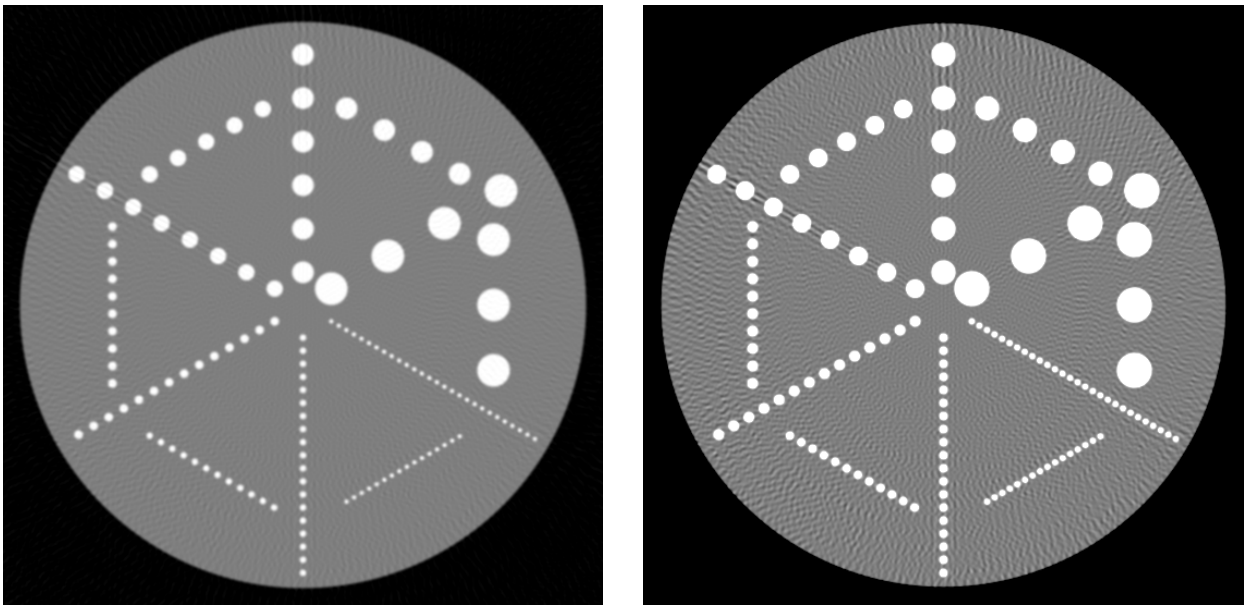

(a) **(b)**

Figure 5.8: Reconstruction computed from the ideal microscopy data $\mathscr{P}^2 v$ of the phantom in Figure 5.7: (a) full grayscale display, (b) narrow grayscale display.

both cases we collected 360 projections uniformly distributed in the range $[0, 2\pi)$. The detector spacing used was $0.01\,\mu$m. Figure 5.8 shows the reconstruction computed from the ideal data $\mathscr{P}^2 v$ in a full display window and in the narrow display window. The image in Figure 5.8b clearly shows that we cannot produce a reconstruction that is identical to the phantom, but it provides information sufficient for identification of even the smallest disks. We used the attenuated distance-dependently blurred data $\mathscr{X}_h^2$ to compute the several different reconstructions. They are discussed below.

Correction and Reconstruction Approaches Unless otherwise stated, all our reconstructions are computed using rho-filtered layergram algorithm, see for example Rowland [45]. This is an algorithm from the backprojection family that is preferred to others in our context because it is easily extended into the defocus-gradient corrected backprojection discussed in Sections 4.2 and 4.3. The reconstruction that was computed using data that were not corrected in any way is shown in Figure 5.9a in the full display window, and in Figure 5.9b in the narrow display window. Due to attenuation in the image formation process that was not corrected for, the reconstruction has much lower values and reduced contrast between features as compared to the phantom. The range

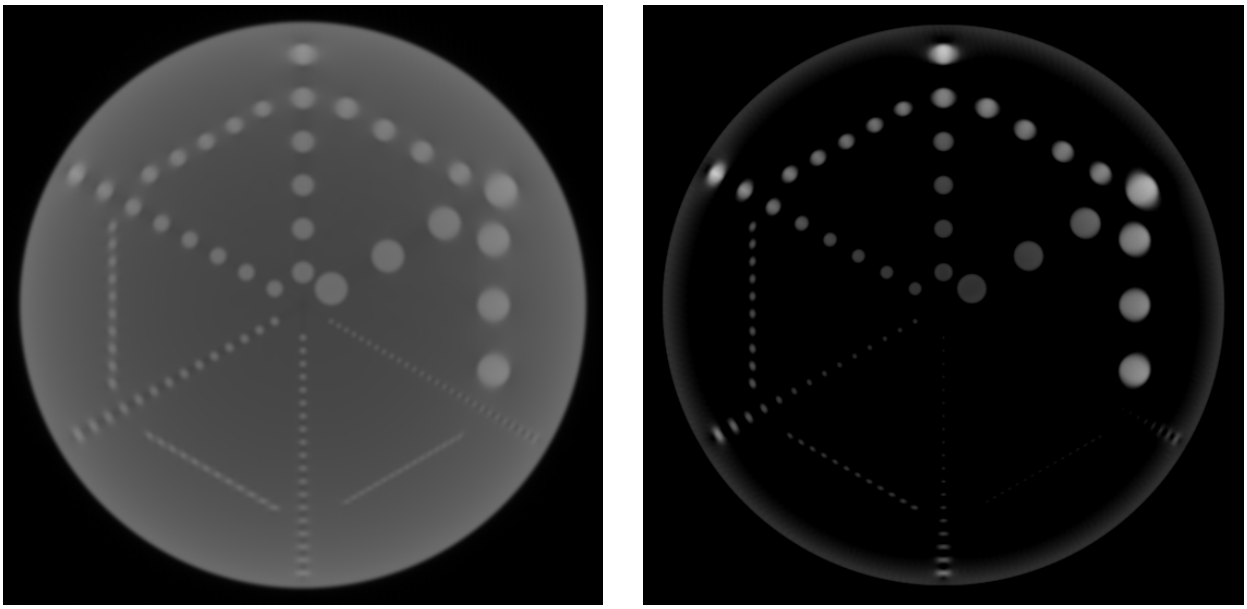

(a) **(b)**

Figure 5.9: Reconstruction computed from the attenuated distance-dependently blurred microscopy data $\mathscr{X}_h^2 v$ of the phantom in Figure 5.7 when no correction is performed: (a) full grayscale display, (b) narrow grayscale display.

of reconstructed values of the linear attenuation coefficients is from -0.00248 to 0.22908 (in the phantom the range of values is from 0.0 to 0.4). The range of grayscale values for displaying this reconstruction can be adjusted to provide more useful information. But it is clear that without correcting for the attenuation effects of x-rays, the true attenuation coefficients cannot be recovered.

Attenuation Correction We computed the reconstructions after correcting the data for attenuation as discussed in Subsection 5.4.1. The reconstruction is shown in Figure 5.10a in the full display window, and in Figure 5.10b in the narrow display window. The range of reconstructed values of the linear attenuation coefficients is from -0.00710 to 0.39153; this matches very closely the values in the phantom. The uncorrected blurring effects are visible clearly, especially in Figure 5.9b and are much more pronounced near the outside of the reconstruction than near its center. The blurring is relatively small in a reconstruction of this size and most of the features are recovered correctly.

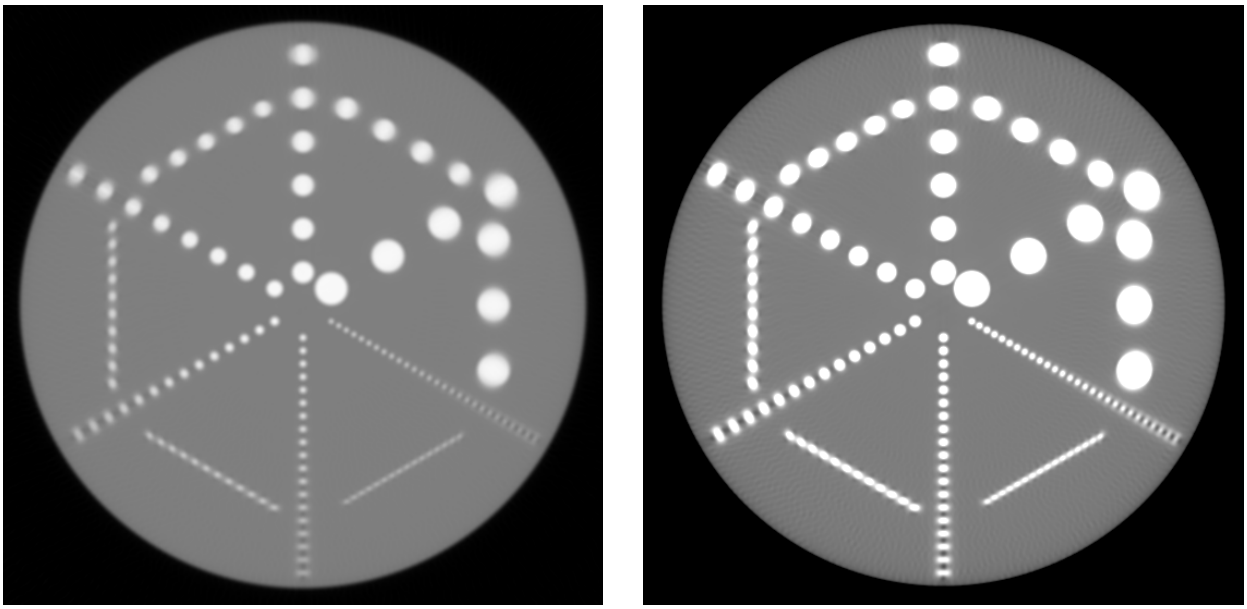

(a) **(b)**

Figure 5.10: Reconstruction computed from the attenuated distance-dependently blurred microscopy data $\mathscr{X}_h^2 v$ of the phantom in Figure 5.7 when data are corrected for attenuation effects as described in Subsection 5.4.1: (a) full grayscale display, (b) narrow grayscale display.

Blurring Correction We computed the reconstructions using the defocus-gradient corrected backprojection as discussed in Subsection 5.4.2. The reconstruction is shown in Figure 5.11a in the full display window, and in Figure 5.11b in the narrow display window. Due to attenuation in the image formation process that was not corrected for, the reconstruction has much lower values and reduced contrast between features as compared to the phantom, as was the case for the reconstruction that did not use any correction. The range of reconstructed values of the linear attenuation coefficients is from -0.02619 to 0.26729. The blurring is relatively small in a reconstruction of this size and most of the features are recovered correctly, although the replication artifact is not corrected for by blurring correction alone as is apparent for the small disks near the outside of the reconstruction.

Attenuation and Blurring Correction Combining the two techniques above, we computed the reconstructions first correcting the data for attenuation and then using the defocus-gradient corrected backprojection as discussed in Subsection 5.4.3. The reconstruction is shown in Fig-

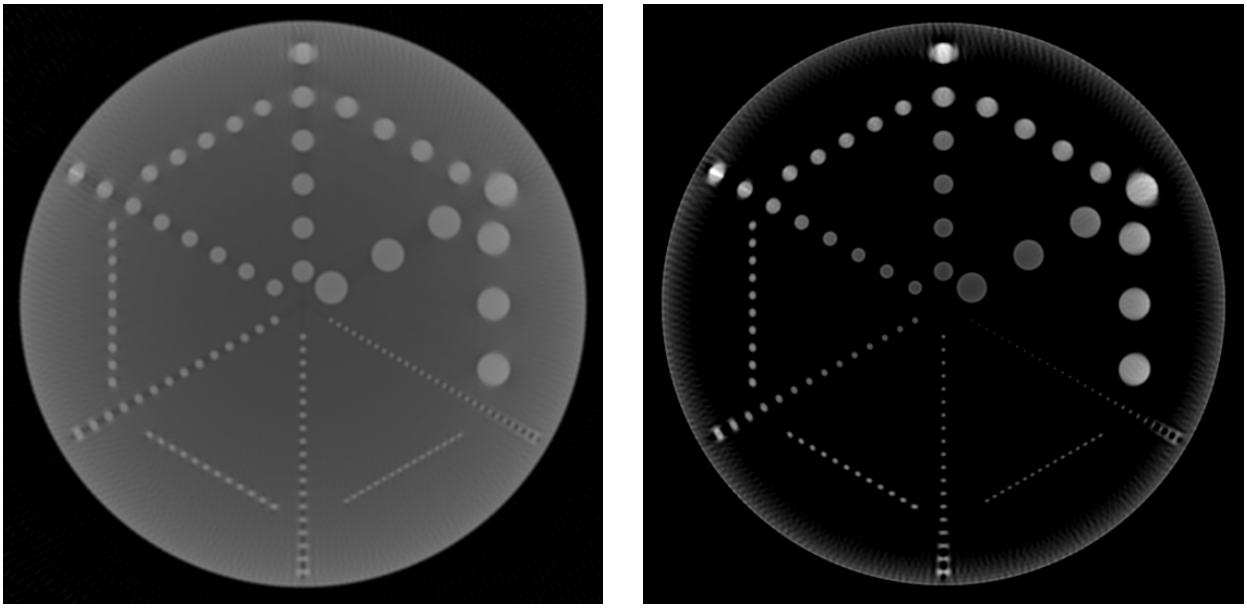

(a) **(b)**

Figure 5.11: Reconstruction computed from the attenuated distance-dependently blurred microscopy data $\mathscr{X}_h^2 v$ of the phantom in Figure 5.7 using the defocus-gradient corrected backprojection as discussed in Subsection 5.4.2: (a) full grayscale display, (b) narrow grayscale display.

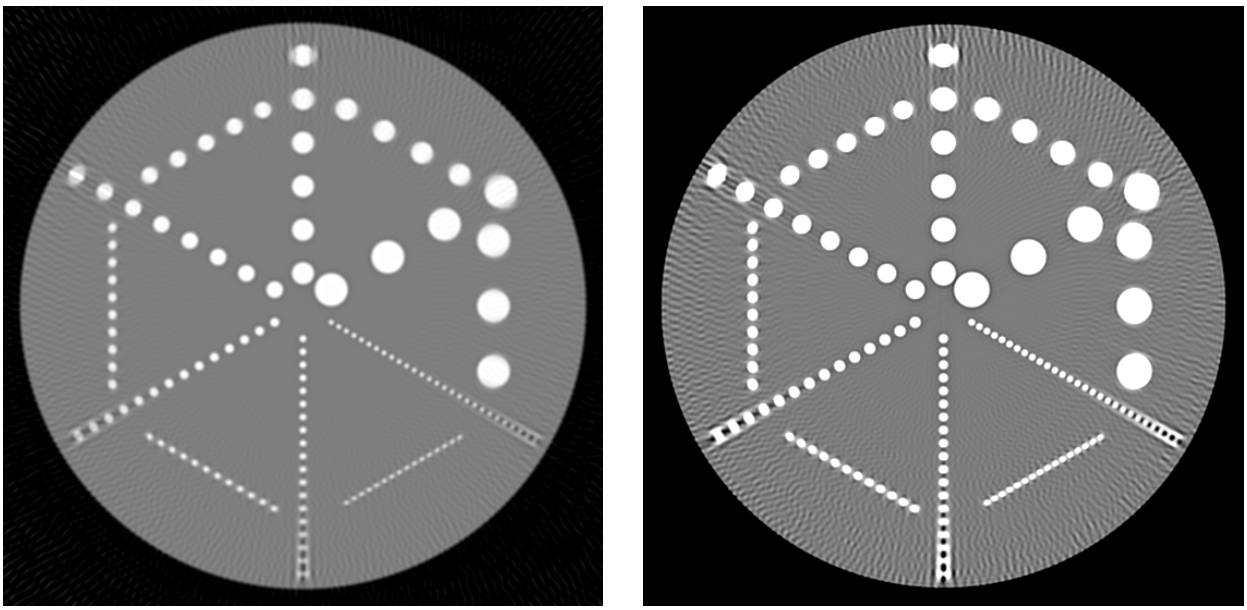

(a) **(b)**

Figure 5.12: Reconstruction computed from the attenuated distance-dependently blurred microscopy data $\mathscr{X}_h^2 v$ of the phantom in Figure 5.7 first correcting the data for attenuation and then using the defocus-gradient corrected backprojection as discussed in Subsection 5.4.3: (a) full grayscale display, (b) narrow grayscale display.

ure 5.12a in the full display window, and in Figure 5.12b in the narrow display window. The values of the linear attenuation coefficients are reconstructed correctly and the contrast between features is recovered. The range of reconstructed values of the linear attenuation coefficients is from -0.07565 to 0.45545; observe that this range is greater that it was when we only corrected for the attenuation. The blurring is reduced when compared to the reconstruction that corrected only for the attenuation, but is not completely removed. The reconstruction in general is worse as we move further away from the center. This approach might be sufficient to restore the linear attenuation coefficients and reduce the blurring. It also shows clearly that applying the two corrections in sequence is not sufficient to handle the combined effects of attenuation and blurring in the data.

5.4.5.2 Large Phantom

The second phantom (see Figure 5.13) measures $11.01\,\mu\text{m} \times 11.01\,\mu\text{m}$. It is digitized in a 1101×1101 array. The pixel size is $0.01\,\mu\text{m} \times 0.01\,\mu\text{m}$. This phantom is used to demonstrate what happens when reconstructing a large specimen centered at the zero-defocus plane. The general structure of the phantom is an extension of the small phantom (see Figure 5.7). It is composed of a large disk with a linear attenuation coefficient of $0.2\,\mu\text{m}^{-1}$, and of sequences of much smaller disks of different sizes. The linear attenuation coefficient of the small disks is $0.4\,\mu\text{m}^{-1}$. Their sizes are, from largest to smallest, $0.3\,\mu$m, $0.2\,\mu$m, $0.15\,\mu$m, $0.08\,\mu$m, $0.06\,\mu$m, and $0.04\,\mu$m. In addition, there are two large ellipses placed symmetrically on the left and right sides of the phantom with linear attenuation coefficient of $0.3\,\mu\text{m}^{-1}$. Figure 5.13 shows the phantom in the full display of grayscale values.

Data Collection We simulated data collection in exactly the same way as for the small version of this phantom. We used the image formation model described by the operator $\mathscr{X}_h^2$. The blurring function and its parameters were the same ones that we discussed in Section 3.2. We collected 360 projections uniformly distributed in the range $[0, 2\pi)$. The detector spacing used was $0.01\,\mu$m.

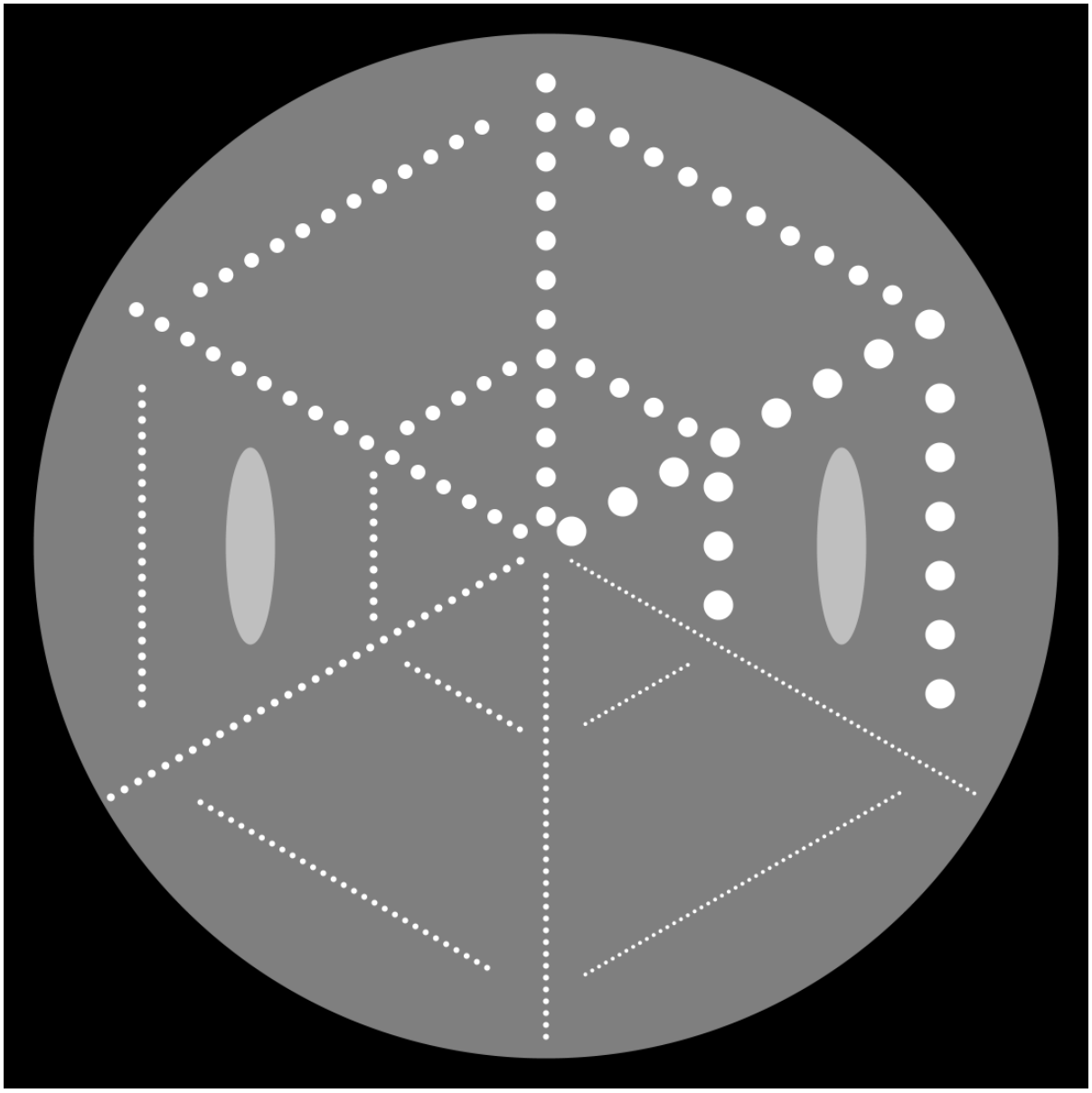

Figure 5.13: A large phantom for illustration of the quality of the reconstructions from soft x-ray microscopy data of large specimen. Size: $11.01\,\mu\mathrm{m} \times 11.01\,\mu\mathrm{m}$, digitization: 1101×1101 array, linear attenuation coefficients $0.2\,\mu\mathrm{m}^{-1}$ for the large disk, $0.3\,\mu\mathrm{m}^{-1}$ for the ellipsis and $0.4\,\mu\mathrm{m}^{-1}$ for the small disks.

Correction and Reconstruction Approaches We first computed a reconstruction using the rho-filtered layergram algorithm using the data without any corrections. This reconstruction is shown in Figure 5.14 in full grayscale display (0.0 - 0.4). The range of reconstructed values of the linear attenuation coefficients is from -0.01018 to 0.17993, and therefore displaying this reconstruction in the narrow range of grayscale values does not provide any useful information. Figure 5.14

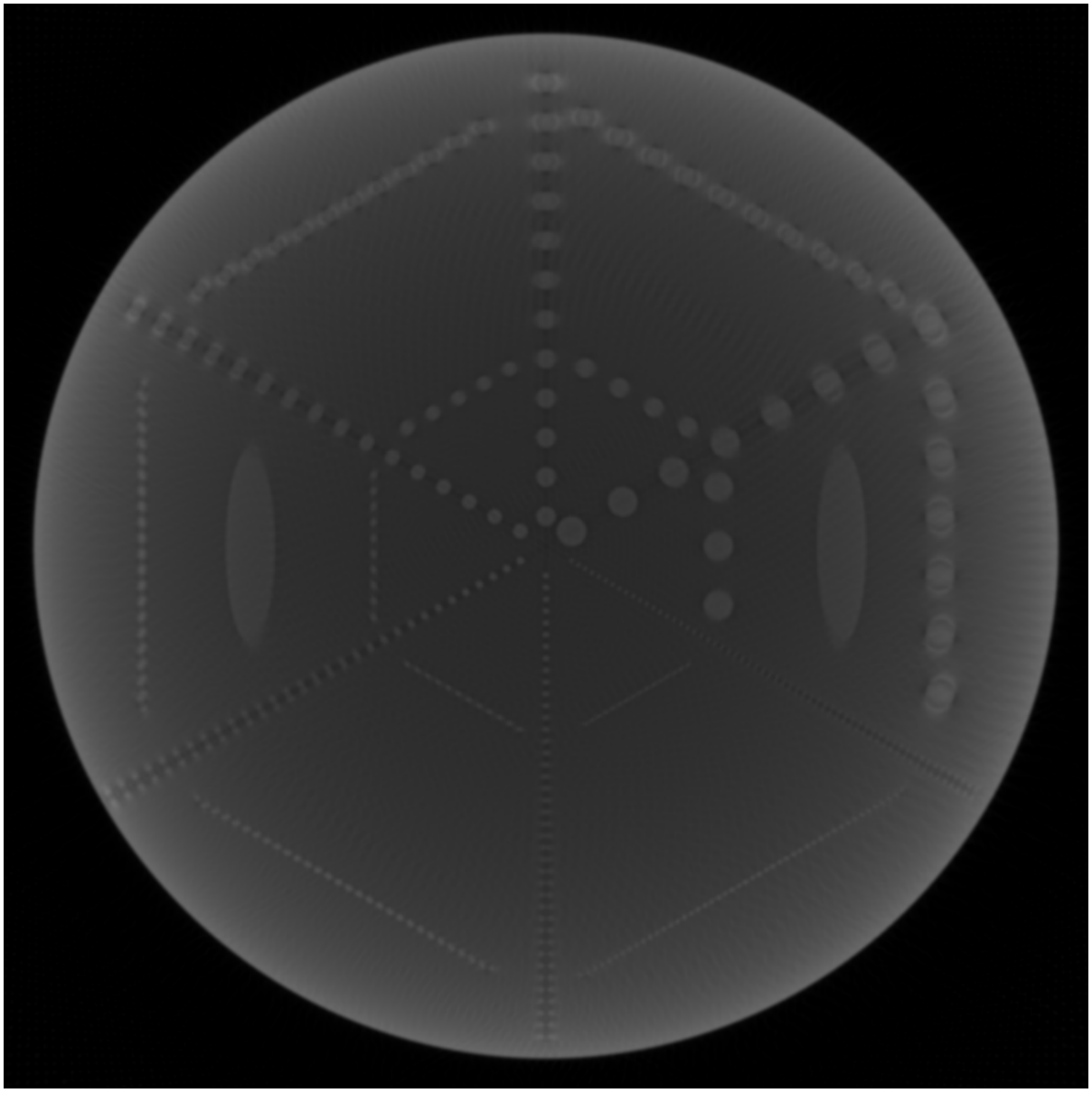

Figure 5.14: Reconstruction computed from the attenuated distance-dependently blurred microscopy data $\mathscr{X}_h^2 v$ of the phantom in Figure 5.13 when no correction is performed

clearly shows that the reduction in contrast between features and the blurring are much more evident when a larger object is reconstructed and using a reconstruction of this kind may provide misinformation about the sample for which the data are collected.

Attenuation Correction We computed the reconstructions after correcting the data for attenuation as discussed in Subsection 5.4.1. The reconstruction is shown in Figure 5.15 in the full

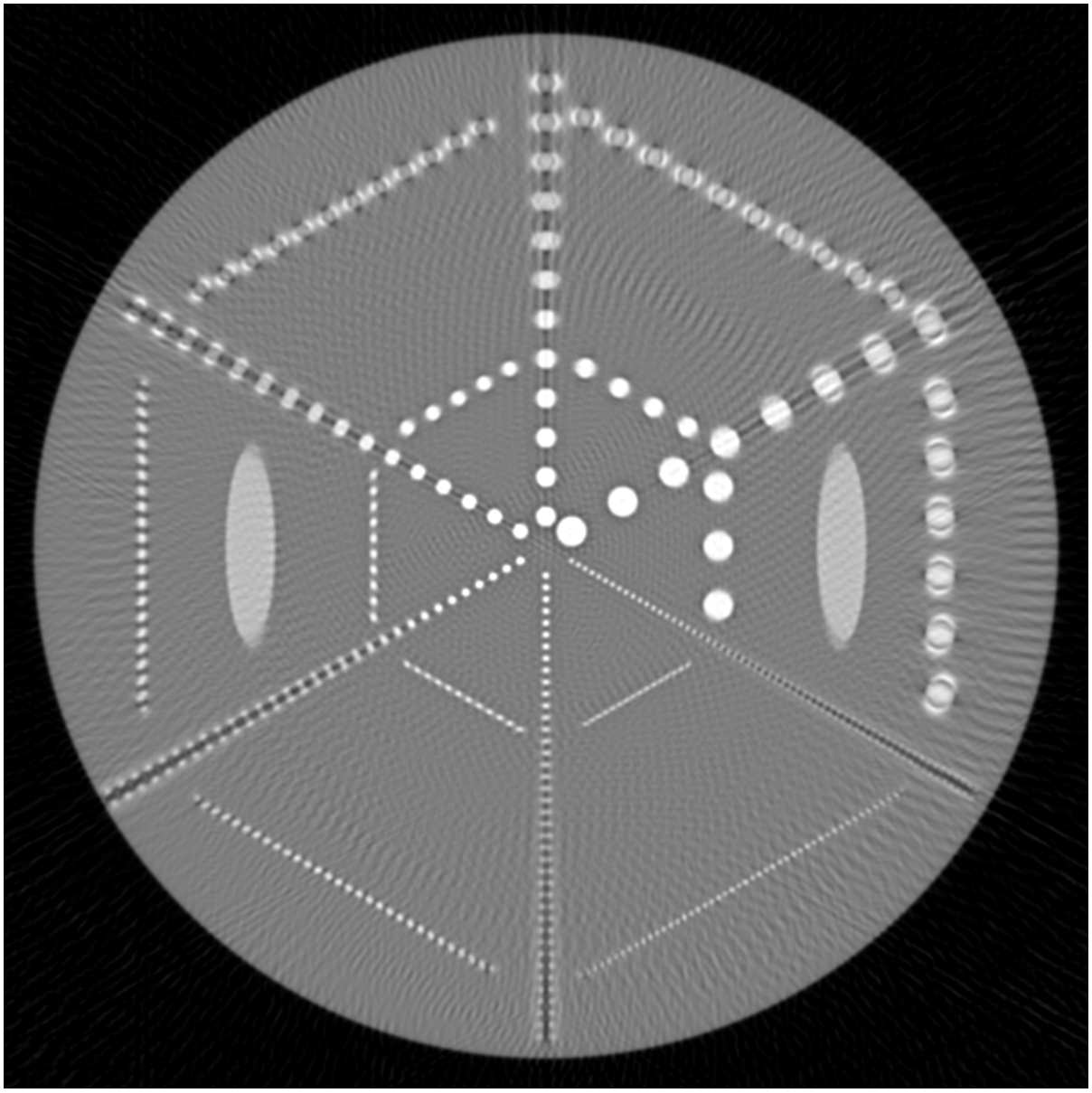

Figure 5.15: Reconstruction computed from the attenuated distance-dependently blurred microscopy data $\mathscr{X}_h^2 v$ of the phantom in Figure 5.13 when data are corrected for attenuation effects as described in Subsection 5.4.1. Reconstruction shown in the full grayscale display.

grayscale display (0.0 - 0.4), and in Figure 5.16 in the narrow grayscale display (0.15 - 0.25). The range of reconstructed values of the linear attenuation coefficients is from -0.05353 to 0.51940, which is larger than that of the phantom. The uncorrected blurring effects are clearly visible, especially in Figure 5.16 and they are significantly more pronounced than in the small phantom. The replication of features effect discussed in Section 5.3 is clearly in evidence.

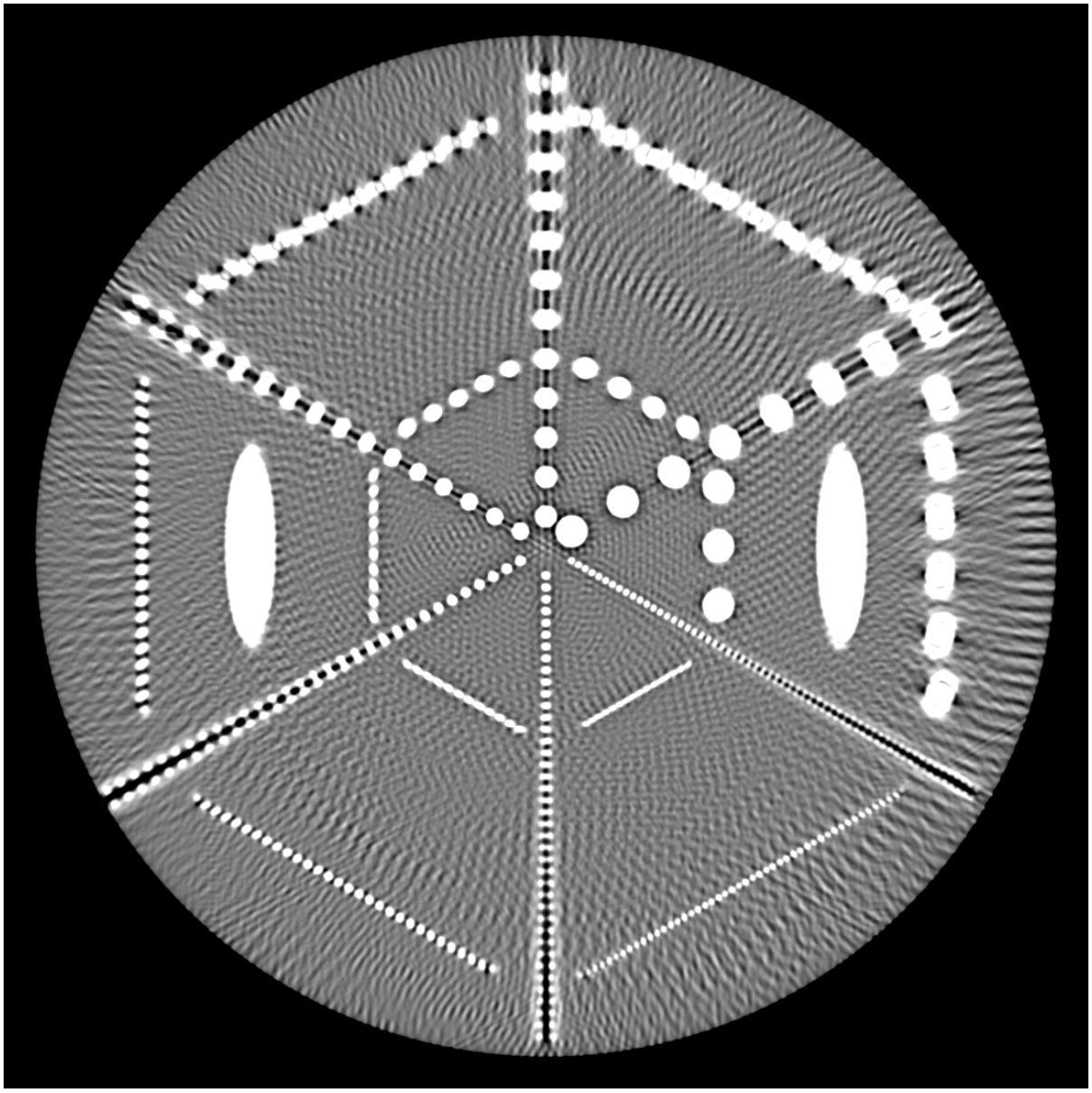

Figure 5.16: Reconstruction computed from the attenuated distance-dependently blurred microscopy data $\mathscr{X}_h^2 v$ of the phantom in Figure 5.13 when data are corrected for attenuation effects as described in Subsection 5.4.1. Reconstruction shown in the narrow grayscale display.

Blurring Correction As for the small phantom, we computed the reconstructions using the defocus-gradient corrected backprojection as discussed in Subsection 5.4.2. The reconstruction is shown in Figure 5.17 in the full grayscale display. The range of reconstructed values is from -0.04451 to 0.23791, which is much smaller than the range of values in the phantom. The features further away from the center of the reconstruction remain blurred and the replication artifact is

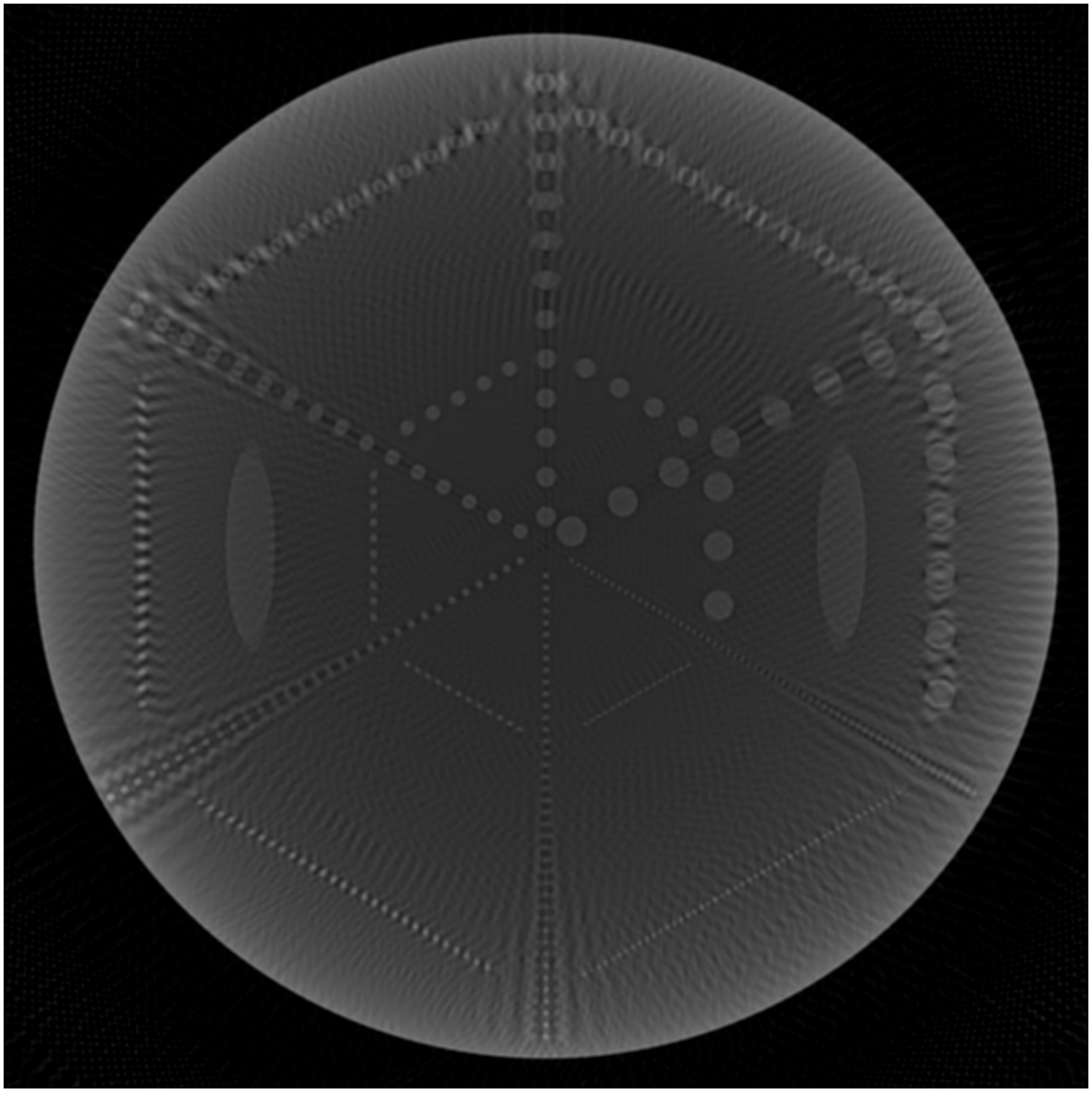

Figure 5.17: Reconstruction computed from the attenuated distance-dependently blurred microscopy data $\mathscr{X}_h^2 v$ of the phantom in Figure 5.13 using the defocus-gradient corrected backprojection as discussed in Subsection 5.4.2. Reconstruction shown in the full grayscale display.

clearly not handled by the blurring correction alone.

Attenuation and Blurring Correction Combining the two techniques above, we computed the reconstruction first correcting the data for attenuation and then using the defocus-gradient corrected backprojection as discussed in Subsection 5.4.3. The reconstruction is shown in Figure 5.18

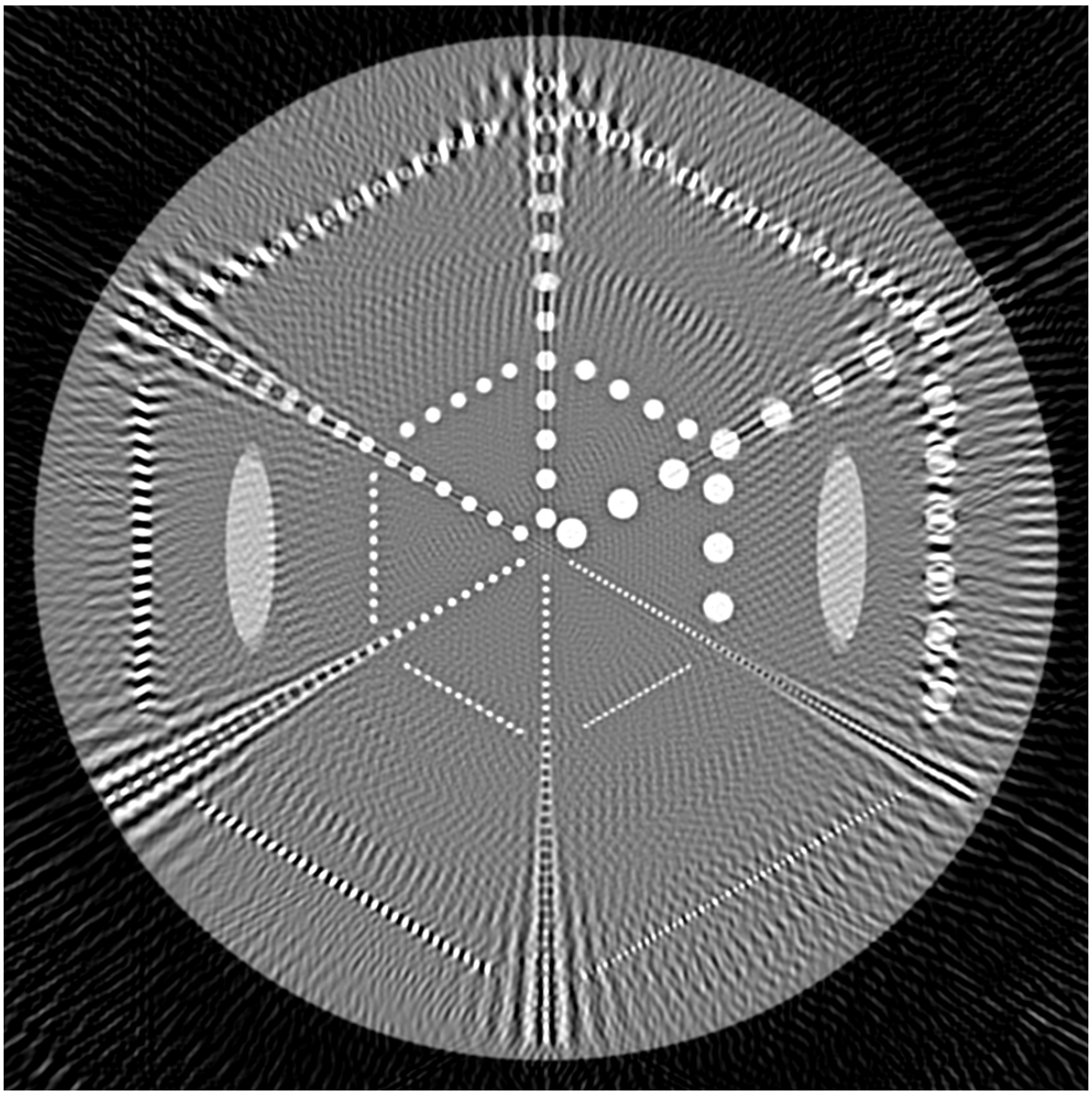

Figure 5.18: Reconstruction computed from the attenuated distance-dependently blurred microscopy data $\mathscr{X}_h^2 v$ of the phantom in Figure 5.13 first correcting the data for attenuation and then using the defocus-gradient corrected backprojection as discussed in Subsection 5.4.3. Reconstruction shown in the full grayscale display.

in the full grayscale display. The range of reconstructed values of the linear attenuation coefficients is from -0.28775 to 0.92195, which is much larger than the range of values for the phantom. There are many problems with this reconstruction approach that were not apparent when we used it with the small phantom. Using the two corrections separately one after another ignores the fact that these are not linear processes in the image formation model and, as a result, neither attenuation nor

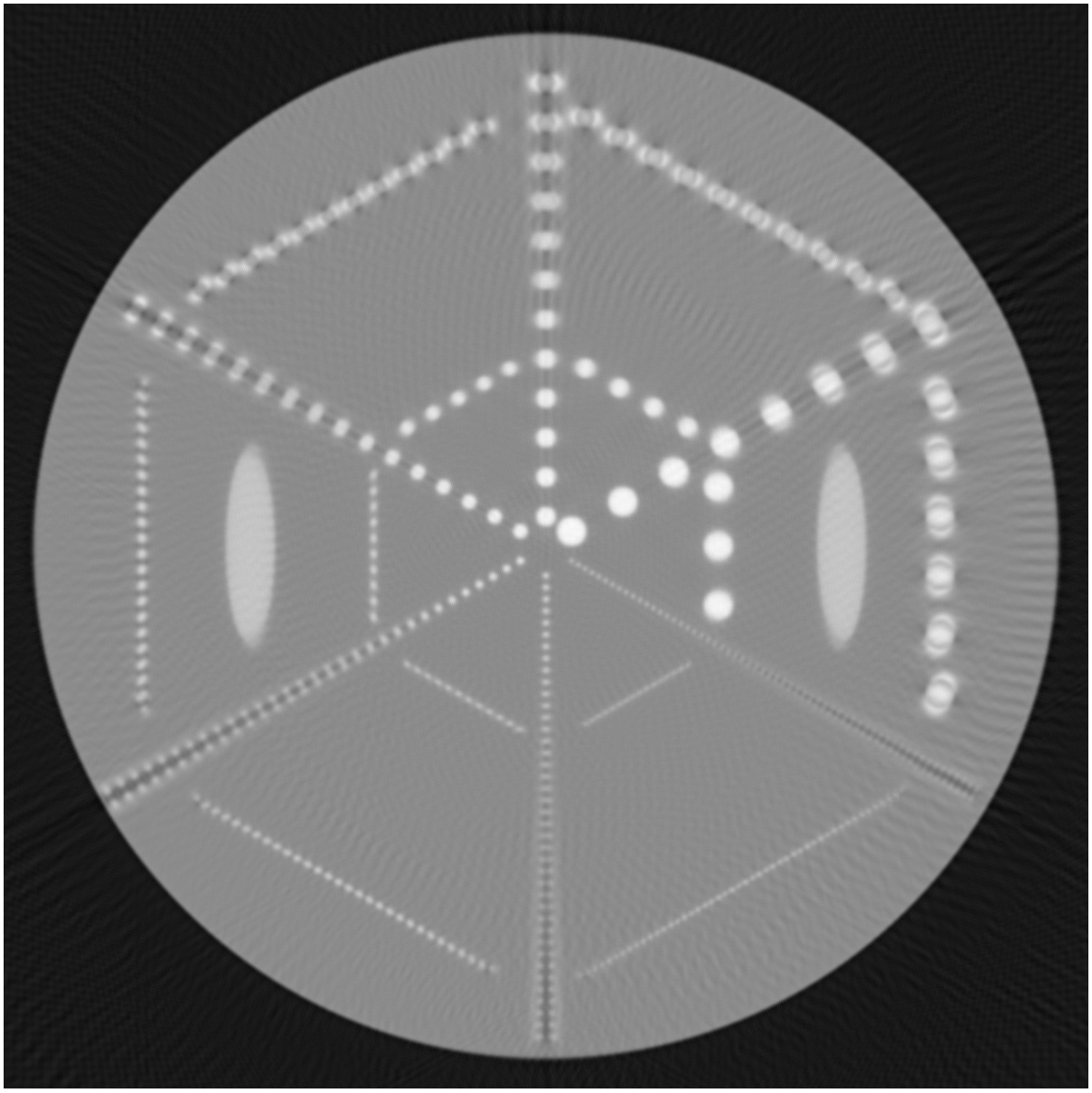

Figure 5.19: Reconstruction computed from the attenuated distance-dependently blurred microscopy data $\mathscr{X}_h^2 v$ of the phantom in Figure 5.13 using iterative data refinement approach discussed in Subsection 5.4.4. Reconstruction shown in the full grayscale display.

blurring is properly corrected-for in the reconstruction. The replication artifacts are also apparent and appear enhanced.

Iterative Data Refinement In our implementation of IDR we used the image formation model described by the operator X_h^2 of Eq. (5.3). The ideal device was modeled by the projec-

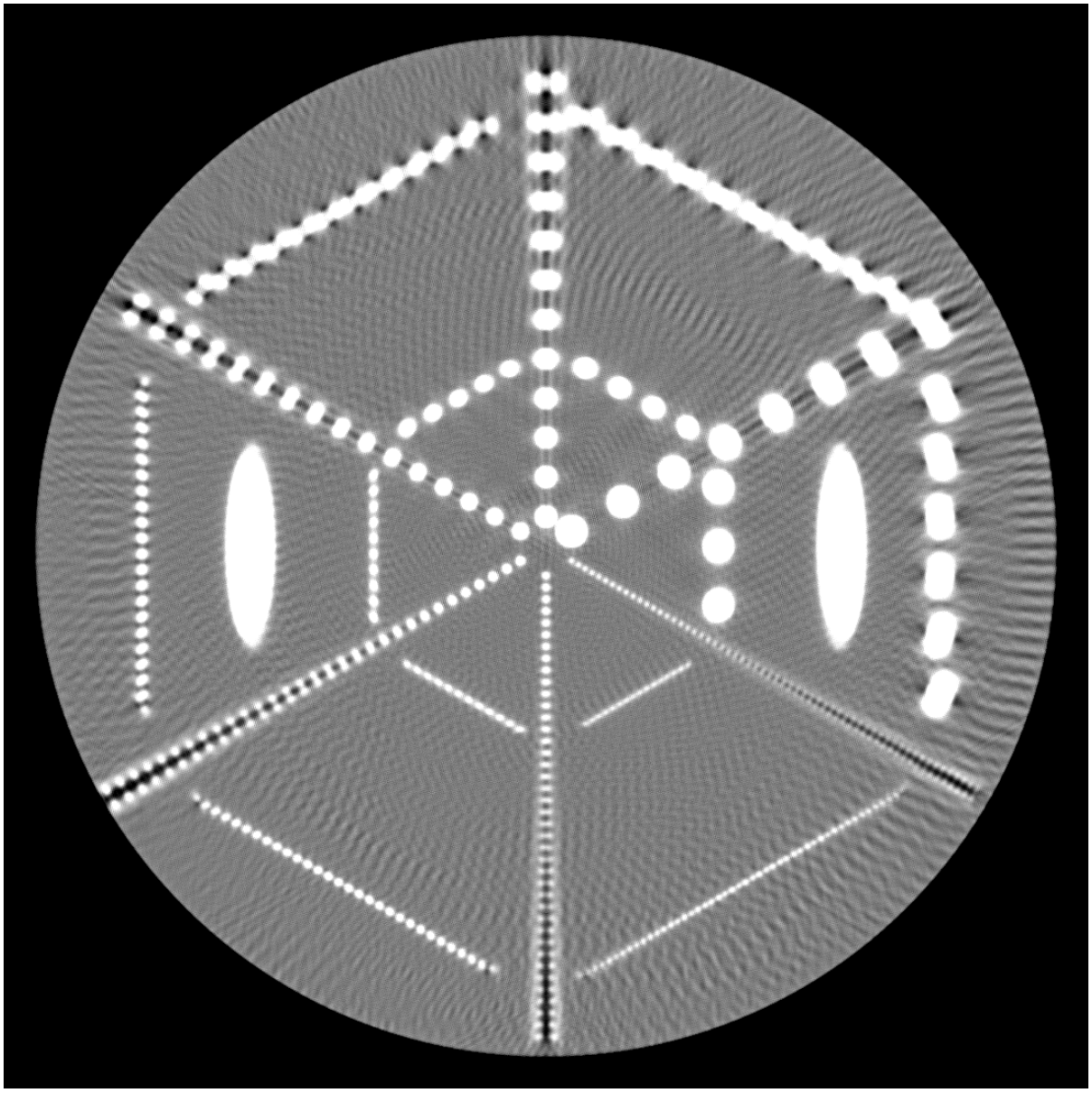

Figure 5.20: Reconstruction computed from the attenuated distance-dependently blurred microscopy data $\mathscr{X}_h^2 v$ of the phantom in Figure 5.13 using iterative data refinement approach discussed in Subsection 5.4.4. Reconstruction shown in the full grayscale display.

tion operator $\mathscr{P}^2$ of Eq. (2.22). The iterative process was started by computing v^0 from data corrected for attenuation as described in Subsection 5.4.1 of this chapter. We found $\mu = 1.7$ to be a relaxation parameter that produces one of the best results in just a few iterations. We used ten iterations of algebraic reconstruction techniques (ART) (see, for example, Herman [21], Chapter 11) with relaxation constant 0.05 as the reconstruction algorithm as it is implemented in the

SNARK09 package (Klukowska et al. [32]).

The reconstruction of the third iteration is shown in Figure 5.19 in the full range of grayscale values and in Figure 5.20 in the narrow range of grayscale values. The range of reconstructed values of the linear attenuation coefficients is from -0.0428592 to 0.3971070, which is very close to the range of values in the phantom. Unfortunately, this reconstruction provides only slight improvement over just attenuation correction: the background is smoother (which is due to a different reconstruction algorithm) and the attenuation values match those of the phantom better, but the blurring, and especially the replication artifact remain uncorrected.

The next section discusses an approach that allows for significantly better reconstructions.

5.5 Using Data from Multiple Defocus Points

During data collection the imaging stage or a capillary that contains the specimen is placed at a specific distance from the zero-defocus plane. In soft x-ray microscopes the objective is to place as much of the specimen within the depth of focus as possible, which naturally leads to centering the specimen at the zero-defocus plane. If the specimen is larger than the depth of focus, then the details of that part may be lost in the reconstruction. The replication artifact discussed in Section 5.3 also becomes more pronounced with larger specimens.

A different approach would be to collect repeated sets of data by moving the specimen to different locations. This results in different parts of the specimen to be in focus in different data sets. In this section, we demonstrate that, in the mathematical limit, one can obtain ideal projection data modeled by $\mathscr{P}^n$ operator of Eq. (2.22) by combining the data obtained at different positions, and applying simple correction steps. Figure 5.21 provides conceptual illustration of such procedure. Rather than collecting data from a sample centered at the zero-defocus plane, we collect multiple projections by shifting the sample to as many positions before and after the zero-defocus plane as possible. Theorem 5.3 and its proof guarantee that if we could obtain projections from all possible

positions, the ideal projection data could be computed. In practice, data from only few positions may be available.

5.5.1 Mathematical Derivation

Using the definitions of operators $\mathscr{X}_h^n$ and $\mathscr{C}_h^n$ of Eqs. (5.3) and (4.1), we write $\mathscr{X}_h^n v$ in its integral form as

$$[\mathscr{X}_h^n v](\boldsymbol{\theta}, x_1, \ldots, x_{n-1}) = \int_{\mathbb{R}} [\mathscr{A}^n \mathscr{R}^n v](\boldsymbol{\theta}, x_1, \ldots, x_n) \underset{x_1,\ldots,x_{n-1}}{*} h(x_1, \ldots, x_n)\, \mathrm{d}x_n. \tag{5.18}$$

Consider an imaging device for which the zero-defocus plane is located at $x_n = x^f$. Assume that we can modify the optics of that device in such a way that x^f can be continuously adjusted without moving the specimen (this is mathematically equivalent to leaving the zero-defocus plane fixed and moving the center of the specimen along the X_n-axis). Let $f : \mathbb{S}^{n-1} \times \mathbb{R}^n \to \mathbb{R}$ be a function that represents a data set for a particular x^f,

$$f\left(\boldsymbol{\theta}, x_1, \ldots, x_{n-1}, x^f\right) = \int_{\mathbb{R}} [\mathscr{A}^n \mathscr{R}^n v](\boldsymbol{\theta}, x_1, \ldots, x_n) \underset{x_1,\ldots,x_{n-1}}{*} h\left(x_1, \ldots, x_{n-1}, x_n - x^f\right) \mathrm{d}x_n. \tag{5.19}$$

Consider also a function $s : \mathbb{S}^{n-1} \times \mathbb{R}^{n-1} \to \mathbb{R}$ that represents the sum of all data sets collected by moving the zero-defocus plane along the X_n-axis. s is defined as the integral of the function f with respect to x^f,

$$s(\boldsymbol{\theta}, x_1, \ldots, x_{n-1}) = \int_{\mathbb{R}} f\left(\boldsymbol{\theta}, x_1, \ldots, x_{n-1}, x^f\right) \mathrm{d}x^f. \tag{5.20}$$

The values of both, f and s are experimentally obtainable by shifting the zero-defocus plane along the X_n-axis.

Theorem 5.3. *If the distance-dependent attenuated x-ray transform of $v \in \mathbb{R}^n$, $n \in \{2,3\}$, is known*

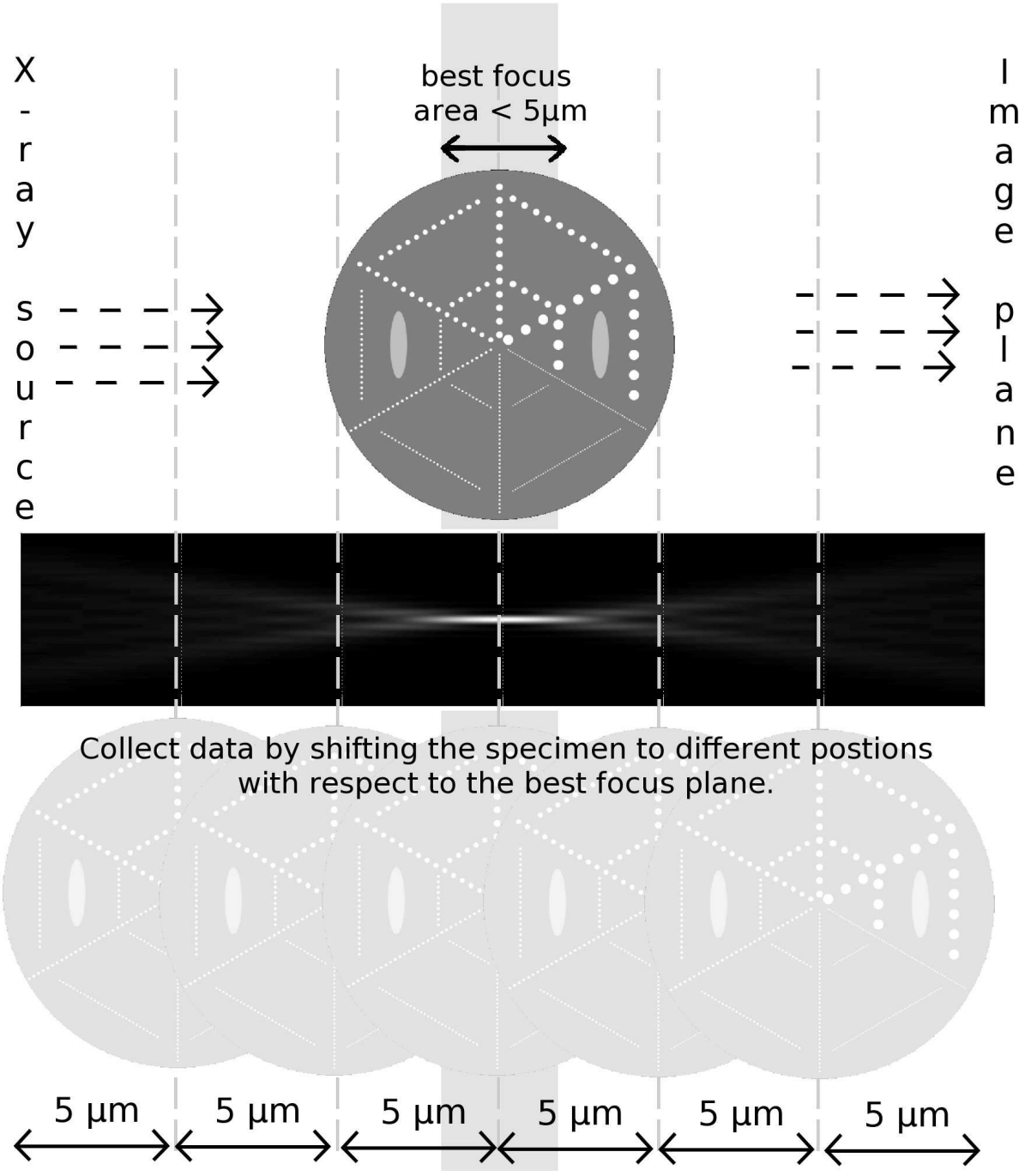

Figure 5.21: TXM data collection by shifting the sample to different positions with respect to the zero-defocus plane leads to more accurate projection data.

for all possible defocus points, then the ideal projection data can be computed as

$$\begin{aligned}
&\left[\mathscr{P}^n v\right](\boldsymbol{\theta}, x_1, \ldots, x_{n-1}) = \\
&= -\ln\left(1 - \frac{(2\pi)^{-n/2}}{p(x_1, \ldots, x_{n-1})}\left[\mathscr{F}^{-1}_{\xi_1,\ldots,\xi_{n-1}} \frac{\left[\mathscr{F}_{x_1,\ldots,x_{n-1}} s\right](\boldsymbol{\theta}, \xi_1, \ldots, \xi_{n-1})}{\left[\mathscr{F}_{x_1,\ldots,x_n} h\right](\xi_1, \ldots, \xi_{n-1}, 0)}\right](\boldsymbol{\theta}, x_1, \ldots, x_{n-1})\right),
\end{aligned} \tag{5.21}$$

where

$$s(\boldsymbol{\theta}, x_1, \ldots, x_{n-1}) = \int_{\mathbb{R}}\int_{\mathbb{R}} \left[\mathscr{A}^n \mathscr{R}^n v\right](\boldsymbol{\theta}, x_1, \ldots, x_n) \underset{x_1,\ldots,x_{n-1}}{*} h\left(x_1, \ldots, x_{n-1}, x_n - x^f\right) \mathrm{d}x_n \mathrm{d}x^f. \tag{5.22}$$

Proof. The Fourier transform of f of Eq. (5.19) with respect to $x_1, \ldots, x_{n-1}$ can be obtained using the convolution theorem of Eq. (2.19) and the linearity of the Fourier transform

$$\begin{aligned}
&\left[\mathscr{F}_{x_1,\ldots,x_{n-1}} f\right]\left(\boldsymbol{\theta}, \xi_1, \ldots, \xi_{n-1}, x^f\right) = \\
&\quad = (2\pi)^{(n-1)/2} \int_{\mathbb{R}} \left[\mathscr{F}_{x_1,\ldots,x_{n-1}} \mathscr{A}^n \mathscr{R}^n v\right](\boldsymbol{\theta}, \xi_1, \ldots, \xi_{n-1}, x_n) \\
&\qquad\qquad \left[\mathscr{F}_{x_1,\ldots,x_{n-1}} h\right]\left(\xi_1, \ldots, \xi_{n-1}, x_n - x^f\right) \mathrm{d}x_n.
\end{aligned} \tag{5.23}$$

Observe that

$$\begin{aligned}
&\left[\mathscr{F}_{x_1,\ldots,x_{n-1}} \mathscr{A}^n \mathscr{R}^n v\right](\boldsymbol{\theta}, \xi_1, \ldots, \xi_{n-1}, x_n) \\
&\quad = \left[\mathscr{F}^{-1}_{\xi_n}\left[\mathscr{F}_{x_1,\ldots,x_n} \mathscr{A}^n \mathscr{R}^n v\right]\right](\boldsymbol{\theta}, \xi_1, \ldots, \xi_{n-1}, x_n) \\
&\quad = (2\pi)^{-1/2} \int_{\mathbb{R}} \left[\mathscr{F}_{x_1,\ldots,x_n} \mathscr{A}^n \mathscr{R}^n v\right](\boldsymbol{\theta}, \xi_1, \ldots, \xi_n) \mathrm{e}^{\mathrm{i}x_n \xi_n} \mathrm{d}\xi_n
\end{aligned} \tag{5.24}$$

and

$$\left[\mathscr{F}_{x_1,\ldots,x_{n-1}} h\right]\left(\xi_1, \ldots, \xi_{n-1}, x_n - x^f\right)$$

$$
\begin{aligned}
&= \left[\mathscr{F}^{-1}_{\xi_n'}\left[\mathscr{F}_{x_1,\ldots,x_n}h\right]\right](\xi_1,\ldots,\xi_{n-1},x_n)\\
&= (2\pi)^{-1/2}\int_{\mathbb{R}}\left[\mathscr{F}_{x_1,\ldots,x_n}h\right]\left(\xi_1,\ldots,\xi_{n-1},\xi_n'\right)\mathrm{e}^{\mathrm{i}\left(x_n-x^f\right)\xi_n'}\mathrm{d}\xi_n'. \qquad (5.25)
\end{aligned}
$$

Substituting Eqs. (5.24) and (5.25) into Eq. (5.23), rearranging the integrals and simplifying using the fact that $\int_{\mathbb{R}}\mathrm{e}^{\mathrm{i}x_n\left(\xi_n+\xi_n'\right)}\mathrm{d}x_n = 2\pi\delta\left(\xi_n+\xi_n'\right)$ (see Eq. (A.7)) and performing the integration with respect to ξ_n', we obtain

$$
\begin{aligned}
&\left[\mathscr{F}_{x_1,\ldots,x_{n-1}}f\right]\left(\boldsymbol{\theta},\xi_1,\ldots,\xi_{n-1},x^f\right) =\\
&\quad= (2\pi)^{(n-1)/2}(2\pi)^{-1}\int_{\mathbb{R}}\int_{\mathbb{R}}\left[\mathscr{F}_{x_1,\ldots,x_n}\mathscr{A}^n\mathscr{R}^nv\right](\boldsymbol{\theta},\xi_1,\ldots,\xi_n)\,\mathrm{e}^{\mathrm{i}x_n\xi_n}\mathrm{d}\xi_n\\
&\qquad\qquad\int_{\mathbb{R}}\left[\mathscr{F}_{x_1,\ldots,x_n}h\right]\left(\xi_1,\ldots,\xi_{n-1},\xi_n'\right)\mathrm{e}^{\mathrm{i}\left(x_n-x^f\right)\xi_n'}\mathrm{d}\xi_n'\mathrm{d}x_n,\\
&\quad= (2\pi)^{(n-1)/2}(2\pi)^{-1}\int_{\mathbb{R}}\int_{\mathbb{R}}\left[\mathscr{F}_{x_1,\ldots,x_n}\mathscr{A}^n\mathscr{R}^nv\right](\boldsymbol{\theta},\xi_1,\ldots,\xi_n)\\
&\qquad\qquad\left[\mathscr{F}_{x_1,\ldots,x_n}h\right]\left(\xi_1,\ldots,\xi_{n-1},\xi_n'\right)\mathrm{e}^{-\mathrm{i}x^f\xi_n'}\int_{\mathbb{R}}\mathrm{e}^{\mathrm{i}x_n\left(\xi_n+\xi_n'\right)}\mathrm{d}x_n\,\mathrm{d}\xi_n'\mathrm{d}\xi_n,\\
&\quad= (2\pi)^{(n-1)/2}\int_{\mathbb{R}}\left[\mathscr{F}_{x_1,\ldots,x_n}\mathscr{A}^n\mathscr{R}^nv\right](\boldsymbol{\theta},\xi_1,\ldots,\xi_n)\\
&\qquad\qquad\int_{\mathbb{R}}\left[\mathscr{F}_{x_1,\ldots,x_n}h\right]\left(\xi_1,\ldots,\xi_{n-1},\xi_n'\right)\mathrm{e}^{-\mathrm{i}x^f\xi_n'}\,\delta\left(\xi_n+\xi_n'\right)\mathrm{d}\xi_n'\mathrm{d}\xi_n,\\
&\quad= (2\pi)^{(n-1)/2}\int_{\mathbb{R}}\left[\mathscr{F}_{x_1,\ldots,x_n}\mathscr{A}^n\mathscr{R}^nv\right](\boldsymbol{\theta},\xi_1,\ldots,\xi_n)\left[\mathscr{F}_{x_1,\ldots,x_n}h\right](\xi_1,\ldots,\xi_{n-1},-\xi_n)\,\mathrm{e}^{\mathrm{i}x^f\xi_n}\mathrm{d}\xi_n.
\end{aligned}
\qquad (5.26)
$$

The Fourier transform with respect to $x_1,\ldots,x_{n-1}$ of s of Eq. (5.20) can be computed by using the linearity of the Fourier transform operator $\mathscr{F}$, the expression for the Fourier transform of f of Eq. (5.26), rearranging the integrals and simplifying using the fact that $\int_{\mathbb{R}}\mathrm{e}^{\mathrm{i}x^f\xi_n}\mathrm{d}x^f = 2\pi\delta(\xi_n)$, see Eq. (A.7), and performing the integration with respect to ξ_n, as follows

$$
\left[\mathscr{F}_{x_1,\ldots,x_{n-1}}s\right](\boldsymbol{\theta},\xi_1,\ldots,\xi_{n-1}) =
$$

$$
\begin{aligned}
&= \int_{\mathbb{R}} \left[\mathscr{F}_{x_1,\ldots,x_{n-1}} f\right]\left(\boldsymbol{\theta}, \xi_1, \ldots, \xi_{n-1}, x^f\right) \mathrm{d}x^f \\
&= (2\pi)^{(n-1)/2} \int_{\mathbb{R}} \int_{\mathbb{R}} \left[\mathscr{F}_{x_1,\ldots,x_n} \mathscr{A}^n \mathscr{R}^n v\right](\boldsymbol{\theta}, \xi_1, \ldots, \xi_n) \\
&\qquad\qquad \left[\mathscr{F}_{x_1,\ldots,x_n} h\right](\xi_1, \ldots, \xi_{n-1}, -\xi_n)\, \mathrm{e}^{\mathrm{i}x^f \xi_n} \mathrm{d}\xi_n \mathrm{d}x^f \\
&= (2\pi)^{(n-1)/2} (2\pi) \int_{\mathbb{R}} \left[\mathscr{F}_{x_1,\ldots,x_n} \mathscr{A}^n \mathscr{R}^n v\right](\boldsymbol{\theta}, \xi_1, \ldots, \xi_n) \\
&\qquad\qquad \left[\mathscr{F}_{x_1,\ldots,x_n} h\right](\xi_1, \ldots, \xi_{n-1}, -\xi_n)\, \delta(\xi_n)\, \mathrm{d}\xi_n \\
&= (2\pi)^{(n+1)/2} \left[\mathscr{F}_{x_1,\ldots,x_n} \mathscr{A}^n \mathscr{R}^n v\right](\boldsymbol{\theta}, \xi_1, \ldots, \xi_{n-1}, 0) \left[\mathscr{F}_{x_1,\ldots,x_n} h\right](\xi_1, \ldots, \xi_{n-1}, 0). \qquad (5.27)
\end{aligned}
$$

The significance of Eq. (5.27) is that the Fourier transform of s, and hence the function s itself, does not depend on the varying blurring function h, but rather on the values of $\mathscr{F}_{x_1,\ldots,x_n} h$ at $\xi_n = 0$ plane only. (This fact was discovered by Dr. Oton while the author of this thesis visited the National Center for Biotechnology of Madrid University in January of 2013.) In the remainder of this proof we show that this allows us to compute $\mathscr{P} v$.

Using Eq. (5.27) we can compute the value of $\mathscr{F}_{x_1,\ldots,x_n} \mathscr{A}^n \mathscr{R}^n v$ at $\xi_n = 0$ by

$$
\left[\mathscr{F}_{x_1,\ldots,x_n} \mathscr{A}^n \mathscr{R}^n v\right](\boldsymbol{\theta}, \xi_1, \ldots, \xi_{n-1}, 0) = \frac{\left[\mathscr{F}_{x_1,\ldots,x_{n-1}} s\right](\boldsymbol{\theta}, \xi_1, \ldots, \xi_{n-1})}{(2\pi)^{(n+1)/2} \left[\mathscr{F}_{x_1,\ldots,x_n} h\right](\xi_1, \ldots, \xi_{n-1}, 0)}. \qquad (5.28)
$$

Note that in practice, depending on the actual values of h this may require regularization.

Another way of deriving the expression for $\left[\mathscr{F}_{x_1,\ldots,x_n} \mathscr{A}^n \mathscr{R}^n v\right](\boldsymbol{\theta}, \xi_1, \ldots, \xi_{n-1}, 0)$ is to take the Fourier transform with respect to $\boldsymbol{x}$ of the function $\mathscr{A}^n \mathscr{R}^n v$ and then evaluate its result at $\xi_n = 0$. Doing this, we obtain

$$
\left[\mathscr{F}_{x_1,\ldots,x_n} \mathscr{A}^n \mathscr{R}^n v\right](\boldsymbol{\theta}, \boldsymbol{\xi}) = (2\pi)^{-n/2} \int_{\mathbb{R}^n} \mathscr{A}^n \mathscr{R}^n v(\boldsymbol{\theta}, \boldsymbol{x})\, \mathrm{e}^{-\mathrm{i}\boldsymbol{x}\boldsymbol{\xi}} \mathrm{d}\boldsymbol{x}, \qquad (5.29)
$$

and

$$
\left[\mathscr{F}_{x_1,\ldots,x_n} \mathscr{A}^n \mathscr{R}^n v\right](\boldsymbol{\theta}, \xi_1, \ldots, \xi_{n-1}, 0)
$$

$$= (2\pi)^{-n/2} \int_{\mathbb{R}^n} \left[\mathscr{A}^n \mathscr{R}^n v\right](\boldsymbol{\theta}, x_1, \ldots, x_n)\, \mathrm{e}^{-\mathrm{i}(x_1\xi_1 + \ldots + x_{n-1}\xi_{n-1})} \mathrm{d}x_1 \ldots \mathrm{d}x_n. \tag{5.30}$$

We then simplify further using the definition of the operator $\mathscr{A}^n$, and the fact that, by the Fundamental Theorem of Calculus, $\int_{\mathbb{R}} \left[\mathscr{R}^n v\right](\boldsymbol{\theta}, x_1, \ldots, x_n) \exp\left(-\int_{-\infty}^{x_n} \left[\mathscr{R}^n v\right](\boldsymbol{\theta}, x_1, \ldots, x_{n-1}, t)\, \mathrm{d}t\right) \mathrm{d}x_n = 1 - \exp\left(-\int_{\mathbb{R}} \left[\mathscr{R}^n v\right](\boldsymbol{\theta}, x_1, \ldots, x_{n-1}, x_n)\, \mathrm{d}x_n\right)$, to obtain

$$\begin{aligned}
&\left[\mathscr{F}_{x_1,\ldots,x_n} \mathscr{A}^n \mathscr{R}^n v\right](\boldsymbol{\theta}, \xi_1, \ldots, \xi_{n-1}, 0) = \\
&\quad = (2\pi)^{-n/2} \int_{\mathbb{R}^n} \left[\mathscr{A}^n \mathscr{R}^n v\right](\boldsymbol{\theta}, x_1, \ldots, x_n)\, \mathrm{e}^{-\mathrm{i}(x_1\xi_1 + \ldots + x_{n-1}\xi_{n-1})} \mathrm{d}x_1 \ldots \mathrm{d}x_n \\
&\quad = (2\pi)^{-n/2} \int_{\mathbb{R}^n} p(x_1, \ldots, x_{n-1}) \left[\mathscr{R}^n v\right](\boldsymbol{\theta}, x_1, \ldots, x_n) \exp\left(-\int_{-\infty}^{x_n} \left[\mathscr{R}^n v\right](\boldsymbol{\theta}, x_1, \ldots, x_{n-1}, t)\, \mathrm{d}t\right) \\
&\qquad\qquad \mathrm{e}^{-\mathrm{i}(x_1\xi_1 + \ldots + x_{n-1}\xi_{n-1})} \mathrm{d}x_1 \ldots \mathrm{d}x_n \\
&\quad = (2\pi)^{-n/2} \int_{\mathbb{R}^{n-1}} \int_{\mathbb{R}} \left[\mathscr{R}^n v\right](\boldsymbol{\theta}, x_1, \ldots, x_n) \exp\left(-\int_{-\infty}^{x_n} \left[\mathscr{R}^n v\right](\boldsymbol{\theta}, x_1, \ldots, x_{n-1}, t)\, \mathrm{d}t\right) \mathrm{d}x_n \\
&\qquad\qquad p(x_1, \ldots, x_{n-1})\, \mathrm{e}^{-\mathrm{i}(x_1\xi_1 + \ldots + x_{n-1}\xi_{n-1})} \mathrm{d}x_1 \ldots \mathrm{d}x_{n-1} \\
&\quad = (2\pi)^{-n/2} \int_{\mathbb{R}^{n-1}} \left(1 - \exp\left(-\int_{\mathbb{R}} \left[\mathscr{R}^n v\right](\boldsymbol{\theta}, x_1, \ldots, x_{n-1}, x_n)\, \mathrm{d}x_n\right)\right) \\
&\qquad\qquad p(x_1, \ldots, x_{n-1})\, \mathrm{e}^{-\mathrm{i}(x_1\xi_1 + \ldots + x_{n-1}\xi_{n-1})} \mathrm{d}x_1 \ldots \mathrm{d}x_{n-1}.
\end{aligned} \tag{5.31}$$

Finally, we take the inverse Fourier transform with respect to $\xi_1, \ldots, \xi_{n-1}$ of $\mathscr{F}_{x_1,\ldots,x_n} \mathscr{A}^n \mathscr{R}^n v$ evaluated at $\xi_n = 0$, by applying the inverse Fourier transform operator $\mathscr{F}^{-1}_{\xi_1,\ldots,\xi_{n-1}}$, rearranging the order of integration, using the fact that
$\int_{\mathbb{R}^{n-1}} \mathrm{e}^{\mathrm{i}\left(\left(x_1' - x_1\right)\xi_1 + \ldots + \left(x_{n-1}' - x_{n-1}\right)\xi_{n-1}\right)} \mathrm{d}\xi_1 \ldots \mathrm{d}\xi_{n-1} = (2\pi)^{(n-1)}\, \delta\left(x_1' - x_1\right) \ldots \delta\left(x_{n-1}' - x_{n-1}\right)$,
from Eq. (A.10), and performing the integration with respect to $x_1, \ldots, x_{n-1}$ as follows

$$\left[\mathscr{F}^{-1}_{\xi_1,\ldots,\xi_{n-1}} \left[\mathscr{F}_{x_1,\ldots,x_n} \mathscr{A}^n \mathscr{R}^n v\right]\right]\left(\boldsymbol{\theta}, x_1', \ldots, x_{n-1}'\right) =$$

$$
\begin{aligned}
&= (2\pi)^{-n/2} (2\pi)^{-(n-1)/2} \int\limits_{\mathbb{R}^{n-1}} \int\limits_{\mathbb{R}^{n-1}} \left(1 - \exp\left(- \int\limits_{\mathbb{R}} \left[\mathscr{R}^n v \right] (\boldsymbol{\theta}, x_1, \ldots, x_{n-1}, x_n) \, \mathrm{d}x_n \right) \right) \\
&\qquad p(x_1, \ldots, x_{n-1}) \, \mathrm{e}^{-\mathrm{i}(x_1 \xi_1 + \ldots + x_{n-1} \xi_{n-1})} \mathrm{e}^{\mathrm{i}\left(\mathrm{x}_1' \xi_1 + \ldots + \mathrm{x}_{\mathrm{n}-1}' \xi_{\mathrm{n}-1} \right)} \mathrm{d}x_1 \ldots \mathrm{d}x_{n-1} \mathrm{d}\xi_1 \ldots \mathrm{d}\xi_{n-1} \\
&= (2\pi)^{-(2n-1)/2} \int\limits_{\mathbb{R}^{n-1}} \left(1 - \exp\left(- \int\limits_{\mathbb{R}} \left[\mathscr{R}^n v \right] (\boldsymbol{\theta}, x_1, \ldots, x_{n-1}, x_n) \, \mathrm{d}x_n \right) \right) p(x_1, \ldots, x_{n-1}) \\
&\qquad \int\limits_{\mathbb{R}^{n-1}} \mathrm{e}^{\mathrm{i}\left((x_1' - x_1) \xi_1 + \ldots + \left(x_{n-1}' - x_{n-1} \right) \xi_{n-1} \right)} \mathrm{d}\xi_1 \ldots \mathrm{d}\xi_{n-1} \; \mathrm{d}x_1 \ldots \mathrm{d}x_{n-1} \\
&= (2\pi)^{-1/2} \int\limits_{\mathbb{R}^{n-1}} \left(1 - \exp\left(- \int\limits_{\mathbb{R}} \left[\mathscr{R}^n v \right] (\boldsymbol{\theta}, x_1, \ldots, x_{n-1}, x_n) \, \mathrm{d}x_n \right) \right) p(x_1, \ldots, x_{n-1}) \\
&\qquad \delta\left(x_1' - x_1 \right) \ldots \delta\left(x_{n-1}' - x_{n-1} \right) \mathrm{d}x_1 \ldots \mathrm{d}x_{n-1} \\
&= (2\pi)^{-1/2} \left(1 - \exp\left(- \int\limits_{\mathbb{R}} \left[\mathscr{R}^n v \right] \left(\boldsymbol{\theta}, x_1', \ldots, x_{n-1}', x_n \right) \mathrm{d}x_n \right) \right) p\left(x_1', \ldots, x_{n-1}' \right). \qquad (5.32)
\end{aligned}
$$

By rearranging the terms in the last equality of the above derivation we get that

$$
\begin{aligned}
&\exp\left(- \int\limits_{\mathbb{R}} \left[\mathscr{R}^n v \right] (\boldsymbol{\theta}, x_1, \ldots, x_{n-1}, x_n) \, \mathrm{d}x_n \right) = \\
&\qquad = 1 - \frac{(2\pi)^{1/2} \left[\mathscr{F}^{-1}_{\xi_1, \ldots, \xi_{n-1}} \left[\mathscr{F}_{x_1, \ldots, x_n} \mathscr{A}^n \mathscr{R}^n v \right] \right] (\boldsymbol{\theta}, x_1, \ldots, x_{n-1})}{p(x_1, \ldots, x_{n-1})}. \qquad (5.33)
\end{aligned}
$$

Taking logarithms of both sides we get

$$
\begin{aligned}
&\int\limits_{\mathbb{R}} \left[\mathscr{R}^n v \right] (\boldsymbol{\theta}, x_1, \ldots, x_{n-1}, x_n) \, \mathrm{d}x_n = \\
&\qquad = -\ln\left(1 - \frac{(2\pi)^{1/2} \left[\mathscr{F}^{-1}_{\xi_1, \ldots, \xi_{n-1}} \left[\mathscr{F}_{x_1, \ldots, x_n} \mathscr{A}^n \mathscr{R}^n v \right] \right] (\boldsymbol{\theta}, x_1, \ldots, x_{n-1})}{p(x_1, \ldots, x_{n-1})} \right). \\
&\qquad (5.34)
\end{aligned}
$$

The left hand side is, by definition, $\mathscr{P}^n v$. Substituting Eq. (5.28) we get Eq. 5.21 , which concludes the proof of Theorem 5.3. □

Algorithm 5.2 outlines the steps required for computation of approximations to ideal projection data in a simulation or an experimental setup.

Algorithm 5.2 TXM reconstruction from data collected for multiple defocus values.

1: **for** each $\boldsymbol{\theta} \in \mathbb{S}^n$ **do**
2: Collect data of a sample represented by a function v for multiple values of x^f (the selection of values for x^f should ensure that all parts of the specimen are placed in the best focus area for some of the collected images).
3: Combine the projections obtained in Step 2 by computing the approximation to the integral $s(\boldsymbol{\theta}, x_1, \ldots, x_{n-1}) = \int_{\mathbb{R}} \int_{\mathbb{R}} \left[\mathscr{A}^n \mathscr{R}^n v\right](\boldsymbol{\theta}, x_1, \ldots, x_n) \underset{x_1,\ldots,x_{n-1}}{*} h\left(x_1, \ldots, x_{n-1}, x_n - x_n^f\right) \mathrm{d}x_n \mathrm{d}x^f$.
4: Using the data computed in Step 3, produce approximations to the ideal projection data $\left[\mathscr{P}^n v\right](\boldsymbol{\theta}, x_1, \ldots, x_{n-1}) =$
$$-\ln\left(1 - \frac{(2\pi)^{-n/2}}{p(x_1, \ldots, x_{n-1})} \left[\mathscr{F}^{-1}_{\xi_1,\ldots,\xi_{n-1}} \frac{\left[\mathscr{F}_{x_1,\ldots,x_{n-1}} s\right](\boldsymbol{\theta}, \xi_1, \ldots, \xi_{n-1})}{\left[\mathscr{F}_{x_1,\ldots,x_n} h\right](\xi_1, \ldots, \xi_{n-1}, 0)}\right](\boldsymbol{\theta}, x_1, \ldots, x_{n-1})\right)$$
5: **end for**
6: Compute the reconstruction using one of many reconstruction algorithms available for ideal projections.

For completeness, we include a version of Theorem 5.3 for obtaining tomographic ideal projection data $\mathscr{P}^{3t} v$ from the soft x-ray microscopy data for all defocus values.

Theorem 5.4. *If the tomographic distance-dependent attenuated x-ray transform of $v \in \mathbb{R}^3$ is known for all possible defocus points, then the ideal projection data can be computed as*

$$\begin{aligned}
&\left[\mathscr{P}^{3t} v\right](\theta_1, x_1, \ldots, x_{n-1}) = \\
&= -\ln\left(1 - \frac{(2\pi)^{-n/2}}{p(x_1, \ldots, x_{n-1})} \left[\mathscr{F}^{-1}_{\xi_1,\ldots,\xi_{n-1}} \frac{\left[\mathscr{F}_{x_1,\ldots,x_{n-1}} s\right](\theta_1, \xi_1, \ldots, \xi_{n-1})}{\left[\mathscr{F}_{x_1,\ldots,x_n} h\right](\xi_1, \ldots, \xi_{n-1}, 0)}\right](\theta_1, x_1, \ldots, x_{n-1})\right),
\end{aligned} \tag{5.35}$$

where

$$s(\theta_1, x_1, \ldots, x_{n-1}) = \int_{\mathbb{R}} \int_{\mathbb{R}} \left[\mathscr{A}^{3t} \mathscr{R}^{3t} v\right](\theta_1, x_1, \ldots, x_n) \underset{x_1,\ldots,x_{n-1}}{*} h\left(x_1, \ldots, x_{n-1}, x_n - x^f\right) \mathrm{d}x_n \mathrm{d}x^f. \tag{5.36}$$

Proof. The proof is identical to the proof of Theorem 5.3. □

5.5.2 Numerical Examples

Theorem 5.3 guarantees that if projection values for all (infinitely many) defocus points are known, then the ideal projections can be recovered. In practice, one cannot obtain projections for all defocus points. An even more important problem is the information loss due to convolution with the blurring function in the image formation model. In the case of the blurring function of Eq. (3.9) that we use for TXM simulations, all frequencies above a certain value (depending on the parameters of the blurring function) are zeroed and cannot be recovered by any correction method.

In this section we provide an illustration of how well the method discussed in the previous section recovers ideal projections when only a finite subset of defocus points is used and the blurring function removes information about all high frequencies.

The implementation details are exactly the same as the ones discussed in Subsection 5.4.5.

5.5.2.1 Correction of Individual Projections

The blurring function that we used in modeling the image formation removes high frequencies in the data. Even though the most desirable correction would be one that arrives at the ideal projection data (one that could be obtained if the microscope collected data according to the projection operator $\mathscr{P}^n$), it is not possible to recover the frequencies that have been set to zero in all data sets. Figure 5.22 compares the true ideal projection of the phantom in Figure 5.1 with the same projections for which the frequencies that are zeroed by the TXM PSF have been removed. Even though in the rest of this section we compare our corrected projections to the ideal projection data, the best possible correction cannot attain a better result than the green plot shown in Figure 5.22.

In earlier sections of this chapter we demonstrated the replication artifact that occurs when both attenuation and distance-dependent blurring are present in the image formation model. We used the phantom from Figure 5.1 to generate several finite sets of projections from the same direction by shifting the zero-defocus plane with respect to the phantom. We repeated the correction by shifting the zero-defocus plane with respect to the center of the specimen in nine different intervals: $(-5\mu\text{m}, 5\mu\text{m})$, $(-10\mu\text{m}, 10\mu\text{m})$, $(-15\mu\text{m}, 15\mu\text{m})$, $(-20\mu\text{m}, 20\mu\text{m})$, $(-25\mu\text{m}, 25\mu\text{m})$,

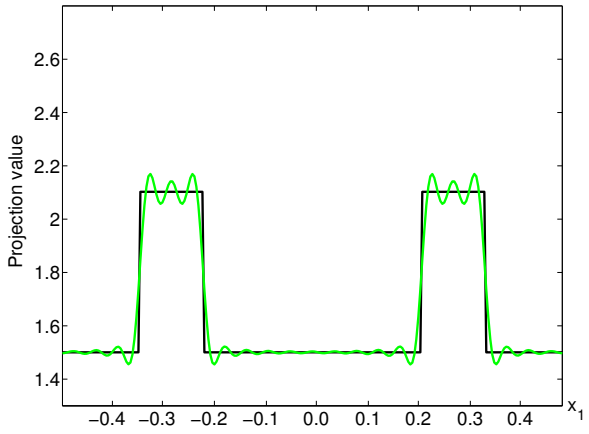

Figure 5.22: The ideal microscope projection, $\mathscr{P}^2 v$ (solid black line) compared to the ideal microscope projection for which the frequencies that are zeroed by the TXM PSF have been removed (solid green line).

$(-30\mu\text{m}, 30\mu\text{m})$, $(-35\mu\text{m}, 35\mu\text{m})$, $(-40\mu\text{m}, 40\mu\text{m})$, $(-45\mu\text{m}, 45\mu\text{m})$, and for each of them the zero-defocus plane was shifted by four different distances : $5\,\mu$m, $1\,\mu$m, $0.5\,\mu$m and $0.004\,\mu$m. Figures 5.23-5.26 (one for each of the four different distances) show the projections obtained by combining the data for $\theta_1 = \pi$ for the nine intervals discussed above (solid red plot). For comparison we included the ideal projection, $\mathscr{P}^2 v$, (solid black plot), and the attenuated distance-dependently blurred projection after the attenuation correction, $-\ln\left(1 - \mathscr{X}_h^2 v\right)$, obtained when the center of the specimen coincides with the zero-defocus plane (dashed light blue plot). These figures show that the projections computed using data from multiple defocus points improve (in the sense of looking closer to the plots of ideal projections) as the interval over which the sample is shifted increases. Another source of improvement is the increase in the number of points at which data are collected within each interval. This change can be observed by comparing the subfigures of Figures 5.23-5.26 with the same labels. The improvement due to increasing the interval size seems to be more significant than the improvement due to increasing the number of points at which data are collected in a fixed interval.

For completeness, the corresponding graphs for data collected at $\theta_1 = 0$ are shown in Appendix C.

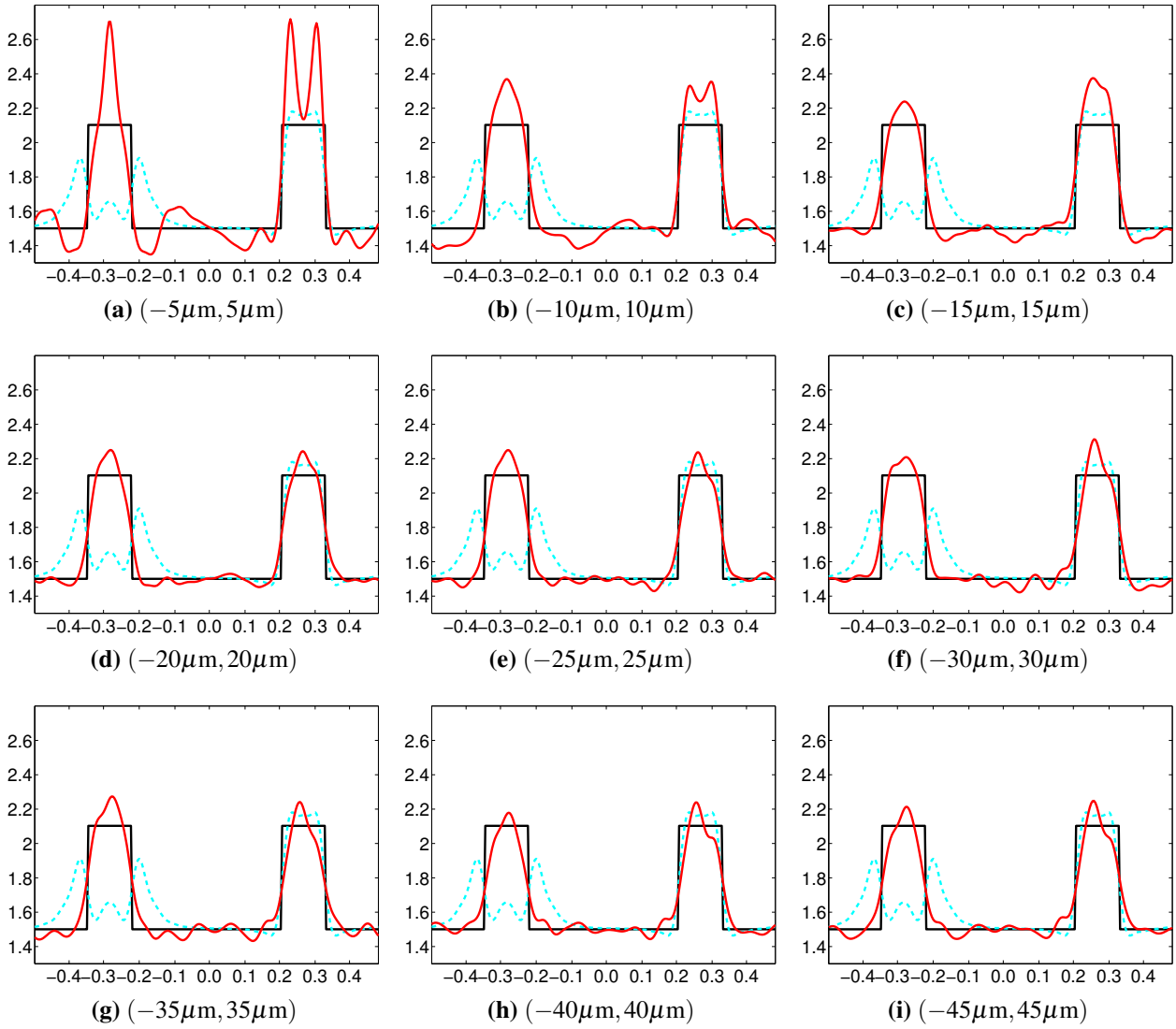

(a) $(-5\mu\text{m}, 5\mu\text{m})$ **(b)** $(-10\mu\text{m}, 10\mu\text{m})$ **(c)** $(-15\mu\text{m}, 15\mu\text{m})$

(d) $(-20\mu\text{m}, 20\mu\text{m})$ **(e)** $(-25\mu\text{m}, 25\mu\text{m})$ **(f)** $(-30\mu\text{m}, 30\mu\text{m})$

(g) $(-35\mu\text{m}, 35\mu\text{m})$ **(h)** $(-40\mu\text{m}, 40\mu\text{m})$ **(i)** $(-45\mu\text{m}, 45\mu\text{m})$

Figure 5.23: Three different types of projections of the phantom in Figure 5.1 for the angle $\theta_1 = \pi$: the ideal microscope projection, $\mathscr{P}^2 v$ (solid black lines); attenuated distance-dependently blurred projections corrected for attenuation, $-\ln\left(1 - \mathscr{X}_h^2 v\right)$ (dashed light blue); projections obtained by combining data collected by shifting the zero-defocus plane along X_2-axis in the interval indicated in the subfigures using $5\,\mu$m increments resulting in increasing number of data sets from intervals increasing in size (red). The numbers of combined data sets are: (a) 3, (b) 5, (c) 7, (d) 9, (e) 11, (f) 13, (g) 15, (h) 17, (i) 19.

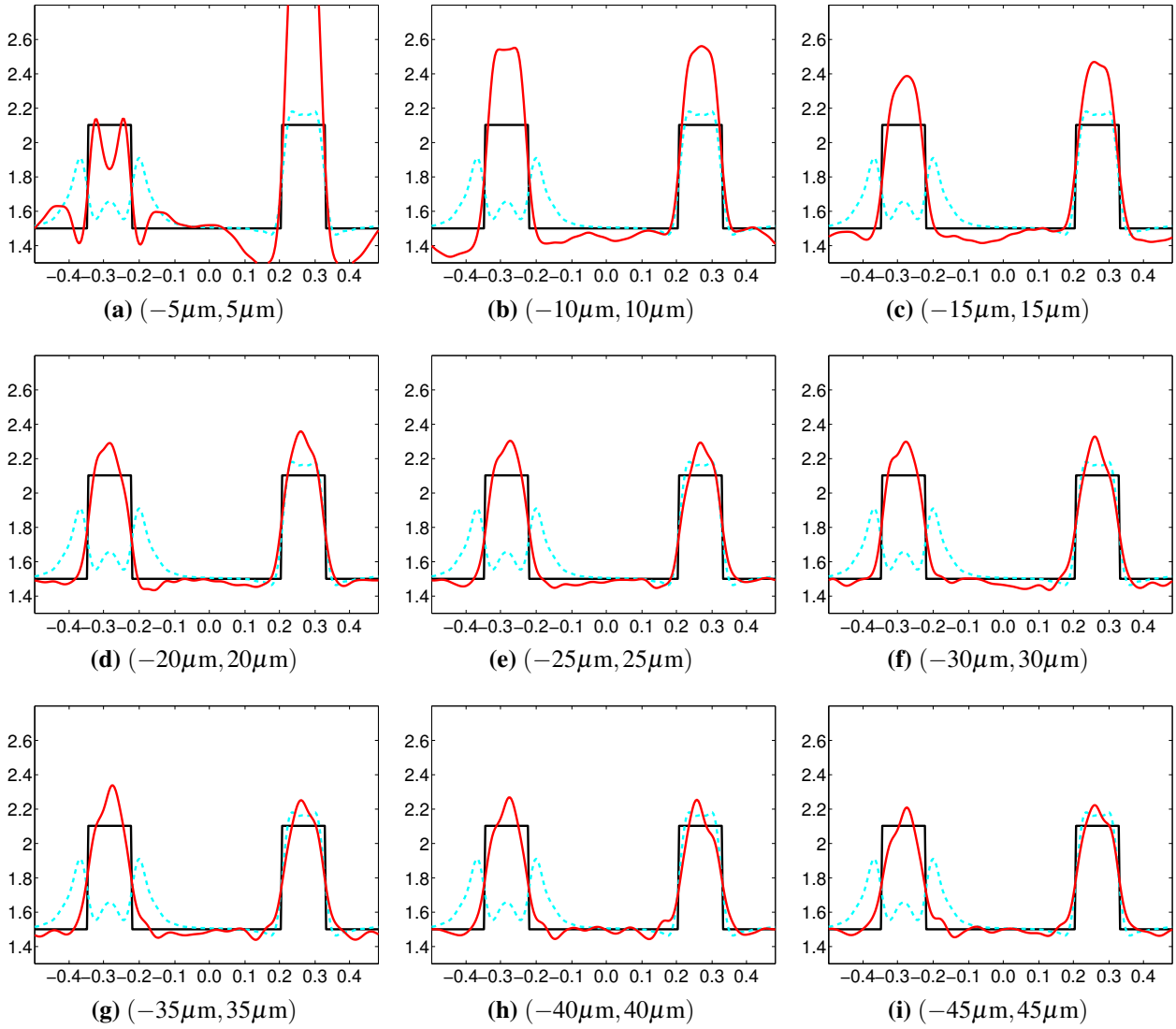

(a) $(-5\mu\text{m}, 5\mu\text{m})$ **(b)** $(-10\mu\text{m}, 10\mu\text{m})$ **(c)** $(-15\mu\text{m}, 15\mu\text{m})$

(d) $(-20\mu\text{m}, 20\mu\text{m})$ **(e)** $(-25\mu\text{m}, 25\mu\text{m})$ **(f)** $(-30\mu\text{m}, 30\mu\text{m})$

(g) $(-35\mu\text{m}, 35\mu\text{m})$ **(h)** $(-40\mu\text{m}, 40\mu\text{m})$ **(i)** $(-45\mu\text{m}, 45\mu\text{m})$

Figure 5.24: Three different types of projections of the phantom in Figure 5.1 for the angle $\theta_1 = \pi$: the ideal microscope projection, $\mathscr{P}^2 v$ (solid black lines); attenuated distance-dependently blurred projections corrected for attenuation, $-\ln\left(1 - \mathscr{X}_h^2 v\right)$ (dashed light blue); projections obtained by combining data collected by shifting the zero-defocus plane along X_2-axis in the interval indicated in the subfigures using $1\,\mu$m increments resulting in increasing number of data sets from intervals increasing in size (red). The numbers of combined data sets are: (a) 11, (b) 21, (c) 31, (d) 41, (e) 51, (f) 61, (g) 71, (h) 81, (i) 91.

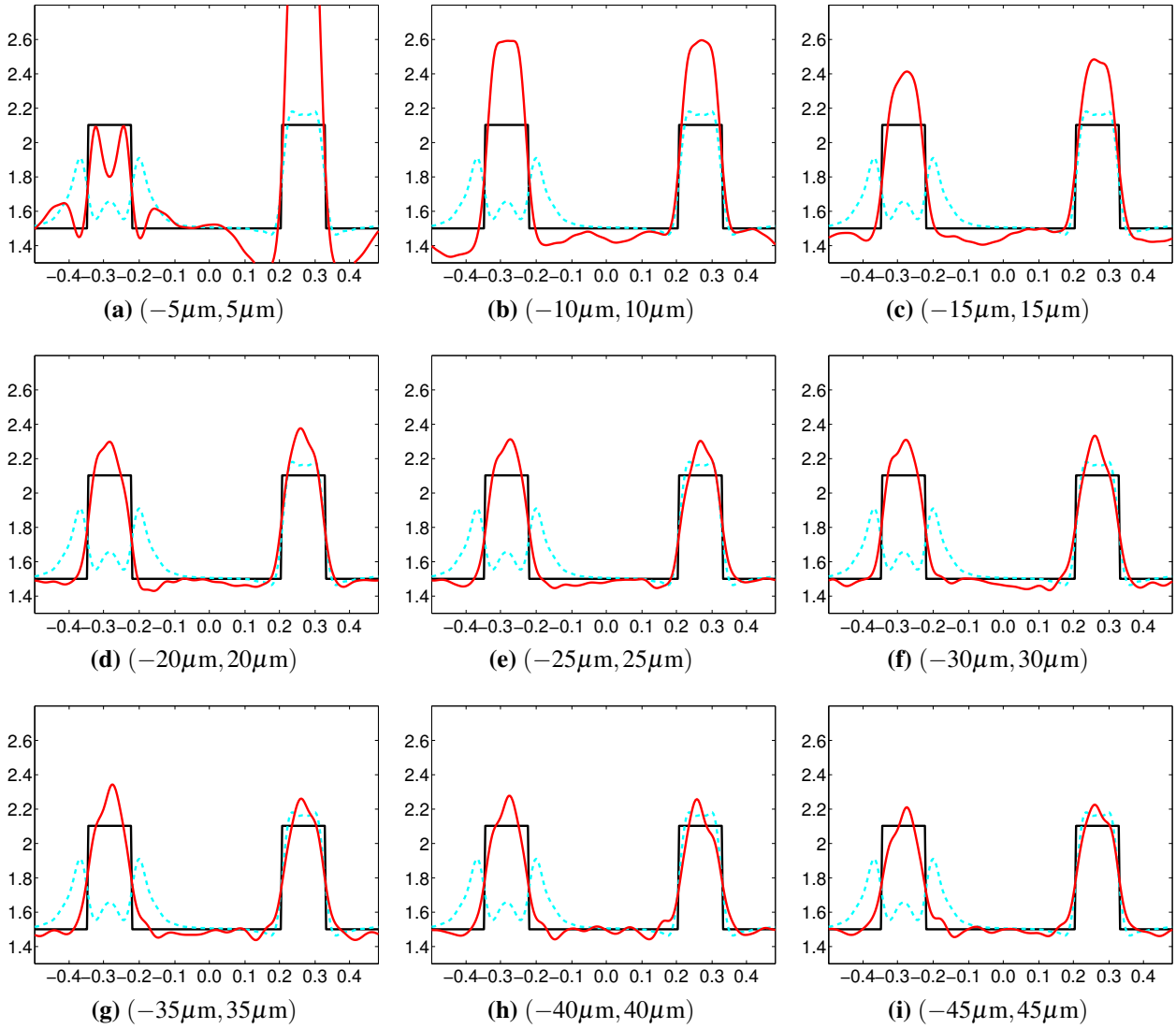

(a) $(-5\mu\text{m}, 5\mu\text{m})$ **(b)** $(-10\mu\text{m}, 10\mu\text{m})$ **(c)** $(-15\mu\text{m}, 15\mu\text{m})$

(d) $(-20\mu\text{m}, 20\mu\text{m})$ **(e)** $(-25\mu\text{m}, 25\mu\text{m})$ **(f)** $(-30\mu\text{m}, 30\mu\text{m})$

(g) $(-35\mu\text{m}, 35\mu\text{m})$ **(h)** $(-40\mu\text{m}, 40\mu\text{m})$ **(i)** $(-45\mu\text{m}, 45\mu\text{m})$

Figure 5.25: Three different types of projections of the phantom in Figure 5.1 for the angle $\theta_1 = \pi$: the ideal microscope projection, $\mathscr{P}^2 v$ (solid black lines); attenuated distance-dependently blurred projections corrected for attenuation, $-\ln\left(1 - \mathscr{X}_h^2 v\right)$ (dashed light blue); projections obtained by combining data collected by shifting the zero-defocus plane along X_2-axis in the interval indicated in the subfigures using $0.5\,\mu$m increments resulting in increasing number of data sets from intervals increasing in size (red). The numbers of combined data sets are: (a) 21, (b) 41, (c) 61, (d) 81, (e) 101, (f) 121, (g) 141, (h) 8161, (i) 181.

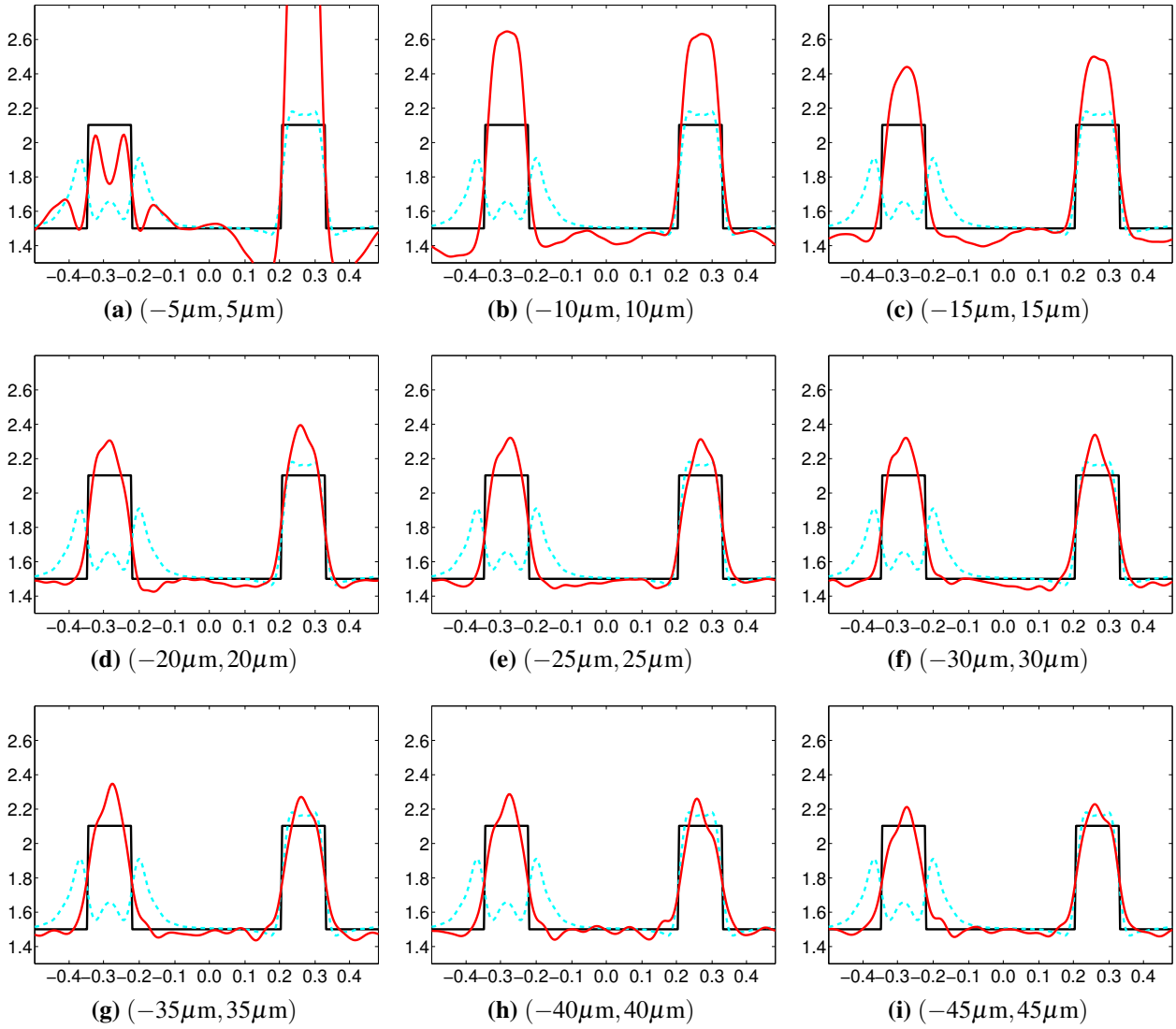

(a) $(-5\mu\text{m}, 5\mu\text{m})$ **(b)** $(-10\mu\text{m}, 10\mu\text{m})$ **(c)** $(-15\mu\text{m}, 15\mu\text{m})$

(d) $(-20\mu\text{m}, 20\mu\text{m})$ **(e)** $(-25\mu\text{m}, 25\mu\text{m})$ **(f)** $(-30\mu\text{m}, 30\mu\text{m})$

(g) $(-35\mu\text{m}, 35\mu\text{m})$ **(h)** $(-40\mu\text{m}, 40\mu\text{m})$ **(i)** $(-45\mu\text{m}, 45\mu\text{m})$

Figure 5.26: Three different types of projections of the phantom in Figure 5.1 for the angle $\theta_1 = \pi$: the ideal microscope projection, $\mathscr{P}^2 v$ (solid black lines); attenuated distance-dependently blurred projections corrected for attenuation, $-\ln\left(1 - \mathscr{X}_h^2 v\right)$ (dashed light blue); projections obtained by combining data collected by shifting the zero-defocus plane along X_2-axis in the interval indicated in the subfigures using $0.004\,\mu$m increments resulting in increasing number of data sets from intervals increasing in size (red). The numbers of combined data sets are: (a) 2501, (b) 5001, (c) 7501, (d) 10001, (e) 12501, (f) 15001, (g) 17501, (h) 20001, (i) 22501.

5.5.2.2 Reconstructing from Corrected Projections of the Large Phantom

We computed and combined the data at multiple positions for the large phantom in Figure 5.13. Recall that none of the attempts at correction and reconstruction discussed in Section 5.4 produced satisfactory results for this phantom.

The reconstruction shown in Figures 5.27 and 5.28 were computed from data that were created by combining a total of 41 projection data sets obtained by shifting the center of the phantom along the X_2-axis from $-20\,\mu$m to $20\,\mu$m using $0.5\,\mu$m shifts. The range of reconstructed values of linear attenuation coefficients is from -0.0347398 to 0.3896942. Figure 5.27 shows the reconstruction in full grayscale display and Figure 5.28 shows the same reconstruction in narrow grayscale display. The replication artifacts that were not handled by any of the techniques discussed in Section 5.4 are completely removed and even the disks closest to the outside edge of the phantom are reconstructed correctly. The loss of high frequencies due to TXM PSF results in other artifacts visible in the background, but they do not reduce the visibility of the phantom's features as badly as it was the case for approaches that used only a single data set collected with the phantom centered at the zero-defocus plane.

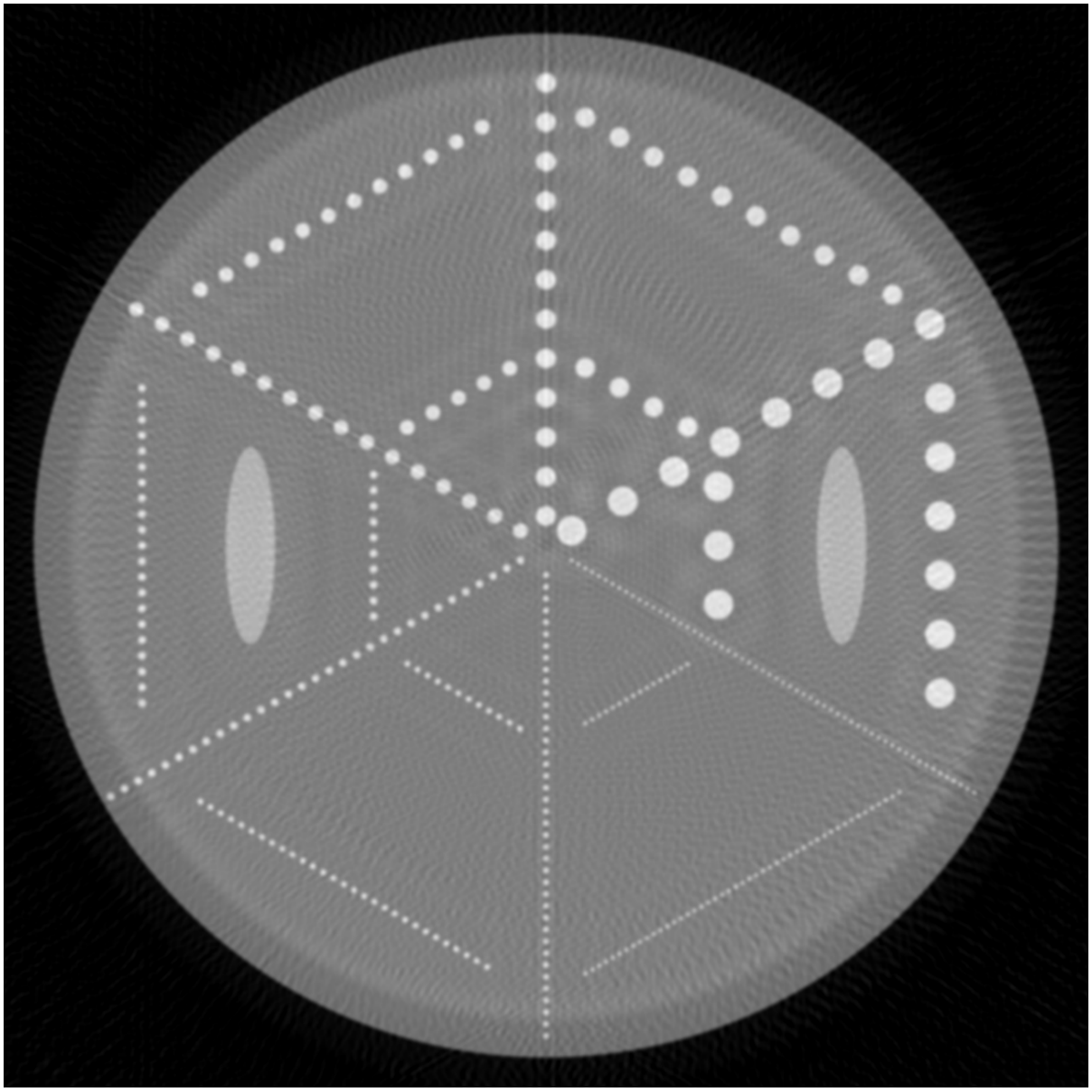

Figure 5.27: Reconstruction computed based on projection data sets of the phantom in Figure 5.13 collected by shifting the phantom along the X_2-axis using $0.5\,\mu$m increments in the interval $-20\,\mu$m to $20\,\mu$m. Reconstruction shown in full grayscale display window.

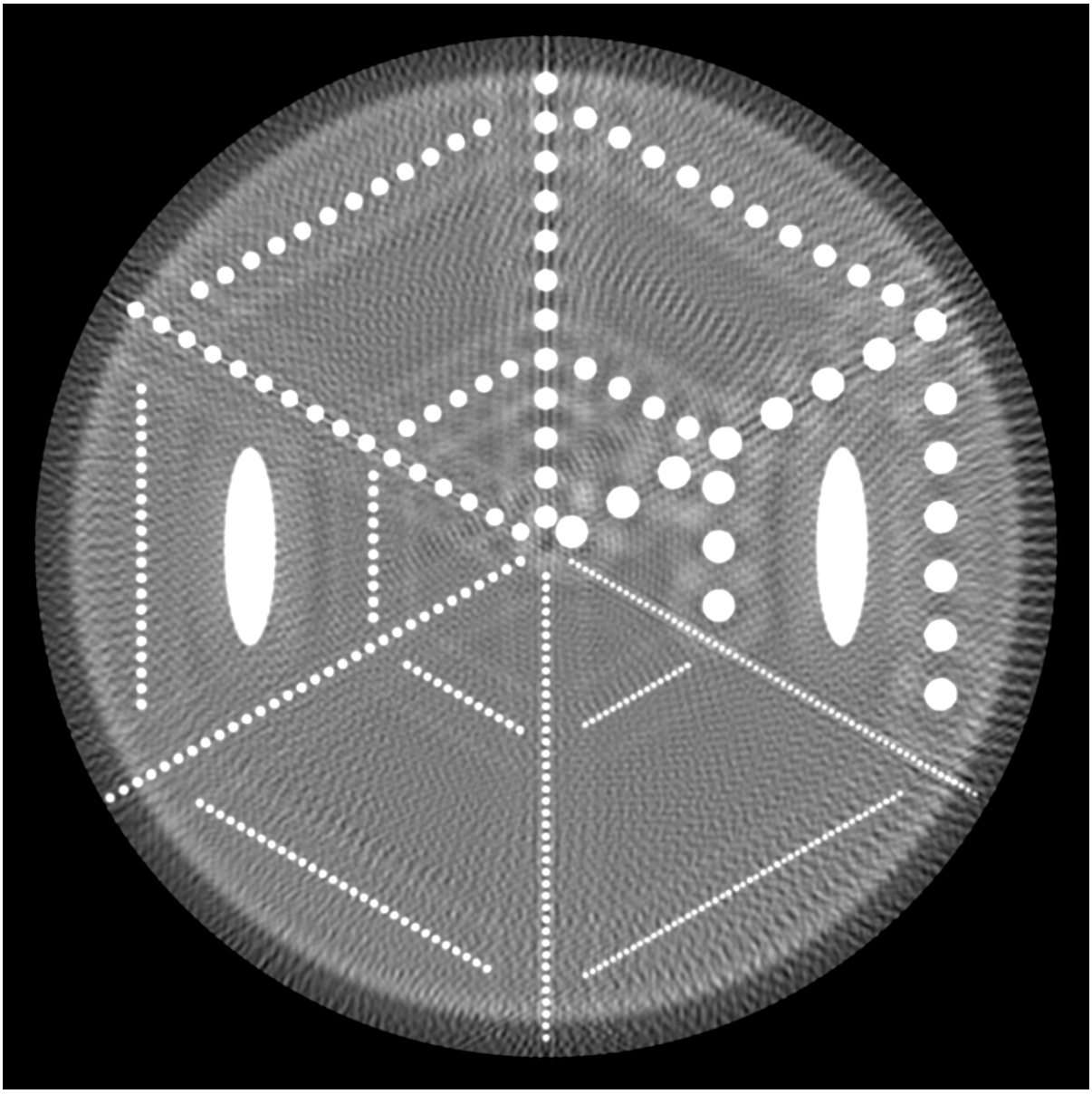

Figure 5.28: Reconstruction computed based on projection data sets of the phantom in Figure 5.13 collected by shifting the phantom along the X_2-axis using $0.5\,\mu$m increments in the interval $-20\,\mu$m to $20\,\mu$m. Reconstruction shown in narrow grayscale display window.

Chapter 6

Conclusions

6.1 Contributions

The contribution of this work is the theoretical development of several correction methods for distance-dependent point spread functions that affect images obtained by transmission electron microscopy and by transmission soft x-ray microscopy of biological specimens. The techniques developed here are based on image formation models for the two types of microscopy that we considered. They do not assume any particular point spread function and are general enough to be applicable when any reasonable blurring function is used. This is true up to the resolution limited by the frequencies that are zeroed during the imaging process and not present in the data, as those cannot be recovered by any method that uses only the data and the knowledge of the PSF to produce the reconstructions.

For transmission electron microscopy (TEM), we discussed the mathematical justification for a reconstruction method known as the defocus gradient backprojection and proposed a data correction method based on the frequency distance relation. We proved mathematically that the defocus gradient corrected backprojection technique that was proposed by Jensen and Kornberg [27] provides the inversion for the forward problem associated with image formation model for TEM. The distance-dependent blurring correction is performed using deconvolution built into the reconstruc-

tion. To allow the use of reconstruction algorithms other than backprojection, we developed a method of data correction based on the frequency distance relation that was first discovered by Lewitt et al. [36] in the context of SPECT. We showed that a similar relation between frequencies in the projection data and the defocus of blurring function also occurs in TEM. This technique handles data in Fourier space and provides a way of computing estimates of ideal projection data based on all distance-dependently blurred projection.

For transmission x-ray microscopy (TXM) we provided detailed analysis of the effects of distance-dependent blurring on projection data in presence of attenuation in the image formation model. We identified artifacts resulting from this interaction of blurring and attenuation and demonstrated that approximate reconstruction techniques that do not take into account the complete image formation model cannot correct for this artifact. We showed that in the mathematical limit, the ideal projection data can be computed by combining the data sets collected at all different positions along the optical axis.

The methods proposed in this thesis provide the theoretical basis for further development of correction and reconstruction tools applicable to imaging modalities that are affected by distance-dependent blurring.

6.2 Future Work

The theoretical developments presented in this dissertation can be extended in numerous ways.

We plan to continue our collaboration with biologists and physicists involved in data collection by actual devices. Although mathematical proofs demonstrate the correctness of our theoretical development, the real test of the methods will be their implementation and use with biological data.

Currently, the imaging in TEM is performed at the positive defocus to take advantage of the larger absolute values of the CTF - the contrast is transferred much better for lower frequencies when the defocus is positive than when it is zero or negative. From the point of view of recovering

higher frequencies, imaging at zero defocus would be more desirable since at that defocus the zeros of the CTF occur much later than for non-zero defocus. We plan to investigate correction techniques that could handle the reduced contrast transfer of low frequencies when imaging is done at zero defocus and, at the same time, take advantage of the better contrast transfer of the high frequencies.

The image formation model for TXM was proposed very recently by Oton et al. [41]. The correction method for distance-dependent blurring may need to change in the future as the model changes and as similar models are proposed for soft x-ray microscopes located at different synchrotrons and in laboratory based x-ray microscopes. The theoretical correction method based on data sets collected at different defocus points needs to be implemented and tested on biological data collected by the actual microscopes. The challenge in practice is the fact that the number of collected data sets is limited by the microscope setup and by the potential damage to the sample during the repeated data collection.

A related theoretical challenge in the area of TXM is development of inversion for the forward problem associated with the image formation model for TXM. Our proposed correction followed by backprojection provides the inverse under the assumption that the projection data are known for all defocus points. The image formation model for a single defocus point is non-linear and its inversion remains the subject of our future work.

Appendix A

The Impulse Symbol

The *1D Dirac delta* δ is a generalized function on $\mathbb{R}$ whose defining property is that, for any function $f : \mathbb{R} \to \mathbb{R}$ and for any $\boldsymbol{x} \in \mathbb{R}$,

$$\int_{\mathbb{R}} f(\boldsymbol{x})\, \delta\left(\boldsymbol{x} - \boldsymbol{x}'\right) \mathrm{d}\boldsymbol{x} = f(\boldsymbol{x}'), \tag{A.1}$$

or, equivalently,

$$\int_{\mathbb{R}} f(\boldsymbol{x})\, \delta\left(\boldsymbol{x}' - \boldsymbol{x}\right) \mathrm{d}\boldsymbol{x} = f(\boldsymbol{x}'), \tag{A.2}$$

We use several properties of the impulse symbol that we state here without proof in Table A.1. The proofs and derivations can be found in books, for example [40].

A.1 *n*-dimensional Impulse Functions

Using δ we define various *n-dimensional impulse functions*. ι is a multidimensional Dirac delta centered at the origin. It is defined by

$$\iota(\boldsymbol{x}) = \delta(x_1) \ldots \delta(x_n). \tag{A.3}$$

κ is a multidimensional Dirac delta centered at an arbitrary point $\widehat{\boldsymbol{x}} \in \mathbb{R}^n$. It is defined by

$$\kappa(\boldsymbol{x}) = \delta(\widehat{x}_1 - x_1) \ldots \delta(\widehat{x}_n - x_n). \tag{A.4}$$

Various Fourier transforms of ι and κ are listed in Table A.1.

A.2 Rotation of n-dimensional Impulse Function

An arbitrary rotation of the impulse function κ defined in Eq. (A.4) is computed according to the rotation operator $\mathscr{R}^n$ of Eq. (2.20) to be

$$\left[\mathscr{R}^n \kappa\right](\boldsymbol{\theta}, \boldsymbol{x}) = \delta\left(\widehat{x}_1 - x_1^F(\boldsymbol{\theta})\right) \ldots \delta\left(\widehat{x}_n - x_n^F(\boldsymbol{\theta})\right). \tag{A.13}$$

For this particular function, the rotation can be computed in an alternative way that is more useful in derivations of several proofs in this dissertation. This alternative form is

$$\delta\left(\widehat{x}_1^B(\boldsymbol{\theta}) - x_1\right) \ldots \delta\left(\widehat{x}_n^B(\boldsymbol{\theta}) - x_n\right). \tag{A.14}$$

We show that both forms are equivalent by demonstrating that they define the same linear operator, provided by the defining property of Dirac delta in Eqs. (A.1) and (A.2), on functions.

Let

$$f(\mathbf{a}) = \int_{\mathbb{R}^n} f(\mathbf{x})\, \delta\left(\widehat{x}_1 - x_1^F(\boldsymbol{\theta})\right) \ldots \delta\left(\widehat{x}_n - x_n^F(\boldsymbol{\theta})\right) \mathrm{d}\boldsymbol{x}$$

and

$$f(\mathbf{b}) = \int_{\mathbb{R}^n} f(\mathbf{x})\, \delta\left(\widehat{x}_1^B(\boldsymbol{\theta}) - x_1\right) \ldots \delta\left(\widehat{x}_n^B(\boldsymbol{\theta}) - x_n\right) \mathrm{d}\boldsymbol{x}.$$

We need to show that $\mathbf{a}$ and $\mathbf{b}$ have the same value. In what follows we use the definitions of $\boldsymbol{x}^F(\boldsymbol{\theta})$

Description	Property	
$x, \xi \in \mathbb{R}$		
integral of $\delta(x-\widehat{x})$	$\int_{\mathbb{R}} \delta(x-\widehat{x})\,\mathrm{d}x = 1$	
1D Fourier transform of $\delta(x)$	$[\mathscr{F}_x \delta](\xi) = \left(\frac{1}{2\pi}\right)^{1/2}$	$(A.5)$
1D inverse Fourier transform of a constant function whose value everywhere is equal to $(2\pi)^{-1/2}$	$\delta(x) = \left[\mathscr{F}_\xi^{-1}\left(\left(\frac{1}{2\pi}\right)^{1/2}\right)\right](x)$	$(A.6)$
integral of the exponential function	$\delta(x) = \frac{1}{2\pi}\int_{\mathbb{R}} \mathrm{e}^{\mathrm{i}x\xi}\mathrm{d}\xi$	$(A.7)$
$\boldsymbol{x}, \boldsymbol{\xi} \in \mathbb{R}^n, \qquad \iota(\boldsymbol{x}) = \delta(x_1)\ldots\delta(x_n)$		
n-dimensional Fourier transform of ι	$[\mathscr{F}_{\boldsymbol{x}}\iota](\boldsymbol{\xi}) = \left(\frac{1}{2\pi}\right)^{n/2},$	$(A.8)$
$(n-1)$-dimensional Fourier transform of ι	$\left[\mathscr{F}_{x_1,\ldots,x_{n-1}}\iota\right](\xi_1,\ldots,\xi_{n-1},x_n) = \left(\frac{1}{2\pi}\right)^{(n-1)/2}\delta(x_n),$	$(A.9)$
integral of the n-dimensional exponential function	$\iota(x) = \left(\frac{1}{2\pi}\right)^n \int_{\mathbb{R}^n} \mathrm{e}^{\mathrm{i}\langle \boldsymbol{x},\boldsymbol{\xi}\rangle}\mathrm{d}\boldsymbol{\xi}$	$(A.10)$
$\boldsymbol{x}, \boldsymbol{\xi} \in \mathbb{R}^n, \qquad \kappa(\boldsymbol{x}) = \delta(\widehat{x}_1 - x_1)\ldots\delta(\widehat{x}_n - x_n)$		
n-dimensional Fourier transform of κ	$[\mathscr{F}_{\boldsymbol{x}}\kappa](\boldsymbol{\xi}) = \left(\frac{1}{2\pi}\right)^{n/2}\mathrm{e}^{-\mathrm{i}\langle\widehat{\boldsymbol{x}},\boldsymbol{\xi}\rangle}$	$(A.11)$
$(n-1)$-dimensional Fourier transform of κ	$\left[\mathscr{F}_{x_1,\ldots,x_{n-1}}\kappa\right](\xi_1,\ldots,\xi_{n-1},x_n) = \left(\frac{1}{2\pi}\right)^{(n-1)/2}\delta(\widehat{x}_n - x_n)\,\mathrm{e}^{-\mathrm{i}(\widehat{x}_1\xi_1+\ldots+\widehat{x}_{n-1}\xi_{n-1})}$	$(A.12)$

Table A.1: Properties of the Dirac delta function.

of Eq. (2.10) and $\mathbf{x}^B(\theta)$ of Eq. (2.11). Observe that a is a solution to the equation

$$\widehat{\mathbf{x}} - D_n^{-1}\mathbf{x} = 0 \tag{A.15}$$

and b is a solution to the equation

$$\mathbf{x} - D_n\widehat{\mathbf{x}} = 0. \tag{A.16}$$

Multiplying the first of these equations by the matrix D_n we obtain the second equation. This implies that a and b are in fact the same, and the two different forms of the expressions for $\mathscr{R}\kappa$ are equivalent

$$\begin{aligned}[\mathscr{R}^n\kappa](\boldsymbol{\theta},\boldsymbol{x}) &= \delta\left(\widehat{x}_1 - x_1^F(\boldsymbol{\theta})\right)\ldots\delta\left(\widehat{x}_n - x_n^F(\boldsymbol{\theta})\right) \\ &= \delta\left(\widehat{x}_1^B(\boldsymbol{\theta}) - x_1\right)\ldots\delta\left(\widehat{x}_n^B(\boldsymbol{\theta}) - x_n\right).\end{aligned} \tag{A.17}$$

Appendix B

Detailed Derivation for Parts of Proof of Theorem 2.1

In the proof of Theorem 2.1 the vector $\boldsymbol{z} \in \mathbb{R}^n$ is defined as $\boldsymbol{z} = D_n^{-1}\left(R_{10}^n \circ \boldsymbol{x}^B(\boldsymbol{\theta})\right)$, the vector $\boldsymbol{x}$ is an arbitrary vector in $\mathbb{R}^n$, and the vector $\boldsymbol{\beta} \in \mathbb{R}^n$ is defined as $\boldsymbol{\beta} = D_n^{-1} R_{01}^n$.

We show that $\boldsymbol{z} = \boldsymbol{x} - \langle \boldsymbol{x}, \boldsymbol{\beta} \rangle \boldsymbol{\beta}$ separately for the cases of $n = 2$ and $n = 3$.

Case 1. $n = 2$. The definitions of D_2^{-1} and $\boldsymbol{x}^B(\boldsymbol{\theta})$ follow from Eqs. (2.1) and (2.9), respectively. The operator $\circ$ denotes the Hadamard product (element-wise product) of two matrices of the same size.

$$\boldsymbol{z} = D_2^{-1}\left(\begin{pmatrix} 1 \\ 0 \end{pmatrix} \circ \boldsymbol{x}^B(\boldsymbol{\theta})\right) = \begin{pmatrix} \cos\theta_1 & \sin\theta_1 \\ -\sin\theta_1 & \cos\theta_1 \end{pmatrix}\left(\begin{pmatrix} 1 \\ 0 \end{pmatrix} \circ \begin{pmatrix} x_1^B(\boldsymbol{\theta}) \\ x_1^B(\boldsymbol{\theta}) \end{pmatrix}\right)$$

$$= \begin{pmatrix} x_1^B(\boldsymbol{\theta})\cos\theta_1 \\ -x_1^B(\boldsymbol{\theta})\sin\theta_1 \end{pmatrix}, \tag{B.1}$$

$$\boldsymbol{\beta} = D_2^{-1}\begin{pmatrix} 0 \\ 1 \end{pmatrix} = \begin{pmatrix} \cos\theta_1 & \sin\theta_1 \\ -\sin\theta_1 & \cos\theta_1 \end{pmatrix}\begin{pmatrix} 0 \\ 1 \end{pmatrix} = \begin{pmatrix} \sin\theta_1 \\ \cos\theta_1 \end{pmatrix}, \tag{B.2}$$

$$\langle \boldsymbol{x}, \boldsymbol{\beta} \rangle = x_1 \sin\theta_1 + x_2 \cos\theta_1, \tag{B.3}$$

$$\langle \boldsymbol{x}, \boldsymbol{\beta} \rangle \boldsymbol{\beta} = \begin{pmatrix} x_1 \sin^2\theta_1 + x_2 \sin\theta_1 \cos\theta_1 \\ x_1 \sin\theta_1 \cos\theta_1 + x_2 \cos^2\theta_1 \end{pmatrix}, \tag{B.4}$$

$$\begin{aligned} \boldsymbol{x} - \langle \boldsymbol{x}, \boldsymbol{\beta} \rangle \boldsymbol{\beta} &= \begin{pmatrix} x_1 - x_1 \sin^2\theta_1 - x_2 \sin\theta_1 \cos\theta_1 \\ x_2 - x_1 \sin\theta_1 \cos\theta_1 - x_2 \cos^2\theta_1 \end{pmatrix} \\ &= \begin{pmatrix} x_1 \cos^2\theta_1 - x_2 \sin\theta_1 \cos\theta_1 \\ -x_1 \sin\theta_1 \cos\theta_1 + x_2 \sin^2\theta_1 \end{pmatrix} \\ &= \begin{pmatrix} (x_1 \cos\theta_1 - x_2 \sin\theta_1)\cos\theta_1 \\ (-x_1 \cos\theta_1 + x_2 \sin\theta_1)\sin\theta_1 \end{pmatrix} = \begin{pmatrix} x_1^B(\boldsymbol{\theta})\cos\theta_1 \\ -x_1^B(\boldsymbol{\theta})\sin\theta_1 \end{pmatrix}. \end{aligned} \tag{B.5}$$

Case 2. $n = 3$. The definitions of D_3^{-1} and $\boldsymbol{x}^B(\boldsymbol{\theta})$ follow from Eqs. 2.4 and 2.11, respectively. The operator $\circ$ denotes the Hadamard product (element-wise product) of two matrices of the same size.

$$\begin{aligned} \boldsymbol{z} &= D_3^{-1} \left(\begin{pmatrix} 1 \\ 1 \\ 0 \end{pmatrix} \circ \boldsymbol{x}^B(\boldsymbol{\theta}) \right) = \\ &= \begin{pmatrix} \cos\theta_1\cos\theta_2 & \sin\theta_1 & -\cos\theta_1\sin\theta_2 \\ -\sin\theta_1\cos\theta_2 & \cos\theta_1 & \sin\theta_1\sin\theta_2 \\ \sin\theta_2 & 0 & \cos\theta_2 \end{pmatrix} \left(\begin{pmatrix} 1 \\ 1 \\ 0 \end{pmatrix} \circ \begin{pmatrix} x_1^B(\boldsymbol{\theta}) \\ x_2^B(\boldsymbol{\theta}) \\ x_3^B(\boldsymbol{\theta}) \end{pmatrix} \right) \\ &= \begin{pmatrix} x_1^B(\boldsymbol{\theta})\cos\theta_1\cos\theta_2 + x_2^B(\boldsymbol{\theta})\sin\theta_1 \\ -x_1^B(\boldsymbol{\theta})\sin\theta_1\cos\theta_2 + x_2^B(\boldsymbol{\theta})\cos\theta_1 \\ x_1^B(\boldsymbol{\theta})\sin\theta_2 \end{pmatrix}, \end{aligned} \tag{B.6}$$

$$\boldsymbol{\beta} = D_3^{-1} \begin{pmatrix} 0 \\ 0 \\ 1 \end{pmatrix} = \begin{pmatrix} \cos\theta_1\cos\theta_2 & \sin\theta_1 & -\cos\theta_1\sin\theta_2 \\ -\sin\theta_1\cos\theta_2 & \cos\theta_1 & \sin\theta_1\sin\theta_2 \\ \sin\theta_2 & 0 & \cos\theta_2 \end{pmatrix} \begin{pmatrix} 0 \\ 0 \\ 1 \end{pmatrix}$$

$$= \begin{pmatrix} -\cos\theta_1 \sin\theta_2 \\ \sin\theta_1 \sin\theta_2 \\ \cos\theta_2 \end{pmatrix}, \tag{B.7}$$

$$\langle \boldsymbol{x}, \boldsymbol{\beta} \rangle = -x_1 \cos\theta_1 \sin\theta_2 + x_2 \sin\theta_1 \sin\theta_2 + x_3 \cos\theta_2, \tag{B.8}$$

$$\begin{aligned} \langle \boldsymbol{x}, \boldsymbol{\beta} \rangle \boldsymbol{\beta} &= \begin{pmatrix} -\cos\theta_1 \sin\theta_2 \left(-x_1 \cos\theta_1 \sin\theta_2 + x_2 \sin\theta_1 \sin\theta_2 + x_3 \cos\theta_2\right) \\ \sin\theta_1 \sin\theta_2 \left(-x_1 \cos\theta_1 \sin\theta_2 + x_2 \sin\theta_1 \sin\theta_2 + x_3 \cos\theta_2\right) \\ \cos\theta_2 \left(-x_1 \cos\theta_1 \sin\theta_2 + x_2 \sin\theta_1 \sin\theta_2 + x_3 \cos\theta_2\right) \end{pmatrix} \\ &= \begin{pmatrix} x_1 \cos^2\theta_1 \sin^2\theta_2 - x_2 \sin\theta_1 \cos\theta_1 \sin^2\theta_2 - x_3 \cos\theta_1 \sin\theta_2 \cos\theta_2 \\ -x_1 \sin\theta_1 \cos\theta_1 \sin^2\theta_2 + x_2 \sin^2\theta_1 \sin^2\theta_2 + x_3 \sin\theta_1 \sin\theta_2 \cos\theta_2 \\ -x_1 \cos\theta_1 \sin\theta_2 \cos\theta_2 + x_2 \sin\theta_1 \sin\theta_2 \cos\theta_2 + x_3 \cos^2\theta_2 \end{pmatrix}, \end{aligned} \tag{B.9}$$

$$\begin{aligned} \boldsymbol{x} - \langle \boldsymbol{x}, \boldsymbol{\beta} \rangle \boldsymbol{\beta} = \\ &= \begin{pmatrix} x_1 - x_1 \cos^2\theta_1 \sin^2\theta_2 + x_2 \sin\theta_1 \cos\theta_1 \sin^2\theta_2 + x_3 \cos\theta_1 \sin\theta_2 \cos\theta_2 \\ x_2 + x_1 \sin\theta_1 \cos\theta_1 \sin^2\theta_2 - x_2 \sin^2\theta_1 \sin^2\theta_2 - x_3 \sin\theta_1 \sin\theta_2 \cos\theta_2 \\ x_3 + x_1 \cos\theta_1 \sin\theta_2 \cos\theta_2 - x_2 \sin\theta_1 \sin\theta_2 \cos\theta_2 - x_3 \cos^2\theta_2 \end{pmatrix} \\ &= \begin{pmatrix} x_1 - x_1 \cos^2\theta_1 + x_1 \cos^2\theta_1 \cos^2\theta_2 \\ \quad + x_2 \sin\theta_1 \cos\theta_1 - x_2 \sin\theta_1 \cos\theta_1 \cos^2\theta_2 + x_3 \cos\theta_1 \sin\theta_2 \cos\theta_2 \\ x_2 + x_1 \sin\theta_1 \cos\theta_1 - x_1 \sin\theta_1 \cos\theta_1 \cos^2\theta_2 \\ \quad - x_2 \sin^2\theta_1 + x_2 \sin^2\theta_1 \cos^2\theta_2 - x_3 \sin\theta_1 \sin\theta_2 \cos\theta_2 \\ x_1 \cos\theta_1 \sin\theta_2 \cos\theta_2 - x_2 \sin\theta_1 \sin\theta_2 \cos\theta_2 + x_3 \sin^2\theta_2 \end{pmatrix} \\ &= \begin{pmatrix} (x_1 \cos\theta_1 \cos\theta_2 - x_2 \sin\theta_1 \cos\theta_2 + x_3 \sin\theta_2) \cos\theta_1 \cos\theta_2 \\ \quad + (x_1 \sin\theta_1 + x_2 \cos\theta_1) \sin\theta_1 \\ (-x_1 \cos\theta_1 \cos\theta_2 + x_2 \sin\theta_1 \cos\theta_2 - x_3 \sin\theta_2) \sin\theta_1 \cos\theta_2 \\ \quad + (x_1 \sin\theta_1 + x_2 \cos\theta_1) \cos\theta_1 \\ (x_1 \cos\theta_1 \cos\theta_2 - x_2 \sin\theta_1 \cos\theta_2 + x_3 \sin\theta_2) \sin\theta_2 \end{pmatrix} \\ &= \begin{pmatrix} x_1^B(\boldsymbol{\theta}) \cos\theta_1 \cos\theta_2 + x_2^B(\boldsymbol{\theta}) \sin\theta_1 \\ -x_1^B(\boldsymbol{\theta}) \sin\theta_1 \cos\theta_2 + x_2^B(\boldsymbol{\theta}) \cos\theta_1 \\ x_1^B(\boldsymbol{\theta}) \sin\theta_2 \end{pmatrix} \end{aligned} \tag{B.10}$$

Appendix C

Additional Figures for Section 5.5

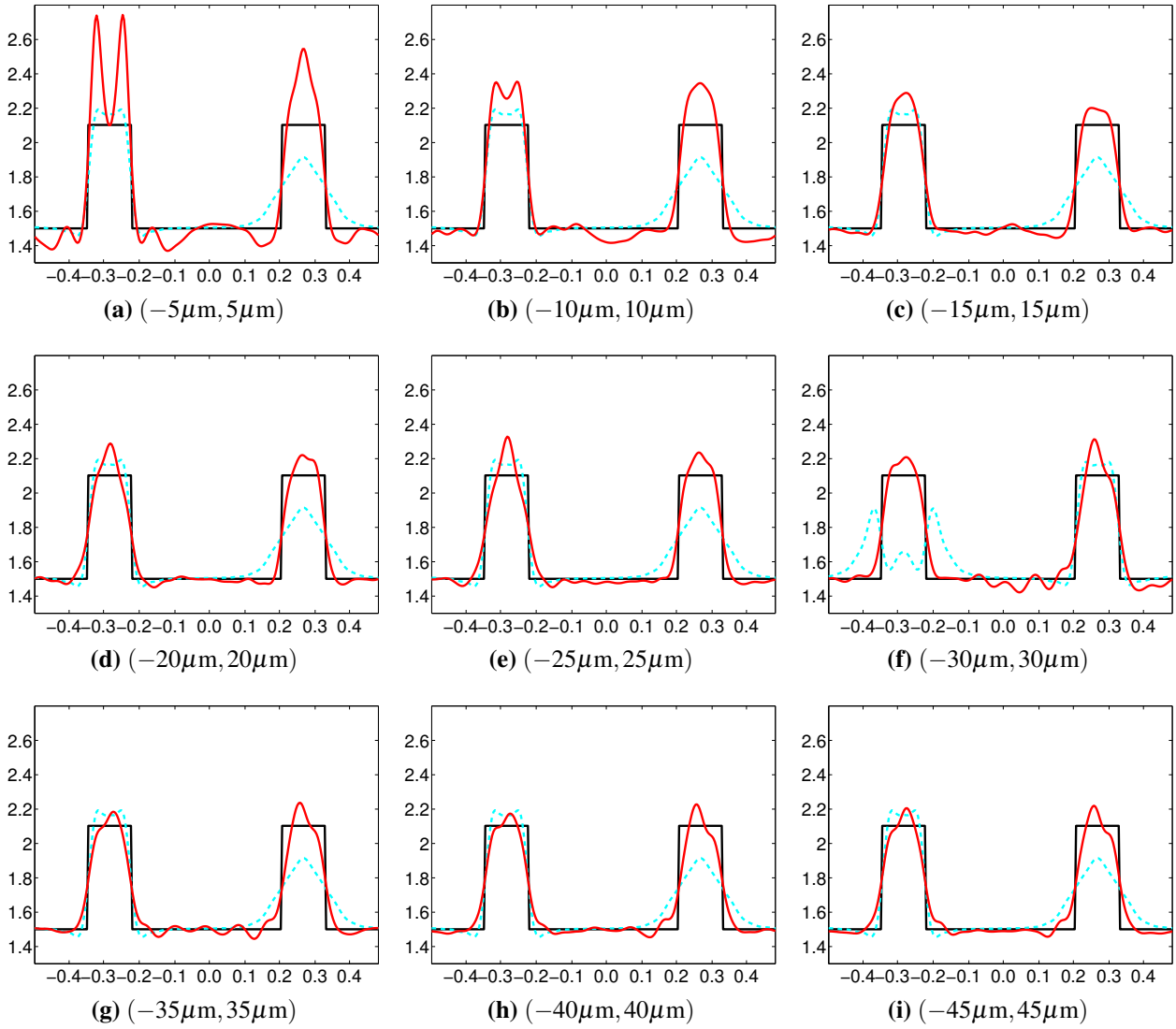

(a) $(-5\mu\text{m}, 5\mu\text{m})$ **(b)** $(-10\mu\text{m}, 10\mu\text{m})$ **(c)** $(-15\mu\text{m}, 15\mu\text{m})$

(d) $(-20\mu\text{m}, 20\mu\text{m})$ **(e)** $(-25\mu\text{m}, 25\mu\text{m})$ **(f)** $(-30\mu\text{m}, 30\mu\text{m})$

(g) $(-35\mu\text{m}, 35\mu\text{m})$ **(h)** $(-40\mu\text{m}, 40\mu\text{m})$ **(i)** $(-45\mu\text{m}, 45\mu\text{m})$

Figure C.1: Three different types of projections of the phantom in Figure 5.1 for the angle $\theta_1 = 0$: the ideal microscope projection, $\mathscr{P}^2 v$ (solid black lines); attenuated distance-dependently blurred projections corrected for attenuation, $-\ln\left(1 - \mathscr{X}_h^2 v\right)$ (dashed light blue); projections obtained by combining data collected by shifting the zero-defocus plane along X_2-axis in the interval indicated in the subfigures using $5\,\mu$m increments resulting in increasing number of data sets from intervals increasing in size (red). The numbers of combined data sets are: (a) 3, (b) 5, (c) 7, (d) 9, (e) 11, (f) 13, (g) 15, (h) 17, (i) 19.

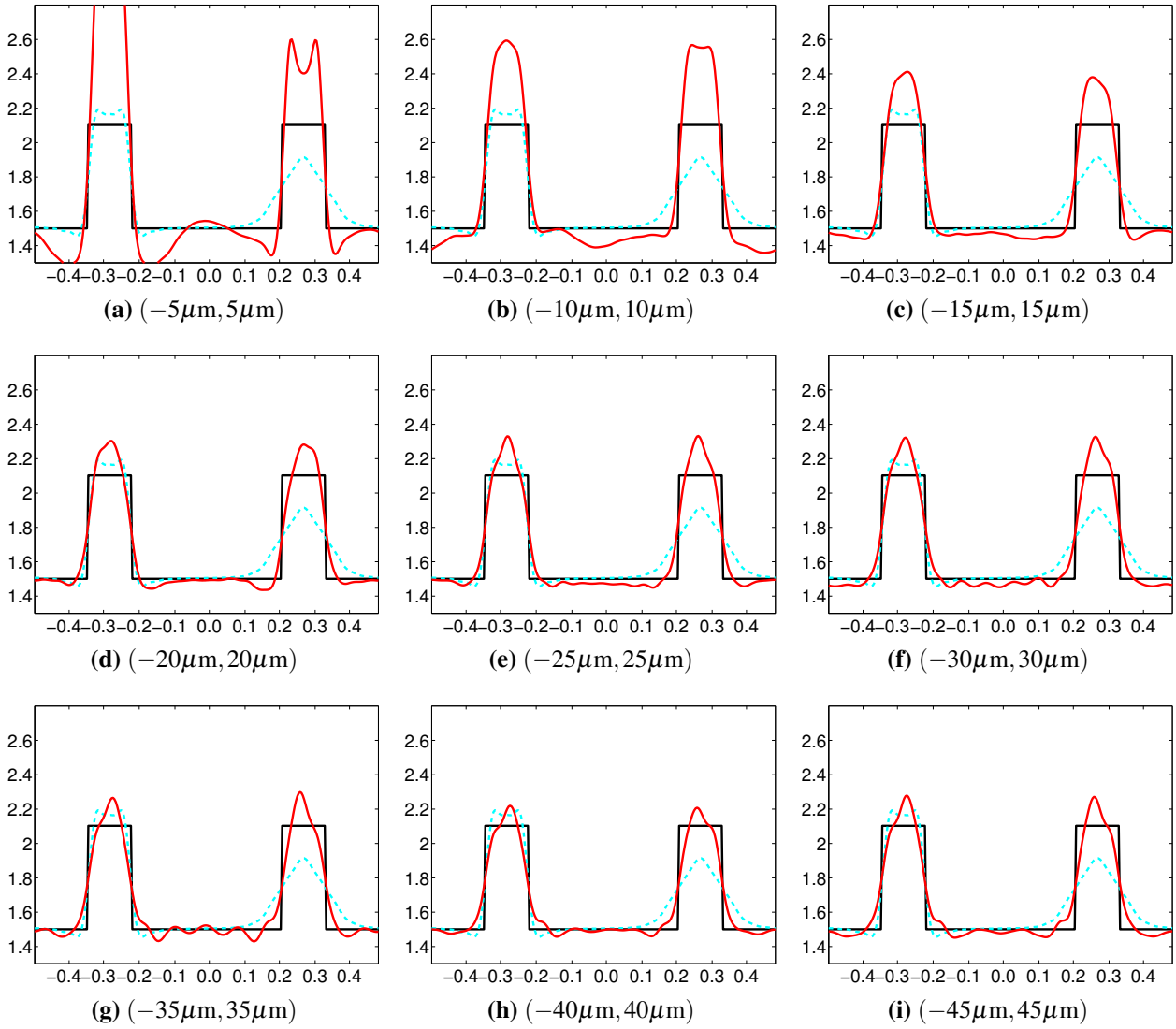

(a) $(-5\mu\text{m}, 5\mu\text{m})$ **(b)** $(-10\mu\text{m}, 10\mu\text{m})$ **(c)** $(-15\mu\text{m}, 15\mu\text{m})$

(d) $(-20\mu\text{m}, 20\mu\text{m})$ **(e)** $(-25\mu\text{m}, 25\mu\text{m})$ **(f)** $(-30\mu\text{m}, 30\mu\text{m})$

(g) $(-35\mu\text{m}, 35\mu\text{m})$ **(h)** $(-40\mu\text{m}, 40\mu\text{m})$ **(i)** $(-45\mu\text{m}, 45\mu\text{m})$

Figure C.2: Three different types of projections of the phantom in Figure 5.1 for the angle $\theta_1 = 0$: the ideal microscope projection, $\mathscr{P}^2 v$ (solid black lines); attenuated distance-dependently blurred projections corrected for attenuation, $-\ln\left(1 - \mathscr{X}_h^2 v\right)$ (dashed light blue); projections obtained by combining data collected by shifting the zero-defocus plane along X_2-axis in the interval indicated in the subfigures using $1\,\mu$m increments resulting in increasing number of data sets from intervals increasing in size (red). The numbers of combined data sets are: (a) 11, (b) 21, (c) 31, (d) 41, (e) 51, (f) 61, (g) 71, (h) 81, (i) 91.

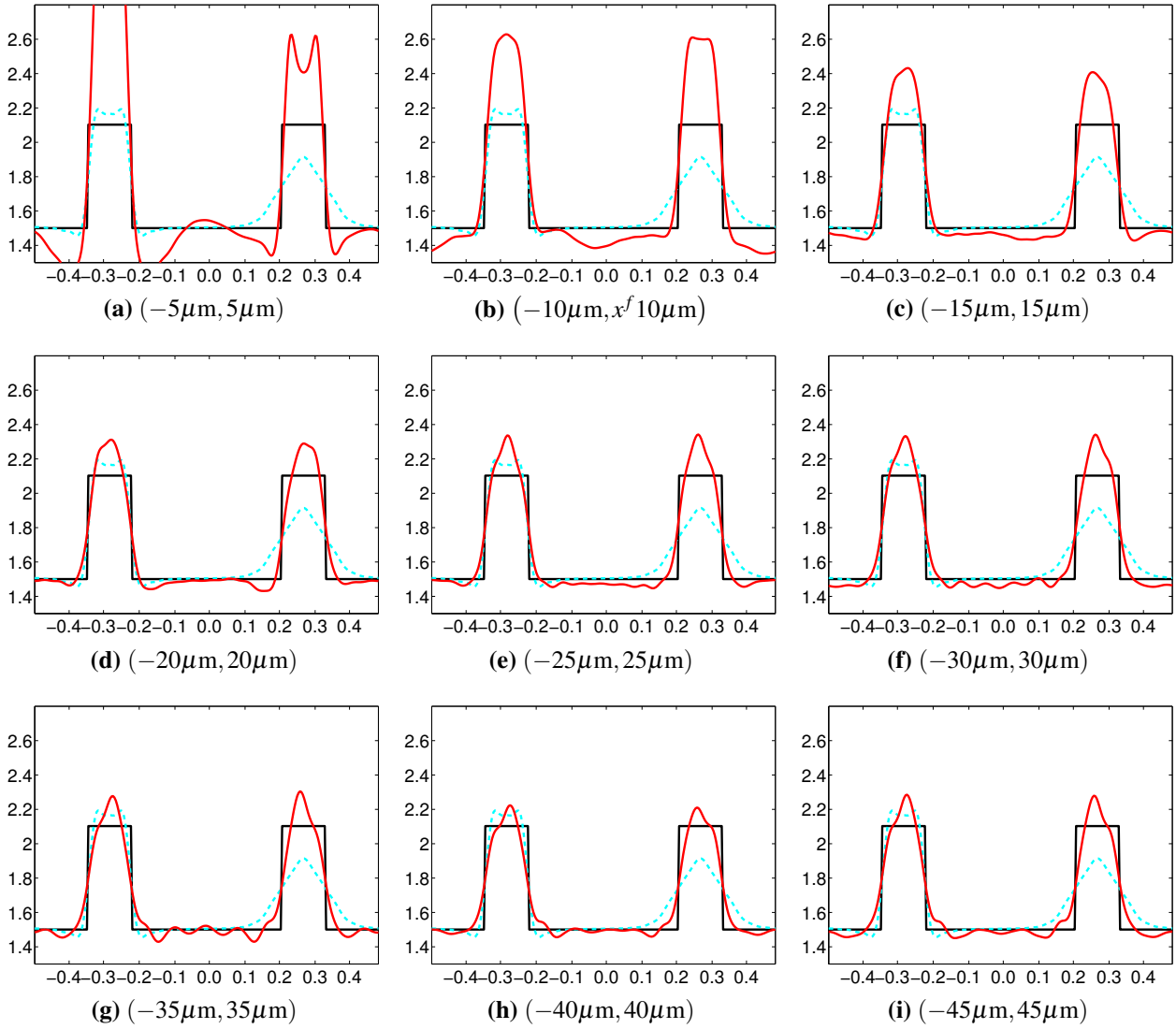

(a) $(-5\mu\text{m}, 5\mu\text{m})$ **(b)** $\left(-10\mu\text{m}, x^f 10\mu\text{m}\right)$ **(c)** $(-15\mu\text{m}, 15\mu\text{m})$

(d) $(-20\mu\text{m}, 20\mu\text{m})$ **(e)** $(-25\mu\text{m}, 25\mu\text{m})$ **(f)** $(-30\mu\text{m}, 30\mu\text{m})$

(g) $(-35\mu\text{m}, 35\mu\text{m})$ **(h)** $(-40\mu\text{m}, 40\mu\text{m})$ **(i)** $(-45\mu\text{m}, 45\mu\text{m})$

Figure C.3: Three different types of projections of the phantom in Figure 5.1 for the angle $\theta_1 = 0$: the ideal microscope projection, $\mathscr{P}^2 v$ (solid black lines); attenuated distance-dependently blurred projections corrected for attenuation, $-\ln\left(1 - \mathscr{X}_h^2 v\right)$ (dashed light blue); projections obtained by combining data collected by shifting the zero-defocus plane along X_2-axis in the interval indicated in the subfigures using $0.5\,\mu$m increments resulting in increasing number of data sets from intervals increasing in size (red). The numbers of combined data sets are: (a) 21, (b) 41, (c) 61, (d) 81, (e) 101, (f) 121, (g) 141, (h) 161, (i) 181.

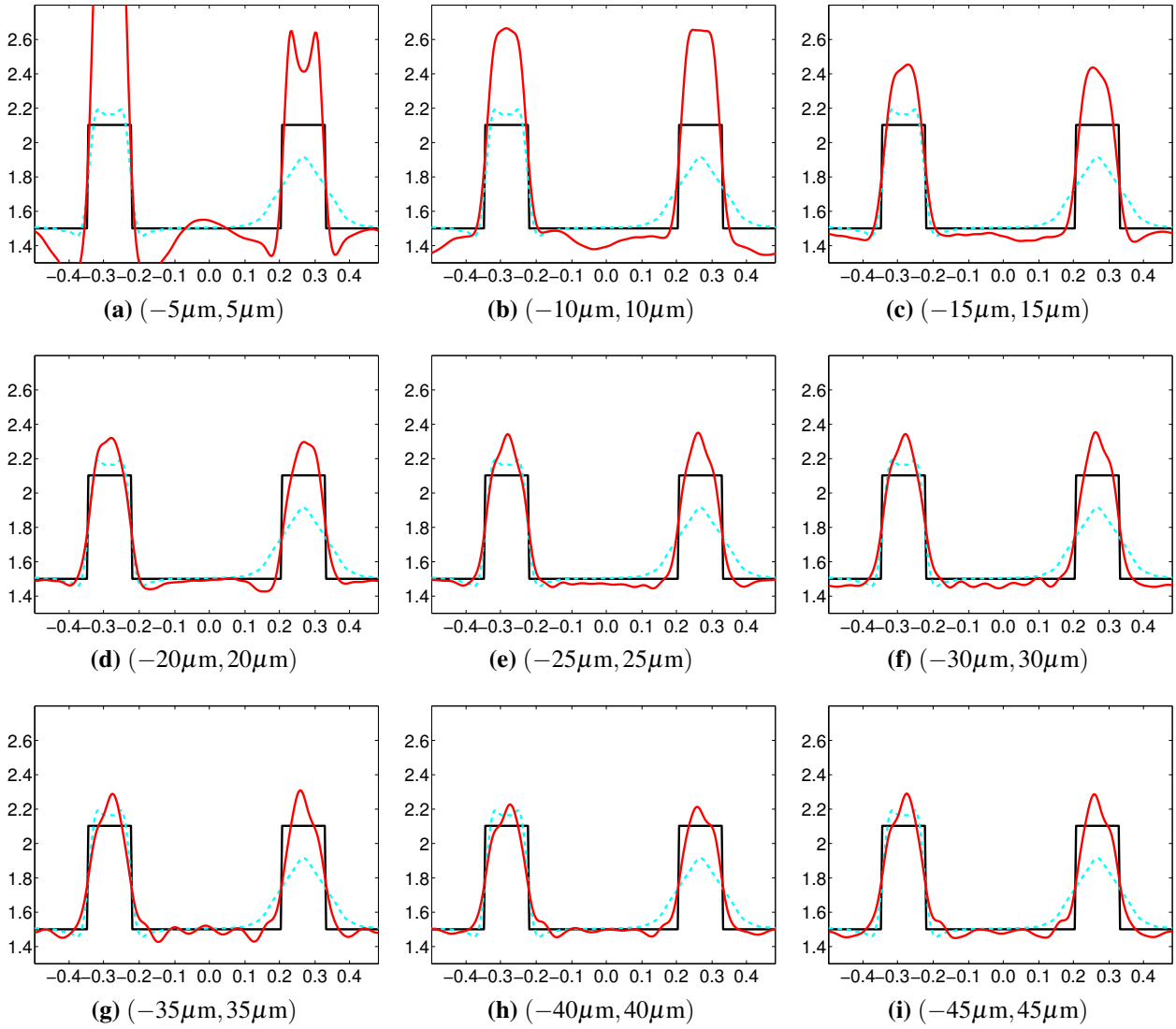

(a) $(-5\mu\text{m}, 5\mu\text{m})$ **(b)** $(-10\mu\text{m}, 10\mu\text{m})$ **(c)** $(-15\mu\text{m}, 15\mu\text{m})$

(d) $(-20\mu\text{m}, 20\mu\text{m})$ **(e)** $(-25\mu\text{m}, 25\mu\text{m})$ **(f)** $(-30\mu\text{m}, 30\mu\text{m})$

(g) $(-35\mu\text{m}, 35\mu\text{m})$ **(h)** $(-40\mu\text{m}, 40\mu\text{m})$ **(i)** $(-45\mu\text{m}, 45\mu\text{m})$

Figure C.4: Three different types of projections of the phantom in Figure 5.1 for the angle $\theta_1 = 0$: the ideal microscope projection, $\mathscr{P}^2 v$ (solid black lines); attenuated distance-dependently blurred projections corrected for attenuation, $-\ln\left(1 - \mathscr{X}_h^2 v\right)$ (dashed light blue); projections obtained by combining data collected by shifting the zero-defocus plane along X_2-axis in the interval indicated in the subfigures using $0.004\,\mu$m increments resulting in increasing number of data sets from intervals increasing in size (red). The numbers of combined data sets are: (a) 2501, (b) 5001, (c) 7501, (d) 10001, (e) 12501, (f) 15001, (g) 17501, (h) 20001, (i) 22501.

Bibliography

[1] D. Attwood. *Soft X-Rays and Extreme Ultraviolet Radiation: Principles and Applications*. Cambridge University Press, 2007.

[2] W. T. Baxter, R. A. Grassucci, H. Gao, and J. Frank. Determination of signal-to-noise ratios and spectral SNRs in cryo-EM low-dose imaging of molecules. *Journal of Structural Biology*, 166:126–132, 2009.

[3] D. B. Carlson, J. Gelb, V. Palshin, and J. E. Evans. Laboratory-based cryogenic soft x-ray tomography with correlative cryo-light and electron microscopy. *Microscopy and Microanalysis*, 19:22–29, 2013.

[4] Y. Censor, T. Elfving, and G. T. Herman. A method of iterative data refinement and is applications. *Mathematical Methods in the Applied Sciences*, 7:108–123, 1985.

[5] F. J. Chichón, M. J. Rodríguez, E. Pereiro, M. Chiappi, B. Perdiguero, P. Guttmann, S. Werner, S. Rehbein, G. Schneider, M. Esteban, and J. L. Carrascosa. Cryo x-ray nanotomography of vaccinia virus infected cells. *Journal of Structural Biology*, 177(2):202–211, 2012.

[6] M. Defrise. A factorization method for the 3D X-ray transform. *Inverse Problems*, 11:983–994, 1995.

[7] M. Defrise, P. E. Kinahan, D. W. Townsend, M. Christian, M. Sibomana, and D. F. Newport. Exact and approximate rebinning algorithms for 3-D PET data. *IEEE Transactions on Medidcal Imaging*, 16:145–158, 1997.

[8] J. N. Dubowy and G. T. Herman. An approach to the correction of distance-dependent defocus in electron microscopic reconstruction. In *IEEE International Conference on Image Processing*, volume 3, pages 748–51, 2005.

[9] P. R. Edholm and B. Lindholm. Novel properties of the Fourier decomposition of the sinogram. In *International Workshop on Physics and Engineering of Computerized Multidimentional Imaging and Processing*, volume 671, pages 8–18, 1986.

[10] M. Eibauer, Ch. Hoffmann, J. M. Plitzko, W. Baumeister, S. Nickell, and H. Engelhardt. Unraveling the structure of membrane proteins in situ by transfer function corrected cryo-electron tomography. *Journal of Structural Biology*, 180(3):488–496, 2012.

[11] Y. C. Eldar and M. Unser. Nonideal sampling and interpolation from noisy observations in shift-invariant spaces. *IEEE Transactions on Signal Processing*, 54:2636–2651, 2006.

[12] R. Falcone, C. Jacobsen, J. Kirz, S. Marchesini, D. Shapiro, and J. Spence. New directions in X-ray microscopy. *Contemporary Physics*, 52:293–318, 2011.

[13] J. J. Fernandez, S. Li, and R. A. Crowther. CTF determination and correction in electron cryotomography. *Ultramicroscopy*, 106:587–596, 2006.

[14] J. J. Fernandez, C. O. S. Sarzano, R. Marabini, and J. M. Carazo. Image processing and 3-D reconstruction in electron microscopy. *IEEE Signal Processing Magazine*, 23:84–94, 2006.

[15] J. Frank. *Three-Dimensional Electron Microscopy of Macromolecular Assemblies*. Oxford Univ. Press, 2006.

[16] M. Frigo and S. G. Johnson. The design and implementation of FFTW3. *Proceedings of the IEEE*, 93:216–231, 2005. Special issue on "Program Generation, Optimization, and Platform Adaptation".

[17] J. W. Goodman. *Introduction To Fourier Optics*. Roberts & Co., 2005.

[18] V. Guillemin and S. Sternberg. *Geometric Asymptotics*. AMS, 1977.

[19] E. Hanssen, Ch. Knoechel, M. Dearnley, M. W. Dixon, M. Le Gros, C. Larabell, and L. Tilley. Soft x-ray microscopy analysis of cell volume and hemoglobin content in erythrocytes infected with asexual and sexual stages of plasmodium falciparum. *Journal of Structural Biology*, 177(2):224–232, 2012.

[20] R. Henderson and P. N. T. Unwin. Three-dimensional model of purple membrane obtained by electron microscopy. *Nature*, 257:28–32, 1975.

[21] G. T. Herman. *Fundamentals of Computerized Tomography: Image Reconstruction from Projections.* Springer-Verlag, 2009.

[22] G. T. Herman and H. K. Tuy. Background from mathematical analysis. In P.C. Sabatier, editor, *Basic Mathods of Tomography and Inverse Problems*, pages 21–68. Institute of Physics Publishing, 1988.

[23] H. M. Hertz, O. von Hofsten, M. Bertilson, U. Vogt, A. Holmberg, J. Reinspach, D. Martz, M. Selin, A. E. Christakou, J. Jerlström-Hultqvist, and S. Svärd. Laboratory cryo soft x-ray microscopy. *Journal of Structural Biology*, 177:267–272, 2012.

[24] M. Howells, C. Jacobsen, T. Warwick, and A. Bos. Principles and applications of zone plate X-ray microscopes. In P.W. Hawkes and J.C.H. Spence, editors, *Science of Microscopy*, pages 835–926. Springer, 2007.

[25] Ch. Jacobsen, J. Kirz, and S. Williams. Resolution in soft x-ray microscopes. *Ultramicroscopy*, 47:55–79, 1992.

[26] G. J. Jensen and A. Briegel. How electron cryotomography is opening a new window onto prokaryotic ultrastructure. *Current Opinion in Structural Biology*, 17:260–267, 2007.

[27] G. J. Jensen and R. D. Kornberg. Defocus-gradient corrected back-projection. *Ultramicroscopy*, 84:57–64, 2000.

[28] I. G. Kazantsev, J. Klukowska, G. T. Herman, and L. Cernetic. Fully three-dimensional defocus-gradient corrected backprojection in cryoelectron microscopy . *Ultramicroscopy*, 110:1128–42, 2010.

[29] J. Kirz, Ch. Jacobsen, and M. Howells. Soft x-ray microscopes and their biological applications. *Quarterly Reviews of Biophysics*, 28:33–130, 1995.

[30] J. Klukowska and G. T. Herman. Reconstruction from microscopic projections with defocus-gradient and attenuation effects. In G. T. Herman and J. Frank, editors, *Computational Methods for Three-Dimensional Microscopy Reconstruction*. Springer, 2013. To appear.

[31] J. Klukowska, G. T. Herman, and I. G. Kazantsev. Correction of distance-dependent blurring in projection data for fully three-dimensional electron microscopic reconstruction. In *Biomedical Imaging: From Nano to Macro, 2010 IEEE International Symposium on*, pages 1117–1120, 2010.

[32] J. Klukowska, R. Davidi, and G. T. Herman. SNARK09 - a software package for reconstruction of 2D images from 1D projections. *Computer Methods and Programs in Biomedicine*, 110:424–440, 2013.

[33] M. Le Gros, C. G. Knoechel, M. Uchida, D. Y. Parkinson, G. McDermott, and C. A. Larabell. Visualizing subcellular organization using soft x-ray tomography. In E. H. Egelman, editor, *Comprehensive Biophysics, Volume 2: Biophysical Techniques for Characterization of Cells*, pages 90–110. Academic Press, 2012.

[34] A. Leis, B. Rockel, L. Andrees, and W. Baumeister. Visualizing cells at the nanoscale. *Trends in Biochemical Sciences*, 34:60–70, 2009.

[35] A. P. Leis, M. Beck, M. Gruska, C. Best, R. Hegerl, W. Baumeister, and J. W. Leis. Cryo-electron tomography of biological specimens. *IEEE Signal Processing Magazine*, 23:95–103, 2006.

[36] R. M. Lewitt, P. R. Edholm, and W. Xia. Fourier method for correction of depth-dependent collimator blurring. In *Society of Photo-Optical Instrumentation Engineers (SPIE) Conference Series*, volume 1092, pages 232–239, 1989.

[37] G. McDermott, M. Le Gros, C. G. Knoechel, M. Uchida, and C. A. Larabell. Soft X-ray tomography and cryogenic light microscopy: the cool combination in cellular imaging. *Trends Cell Biology*, 19:587–595, 2009.

[38] P. A. Midgley, E. P. W. Ward, A. B. Hungría, and J. M. Thomas. Nanotomography in the chemical, biological and materials sciences. *Chemical Society Reviews*, 36:1477–1494, 2007.

[39] W. G. Müller, J. B. Heymann, K. Nagashima, P. Guttmann, S. Werner, S. Rehbein, G. Schneider, and J. G. McNally. Towards an atlas of mammalian cell ultrastructure by cryo soft X-ray tomography. *Journal of Structural Biology*, 177:179–192, 2012.

[40] F. Natterer and F. Wübbeling. *Mathematical Methods in Image Reconstruction*. SIAM, 2001.

[41] J. Oton, C. O. S. Sorzano, E. Pereiro, J. Cuenca-Alba, R. Navarro, J. M. Carazo, and R. Marabini. Image formation in cellular X-ray microscopy. *Journal of Structural Biology*, 178: 29–37, 2012.

[42] M. Radermacher. Weighted back-projection methods. In J. Frank, editor, *Electron Tomography: Methods For Three-Dimensional Visualization of Structures in the Cell*. Springer, 2006.

[43] L. Reimer and H. Kohl. *Transmission Electron Microscopy: Physics of Image Formation*. Springer, 2008. ISBN 9780387400938.

[44] A. Rosenfeld and A. C. Kak. *Digital Picture Processing*, volume 1. Academic Press, 2 edition, 1982. ISBN 9780125973014.

[45] S. W. Rowland. Computer implementation of image reconstruction formulas. In G.T. Herman, editor, *Image Reconstruction from Projections: Implementation and Applications*, pages 9–79. Springer-Verlag, 1979.

[46] G. Schneider, P. Guttmann, S. Heim, S. Rehbein, F. Mueller, K. Nagashima, J. B. Heymann, W. G. Müller, and J. G. McNally. Three-dimensional cellular ultrastructure resolved by x-ray microscopy. *Nature Methods*, 7(12):985–987, 2010.

[47] C. O. S. Sorzano, R. Marabini, G. T. Herman, Y. Censor, and J. M. Carazo. Transfer function restoration in 3D electron microscopy via iterative data refinement. *Physics in Medicine and Biology*, 49:509–522, 2004.

[48] P. Thévenaz, T. Blu, and M. Unser. Interpolation revisited. *IEEE Transactions on Medical Imaging*, 19:739–758, 2000.

[49] T. Varslot, C. E. Yarman, M. Cheney, and B. Yazici. A variational approach to waveform design for synthetic-aperture imaging. *Inverse Problems and Imaging*, 1:577–592, 2007.

[50] L. M. Voortman, S. Stallinga, R. H. M. Schoenmakers, L. J. van Vliet, and B. Rieger. A fast algorithm for computing and correcting the CTF for tilted, thick specimens in TEM. *Ultramicroscopy*, 111:1029–1036, 2011.

[51] L. M. Voortman, E. M. Franken, L. J. van Vliet, and B. Rieger. Fast, spatially varying CTF correction in TEM. *Ultramicroscopy*, 118:26–34, 2012.

[52] D. Weiss, G. Schneider, B. Niemann, P. Guttmann, D. Rudolph, and G. Schmahl. Computed tomography of cryogenic biological specimens based on X-ray microscopic images. *Ultramicroscopy*, 84:185–197, 2000.

[53] H. Winkler and K. A. Taylor. Focus gradient correction applied to tilt series image data used in electron tomography. *Journal of Structural Biology*, 143:24–32, 2003.

[54] W. Xia, R. M. Lewitt, and P. R. Edholm. Fourier correction for spatially variant collimator blurring in SPECT. *IEEE Transactions on Medical Imaging*, 14:100–115, 1995.

[55] X. Zhang and Z. H. Zhou. Limiting factors in atomic resolution cryo electron microscopy: No simple tricks. *Journal of Structural Biology*, 175(3):253–263, 2011.

Index